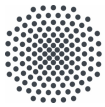

Universität Stuttgart

Numerical simulation of fracture in high-velocity impact

Von der Fakultät Informatik, Elektrotechnik und Informationstechnik der Universität Stuttgart sowie dem SC SimTech zur Erlangung der Würde eines Doktors der Naturwissenschaft (Dr. rer. nat.) genehmigten Abhandlung

Vorgelegt von

Marvin BECKER

aus Ostfildern

Hauptberichter: Prof. Dr. Miriam MEHL

Mitberichter: Dr. Tom DE VUYST
Prof. Dr. Thomas ERTL

Tag der mündlichen Prüfung: 23.02.2021

Institut für Parallele und Verteilte Systeme der Universität Stuttgart

2021

"Essentially, all models are wrong, but some are useful." (George E. P. Box)

Declaration of authorship

I, Marvin Becker, hereby certify that the dissertation entitled "Numerical simulation of fracture in high-velocity impact" is entirely my own work except where otherwise indicated. Passages and ideas from other sources have been clearly indicated.

Rheinfelden, March 4^{th}, 2021

Marvin Becker

Acknowledgments

This work was conducted at the Institute of Saint-Louis, which funded this study.

First of all, I would like to thank my supervisor at the University of Stuttgart, Miriam Mehl. Thanks, Miriam, for your patience, your shared expertise, your always positive attitude, and all the valuable discussions. Despite all your obligations at university and in private, I could always 100% rely on you. This inspired me to stay strong, to maintain friendships over distance and to not stop training despite all the workload and obligations. For the thesis, you always had the bigger picture in mind and guided me through this time. In particular, in times of corona, you respected and supported all my decisions. I would also like to thank you for your honest and constructive feedback on my work. This has greatly contributed to my personal and professional development.

I would like to thank my supervisor at ISL, Marina Seidl. Thanks, Marina, for your trust and support throughout this time, and your ability to listen. You realized the best working conditions possible at ISL, despite all the bureaucratic hurdles. Thanks to you, I was able to attend six conferences all around the world and extend my horizon. You were always there when I needed advice for the PhD and beyond.

I would like to thank Tom de Vuyst, the second reporter and supervisor of my stay abroad. Thanks, Tom, for realizing this stay abroad, for sharing your professional experience and for your positiveness. It was such an insightful collaboration in Hertfordshire, and I also enjoyed the off-topic discussions during lunch with you. Without your help, I would not have been able to implement such a big amount of functionality in three different code sources.

I would like to thank the third reporter Thomas Ertl for taking on this task. In particular, in defence research, this is not obvious. Furthermore, I have received great support from his group member Guido Reina in using the internal software. Thanks for that as well.

At ISL, I had the pleasure to work in a very harmonic and helpful group. Everyone was there for me, whenever I had questions, needed review of my work or other support. For the preparation and conduction of the experiments, I would like to thank Christian Doenlin, Norbert Faderl, Paul Beillard, Rainer Nüsing, and Thomas Wolf. For the professional support, I would like to thank, apart from my supervisors, Andreas Klavzar, Teresa Fras, and our group leader Jean-François Legendre. Many thanks to my two fellow PhD students, roommates, and friends: thanks, Magda and Evaristo for the nice time.
I also appreciated the days I worked in Stuttgart, where I was always welcome in a different office at SGS/SSE, and this way got to know everyone. Besides broadening my horizon in terms of sailing, I had valuable discussions on a more technical level which inspired my algorithms that are a central part of my work.

I acknowledge the support from *LS-DYNA®* in setting up the simulation and the technical discussions with Eduard Yreux, Julien Lacambre and Mhamed Souli.
I acknowledge the support from the team of *IMPETUS®* France, in particular Anthony Collé and Jérôme Limido. Thanks, Jérôme, for your feedback, insightful discussions, and support with the software *IMPETUS®*. It was always a pleasure to discuss on eye-level about modelling and recent developments in SPH.

For the thorough review of this work, I would like to thank Dawid Machalow, Evaristo Santamaria Ferraro,

Lisa Kriks, Lorin Kazaz, Louise Sarrabezolles, and Tobias Willmann.

Last but not least, I would like to thank my family and friends. In particular, I would like to thank Lorin, my mother Corina, and my grandparents Elsa and Eugen for hosting me in Stuttgart during all my appointments at the university. Furthermore, I would like to thank my team, trainers, and training partners for the mental support beyond the PhD. My final thanks go to my partner Lisa who has always supported me during this exciting, eventful but also exhausting time and has shown me true love.

Abstract

The description of high-velocity impact is highly complex from both the numerical and experimental side. For classical numerical methods, the description of the fracture behaviour of projectiles in terminal ballistics poses significant difficulties. For real-world experiments, the measurement is associated with considerable challenges. This makes it difficult to obtain validation data for numerical experiments in high-velocity impact.

The finite element method (FEM) has been used in state-of-the-art numerical models. With FEM, a fracture is usually described with the numerical erosion of elements. Smoothed-particle hydrodynamics (SPH) is a promising alternative that does not require such additional fracture criteria and has been used in the past for similar applications. Therefore, it is assumed to be advantageous for high-velocity impact applications as well. On the experimental side, real-world experiments can only be observed with flash X-ray if large dust development occurs. Flash X-ray creates shadow images, and the high-energy rays pass through low-density material, such as dust, in contrast to photons. Up to three individual images are photographed on one image plate. However, this parallax multi-exposure represents the dynamics of the impact only to a limited extent. A second observation technique that can capture more images without parallax is using high-speed cameras. However, they can only be used when there is little dust. As part of this work, a new observation method (Multi-anode X-ray cinematography) was used that combines the two methodologies and can take several single images, even in poor optical conditions.

The following questions arise from this analysis: (i) How can the existing numerical model be improved in such a way that it better represents the fracture behaviour? (ii) What adjustments have to be made to SPH to describe the high-velocity impact? (iii) How can the individual images of the new observation method be processed in such a way that a high-quality database is obtained for validating the numerical models? (iv) What are the requirements for a suitable validation attempt? (v) How can the results be transferred to other applications?

These questions are addressed with the following methodology: For (i), different material models were implemented, and modifications of the fracture criteria are suggested. Moreover, a validation case to determine suitable contact settings was developed. For (ii), the initial particle distribution was identified as a critical parameter to the stability of the solution. Different methodologies to create particle distributions were designed. For (iii), software based on the *OpenCV* image processing library was implemented to improve image quality and identify the fragment outline. Furthermore, a methodology is suggested to track fragments based on least-square minimization. For (iv), a validation case was developed that represents the fracture of small calibre projectiles. The impacting bodies consist of a well-characterized material, and the threat has a simple geometry that is not sensitive to projectile nutation. In this context, a methodology is proposed to compute the yawing angle based on the perforation holes of paper sheets that are placed in the flight axis. For (v), a black-box model was implemented that can generate an input deck for arbitrary impact scenarios.

The main findings of this research are: (i), that the modification of the fracture model is the most important aspect for a correct prediction of the fragmentation. (ii), that particle distributions based on the FEM discretization or a regular grid are unsuitable, and the most reasonable approach for cylindrical impactors is a particle distribution based on cylindrical coordinates. (iii), that fragments can be detected, and the motion of the remainder after impact can be calculated from the real-world experiments for our validation. (iv), that the yaw angle increases with flight distance. (v), that our developed model can be applied for

energetic fragments, multi-layered impactor, perforated plates and kinetic energy penetrators as well.

This work provides a central contribution to terminal ballistics modelling: (1.), the database of our experiments can be used for validation of further numerical models. (2.), FXRIP is used to evaluate upcoming experiments with the new observation technique. (3.), the black-box model allows to set up numerical models for different applications quickly and accelerates the development of protective structures.

Kurzfassung

Untersuchungen in der Endballistik sind sowohl numerisch als auch experimentell hochkomplex. Für klassische numerische Methoden stellt die Beschreibung des Bruchverhaltens große Schwierigkeiten dar. Bei realen Experimenten ist das Messen von Ergebnissen mit erheblichen Herausforderungen verbunden. Dadurch ist es komplex, Validierungsdaten für numerische Experimente im Bereich Hochgeschwindigkeitseinschlag zu extrahieren.

Bislang wird als numerische Methode die Finite-Elemente-Methode (FEM) angewendet. Zur Bruchbeschreibung werden hierbei in der Regel Elemente aufgrund von phänomenologischen Kriterien erodiert. Smoothed Particle Hydrodynamics (SPH) stellt eine vielversprechende Alternative dar, die ohne diese numerischen Kriterien Brüche simulieren kann und bisher bei ähnlichen Anwendungen verwendet wurde. Die realen Experimente können bei starker Staubentwicklung nur mit Flash X-ray abgelichtet werden. Flash X-ray erzeugt Schattenbilder durch hochenergetische Röntgenstrahlung, die Material mit geringer Dichte (z. B. Staubpartikel), im Gegensatz zu Photonen, durchdringt. Es werden hierbei bis zu drei Einzelbilder auf einer Trägerplatte abgelichtet. Durch diese parallaxenbehaftete Mehrfachbelichtung lässt sich jedoch die Dynamik des Einschlags nur bedingt darstellen. Eine weitere Observationsmethode, welche mehrere Bilder ohne Parallaxenfehler abbilden kann, ist das Ablichten mit einer Hochgeschwindigkeitskamera. Dieses Verfahren kann jedoch nur bei geringer Staubentwicklung verwendet werden. Im Rahmen dieser Arbeit wurde eine neue Observationsmethode (Multi-Anode X-Ray Cinematography) verwendet, welche die beiden Verfahren kombiniert, und mehrere Einzelbilder auch bei Staubentwicklung ablichten kann.

Aus dieser Analyse ergeben sich die folgenden Fragestellungen: (i) Wie kann das bestehende numerische Modell so verbessert werden, dass es das Bruchverhalten wirklichkeitsgetreuer darstellt? (ii) Welche Anpassungen müssen bei SPH durchgeführt werden, um den Hochgeschwindigkeitseinschlag korrekt zu beschreiben? (iii) Wie können die Einzelbilder der neuen Beobachtungsmethode so verarbeiten werden, dass eine hochwertige Datengrundlage zur Validierung der numerischen Modelle entsteht? (iv) Welche Anforderungen bestehen für einen realitätsnahen Validierungsversuch? (v) Lassen sich die Ergebnisse auf weitere Anwendungen übertragen?

Diese Fragestellungen wurden mit folgender Methodik behandelt: Für (i) wurden verschiedene Materialmodelle implementiert und Modifikationen der Bruchkriterien vorgeschlagen. Darüber hinaus dient der Entwurf eines weiteren Validierungsfalles dazu, geeignete Einstellungen des numerischen Kontaktes zu ermitteln. Für (ii) wurde die initiale Partikelverteilung als ein kritischer Parameter für die Stabilität der Lösung identifiziert. Im Rahmen dieser Arbeit wurden verschiedene Methoden entwickelt, um Partikelverteilungen zu erstellen. Für (iii) wurde im Rahmen dieser Arbeit eine Software (FXRIP) basierend auf der *OpenCV*-Bildverarbeitungsbibliothek implementiert. *OpenCV* diente dabei vor allem dazu, die Bildqualität zu verbessern und den Fragmentumriss zu identifizieren. Darüber hinaus wurde eine Methode zur Verfolgung von Fragmenten entworfen. Diese basiert auf der Minimierung der kleinsten Fehlerquadrate. Für (iv) wurde ein Validierungsfall zur Beschreibung des Bruchverhaltens von Kleinkalibergeschossen entwickelt. Dieser verwendet ein bereits charakterisiertes Material und eine einfache Geometrie, die unempfindlich bezüglich Projektilnutation (Gierwinkel) beim Aufprall ist. Zur Bestimmung des Gierwinkels wurden vor dem Experiment Papierbögen in der Flugachse platziert. Aufgrund der sich ergebenden Perforationslöcher wurde der Gierwinkel bestimmt. Für (v) wurde ein Black-Box-Modell implementiert, welches ein Eingabedeck für beliebige Aufprallszenarien generieren kann.

Die Hauptfolgerungen dieser Untersuchung ergaben: (i), dass die Modifikation des Bruchmodells der wichtigste Aspekt für eine korrekte Vorhersage der Fragmentierung ist. (ii), dass eine Partikelverteilung basierend auf der FEM-Diskretisierung oder einem regulären Gitter ungeeignet ist und stattdessen für zylinderförmige Penetratoren eine Partikelverteilung basierend auf Zylinderkoordinaten verwendet werden sollte. (iii), dass die Fragmente erkannt und die Bewegung des Restprojektils nach dem Aufprall aus den realen Experimenten für die Validierung berechnet werden können. (iv), dass der Gierwinkel in den Experimenten mit der Flugentfernung zunimmt. (v), dass unser Modell sowohl für energetische Fragmente, als auch mehrschalige Projektile, Lochplatten und Pfeilgeschosse verwendet werden kann.

Diese Arbeit liefert einen wesentlichen Beitrag zur endballistischen Modellierung: (1.) kann die Datenbank der Experimente zur Validierung weiterer numerischer Modelle verwendet werden. (2.) können mit FXRIP zukünftige Experimente mit der neuen Observationsmethode präzise und schnell ausgewertet werden. (3.) ermöglicht das Black-Box-Modell ein schnelles Aufsetzen von numerischen Modellen für verschiedene Anwendungsszenarien und beschleunigt die Entwicklung von Schutzstrukturen.

List of publications

Parts of this work has been previously published in peer-reviewed papers:

[1] Marvin Becker, Marina Seidl, Miriam Mehl, Mhamed Souli. Automatic mesh-generation (FEM /SPH) for HVI-simulations of arbitrary rotational symmetric impactors. In Proceedings of the 2019 15th Hypervelocity Impact Symposium. 2019 15th Hypervelocity Impact Symposium, 2019.

[2] Marvin Becker, Marina Seidl, Tom de Vuyst, Miriam Mehl, and Mhamed Souli. Numerical and experimental evaluation of natural fragmentation of explosively driven cylinders rings. In Proceedings of the Light-Weight Armor Group Symposium 2019, 2019.

Parts of this work has been previously published in non peer-reviewed papers:

[3] Marvin Becker, Marina Seidl, Miriam Mehl. Numerical ricochet model of a 7.62 mm projectile penetrating an armor steel plate. In 15th International LS-DYNA Users Conference, 2018.

[4] Norbert Faderl, Marvin Becker. High-speed 300keV flash X-ray cinematography for investigations of the ballistic impact behavior of target materials and structures. Technical report, Institute of Saint-Louis, 2018.

[5] Marvin Becker. FXRIP - flash X-ray image processing and analyzing software for ballistic impact applications. Technical report, Institute of Saint-Louis, 2019.

[6] Marvin Becker, Marina Seidl, Miriam Mehl, Mhamed Souli. Numerical and experimental investigation of SPH, SPG, and FEM for high-velocity impact applications. In Proceedigns of 12th European LS-DYNA Conference, 2019

[7] Marvin Becker. Fragment detection algorithm for postprocessing high velocity impact and natural fragmentation. In Proceedings of 8th GACM Colloquium on Computational Mechanics, 2019.

Parts of this work has been orally presented in conferences:

[8] Marvin Becker, Marina Seidl, Miriam Mehl, Mhamed Souli. A study on initial conditions in smoothed particle hydrdynamics modelling of high-velocity impact. In 2018 Nordic LS-DYNA User Conference, 2018

[9] Marvin Becker. Numerical ricochet model of a 7.62 mm projectile impacting an armor steel plate. In 7^{th} Budding Science Colloquium at ISL, 2018

[10] Marvin Becker. Fragmentation in SPH. 8th Budding Science Colloquium at ISL, 2019

Parts of this work has been presented in poster sessions:

[11] Marvin Becker. Numerical description of fracture during high velocity impact events. 11th SimTech Status Seminar, 2018

[12] Marvin Becker. Endballistisches Verhalten von 7.62mm Projektil-Surrogate. Angewandte Forschung für Verteidigung und Sicherheit in Deutschland, 2020

A publication still pending which describes part of Application I is work in progress.

Nomenclature

Abbreviations

ALE	Arbitrary Lagrangian Eulerian
AP	Armour Piercing
CFD	Computational Fluid Dynamics
CS	Cowper-Symonds
DBSCAN	Density-Based Spatial Clustering of Applications with Noise
DEM	Discrete Element Method
DYNA3D	Predecessor of *LS-DYNA*®
EB	External Ballistics
EOS	Equation Of State
FDM	Finite Difference Method
FEM	Finite Element Method
FVM	Finite Volume Method
FXR	Flash X-Ray
FXRIP	Flash X-Ray Image Processing software
HHA	High Hardness Armour steel
HVI	High-Velocity Impact
IB	Internal Ballistics
IMPETUS ®	Tailormade software for 3D numerical simulation of defence applications
IO	Input-Output
JC	Johnson-Cook

JWL	Jones-Wilkins-Lee (EOS)
LS-DYNA®	Multi-purpose, multiphysics, commercial simulation software package developed by LSTC
LSD	Linear-Spring-Dashpot
LSTC	Livermore Software Technology Corporation
MCM	Meshless Continuum Mechanics (PDE solver)
MD	Molecular Dynamics
MLS	Moving Least-Squares
MM	Meshless Method
NNA	Nearest-Neighbour Algorithm
PDE	Partial Differential Equation
PMA	Point Matching Algorithm
PRODAS	Projectile Rocket Ordnance Design and Analysis Software
PSED	Plastic Strain Energy Density
RHA	Rolled Homogenous Armour steel
RK	Rusinek-Klepacko
RKPM	Reproducing Kernel Particle Method
SHPB	Split-Hopkinson Pressure Bar
SPG	Smoothed-Particle Galerkin
SPH	Smoothed-Particle Hydrodynamics
STANAG	STANdardisation AGreement
TB	Terminal Ballistics
UHHA	Ultra-High Hardness Armour steel
XFEM	eXtended FEM

Mathematical Notations

$\mathcal{C}^n$	n times piecewise continuous function
$\dot{x}$	Time derivative
$\hat{x}$	Vector in principal directions
$\mathbb{R}$	Real numbers

$\nabla \cdot A$	Divergence of vector A
∇A	Gradient of vector A
$\mathcal{O}$	Landau O notation
$A : B$	Inner tensor product of A and B
$A \times B$	Outer tensor product of A and B
A^T	Transpose of A

Latin Symbols

$\boldsymbol{a}$	Acceleration
A	Area
b_{plate}	Plate bending
$\boldsymbol{b}$	Left Cauchy-Green tensor
$\boldsymbol{B}$	B-matrix (FEM)
$\bar{\boldsymbol{b}}$	Volume force
$\boldsymbol{C}$	Right Cauchy-Green tensor
c	Speed of sound
C^S	Viscous damping
C_D	Reduction in yield strength due to damping
$\tilde{C}$	Fourth order coefficient for elastic material response
d	Diameter
d_{P}	Depth of penetration
$\tilde{D}$	Damping factor
$\tilde{D}_{cr}$	Critical damping
D_c	Damage at failure
D	Damage
E	Young's modulus
f	Yield function / Weighting function (SPH)
$\boldsymbol{f}, \boldsymbol{f}_{\text{ext}}, \boldsymbol{f}_{\text{int}}$	Force (external, internal)
$\boldsymbol{F}$	Deformation gradient

h	Height / smoothing length (SPH)
$\boldsymbol{I}, \boldsymbol{I}^{dev}$	Second order unit tensor, Deviatoric second order unit tensor
J	Jacobian
k	Spring stiffness
l	Penetration depth (contact)
L, L_{red}	Length (Length reduction)
m	Mass of a body
$\boldsymbol{M}$	M-matrix (FEM)
$\boldsymbol{N}$	Shape function (FEM)
$\boldsymbol{n}$	Normal vector
p	Pressure [Pa]
q	Hardening function
r	Radius
$\boldsymbol{r}$	Position (SPH)
$\boldsymbol{s}$	Deviatoric stress tensor
S_i	Shock coefficients
$\boldsymbol{t}$	Tangential vector
t	Time
t_{if}	Interframe time
T (T_m, T_{cr}, T_{ch})	Temperature (melting, critical, characteristic)
$\boldsymbol{u}, \partial\boldsymbol{u}$	Displacement, Virtual displacement
$\boldsymbol{v}$, $\boldsymbol{v}_s$	Velocity (shock velocity)
V	Volume
V^*	Relative volume $V^* = \dfrac{V}{V_0}$
w	Width
W	Energy (W^{ext}, W^{int}, W^{kin}, W^p external, internal, kinetic, plastic)/ Kernel function (SPH)
$\boldsymbol{x}$	Eulerian coordinate
$\boldsymbol{X}$	Lagrangian coordinate

Greek Symbols

α	Thermal expansion coefficient
γ	Yaw angle
γ_0	Grüneisen parameter
$\dot{\gamma}$	Plastic multiplier
$\boldsymbol{\varepsilon}(\varepsilon_v, \bar{\varepsilon}^p)$	Strain (volumetric, equivalent plastic)
δ	Dirac delta function
ε $(\varepsilon_a, \varepsilon_d, \varepsilon_m)$	Error (approximation, discretisation, matching)
κ	Bulk modulus
η	Stress triaxiality
μ	Shear modulus
ν	Poisson ratio
Ω	Continous domain
ϕ	Deformation mapping / Oblique angle (NATO)
Π	Aritficial viscous pressure term
ρ	Density
$\boldsymbol{\sigma}$ $(\sigma_{eq},\ \sigma_m,\ \sigma_y)$	Cauchy stress tensor/ Stress (equivalent von-Mises, mean, yield)
$\boldsymbol{\tau}$	Kirchhoff stress
Θ	Lode angle
ξ	Local element coordinate (FEM)

LS-DYNA

DFACT	Damping factor, which determines the damping of kinetic energy (SPH)
FEM2SPH	Adaptively transform finite elements in SPH particles
ISOFT	SOFT-contact option similar to the FEM (SPH)
PFACT	Penalty factor, which influences the contact forces (SPH)
SFS/ SFM	Scaling factor slave / scaling factor master (FEM)
SOFT	SOFT-contact option (FEM)
SRAD	Minimum distance for two particles to be in contact (SPH)

Superscripts

$\hat{x}$	Principal value
x^M	Master
x^S	Slave
x^{dev}	Deviatoric part of tensor

Subscripts

x_c	Contact
x_{cr}	Critical
x_u	Dirichlet (boundary condition)
x_{el}	Elastic
x_0	Initial
x_σ	Neumann (boundary condition)
x_s	Smoothed variable
x_p	Plastic

Contents

1

Introduction

1.1 Motivation

Understanding the fracture and ricochet behaviour of small calibre ammunition is essential to design protective structures for close combat [45, 160].
Numerical simulation is a promising methodology to investigate these phenomena, which can only be measured to a certain extent in real-world. For this methodology, the high-velocity impact also poses difficulties as the model needs to capture complex physics. The impact initiates shock waves that propagate through the material, and the material deforms plastically due to high stresses. Furthermore, the plastic deformation induces heat and weakens the material until it ultimately fractures. An appropriate numerical model is required to describe the physical effects correctly on a macroscopic level to give predictive results. The state of the art discretisation method in terminal ballistics is the finite element method (FEM), which realises fracture with additional erosion criteria that are based on phenomenological observation. These phenomenologically-based erosion criteria are not always sufficient to describe a wide range of applications in terms of impact velocity, impact angle, and impactor shape. Thus, the approximation is not fully predictive yet. Instead, numerical simulations are mainly used as a postprocessing and visualisation tool of existing real-world experiments. It is not clear whether the numerical method, including time and spatial discretisation, or the underlying material and failure model, are unsuited for the corresponding problem.
Therefore, a detailed comparison of existing approximation techniques and fracture modelling approaches is required to identify a suitable approach. This work aims to develop a model that is predictive in a wide range of applications in terminal ballistics.

1.2 Methodology and definitions

This work combines different methodologies that we refer to frequently. This section outlines the main terminology and the corresponding abbreviations briefly. Due to conflicting use of some terms in literature, the following definitions also clarify our understanding of the terminology.

1.2.1 Numerical methods

We apply two different numerical methods in this work that are explained briefly. Chapter 3 explains and compares them in more detail.

Finite element method (FEM)

The FEM is the state of the art numerical approach in terminal ballistics to solve partial differential equations using a mesh-based discretisation. A basis that consists of shape functions approximate the solution in the computational domain. We use the method to predict the material response in three-dimensional structures.

Smoothed-particle hydrodynamics (SPH)

SPH is another numerical approach to solve partial differential equations. However, instead of a computational mesh, virtual particles contain all physical information and kernel functions describe the interactions between the SPH particles. We include SPH in our numerical model as it describes fracture in a more natural way.

State of the art methods in numerical modelling of HVI

Investigating TB behaviour with numerical simulations is essential to understand the underlying mechanisms during impact and develop better protective structures. Due to the complexity of the impact event, each impactor and the respective materials need thorough validation until they can be used predictively in a numerical model. E.g., the same material can have different properties based on how it is manufactured into its final shape. Therefore, many contributions deal with the validation of a numerical model of a specific impactor. Although the majority of publications still use FEM [27, 2, 111, 56, 10], there are also publications, in particular for hyper-velocity, that apply SPH [121, 150, 44, 124]. Bresciani et al. [32] gives a solution to combat the difficulty of modelling fracture in FEM (compare Section 3.2.5). The paper proposes a pre-fragmentation discretisation where the impactor consists of fragments that are connected with tied-contact and define surfaces where cracks can form without the need for node splitting. The authors observe better accordance with the results of HVI real-world experiments compared to the erosion criteria, but the methodology is not easy to apply as it requires preprocessing software to perform the pre-fragmentation. Besides Bresciani's approach, which improves the FEM for HVI applications, different new meshless methods (SPH and SPG in *LS-DYNA®*) have been developed that can be used for this purpose. HVI results are often used as a benchmark problem to validate new methods in this field [220, 216]. State of research updates for meshless methods in *LS-DYNA®* are shared on the Computational and Multi-scale Mechanics Group (CMMG) website [203].

As can be seen, the prediction of HVI-phenomena using numerical methods is not yet fully understood. Each model is applicable for a particular impact scenario in terms of velocity and impact angle, and some

models need scaling of material properties to reproduce the observed phenomena [27]. Also, some models are only accurate in partial aspects: e.g., for the modelling of small calibre, the FEM predicts the residual velocity well but is not able to reproduce the fragmentation [17]. A model that is applicable to a wide range of applications and describes all relevant aspects of the impact can be seen as the holy grail in TB simulation.

1.2.2 Tests in terminal ballistics (TB)

In ballistics, we distinguish between internal ballistics (IB), external ballistics (EB) and terminal ballistics (TB). In simple words, IB describes the physics in the barrel, EB investigates the behaviour during flight, and TB describes the impact on the target. This work focuses on TB. In the following, we discuss the velocity regimes that are relevant in high-velocity impact first. Then, we define the different cases that occur during projectile penetration and discuss two test setups to determine the ballistic performance of a protective structure.

Velocity regimes in high-velocity impact (HVI)

According to the impact velocity-dependent dynamic pressure, a different material response occurs: For a dynamic pressure below the dynamic yield strength, the material is elastic (reversible deformation). If the dynamic pressure exceeds the yield strength, the material goes into the plastic phase (irreversible deformation) and the quasi-fluid state (material erosion). While the material strength plays an essential role in the elastic and plastic phase, the compressibility determines the quasi-fluid state. Our applications are dominated by plastic deformation but are close to the transition between plastic and quasi-fluid state.

Projectile penetration

Projectile penetration is the process of a projectile interacting with a target, no matter whether it perforates or not. Sometimes, penetration occurs as a result of many impacts against the same substructure. Penetration in that sense involves perforation, embedment and ricochet in the course of the sequence of events. If the projectile creates a hole in the target, the process is called “perforation”. If the target stops the projectile, the process is called “embedment”. A rebound of the projectile under an angle is called “ricochet”. These definitions are consistent with Backman [8].

Ballistic limit tests

Due to material variations and small yaw during impact, the actual effect of perforation is stochastically distributed; with the same velocity, different extends of perforation and embedment can be observed in identical experiments. Therefore, the ballistic limit is defined stochastically: Let P be a probability, then v_P describes the velocity where the target defeats P% of the impacts. A probability of 50% correlates with the ballistic limit (also known as v_{50}) and describes the critical impact velocity. Below this velocity, a structure probably sustains the impact, and above this velocity, it is more likely to fail. The ballistic limit is a helpful metric to quantify the protective property of a structure for a specific threat. In our study, we determine the ballistic limit of three different plate thicknesses.

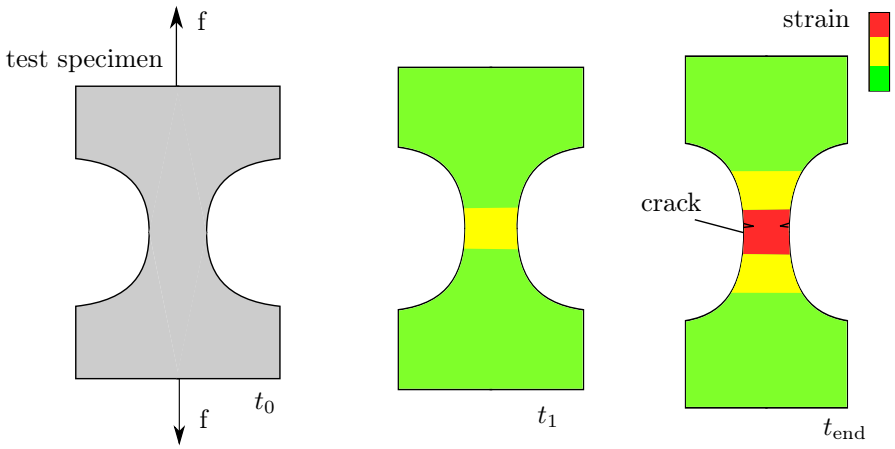

FIGURE 1.1 Tensile test. A force is applied on both sides of the test specimen that induces a strain in the material. The strain is computed from digital image correlation at several time steps. The material parameters are optimised to best describe the evolution of the strain in the material.

Depth of penetration tests

The "depth of penetration" d_{P} is according to STANAG (NATO Standardisation) [77] the crater depth minus the bulging thickness. For larger calibres impacting with hyper-velocity in the quasi-fluid state, the strength of the material is secondary. Therefore, instead of the ballistic limit velocity, the thickness that is required to stop a threat is a suitable metric to determine the protection level of a protective structure.

1.2.3 Material tests

Material characterisation is essential to model the material behaviour under dynamic loads. In the following, we outline the three most common test methods.

Tensile tests

Tensile tests are well-suited to characterise sheet material. Figure 1.1 depicts the setup: The specimen is clamped in a device that applies a defined force on both ends. The strain-field in the specimen is observed with digital image correlation. Material parameters of the numerical model are optimised to match the strain-field of these experiments. The thickness of the specimens and the maximum strain-rate are orders of magnitude lower than those investigated in TB. Tensile tests are, in particular, used to determine the quasi-static material behaviour. Different types of specimens realise different loading conditions regarding triaxiality and loading angle.

Split-Hopkinson pressure bar (SHPB)

In the SHPB, the test specimen is sandwiched between an incident bar and a transmission bar (compare Figure 1.2). A striker bar generates a stress wave by striking the incident bar at a velocity v_0. The stress wave propagates through the incident bar, the specimen, and the transmission bar. Based on the stress-time

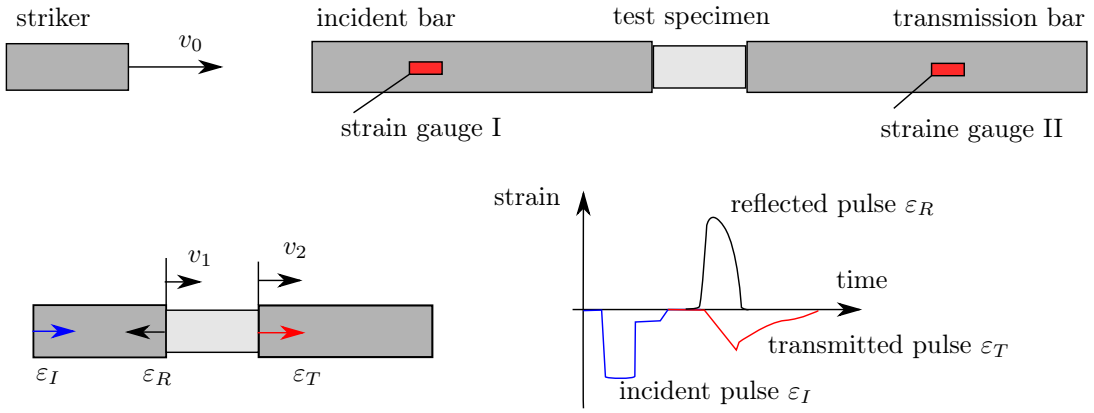

FIGURE 1.2 Split-Hopkinson pressure bar. A striker hits the incident bar and creates an incident strain pulse. This pulse is transmitted via the specimen to the transmission bar. Part of the momentum is reflected and measured at strain gauge I. Based on the strain-time curves, the material properties can be evaluated.

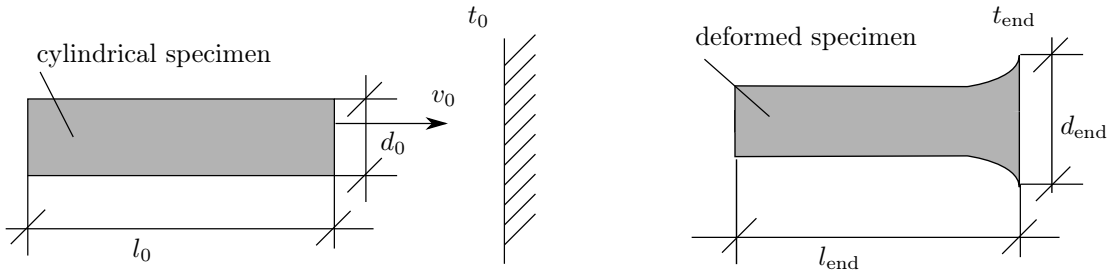

FIGURE 1.3 Taylor bar impact. A cylinder is accelerated against a highly rigid metal plate. The change of shape of the specimen is used to tune the material parameters.

pulse measured in the incident and the transmission bar, the stress-strain response of the specimen can be evaluated. In comparison to tensile tests, higher testing strain rates can be obtained with SHPB.

Taylor bar impact

A test method which is very close to TB experiments is the Taylor bar impact test. A cylindrical bar is accelerated against a thick, highly rigid metal plate (compare Figure 1.3). The bar deforms plastically during the impact. The optimisation of the material parameters with a given numerical model targets the best representation of the resulting mushrooming of the deformed bar for the performed experiments. Generally, different specimen sizes and impact velocities are used for the material parameter tuning. The limitation of the Taylor bar impact test is the characterisation of a too brittle material that fractures during the experiment.

1.2.4 Software

In the following, we give an overview of the software used in this work.

LS-DYNA®

LS-DYNA® is a multi-purpose, multiphysics, commercial simulation software package developed by LSTC [208] (Livermore Software Technology Corporation), which was acquired by Ansys, Inc. in 2019. The predecessor DYNA3D is available to the public and was developed for 3D explicit dynamics by Hallquist [86]. After the foundation of LSTC, the company continued the software development in a more focused manner under the name LS-DYNA. Besides explicit finite element analysis, it contains various numerical frameworks (e.g., implicit FEM, SPH), physics (e.g., continuum mechanics, electromagnetics, thermodynamics) and materials. For our work, we apply the explicit FEM and SPH in a continuum mechanics framework.

Meshless Continuum Mechanics (MCM)

MCM is an in-house SPH solver that Brunel University developed based on DYNA3D [50]. It contains different implementations of SPH and is optimised for aerospace and defence applications. We extended the code with an improved plasticity algorithm and additional material models.

IMPETUS®

IMPETUS® is a tailormade software for 3D numerical simulation of defence applications [205]. It contains a higher-order nonlinear FEM solver, which improves the description of large deformations which are present in impact. Furthermore, it contains an SPH-solver. Unlike the other simulation software, *IMPETUS®* is optimised for the GPU (graphics processing unit) instead of CPU (central processing unit).

MegaMol

We use the particle visualisation software *MegaMol* [79] for postprocessing. *MegaMol* is a library for the visualisation of point-based simulation data. It contains advanced visualisation techniques and scripting capabilities to write own applications including different packages of *MegaMol*. In the scope of this work, we created an application that outputs images and videos to visualise the fragment motion. *MegaMol* is available on GitHub [1] and compatible with Windows and Linux systems.

Flash X-Ray Image Processing (FXRIP)

FXRIP is a software developed in the scope of this work that post processes a series of flash X-ray images and extracts the velocities of the largest fragments. Furthermore, it improves the visualisation of the impact event.

[1] `https://github.com/UniStuttgart-VISUS/megamol`

1.3 Applications

In this work, we investigate three different benchmark applications in Chapters 6 - 8 in detail and showcase the full range of applications of our framework in Chapter 9. As we relate to the application cases already earlier in this work, we explain them briefly here (compare Figure 1.4):

- Application I investigates the natural fragmentation of explosively driven cylinder rings.
- Application II investigates a sphere impact against a plate.
- Application III investigates an oblique high-velocity impact of a surrogate against a plate.

Application I is only secondary related to TB. However, the application is better suited to investigate fragmentation and is chosen for that purpose. Application II is a simplified TB-scenario which allows us to investigate the contact description thoroughly. Application III has been developed in the scope of this work. We designed the surrogate, which is an academic representative of a small calibre projectile, and the test-cases. Applications I and II are used to predefine model and numerical settings for Application III. For Application III, we developed a general TB-template that creates the input for *LS-DYNA®* to simulate TB-applications. Chapter 9 demonstrates the capabilities of this framework for some further applications.

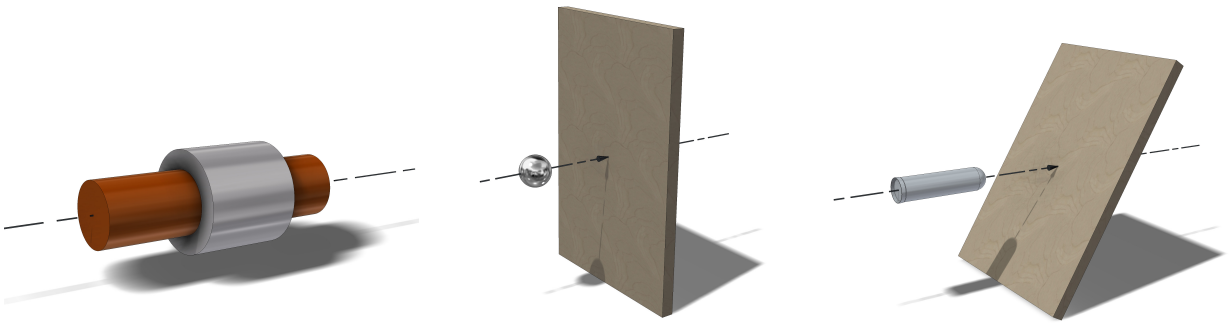

A Application I **B** Application II **C** Application III

FIGURE 1.4 Illustration of the three applications that are investigated in the scope of this work. In **A**, the cylinder ring (silver) is filled with an explosive (red). In **B**, a metal sphere impacts a metal plate perpendicular. In **C**, a projectile-surrogate extruded from a metal block impacts at a variable angle.

1.4 Overview of the thesis

The work is structured as follows:

Chapter 2 presents an introduction to continuum mechanics, which lays the foundation of the boundary-value problem, which the FEM and SPH approximate. In this context, we also present the relevant material theory, which explains where the hardening rule and fracture criterion influence the equations and how the model addresses shock waves.

Chapter 3 describes and compares the FEM and SPH method concerning the strengths and weaknesses for our application.

Chapter 4 shows specific modelling techniques that were developed and applied in the scope of this work regarding the numerical simulation. The modelling techniques include specific material models as well as a strategy for simulation pre- and postprocessing.

Chapter 5 presents the methodology that we developed to process real-world HVI simulations. The focus lies on the software that we implemented to process X-ray images. The data extracted by the software are essential for the validation of the numerical models with real-world experiments.

Chapter 6 contains the first application, which investigates how we can improve the material modelling to describe fracture during highly dynamic events.

Chapter 7 presents the second application, which determines an appropriate contact description for HVI applications.

Chapter 8 shows our main application. First, we describe the design of the projectile surrogate and the corresponding experiments. Then, we present the results of the real-world and numerical experiments. In particular, we validate our developed models and compare the accuracy of the FEM and SPH model.

Chapter 9 showcases how we can apply our terminal ballistics template to other applications that are relevant for the defence industry. There, we analyse the impact of energetic fragments, a real-world small calibre projectile, the defence mechanisms of a plate with holes, and a kinetic energy penetrator.

Chapter 10 gives a conclusion to the findings in this work.

2

Continuum mechanics

This chapter explains the theoretical framework and underlying equations that describe high-velocity impact. In this context, we apply the theory of continuum mechanics for large deformations, finite plasticity, fracture mechanics, and shock physics. The derived set of equations will be approximated with numerical solvers that are introduced in Chapter 3. Particular models for HVI are not part of this chapter either but will be described in detail in Chapter 4. Comprehensive and state-of-the-art descriptions of continuum mechanics are published by Stein and Barthold [186], Holzapfel [91], Zienkiewicz and Taylor [227], Simo and Hughes [185] and Belytschko [22]. Some of the formulations in this chapter are inspired by the work of Erhart [61].
This chapter is structured as follows:

- Section 2.1 gives a general definition of a material body and discusses how continuum mechanics treat deformations.
- Section 2.2 uses this formalism to describe the conservation laws which define the underlying equations. To close these equations, constitutive laws are required that express the stresses in terms of the occurring strains. The stress tensor can be decomposed in a deviatoric and a volumetric part.
- Section 2.3 derives expressions for the deviatoric part: With increasing strain, the loading condition is first elastic, then plastic, and ultimately fracture. First, we describe an equation for the elastic response. Then we propose the decomposition of strain in elastic and plastic deformation applying the theory of finite plasticity. Next, we introduce the commonly used von Mises plasticity model as a yield criterion for metal plasticity. There, the yield stress is given by a flow stress model. Particular choices for the flow stress model are outlined in Chapter 4. Finally, we discuss how to model fracture in HVI. Besides reviewing existing fracture approaches, we show how the fracture and plasticity model can be coupled. Furthermore, we analyse the qualitative failure modes that occur during HVI.
- Section 2.4 derives an expression for the volumetric part based on shock wave theory in solids. At the

end of the derivation, we obtain the Grüneisen equation of state, which expresses the pressure in terms of temperature and internal energy.

- Combining the conservation equations, the constitutive equation and the equation of state, we have a framework that predicts how a material body responds to a given deformation. To conclude the theoretical framework, we define external restrictions in terms of boundary conditions in Section 2.5. In particular, we highlight contact as the essential boundary condition in HVI.

To sum it up, this chapter provides the whole set of equations, needed to describe the response of bodies during high-velocity impact in a continuum mechanics framework.

2.1 Kinematics of large deformations

This section describes the kinematics of a material body in a Lagrangian framework and derives suitable strain tensors. A material body is an object with physical properties, e.g., density or strength. Without loss of generality, in continuum mechanics, one assumes that these properties are continuous. For instance, continuum mechanics does not model density discontinuities at the atomic level or voids in foams explicitly.

Figure 2.1 explains the motion and deformation of a material body in a Lagrangian framework. The body is defined as a set of material points $P \in \Omega$, that are placed in the Euclidean space. The configuration of a body is a region of space Ω occupied by the body, with each material point being at a unique position X. A motion of such a body is a sequence of configurations, parameterised by the time t. At a given time t the body fills a region $\phi(\Omega) \subset \mathbb{R}^3$. In more detail, we always consider two configurations at every point in time: the reference configuration Ω and the current or deformed configuration $\phi(\Omega)$. In solid mechanics, the reference configuration Ω with surface Γ corresponds, in general, to a tension-free, and a load free initial state. The deformed configuration $\phi(\Omega)$ with surface $\phi(\Gamma)$ represents the current or deformed state. It is defined by the deformation mapping

$$\phi : \Omega \to \phi(\Omega) \subset \mathbb{R}^3. \tag{2.1.1}$$

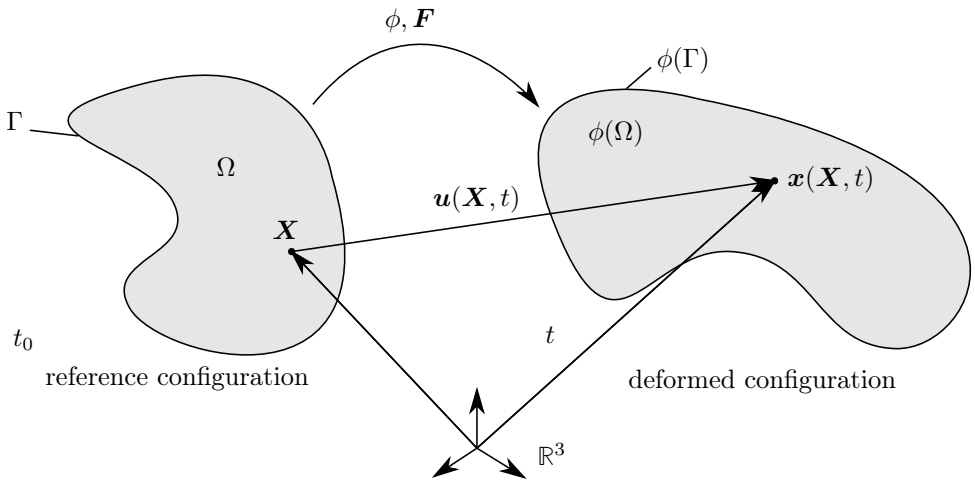

FIGURE 2.1 Motion and deformation of a material body Ω with surface Γ in a Lagrangian framework (the position at time t is expressed in terms of the initial state $\boldsymbol{x}(\boldsymbol{X}, t)$). The motion is described by the displacement $\boldsymbol{u}$. ϕ describes the deformation mapping and $\boldsymbol{F}$ is the deformation gradient.

The mapping ϕ maps the coordinate $\boldsymbol{X}$ in the reference configuration Ω to the coordinate $\boldsymbol{x} = \phi(\boldsymbol{X}, t)$ in the deformed configuration. In a Lagrangian description, $\boldsymbol{X}$ are the points which are tracked. The essential unknown is the displacement field $\boldsymbol{u}$, that results from the difference of the local vectors in the reference and deformed configuration

$$\boldsymbol{u}(\boldsymbol{X}, t) = \boldsymbol{x}(\boldsymbol{X}, t) - \boldsymbol{X}. \tag{2.1.2}$$

The history of dynamic processes is important to describe plasticity correctly. Thus, the path dependence of the deformation has to be considered, which is expressed by time derivatives of kinematic values: The velocity $\boldsymbol{v}$ of the material point in the reference configuration is described by the material time derivative

$$\boldsymbol{v}(\boldsymbol{X}, t) = \frac{\partial \phi(\boldsymbol{X}, t)}{\partial t} = \frac{\partial \boldsymbol{x}(\boldsymbol{X}, t)}{\partial t} =: \dot{\boldsymbol{x}}, \tag{2.1.3}$$

and the acceleration $\boldsymbol{a}$ is given by the second time derivative

$$\boldsymbol{a}(\boldsymbol{X}, t) = \frac{\partial^2 \phi(\boldsymbol{X}, t)}{\partial t^2} = \frac{\partial \boldsymbol{v}(\boldsymbol{X}, t)}{\partial t} =: \ddot{\boldsymbol{x}}. \tag{2.1.4}$$

The non-symmetric deformation gradient $\boldsymbol{F}$

$$\boldsymbol{F}(\boldsymbol{X}, t) = \frac{\partial \phi(\boldsymbol{X}, t)}{\partial \boldsymbol{X}} = \frac{\partial \boldsymbol{x}}{\partial \boldsymbol{X}} \tag{2.1.5}$$

is essential for the description of the kinematics of finite strain. Since ϕ has to preserve the orientation of the body, $\boldsymbol{F}$ needs to satisfy

$$J = \det(\boldsymbol{F}) > 0, \tag{2.1.6}$$

where J is the Jacobian of $\boldsymbol{F}$. For the derivation of the constitutive equation, we introduce the right Cauchy-Green tensor

$$\boldsymbol{C} = \boldsymbol{F}^T \boldsymbol{F}, \tag{2.1.7}$$

and the left Cauchy-Green tensor

$$\boldsymbol{b} = \boldsymbol{F} \boldsymbol{F}^T. \tag{2.1.8}$$

2.1.1 Measures of stress and strain

Subsequently, we introduce tensors for stress and strain. The material law, which closes the conservation equations, defines a relation between stress and strain (compare Section 2.3). The stress tensor is a second-order tensor with nine entries and defines the state of stress at a point of the material. The diagonal entries are the normal stresses, and the off-diagonals are the shear stresses at the material point. The strain tensor is of the same shape as the stress tensor and defines how much the current displacement differs from a rigid body displacement [136]. The choice of a pair of stress and strain tensor is application dependent. The only strict requirement is that the strain and the stress measure are compatible. Some measures are defined in the reference configuration (material frame) and others in the deformed configuration (Eulerian frame). We discuss application relevant measures in the following and highlight the ones which are applied in this work.

Strain measures

Based on (2.1.7) and (2.1.8), different strain tensors can be defined, compare Hill [90]. For simplicity, we limit ourselves to the first-order approximations

$$\boldsymbol{E}_{(m)} = \frac{1}{2m}\left(\boldsymbol{C}^m - \boldsymbol{I}\right), \tag{2.1.9}$$

where $\boldsymbol{I}$ is the second order unit tensor and $\boldsymbol{E}_{(m)}$ are the Seth-Hill family of strain tensors for $m \in \{-1, -0.5, 0, 0.5, 1\}$. For instance, the strain tensor of Hencky-type, can be derived when evaluating the limit $(m \to 0)$

$$\boldsymbol{E}_{(0)} = \lim_{m\to 0} \frac{\left(\boldsymbol{C}^m - \boldsymbol{I}\right)}{2m} \overset{\text{l'Hôpital}}{=} \lim_{m\to 0} \frac{\boldsymbol{C}^m ln(\boldsymbol{C})}{2} = \frac{1}{2}\ln(\boldsymbol{C}), \tag{2.1.10}$$

which is also known as true strain, and is well suited for the description of the plastic behaviour under large deformation. Whenever the strain is not further specified we imply true strain

$$\boldsymbol{\varepsilon} := \boldsymbol{E}_{(0)}. \tag{2.1.11}$$

Other strain-measures that are frequently used in solid mechanics are the Green-Lagrangian strain $(m = 1)$ or the Almansi strain $(m = -1)$. In engineering, scalar values of the strain tensor are used to compare different loading conditions. The so-called engineering strain is defined as

$$e = \frac{\Delta L}{L}\,, \tag{2.1.12}$$

where L is the distance between two material points in the reference state and ΔL is the difference between two material points in the deformed state. Similarly, we can define a scalar version of the true strain, which is

$$d\varepsilon = \frac{dL}{L + dL}\,, \qquad \varepsilon = \ln\left(\frac{L + \Delta L}{L}\right) = \ln(1 + e). \tag{2.1.13}$$

Stress measures

Similarly to the strain measures, we introduce the following stress measures that are used in this work. A common stress measure is the Cauchy stress tensor $\boldsymbol{\sigma}$, which is often referred to as "the stress tensor" or "true stress". The Cauchy stress is a measure of the force $\boldsymbol{f}$ acting on the material point in the deformed configuration with respect to the normal direction $\boldsymbol{n}$

$$\boldsymbol{f} = \boldsymbol{\sigma}\boldsymbol{n}\ . \tag{2.1.14}$$

The equations in metal plasticity are generally expressed with the Kirchhoff stress $\boldsymbol{\tau}$. Besides these two measures, the nominal stress $\boldsymbol{N}$ and its transpose $\boldsymbol{P} = \boldsymbol{N}^T$ (first Piola-Kirchhoff stress), the second Piola-Kirchhoff stress $\boldsymbol{S}$ and the Biot stress $\boldsymbol{T}$ are widely used in continuum mechanics. Each stress measure can be transferred to one another. For instance, the relation between Cauchy and Kirchhoff stress is

$$\boldsymbol{\tau} = J\boldsymbol{\sigma}. \tag{2.1.15}$$

This implies that the Kirchhoff stress is defined in reference configuration and is, therefore, often used for finite deformations. In this context, we want to introduce the engineering scalar variants for stress measurement as well. They are no real stress measures in a continuum mechanics sense. The first of them is the engineering stress, which is defined as

$$\sigma_{\text{eng}} = F/A_0, \tag{2.1.16}$$

where F is the overall load and A_0 is the size of the area in reference configuration. Similarly, scalar true stress measure can be defined as

$$\sigma_{\text{true}} = F/A. \tag{2.1.17}$$

The main difference is that the true stress considers necking, and engineering stress does not. Therefore, engineering stress is less accurate for finite deformations, but a simple measure which is used exclusively for material testing.

2.2 Conservation laws

Balance principles are universal physical expressions for continua. They express fundamental relations of continuum mechanics, applicable to arbitrary material and state of matter, and have to be satisfied at any time. This section summarises the conservation equations of mass, momentum, and energy, concerning the reference configuration Ω. The so-called Lagrangian description is typically used for solid mechanics applications. The formulations are inspired by Vignjevic [197]. The first conservation law, mass conservation, states that mass does not change in a closed system

$$\frac{d\rho}{dt} = \rho \nabla \cdot \boldsymbol{v}. \tag{2.2.1}$$

The second conservation law, momentum conservation, consists of the conservation of linear and angular momentum. Conservation of linear momentum means that the temporal change of momentum $\rho \boldsymbol{a}$ is equal to the sum of internal forces $\nabla \cdot \boldsymbol{\sigma}$ and external forces $\rho \bar{\boldsymbol{b}}$ acting on the volume element and corresponds to Newton's second law of motion. The local formulation with respect to the reference configuration reads

$$\rho \frac{d\boldsymbol{v}}{dt} = \nabla \cdot \boldsymbol{\sigma} + \rho \bar{\boldsymbol{b}}, \tag{2.2.2}$$

where $\boldsymbol{\sigma}$ is the Cauchy stress tensor, and $\rho \bar{\boldsymbol{b}}$ is the external force (e.g., gravity) acting on the volume element. Angular momentum is conserved if and only if $\boldsymbol{\sigma}$ is symmetric

$$\boldsymbol{\sigma} = \boldsymbol{\sigma}^T. \tag{2.2.3}$$

The first law of thermodynamics postulates the conservation of energy.

$$\frac{dW^{int}}{dt} = \frac{1}{\rho} \boldsymbol{\sigma} : \nabla \boldsymbol{v}, \tag{2.2.4}$$

where the colon denotes the inner tensor product, W^{int} is the internal energy in the system and $\nabla \boldsymbol{v}$ is the gradient of the velocity vector. The model uses the integration of the energy equation (2.2.4) to evaluate the equation of state and to track the global energy balance (compare Section 2.4). The Lagrangian description

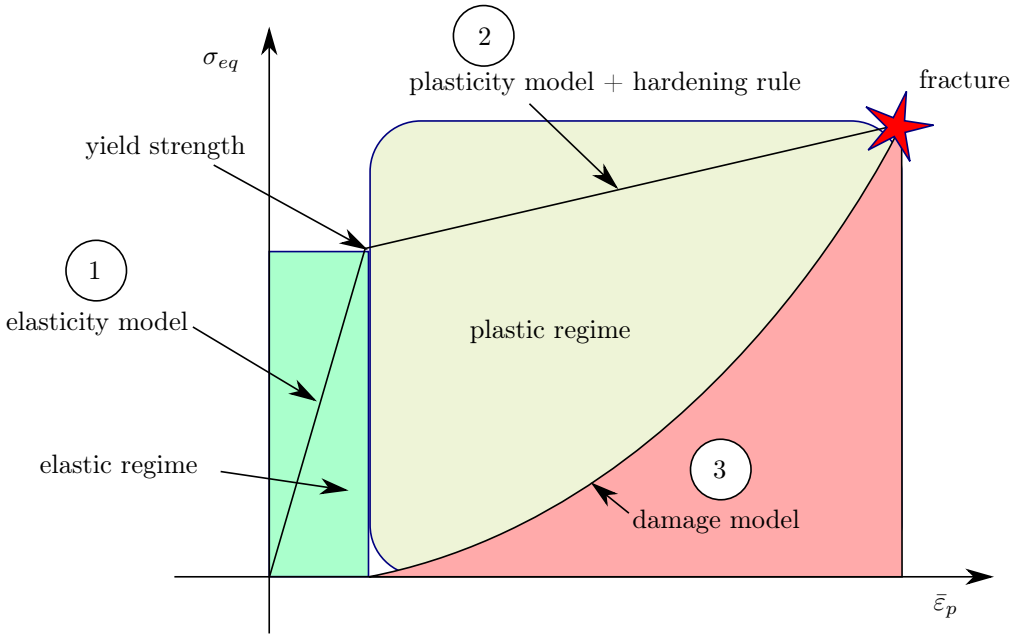

FIGURE 2.2 Material theory: the material model describes the relationship between stress and strain. This figure shows the essential parts in material modelling in terms of a typical stress-strain curve, like it is observed in a typical tensile test for metals. We explain (1) linear elasticity, (2) plasticity and (3) fracture modelling.

fulfils mass conservation directly, and we are further not interested in density changes as they are negligible in plastic deformation. Therefore, (2.2.2),(2.2.3) are the underlying equation for the boundary-value problem, which is solved numerically. The next two sections explain how the stresses are computed from the strains that occur during the deformation of the body.

2.3 Material theory

In the previous section, we have discussed the conservation laws. The conservation of momentum expresses the acceleration in terms of internal stresses. The final goal is to compute the displacement, which is directly related to the acceleration in (2.2.2). Therefore, we need an equation that expresses stress as a function of strain—the material law:

$$\boldsymbol{\sigma} = \hat{\boldsymbol{\sigma}}(\boldsymbol{\varepsilon}). \tag{2.3.1}$$

This section describes three aspects of material modelling which are relevant for high-velocity impacts:
(1) the response under elastic deformation, (2) the plastic response, and (3) the damage evolution and fracture of the material. Figure 2.2 visualises these aspects, and we return to the figure throughout this section. In addition to elasticity, plasticity and fracture, the material is described with an equation of state which will be addressed by the next section.

2.3.1 Elastic response

In the first regime in Figure 2.2, the material is linearly elastic and behaves like a linear spring that follows Hooke's law. Then, we can compute the stress-strain relationship for this one-dimensional example

$$\sigma = E\varepsilon, \tag{2.3.2}$$

where E is the Young's modulus. For the case of three-dimensional non-isotropic material, this equation gets more complex. In general, the equation reads

$$\boldsymbol{\sigma} = \boldsymbol{C}\boldsymbol{\varepsilon}, \tag{2.3.3}$$

where $\boldsymbol{C}$ is a fourth order constitutive tensor of linear elasticity with 81 entries for the three-dimensional case. Applying symmetry assumptions for the stress ($\sigma_{ij} = \sigma_{ji}$), strain ($\varepsilon_{ij} = \varepsilon_{ji}$) and mixed partial derivatives ($C_{ijkl} = C_{klij}$), the number of constants reduces to 21, e.g., Itin et al. [97]. For isotropic material, the number of unknowns reduces to two, e.g., Young's modulus E and Poisson's ratio ν. Typically, the tensor is then written in Voigt notation. There, stress and strain are expressed as vectors

$$\begin{bmatrix} \sigma_{11} \\ \sigma_{22} \\ \sigma_{33} \\ \sigma_{23} \\ \sigma_{31} \\ \sigma_{12} \end{bmatrix} = \begin{bmatrix} C_{11} & C_{12} & C_{12} & 0 & 0 & 0 \\ C_{12} & C_{11} & C_{12} & 0 & 0 & 0 \\ C_{12} & C_{12} & C_{11} & 0 & 0 & 0 \\ 0 & 0 & 0 & (C_{11}-C_{12})/2 & 0 & 0 \\ 0 & 0 & 0 & 0 & (C_{11}-C_{12})/2 & 0 \\ 0 & 0 & 0 & 0 & 0 & (C_{11}-C_{12})/2 \end{bmatrix} \begin{bmatrix} \varepsilon_{11} \\ \varepsilon_{22} \\ \varepsilon_{33} \\ \varepsilon_{23} \\ \varepsilon_{31} \\ \varepsilon_{12} \end{bmatrix}, \tag{2.3.4}$$

where

$$C_{11} = \frac{E(1-\nu)}{(1+\nu)(1-2\nu)}; \quad C_{12} = \frac{E\nu}{(1+\nu)(1-2\nu)}; \quad \text{and } (C_{11}-C_{12})/2 = \frac{E}{2(1+\nu)} = \mu. \tag{2.3.5}$$

If we use matrix notation we can express this equation in a compact notation with shear and bulk modulus. With regard to the Young's modulus the 3×3 matrix has the symbol $\boldsymbol{E}$:

$$\boldsymbol{\sigma} = \boldsymbol{E} : \boldsymbol{\varepsilon} = (2\mu I^{\mathrm{dev}} + 3\kappa I) : \boldsymbol{\varepsilon}. \tag{2.3.6}$$

This equation describes the elastic behaviour of isotropic material. In Figure 2.2 this describes the region (1). For larger deformations, the theory of finite plasticity described in the following is applied (region (2)).

2.3.2 Finite plasticity

For transient impact scenarios, one observes nonlinear and elastoplastic behaviour of the material. This phenomenon will be described with the theory of finite plasticity. A detailed formulation is given by Simo and Miehe [99], Miehe [35] and Simo and Hughes [184].

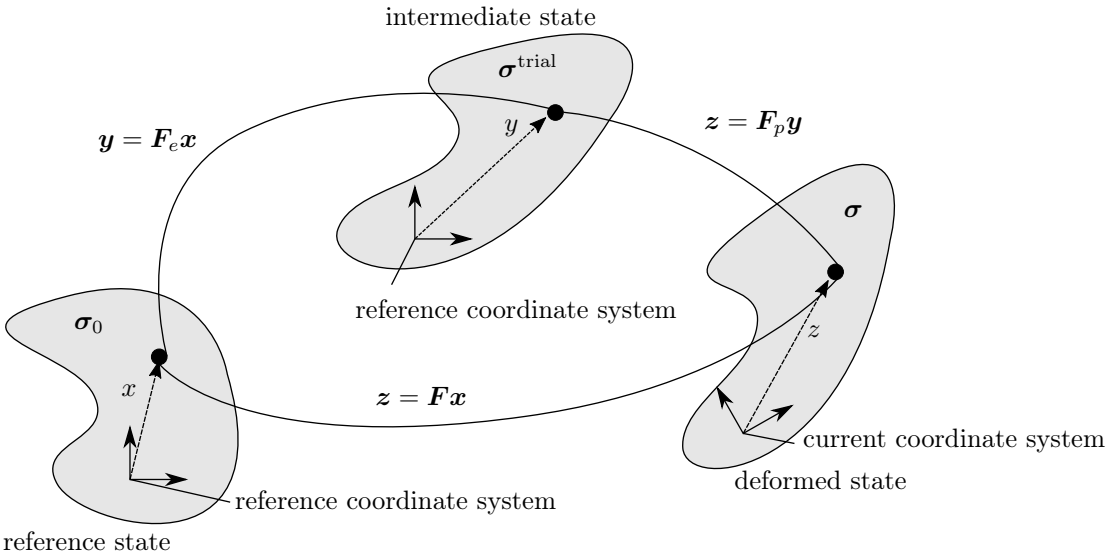

FIGURE 2.3 Decomposition of the deformation gradient into an elastic deformation gradient $\boldsymbol{F}_e$ and a plastic deformation gradient $\boldsymbol{F}_p$. The algorithm first calculates the intermediate state $\boldsymbol{\sigma}^{\text{trial}}$ and then backprojects the trial stress to the actual deformed state $\boldsymbol{\sigma}$.

We outline the main ideas in the following: First a convex, elastic domain,

$$E_\sigma := \{(\boldsymbol{\sigma}, q) \in \boldsymbol{S} \times \mathbb{R} \mid f(\boldsymbol{\sigma}, q) \leq 0\}, \tag{2.3.7}$$

defines the area of valid stress states. Stress states outside this area are physically not reachable. The flow criterion f is depending on the stress and a hardening function q. $\boldsymbol{S}$ is the vector space of symmetric second order tensors. The first basic assumption $f(\boldsymbol{\sigma}, q) \leq 0$ ensures that the history-dependent stress state stays in a valid area. If $f(\boldsymbol{\sigma}, q) = 0$, the material is yielding. The second assumption of elastoplasticity of finite distortions is that the deformation gradient can be expressed as the product of an elastic and a plastic part

$$\boldsymbol{F} = \boldsymbol{F}_e\boldsymbol{F}_p. \tag{2.3.8}$$

This postulate was first introduced by Lee [120], motivated by the structure of crystal-plastic. From a micro-mechanical point of view, the tensor $\boldsymbol{F}^p$ is an internal variable, which describes the irreversible distortion in a crystal grid. The inverse of $\boldsymbol{F}^e$ describes a fictional, intermediate stress-free state, assuming there is no plastic deformation [61]. Figure 2.3 illustrates the decomposition of the deformation gradient. For the derivation of the evolution equation of plasticity, some more technical transformations are required. These are not mandatory to understand the models described in the following. Instead, we discuss the back transformation of the intermediate state to the deformed state. This correction is expressed with a plastic multiplier $\dot{p}$.

The following description is inspired by Goméz [73] and due to the theory of Wang [200]. The strain increment $\Delta\boldsymbol{\varepsilon}$ can be composed into an elastic, a plastic, and a thermal part

$$\Delta\boldsymbol{\varepsilon} = \Delta\boldsymbol{\varepsilon}_e + \Delta\boldsymbol{\varepsilon}_p + \Delta\boldsymbol{\varepsilon}_T, \tag{2.3.9}$$

which is illustrated in Figure 2.4. First, we assume that the material behaves perfectly elastic and compute a

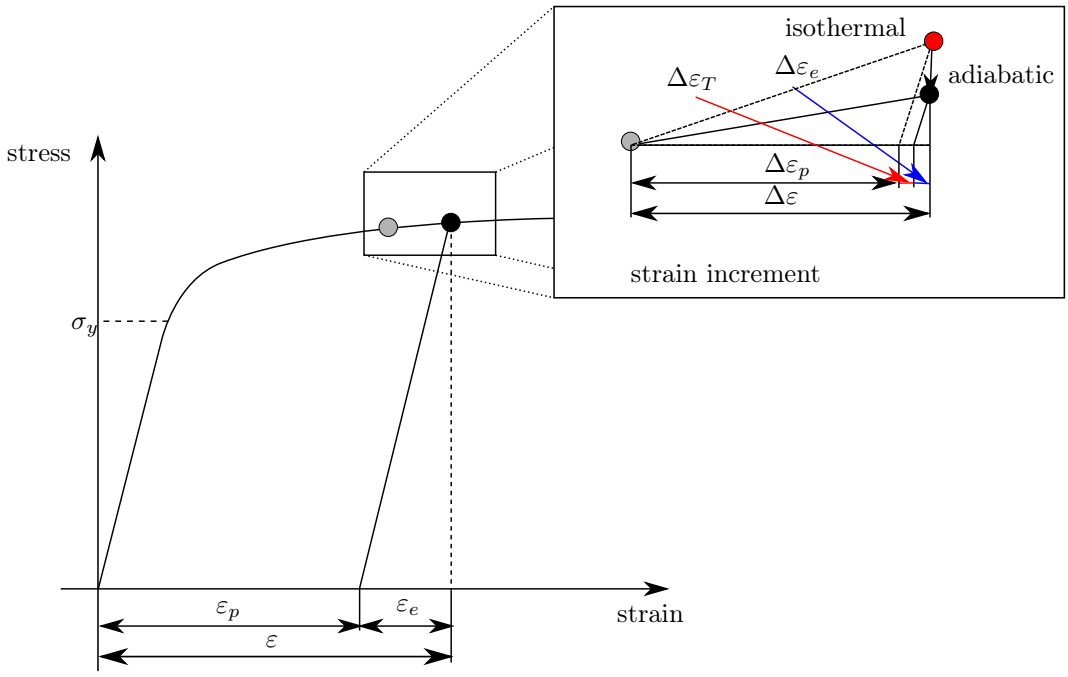

FIGURE 2.4 Decomposition of the strain increment into elastic $\Delta\boldsymbol{\varepsilon}_e$, plastic $\Delta\boldsymbol{\varepsilon}_p$ and thermal strain increment $\Delta\boldsymbol{\varepsilon}_T$. The thermal strain increment is the difference between isothermal and adiabatic state.

trial stress (corresponding to the intermediate state in Figure 2.3).

$$\boldsymbol{\sigma}^{\text{trial}} = \boldsymbol{E}(T) : \Delta\boldsymbol{\varepsilon}, \tag{2.3.10}$$

where $\boldsymbol{E}$ is the constitutive relation from (2.3.6). The tensor can be divided into a deviatoric and a volumetric part

$$\boldsymbol{E}(T) = 2\mu(T)\boldsymbol{I}^{\text{dev}} + \kappa(T)\boldsymbol{I}. \tag{2.3.11}$$

The deviatoric second order tensor $\boldsymbol{I}^{\text{dev}}$, the shear modulus $\mu(T)$ and bulk modulus $\kappa(T)$ are defined as

$$\boldsymbol{I}^{\text{dev}} := \mathbf{1} - \boldsymbol{I}, \qquad \mu(T) = \frac{E(T)}{2(1+\nu)}, \text{ and } \quad \kappa(T) = \frac{E(T)}{3(1+\nu)}, \tag{2.3.12}$$

where ν is the Poisson's ratio, E is the scalar Young's modulus, and the second order tensor $\mathbf{1}$ is one in all entries. This decomposition can be derived physically using a proper free energy function. The partial derivative of this function with respect to the elastic strain yields this corelation (see [98, 61]). The yield function is defined as the difference between the equivalent trial stress $\sigma_{eq}^{\text{trial}}$ and the yield stress $\sigma_y := q(\alpha)$ at the current loading conditions

$$f(\boldsymbol{\sigma}^{\text{trial}}, \bar{\varepsilon}_p, \dot{\bar{\varepsilon}}_p, T) = \sigma_{eq}^{\text{trial}} - q(\bar{\varepsilon}_p, \dot{\bar{\varepsilon}}_p, T). \tag{2.3.13}$$

The equivalent stress σ_{eq} is a normalized value of the stress that is expressed in terms of principal stresses. In the next section we will introduce the von Mises equivalent stress which defines the relation between $\boldsymbol{\sigma}$ and

σ_{eq}. The equivalent plastic strain $\bar{\varepsilon}_p$ is defined as an integral of the contraction of the plastic deformation rate tensor $\dot{\boldsymbol{F}}_p$:

$$\bar{\varepsilon}^p = \int_t \sqrt{\frac{2}{3}\,\dot{\boldsymbol{F}}_p : \dot{\boldsymbol{F}}_p}\,dt, \tag{2.3.14}$$

and we can identify the equivalent plastic strainrate $\dot{\bar{\varepsilon}}_p$

$$\dot{\bar{\varepsilon}}_p = \sqrt{\frac{2}{3}\,\dot{\boldsymbol{F}}_p : \dot{\boldsymbol{F}}_p}. \tag{2.3.15}$$

If $f < 0$ the material is in the elastic regime and requires no plasticity model. Otherwise, we can correct the trial stress by combining equations (2.3.9) and (2.3.10)

$$\begin{aligned} \boldsymbol{\sigma} &= \boldsymbol{E} : (\Delta\boldsymbol{\varepsilon} - \Delta\boldsymbol{\varepsilon}_p - \Delta\boldsymbol{\varepsilon}_T) \\ &= \boldsymbol{\sigma}^{\text{trial}} - \boldsymbol{E} : (\Delta\boldsymbol{\varepsilon}_p + \Delta\boldsymbol{\varepsilon}_T) \\ &= \boldsymbol{\sigma}^{\text{trial}} - 3\mu\Delta p\frac{\boldsymbol{s}}{\sigma_{eq}} - 3\kappa\alpha\Delta T\boldsymbol{I}, \end{aligned} \tag{2.3.16}$$

where Δp is the plastic increment and α is the thermal expansion coefficient. The factor of three is due to the flow rule of Prandtl and Reuss

$$\dot{\bar{\boldsymbol{\varepsilon}}}_{\boldsymbol{p}} = \dot{p}\frac{3}{2}\,\frac{\boldsymbol{s}}{\sigma_{eq}}\,. \tag{2.3.17}$$

Considering only the deviatoric part we obtain a simple relationship between actual stress and predictor stress which only depends on Δp:

$$\sigma_{eq} = \sigma_{eq}^{\text{trial}} - 3\mu\Delta p. \tag{2.3.18}$$

If there is plastic deformation we have to ensure that

$$f(\sigma_{eq}, \bar{\varepsilon}_p, \dot{\bar{\varepsilon}}_p, T) = 0. \tag{2.3.19}$$

Since the function has to be evaluated at the unknown corrected stress state, an iterative scheme is required to approximate the actual stress state. An example of an iterative scheme, which we implemented for our model, is the Newton-Raphson solver.

2.3.3 Constitutive modelling with the von Mises plasticity model

The theory of finite plasticity describes a generic framework for viscoplastic materials. To calculate the elastic strains, principal stresses, and hardening, a constitutive model that describes the yield criterion and predicts the plastic multiplier is required. Especially during a high-velocity impact, von Mises plasticity models are used to describe the behaviour of metals under plastic deformation. There, the yield surface is defined by the second invariant of the stress deviator J_2. Thus, the von Mises model is a J_2-plasticity model. The von Mises plasticity describes the yield criterion, and the flow stress model calculates the plastic multiplier.

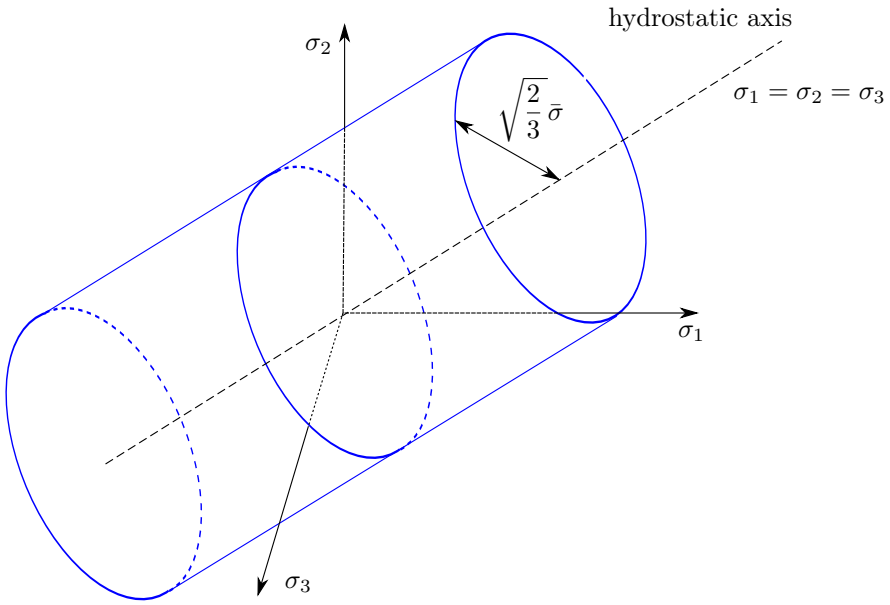

FIGURE 2.5 Von Mises yield surface (blue) in 3-D principal Cauchy-stress state $(\sigma_1, \sigma_2, \sigma_3)$. The surface describes a cylinder around the hydrostatic axis.

Von Mises plasticity

The classical J_2-plasticity or von Mises plasticity is the starting point for the thermo-viscoplastic material model we implement in the scope of this work. The elastic domain of the classical J_2-plasticity is constrained by the von Mises yield surface (compare Figure 2.5), and all valid states are defined by

$$f(\boldsymbol{\sigma}, q) = \sigma_{eq} - q(\alpha) \leq 0, \qquad \text{with} \qquad \sigma_{eq} = ||\boldsymbol{s}|| \qquad \text{and} \qquad \boldsymbol{s} = \text{dev}(\boldsymbol{\sigma}). \tag{2.3.20}$$

Here, $q(\alpha)$ denotes the hardening and softening dependent yield strength in terms of the internal variables α (e.g., $\bar{\varepsilon}^p, \dot{\bar{\varepsilon}}^p, T$,...). For the von Mises plasticity, the choice of $||\cdot||$ is

$$\sigma_{eq} = ||\boldsymbol{s}|| := \sqrt{2J_2} \qquad \text{with} \qquad J_2 := \sqrt{(\sigma_1 - \sigma_2)^2 + (\sigma_1 - \sigma_3)^2 + (\sigma_2 - \sigma_3)^2}, \tag{2.3.21}$$

or more descriptive, the yield surface describes a cylinder around the hydrostatic axis $\sigma_1 = \sigma_2 = \sigma_3$ (compare Figure 2.5). Plastic flow occurs when the equivalent, or von Mises stress

$$||\boldsymbol{s}|| > q(\alpha), \tag{2.3.22}$$

exceeds the flow stress q which is defined on the right hand side. Only stress states satisfying (2.3.20) are allowed. If a stress state is outside the valid domain it has to be projected on the yield surface according to

$$\dot{\boldsymbol{s}} = -3\kappa\dot{p}\frac{\boldsymbol{s}}{||\boldsymbol{s}||} \qquad \text{and} \qquad \dot{\boldsymbol{\varepsilon}}^p = \frac{3}{2}\,\dot{p}\frac{\boldsymbol{s}}{||\boldsymbol{s}||}\,, \tag{2.3.23}$$

where κ is the bulk modulus. For this correction, we have to approximate the plastic multiplier $\dot{p}$. Combining the back projection (2.3.23) with the yield condition (2.3.20) leads to a nonlinear equation for $\dot{p}$. This system

of equations can be solved with a Newton-Raphson iterative solver. The von Mises plasticity flow rule has to be combined with a hardening rule. Application specific hardening rules close the constitutive model (2.3.22) and are given in Section 4.1.1. The hardening rule defines the shape of the stress response in region (2) in Figure 2.2 and describes the material and loading specific flow-stress with a hardening function. Depending on the choice of the hardening function $q(\alpha)$ the plastic corrector $\dot{p}$ can be calculated directly. An example of such a simple constitutive model is the isotropic linear hardening with initial flow limit σ_y and hardening ξ

$$q(\alpha) = q(\bar{\varepsilon}^p) = \sigma_y + \xi\bar{\varepsilon}^p. \tag{2.3.24}$$

In this section, we have seen an approach to describe the plastic response of a material. In principle, this closes the equations. However, the material will not be able to sustain the loading at all loading conditions. Therefore, we need a model that describes at which point the material fractures. This aspect is discussed in the subsequent section.

2.3.4 Fracture in solids

At a certain point of deformation, the material can not sustain the load; voids start to grow, leading to cracks, which in its ultimate stage provoke the fracture of the body [78]. Considering a stress-strain diagram of a classical tension test, a fracture describes the point where the curve ends or takes on the value zero (star in Figure 2.2). The books of Gross [78], Ochsner [152] and Perez [158] give a state of the art overview of the topic. Mott provides one of the pioneering works in fracture mechanics. A new version about his legacy is published by Grady [74]. It deals in particular with rings and shells that we will investigate in Application I. This section first clarifies the terminology of different expressions that are often used in the context of fracture. Then we review different fracture approaches and argue the one which we use for the modelling. With this definition, we further illustrate how the coupling between damage and plasticity model can be realised. Finally, we perform a qualitative analysis of failures that occur during HVI. In the course of this work, we will get back to this analysis of failure modes.

Terminology

In the following, we define the terms of damage, failure, fracture, and fatigue:

- Damage means any change of a thing that degrades it from its original state. Damage can be defined as the reaching of the plastic range or the onset of failure of the material.
- Failure is the opposite of success. Thus, the umbrella term failure includes buckling, ductile and brittle fracture, as well as fatigue.
- Fracture is a specific failure type, which emphasises that a part fails due to stresses that exceed the normal tensile strength and breaks into several pieces [163]. It can be both ductile or brittle fracture.
- Fatigue is failure due to cyclic loading, which does not occur during a high-velocity impact.

We will see that some ductile fracture models define the onset of fracture as the result of accumulated threshold damage.

Review of fracture approaches in high-velocity impact

In the following, we review four different fracture approaches in terms of their applicability to high-velocity impact problems: J-integrals, cohesive element methods, the Gurson model, and ductile fracture criteria.

- J-integrals are designed to predict crack formation and growth under static and dynamic loading. This model assumes, in general, an initial crack or notch from where a stress singularity propagates. Since the application of high-velocity impact investigates initially uncracked bodies, it is not suitable.
- The cohesive element method incorporates the physics of material separation in the numerical formulation but is supposed to be more suitable for brittle material than ductile fracture. Void nucleation, growth, and coalescence are the predominant mechanism of ductile fracture [152, 78].

Based on the works of McClintock's [142] and Rice and Tracey [168], two types of approaches for ductile fracture mechanics have been developed in the literature.

- The first class includes material softening due to the growth of micro-voids directly in the constitutive continuum law. Moreover, failed elements lose their load-carrying capability. With reference to Gurson [82], these kinds of models are called Gurson models. The main drawback of Gurson models is that they contain several material coefficients that have to be calibrated. Furthermore, the calibration appears to be difficult due to the strong coupling between the constitutive model and damage accumulation.
- Therefore, the fourth and last fracture criterion that ranks among the second class of the aforementioned ductile fracture approaches is the only reasonable choice for the given application. In ductile fracture criteria, the damage accumulation is uncoupled from the material constitutive equation. A generic form of a ductile fracture criterion is given in the following for the effective plastic strain $\bar{\varepsilon}_p$:

$$\int_0^{\bar{\varepsilon}_p} f\ (\text{stress states, strain rates, temperature, ...})\ d\bar{\varepsilon}_p = \ D_c(\text{material}), \tag{2.3.25}$$

  where D_c is the critical damage that determines the material dependent onset of fracture, the function f takes into account the components or invariants of the stress tensor, strain rates and temperature. The stress state includes in particular triaxiality η, which is defined as the ratio of the hydrostatic pressure or mean stress σ_m to the equivalent von Mises stress σ_{eq}:

$$\eta = \frac{\sigma_m}{\sigma_{eq}}\,. \tag{2.3.26}$$

  Depending on the choice of f, we obtain different types of ductile fracture models. Those frequently used for our applications are explained in Section 4.1.2.

For further reading, Teng gives a comprehensive review of different fracture approaches [193].

Coupling of the damage and the plasticity model

The motivation for coupling the plasticity and the fracture model is to improve the description of material weakening during the necking phase. The coupling of plasticity and fracture model can be realized by different means: the strength can be reduced by changing the parameters of the hardening rule, or by reducing the Young's modulus. We decided to apply the weakening to both the strength and the two stress moduli. Furthermore, we can define the amount of interaction by a coupling function. By analogy with the energy failure criterion by Rittel (compare Section 4.1.2), we use a polynomial relation that decreases the material strength particularly when the damage accumulation is already significant:

$$\sigma_y = C_D \sigma_y^0, \qquad \text{with} \qquad C_D = (1 - D^{1/c}), \tag{2.3.27}$$

where C_D defines the reduction in yield strength σ_y due to damage D with the constant c and the initial yield strength σ_y^0.

Qualitative analysis of failure modes

Many studies have been conducted in the past 50 years concerning the qualitative behaviour of high-velocity impact. They can be found in textbooks of Backman and Goldsmith [8], Anderson and Bodner [5] and Corbett et al. [46]. Non-standard collision such as oblique impact is summarised in the book of Goldsmith [72].

This paragraph is essential, as we compare the observed fracture modes of our experiments with the ones described below and use the terminology of Figure 2.6. For this work, failure of blunt projectiles is of particular interest. The three corresponding modes in the figure are a ductile failure, adiabatic shear and the extrusion of a disc or plug. The qualitative properties depend on the material used, shape and impact speed of the impactor as well as the plate thickness. Moreover, the figure shows various break scenarios such as thin targets, pointed or blunt penetrators and mixed-mode failures. Brittle material can lead to significantly smaller fragments. At very high speeds or explosions, spalling can occur.

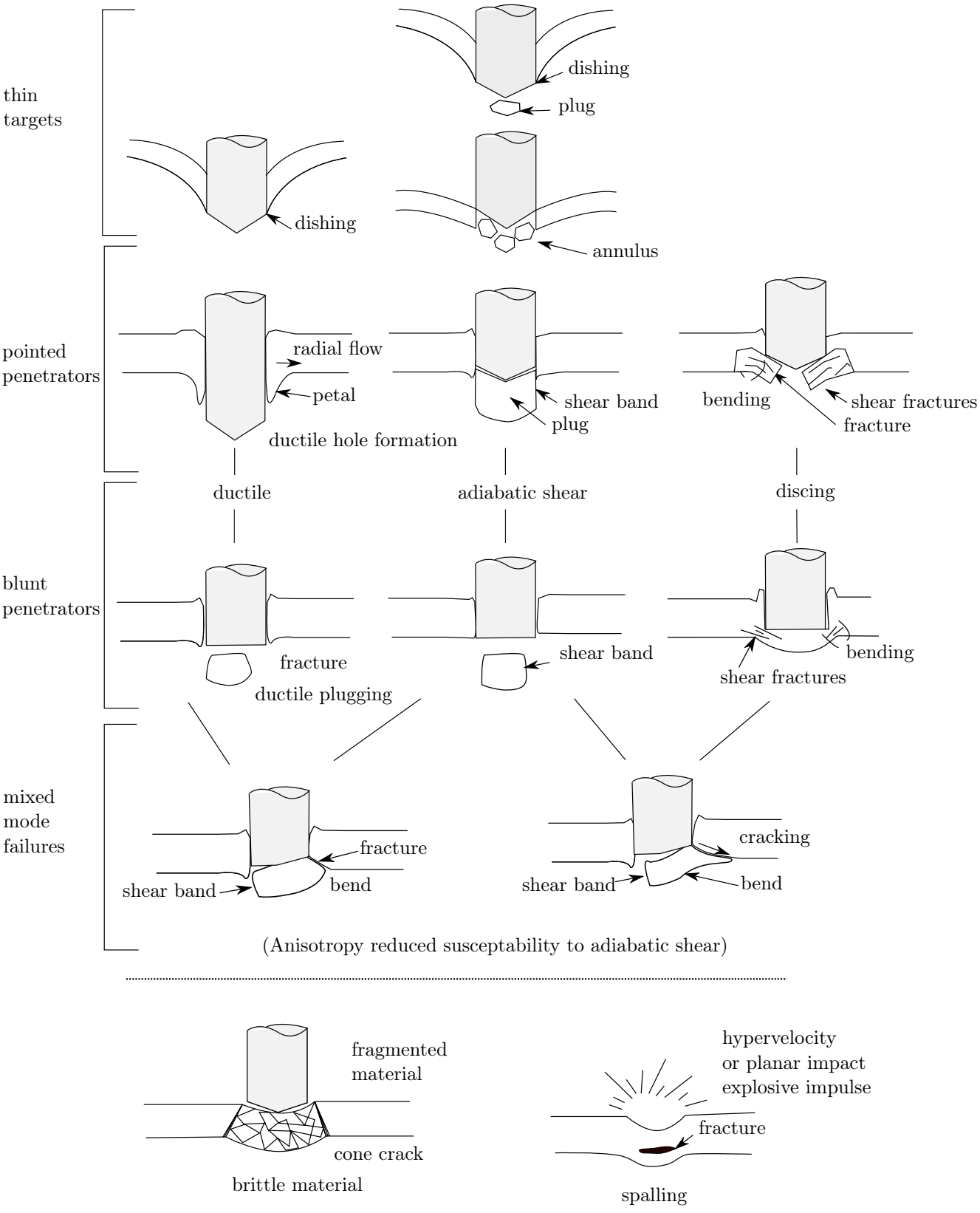

FIGURE 2.6 Schematic representation of fracture modes in perforation problems according to Woodward [228].

2.4 Shock waves in solids and the equation of state (EOS)

For high-strain rate phenomena, shock waves play an essential role. In terms of our final model, they define how discontinuities travel through matter and influence the input values of our material law. This section explains what shocks and shock waves are, how they are related to an equation of state (EOS), why an EOS is needed for highly dynamic processes and suggests a suitable EOS for our application. Since this work does not investigate different shock physics, this section is kept short. For further reading, the following three books cover all essential aspects: Meyers [144] explains the dynamic behaviour of materials exclusively with wave theory, Scapin [176] gives a good overview of different equations of state, and Zukas [230] covers the numerical aspects by explaining the relevance of shock physics in hydrocodes.

We start with an illustrative example: In the case of highly dynamic loading, the material is subjected to quite different processes compared to quasi-static situations. For instance, if we compare the protection capabilities of two materials against the two defeat mechanisms knife and missile, we observe the following: While sand is very effective against missile impact, it is useless against a knife. On the other hand, a knife is not able to penetrate a piece of wood that is easily penetrated by a bullet. Therefore, we have to consider shock wave propagation in solids to provide reliable methods for the prediction of dynamic events such as HVI. These events contain high compression and expansion that lead to a change in the physical, mechanical, and thermodynamic properties of the involved materials. Furthermore, the impact includes a wide range of deformation states, temperatures, pressures, and densities. While shock wave experiments provide data of thermodynamically possible states, the EOS describes the set of surfaces in the p-v-T-space which define all possible thermodynamic states. In the following, we first show which part of our material law is modelled with the EOS, then we explain shock wave properties and conclude with an EOS.

Decomposition of the material law

In general, the material behaviour is described by the relation of stress tensor $\boldsymbol{\sigma}$ and strain tensor $\boldsymbol{\varepsilon}$. (compare (2.5.2)). For the following derivation, we split these tensors into deviatoric ($\mathrm{dev}(\boldsymbol{\sigma}) = \boldsymbol{s}$, $\mathrm{dev}(\boldsymbol{\varepsilon})$) and hydrostatic components ($\boldsymbol{I}p, \boldsymbol{I}\varepsilon_v/3$), where $\boldsymbol{I}$ is the identity matrix, p is the pressure, and ε_v is the volumetric strain. They are defined as

$$p = -\mathrm{tr}(\boldsymbol{\sigma})/3 \qquad \text{and} \qquad \varepsilon_v = \mathrm{tr}(\boldsymbol{\varepsilon}). \tag{2.4.1}$$

While the constitutive law (2.3.20), (2.3.23) presented in Section 2.3.3, defines the relation between the deviatoric parts of stress and strain tensor, an EOS defines the relation between the hydrostatic components. If no EOS is defined the volumetric part is computed with the bulk modulus.

Shock waves in general

To motivate the demand for an EOS in our model, we first have to explain shocks in general: A shock is characterised as a moving surface with continuous displacement, but discontinuities in properties, such as density, pressure (or stress) and particle velocity. The shock wave behaviour of fluids can be investigated in a shock tube (see Figure 2.7). In the typical shock tube experiment, two gases of different pressure are separated by a membrane, and a shock is initiated when the membrane is being opened. Similarly, a piston can be used in the shock tube to generate a shock. Therefore, the piston is accelerated to a particle velocity v_{p1},

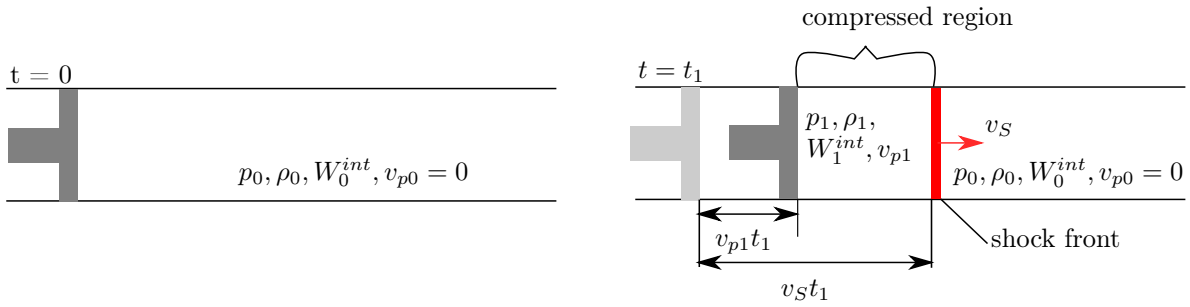

FIGURE 2.7 Shock wave in a compressible fluid. Left part: undisturbed initial state, right part: disturbed and compressed region separated by the shock front. The state variables are pressure p, density ρ, and internal energy W^{int}. Furthermore, v_p denotes the particle velocity, and v_S is the shock velocity.

that causes the generation of a shock wave on the piston surface. The shock wave starts to travel inside the material with a velocity $v_S > v_{p1}$. Material passing through the shock front is instantaneously accelerated to reach the new conditions $\rho_1, p_1, W_1^{int}, v_{p1}$. Ahead of the shock front, the material stays in undisturbed, initial conditions. The relation between shock velocity v_S and particle velocity v_{p1} is modelled with a polynomial

$$v_S = c + \sum_{i=1}^{N} S_i v_{p1}^i, \tag{2.4.2}$$

where c is the speed of sound and S_i are material specific coefficients for the term with exponent i up to polynoms of degree N. In practice, the approximation is simplified to the linear form ($N = 1$) and in some particular cases to $N = 2$. To relate the physical values behind and ahead of the shock front, the following conservation equations have to be fulfilled for $\boldsymbol{v}_{p0} = 0$ (similar to Section 2.3.3):

$$\begin{aligned} \rho_0 v_S &= \rho_1 (v_S - v_{p1}) && \text{mass conservation,} \\ p_1 - p_0 &= \rho_0 v_S v_{p1} && \text{momentum conservation, and} \\ p_1 v_{p1} &= \frac{1}{2}\rho_0 v_S v_{p1}^2 + \rho_0 v_s (W_1^{int} - W_0^{int}) && \text{energy conservation.} \end{aligned} \tag{2.4.3}$$

These equations can be combined to a single equation that only contains the state variables ρ, p and W^{int}:

$$W_1^{int} = W_0^{int} + \frac{(p_1 + p_0)(\rho_1 - \rho_0)}{2\rho_0\rho_1}\,. \tag{2.4.4}$$

Equation (2.4.4) is called Hugoniot condition and is fundamental in shock wave theory.

Closing the system with an EOS

To define the final state of a system, one additional equation to (2.4.4) is required that relates the state variables:

$$p = \bar{f}(W^{int}, \rho), \tag{2.4.5}$$

where $\bar{f}$ denotes a material-specific function. This equation is called EOS (equation of state) and accounts for the influence of a change in internal energy and density on the pressure and vice versa. Combining the

EOS with equation (2.4.4), the internal energy can be eliminated, and one obtains an expression $p = \bar{g}(\rho)$ that describes one form of the Hugoniot curve. Theoretically, an ideal EOS describes all phases and phase transitions. For our application, only the solid-state is of importance. A very simplified relation is the linear EOS

$$p(\rho) = \kappa \left(\frac{\rho}{\rho_0} - 1 \right), \tag{2.4.6}$$

where κ is the bulk modulus. The linear EOS is limited to barotropic conditions and neglects energy effects. To account for this, we expand this equation to

$$p(\rho) = \kappa \left(\frac{\rho}{\rho_0} - 1 \right) + \gamma_0 W^{int}, \tag{2.4.7}$$

in which γ_0 is the Grüneisen parameter γ in norm conditions. The EOS which we apply in this work is the Mie-Grüneisen EOS. It is, in particular, used to determine the pressure state of shocked solids [176]. In general, it reads

$$p - p_0 = \frac{\gamma}{\nu} (W^{int} - W_0^{int}), \tag{2.4.8}$$

where p_0 is the pressure in the unloaded reference state, W_0^{int} is the energy in reference state, ν is the specific volume, and γ is again the Grüneisen parameter. Before we can give the final formulation of the Mie-Grüneisen EOS, we have to elaborate on the Grüneisen parameter. The parameter was originally defined by Harris [87] as

$$\gamma = \nu \left(\frac{dp}{dW^{int}} \right) \Bigg|_v = \nu \frac{\alpha \kappa}{c_\nu}, \tag{2.4.9}$$

where α is the thermal expansion coefficient, and c_ν is the specific heat for a constant volume. Meyers [144] proposes a simplification

$$\frac{\gamma}{\nu} = \frac{\gamma_0}{\nu_0}, \tag{2.4.10}$$

where ν_0 is the specific volume at reference state. It was then improved with a linear corrector a

$$\frac{\gamma}{\nu} = \frac{\gamma_0}{\nu_0} + a \left(1 - \frac{\nu}{\nu_0} \right). \tag{2.4.11}$$

Using this approximation, the definition for compression $\mu = \frac{\rho - \rho_0}{\rho_0}$, and the polynomial approximation given in (2.4.2), we obtain the formulation of the Mie-Grüneisen EOS used in most FE codes

$$p(\mu, E) = \frac{\rho_0 c_0^2 \mu \left[1 + \left(1 - \frac{\gamma_0}{2} \right) \mu - \frac{a}{2} \mu^2 \right]}{\left[1 - (S_1 - 1)\mu - S_2 \frac{\mu^2}{1+\mu} - S_3 \frac{\mu^3}{(1+\mu)^2} \right]^2} + (\gamma_0 + a\mu) W^{int}, \tag{2.4.12}$$

where c_0 is the elastic speed of sound and S_1, S_2, S_3 describe the cubic $\boldsymbol{v}_S$-$\boldsymbol{v}_{p1}$ relationship (compare (2.4.2)). The Mie-Grüneisen EOS (2.4.12) models the pressure in terms of density and internal energy. In the context of our modelling framework, the EOS is needed to describe the volumetric part of the stress tensor (compare (2.4.1)). For a predictive model, it is essential to find the correct material parameters and respect the limitations of the models. For instance, the EOS describes the state of shocked solids well, but for other applications like hypervelocity impact, where phase transition takes place, it will be inaccurate [124].

2.5 Boundary-value problem of continuum mechanics

In the following, we present the boundary-value problem, which is solved by the numerical solvers described in the next chapter. We dedicate one paragraph in this section to contact, which is an essential part of an HVI model.

The strong formulation of the boundary-value problem of non-linear continuum mechanics consists of two components. First, the following field equations for the unknown displacement $\boldsymbol{u}$:

$$\rho \boldsymbol{a} = \nabla \cdot \boldsymbol{\sigma} + \rho \bar{\boldsymbol{b}} \qquad \text{with} \qquad \boldsymbol{a} = \ddot{\boldsymbol{u}} \qquad \text{(dynamic equilibrium)}, \tag{2.5.1}$$

$$\boldsymbol{\sigma} = \hat{\boldsymbol{\sigma}}(\boldsymbol{\varepsilon}) \qquad \text{(material law), and} \tag{2.5.2}$$

$$\boldsymbol{\varepsilon} = \frac{1}{2} \ln(\boldsymbol{F}^T \boldsymbol{F}) \qquad \text{with} \qquad \boldsymbol{F} = \frac{\partial \boldsymbol{u}}{\partial \boldsymbol{X}} + \boldsymbol{I} \qquad \text{(kinematics)}, \tag{2.5.3}$$

where $\bar{\boldsymbol{b}}$ is the volume force. Second, it includes initial and boundary conditions. Here, the material law (2.5.2) describes the functional correlation between Cauchy stresses $\boldsymbol{\sigma}$ and the strain tensor $\boldsymbol{\varepsilon}$ for nonlinear isotropic material. The initial conditions at time $t = 0$ for $\boldsymbol{u}$ and $\boldsymbol{v}$ are

$$\boldsymbol{u}(t = 0) = \boldsymbol{u}_0 \quad \text{and} \quad \boldsymbol{v}(t = 0) = \boldsymbol{v}_0. \tag{2.5.4}$$

Furthermore, displacements and stresses can be defined on the domain boundary $\phi(\Gamma)$. The geometric boundary conditions are prescribed on the Dirichlet boundary $\phi(\Gamma_u)$, where $\boldsymbol{u}$ is

$$\boldsymbol{u} = \bar{\boldsymbol{u}} \quad \text{on} \quad \phi(\Gamma_u). \tag{2.5.5}$$

The second order boundary conditions apply to the derivates and are described on the Neumann boundary $\phi(\Gamma_\sigma)$. Let $\boldsymbol{n}$ be the outward normal on the boundary and $\bar{\boldsymbol{\xi}}$ the prescribed stress, then

$$\boldsymbol{\xi} = \boldsymbol{\sigma}\boldsymbol{n} = \bar{\boldsymbol{\xi}} \quad \text{on} \quad \phi(\Gamma_\sigma). \tag{2.5.6}$$

This set of equations characterizes the continuum mechanis problem that is adressed with numerical methods in the next chapter. Before closing the chapter, we give a short remark on a particular boundary condition which dominates the behaviour during HVI.

Contact in a Lagrangian framework

During the contact, momentum is transferred between the interacting bodies that causes deformation, shock waves, plastic flow or fracture as discussed in the previous sections. From a continuum mechanics point of view, we only discuss normal contact here and neglect tangential contact. Assume there are two bodies—later we call them slave and master—which are moving towards each other as illustrated in Figure 2.8. If there is no contact definition, they occupy the same space after a particular time t_1. This non-uniqueness is not allowed due to the underlying assumption of continuum mechanics that every position can only be occupied

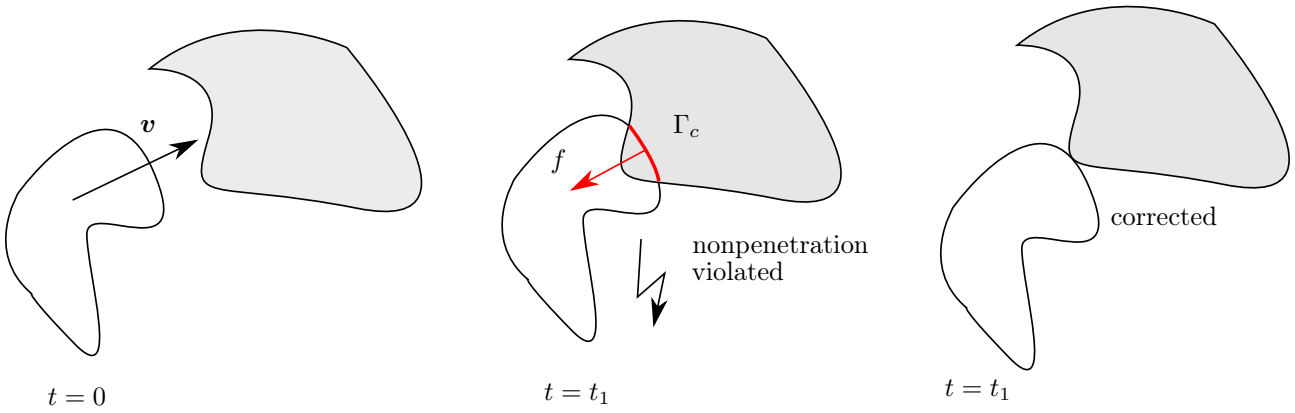

FIGURE 2.8 Nonpenetration condition and correction with a contact force. $t = 0$: the white body is moving with velocity v towards the grey body. $t = t_1$ before the contact is corrected: The bodys overlap; this is not allowed in a continuum mechanics sense. Therefore, the model applies a force on the contact boundary that pushes the two bodies into a valid position (third sketch). If the force exceeds the strength of the material this leads to a deformation of the contact partners.

by one material point at a time. We solve this problem by applying a force such that the non-penetration condition is again satisfied. This approach fulfils the criterion only in an approximate sense. During penalty contact, a small penetration can remain. This force is calculated based on the depth of penetration and the stiffness of the material. In the context of Section 2.5, contact is nothing but a specific type of boundary condition. If the implementation enforces displacement, it is a Dirichlet boundary. If a force-constraint is deployed, it is a Neumann boundary. More details on algorithmic aspects are given in Chapter 4.

2.6 Conclusion

This theoretical chapter derived the equations that describe HVI. We started with a very general description of a material body. There we highlighted, in particular, the importance of different stress and strain measures and introduced the deformation gradient, which is important for the description of the material. Next, we presented the conservation equations that are essential for the final boundary-value problem. At that point, we clarified where the material description goes into the equations. To describe the material, we need a relationship that predicts the stress response to a given deformation in terms of the strain. We can split the stress tensor in the deviatoric and volumetric part.

The deviatoric part is described by the theory of finite plasticity. There, we highlighted how the plastic strain increment is calculated. Based on this theory, we implement a plasticity model in the scope of this work into a numerical solver. We introduced the von Mises plasticity model and a simplified hardening rule to give an example of how the equations of plasticity can be closed. In terms of material theory, we further illustrated how fracture can be modelled in solids and compared fracture mechanisms that can occur during HVI.

The volumetric part is approximated with the Grüneisen equation of state. This equation was derived in the subsequent section based on fundamental principles on shock waves. After the material response had been defined, we recapitulated the conservation equations and added the initial and boundary conditions which define the full set of equations.

In the next chapter, we compare two numerical frameworks that are applied in this work to approximate

this boundary-value problem.

3

General numerical methods for partial differential equations

In the previous chapter, we derived a set of partial differential equations to describe continuum mechanics. There are no trivial analytical solutions for such kind of problems in general. However, numerical methods can approximate the solution. These methods assume that in a small enough subdomain and for a short time, a sufficiently continuous function is a good representative of the solution. The small subdomains are realised with a spatial discretisation. The approximation is then evolved in short time increments. We call this the time discretisation. Two classes of methods can be distinguished based on spatial discretisation: mesh-based and meshfree approaches. Mesh-based methods require a computational mesh, or grid, that contains the connectivity in terms of neighbouring discretisation points. On the contrary, in meshfree methods, no mesh is required, and each discretisation point interacts with a subset of the other points. In terms of time discretisation, the equations can be solved explicitly or implicitly. An implicit formulation allows to compute larger time steps but has increased memory and computation demands. On the other hand, an explicit time discretisation limits the time step but is leaner in terms of computational resources. For highly dynamic applications, like ours, a small time step is favourable to resolve the wave propagation. Therefore, there is no benefit in an implicit method, and our model uses an explicit time integration. Typical applications for implicit calculations are stiff problems like static or quasi-static computations.

This chapter first gives a broad overview of discretisation methods. Then, in the two subsequent sections, we outline the theoretical background of the applied methods FEM and SPH in more detail. The last section complements with a detailed comparison of the strengths and weaknesses of these two methodologies.

3.1 Overview of mesh-based and meshfree methods

In this section, we present a survey of existing mesh-based and meshfree methods and discuss the advantages of coupling two discretisation methods. The purpose is to determine suitable methods to model high-velocity impact. Therefore, we give only a short description of each method and discuss typical applications and whether it is accessible in our applied codes.

3.1.1 Mesh-based methods

Mesh-based methods discretise the computation domain with a computational mesh and approximate the function at the node points, in the volume element or the whole interior. There are three principal mesh-based approaches:

- The finite element method (FEM) discretises the domain with elements and approximates the solution as a linear combination of shape functions. The standard FEM uses continuous shape functions which results in a continuous solution. The method is flexible and robust and can be applied to a wide range of applications and geometries. Eulerian, Lagrangian, and Arbitrary-Eulerian-Lagrangian (ALE) frameworks of the FEM exist. The difference lies in the frame of reference. The Lagrangian method uses a moving frame of reference, and the Eulerian method uses a stationary frame. The ALE framework combines both frameworks. The Eulerian and the ALE framework are mainly used for CFD applications, but also explosion and hypervelocity impact. If the deformations are small enough, the Lagrangian approach is used, this is mainly the case for structural applications. The approximation space of the standard Lagrangian FEM does not include discontinuous solutions. Therefore, it can not represent cracks without shape function enrichment, erosion, or a node-splitting technique.

- The finite difference method (FDM) is the oldest discretisation method, and discrete points in space approximate the solution. Difference stencils describe differential operators in the continuous equations. The physical values are saved and computed for these grid points resulting in a discrete solution. Finite differences are mainly applied by academia for fluid dynamics, meteorology, astrophysics but also structural design. Barton et al. investigate an adaptive FDM in the Eulerian frame for a similar application [13]. They obtain good accordance for a hypervelocity impact but also highlight the limitations due to mass error. The main advantage of finite differences is that it is more efficient for particular applications with tuned stencils. Stencils are discretised, differential operators. A significant difference is that in the FEM, the designer does not create the stencils explicitly. Instead, they are computed inside the code via integration over chosen shape functions. Therefore, the stencils are not explicitly visible in the FEM. The main disadvantage of the FDM is that it is primarily constructed for the Eulerian description. We prefer a Lagrangian approach to track the material surface explicitly. Furthermore, the FDM requires fixed grid points at known points—ideally in a regular or at least structured mesh. Hence, the finite difference method is unsuited for our application.

- The finite volume method (FVM) discretises the domain with volume cells and computes fluxes between cell boundaries. This approach results in a strict volume and energy-conserving scheme, which is an essential property for fluid applications, in particular. Hydrodynamic behaviour in hyper-velocity impact of 10 km/s was investigated with the FVM by Hertel et al. [89]. Besides standard finite volume

approaches, higher-order finite volume methods such as discontinuous Galerkin or spectral methods that use higher-order polynomials have been developed. These methods are mainly designed for fluid applications and not of interest to this research as well.

Generally speaking, the finite volume methods and finite difference methods are mainly used for fluid applications and solid mechanics applications deploy the FEM in general. In terms of mesh-based methods, the Lagrangian FEM is the state of the art choice to model HVI [10, 28, 129, 193].

3.1.2 Meshfree methods

Meshfree methods do not require a computational mesh and instead consist of independent approximation points. Although particle methods are solely a subset of meshfree methods, we call these approximation points particles. Momentum and thermodynamical properties between neighbouring particles are exchanged depending on the chosen method. Since it bears advantages to do the computation without a mesh, various approaches have been developed. For instance, *LS-DYNA®* supports element free Galerkin (EFG), peridynamics and smoothed-particle hydrodynamics (SPH).

In the next section, we see that the inherited difficulties of the mesh-based structure limit the range of applications of the FEM. Large mesh deformation and discontinuities in the solution are the main problems. To address the deficiency of the classical mesh-based methods, researchers derived various meshless methods in the past decades. Fries et al. give a comprehensive overview and classification of meshfree methods (MM) [69]. The most common meshfree approaches apart from SPH, are the discrete element method, the reproducing kernel particle method, the element free Galerkin method, and peridynamics.

- SPH associates particles with kernel functions of compact support. Physical values are saved at the particle positions, and the functions are only evaluated at the particle positions (collocation method). Originally, SPH was developed for astronomy and has been extended for the simulation of material strength. Its main advantage is that additional physical laws can be implemented quickly, modelling of fracture does not require a modification of the model, and that an initial configuration can be generated quickly.

- The discrete element method (DEM) is mainly used to simulate granular material. Each element describes the motion of a set of particles. Therefore, DEM reduces the degrees of freedom drastically, and the run time becomes feasible. Discrete elements can be used to represent eroded elements which behave similar to granular material.

- For mainly continuous material, methods based on the moving least squares approach (MLS) or the reproducing kernel particle method (RKPM) were developed. For monomial basis functions, both methods lead to the same approach.

- The element free Galerkin (EFG) method in *LS-DYNA®* is based on the MLS. The idea is to minimise the weighted L_2-error norm. It is mainly applied in machining for tasks such as cutting, bulk-forming and forging processes.

- The motivation for peridynamics is the modelling of natural cracks, where the mathematical framework of finite elements is ill-suited. The theory is due to Silling [182], who proposed the method in the year

2000 and later presented peridynamic modelling of the Kalthoff-Winkler experiment (ductile) with good accordance. This finding symbolises a milestone in fracture prediction [183]. However, initially, the method was developed for brittle fracture, and the previous result mainly shows that the range of applications is much more extensive. The two commercial codes *LS-DYNA®* [167] and Abaqus [20] support the method partly. The latter embeds it into the finite element solver PIFEA (Peridynamics Implemented Finite Element Analysis) [139].

We focus on SPH in this work as SPH experienced more development in the numerical codes we utilise.

3.1.3 Coupling of numerical methods

The introduced numerical methods are not incompatible, which means that we can combine the benefits of several methods in a coupling framework. The coupling can be done in space or in time. For our model, we propose a spatial combination of the FEM and SPH approach, where the FEM is used in areas of little deformation to propagate the shockwaves, and SPH is used to model the impact and material fracture (compare Figure 3.1). Kilic [110] gives an example of a hybrid approach in time. He models the displacements with the FEM and the crack propagation with peridynamics and merges both solutions in time. Kumar [117] describes a coupled finite element and element free Galerkin approach for the simulation of stable crack growth in ductile materials. Macek and Silling [139] show how the peridynamic approach can be implemented into the FEM using truss elements and demonstrate the equivalence of the FEM and the meshless peridynamic approach. These examples show how active coupling of different models is used to combine the best out of several methods in order to obtain a more powerful numerical method.

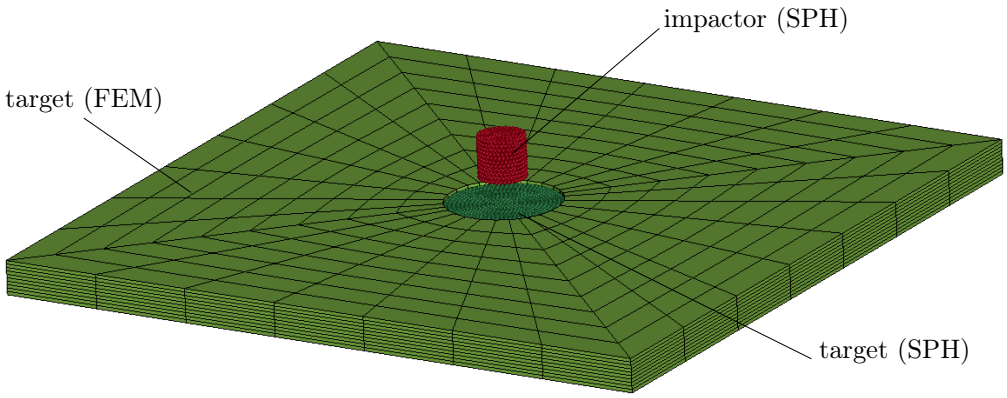

FIGURE 3.1 Coupling of the FEM and SPH for the impact of a fragment against a plate. The target consists of finite elements and SPH particles and the impactor consists of particles only. Besides this coupling approach, an adaptive transformation from finite elements to SPH particles exists in *LS-DYNA®*.

3.2 Finite element method (FEM)

This section presents the FEM as a discretisation method for HVI dynamics. The section is structured as follows: First, we outline the history of the FEM and give a broad overview of typical applications. Next, we present the basic theory of the FEM. We highlight the difficulties related to our application of HVI, that are inherited from the FEM framework and discuss the state of the art solutions for them.

3.2.1 History and applications

The finite element method originated from the need to solve complex problems in aeronautical and civil engineering. Early contributions for solving partial differential equations were developed in the 19th century by Rayleigh, Ritz and Galerkin. Courant [47] proposed the idea to divide the domain into finite triangular subregions to solve elliptic partial differential equation in the early 1940s. At the same time, Hrennikoff [94] used a lattice analogy for discretisation. In 1956, it was Turner et al. [195] who developed the triangular element stiffness matrix and elaborated the framework for the FEM. His co-worker Clough [42] popularised the term finite elements to distinguish the method from the continuous analysis. From then on, different research groups started to intensify the development of the method. Apart from Clough with co-workers at UC Berkley, Argyris and co-workers in Stuttgart [7, 6], Zienkiewicz with co-workers in Swansea University [226], and groups in Paris and Cornell contributed with their research [39, 12]. The FEM code NASTRAN developed at the NASA and SAP IV from Berkeley was soon made available open-source and thereby increased the impetus of the FEM. Since then, software companies developed different open-source and commercial FEM codes such as *ANSYS*®, *ABAQUS*®, *IMPETUS*®, *LS-DYNA*®, *PERMAS*, *SIMSCALE* and others [202, 201, 205, 208, 210, 211]. The method, which was initially developed for civil and aeronautical engineering, has been generalised. Now, it is used for numerical modelling of physical systems in various engineering disciplines like thermodynamics, electromagnetism, fluid dynamics, and mechanics. In 1999, Belytschko invented the extended finite element method (XFEM), that allows for discontinuities in the model [145]. Discontinuities can be either weak (material interfaces) or strong (cracks). Among others, Jiang showed that embedding the problem's feature into the approximation space can improve convergence rates and accuracy significantly [101]. At the present moment, the FEM is the most common numerical framework for problems in structural mechanics. Parallelisation techniques and faster computer systems with huge memory allowed to calculate more complex tasks. Authors implemented various types of finite element methods for different applications. Among other improvements, the development of higher-order finite elements increased the accuracy and range of application for the FEM [154, 187]. For instance, the spectral element method combines in a similar way the accuracy of the spectral method with the geometric flexibility of finite elements to obtain higher accuracy [122].

3.2.2 Basic formulation

This section explains the FEM with regard to the given application of HVI. More comprehensive explanations on nonlinear finite elements can be found in various books, e.g., Wriggers [215], Belytschko [22], Öchsner [153] or Neto [151]. For the FEM, we have to transfer the boundary value problem described in Section 2.5 to a weak formulation for the standard FEM. Strong formulations of the FEM do also exist, e.g. Tornabene [194]

but are not in the scope of this work. We recall the equation for momentum conservation (2.5.1)

$$\rho \boldsymbol{a} = \nabla \boldsymbol{\sigma} + \rho \bar{\boldsymbol{b}}, \tag{3.2.1}$$

where $\nabla(\cdot)$ denotes the gradient of a function in space, and $\bar{\boldsymbol{b}}$ is the outer body force. The transformation to the weak formulation is done with the framework of Galerkin, multiplying the local momentum balance (3.2.1) with a test function $\delta \boldsymbol{u}$ and integrating it over the current domain

$$\int_{\phi(\Omega)} \delta \boldsymbol{u} \rho \boldsymbol{a} = \int_{\phi(\Omega)} \delta \boldsymbol{u} (\nabla \boldsymbol{\sigma} + \rho \bar{\boldsymbol{b}}) dv. \tag{3.2.2}$$

In continuum mechanics, the test function is interpreted as a virtual displacement $\delta \boldsymbol{u}$. Applying integration by parts, the Cauchy integral theorem, and defining the boundary tension $\bar{\boldsymbol{t}} = \boldsymbol{\sigma} \boldsymbol{n}$ on the Neumann-boundary $\phi(\Gamma_\sigma)$, the final equation reads

$$\underbrace{\int_{\phi(\Omega)} \delta \boldsymbol{u} \cdot \rho \boldsymbol{a}}_{\delta W^{kin}} = \underbrace{- \int_{\phi(\Omega)} \nabla \delta \boldsymbol{u} : \boldsymbol{\sigma} dv}_{-\delta W^{int}} + \underbrace{\int_{\phi(\Omega)} \delta \boldsymbol{u} \cdot \rho \bar{\boldsymbol{b}} dv + \int_{\phi(\Gamma_\sigma)} \delta \boldsymbol{u} \cdot \bar{\boldsymbol{t}} da}_{\delta W^{ext}}. \tag{3.2.3}$$

The framework includes nonlinearity as it evaluates stress and strain measures in the current configuration. To approximate the weak formulation of structural dynamics numerically, the FEM uses a computational grid for the spatial discretisation. Approximated values are indicated with the superscript $(\cdot)^h$. Formally, the continuous domain $\Omega \in \mathbb{R}^3$ is distributed into n_e disjoint finite elements

$$\Omega \approx \Omega^h = \bigcup_{e=1}^{n_e} \Omega_e, \tag{3.2.4}$$

where $\bigcup(\cdot)$ denotes the union of elements. To approximate the unknowns in (3.2.3), we define shape functions $\boldsymbol{N}_{(e)}$ for each element e constituting a basis for the approximative function space. These shape functions fulfil the Kronecker delta property being one at one node and zero at all other nodes. In general, they are defined in local element coordinates $\boldsymbol{\xi}$. The following derivation is done in Voigt-notation. This notation exploits the symmetry and writes $[3 \times 3]$ matrices in $[6 \times 1]$

$$\boldsymbol{A} = \begin{bmatrix} A_{11} & A_{12} & A_{13} \\ A_{21} & A_{22} & A_{23} \\ A_{13} & A_{13} & A_{33} \end{bmatrix} \Rightarrow \begin{bmatrix} A_{11} \\ A_{22} \\ A_{33} \\ A_{23} = A_{32} \\ A_{13} = A_{31} \\ A_{12} = A_{21} \end{bmatrix}. \tag{3.2.5}$$

The simplest form of shape functions are linear functions. Without loss of generality, we explain the approximation for a 1D example in the following (compare Figure 3.2). In this simplified example, the shape functions are

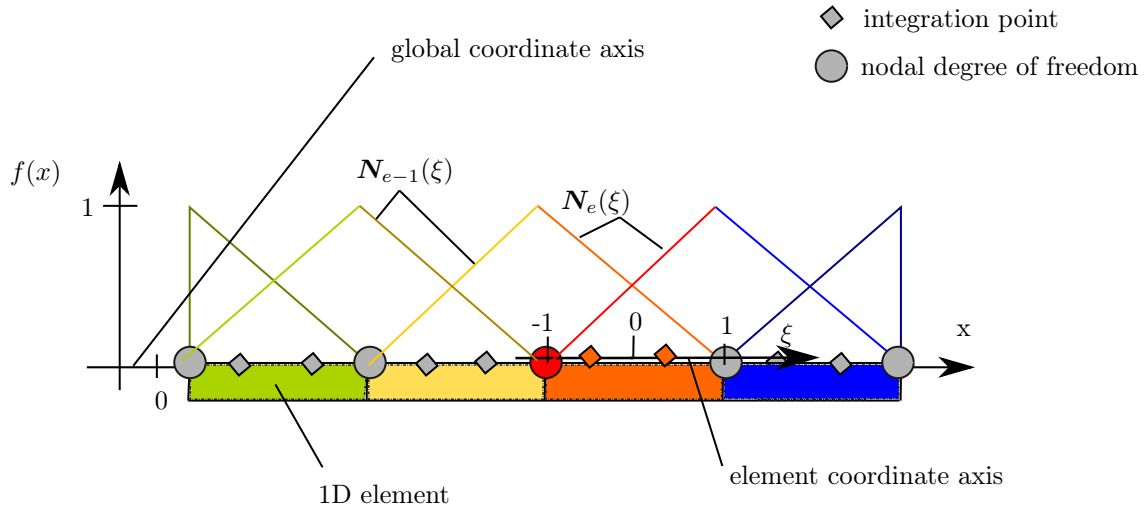

FIGURE 3.2 Illustration of a shape function for linear 1D finite elements. In each element there are shape functions to all boundary nodes. These shape functions are expressed in local coordinate ξ.

$$\boldsymbol{N}_{(e)}(\xi) = \begin{bmatrix} 0.5\ (1+\xi) \\ 0.5\ (1-\xi) \end{bmatrix}. \tag{3.2.6}$$

Further, we introduce the $\boldsymbol{B}$ matrix

$$\boldsymbol{B} = \nabla \boldsymbol{N}. \tag{3.2.7}$$

In our simple example $\nabla = \dfrac{\partial}{\partial \xi}$, and the B-matrix is

$$\boldsymbol{B}_{(e)}(\xi) = \begin{bmatrix} \dfrac{\partial}{\partial \xi} \end{bmatrix} \begin{bmatrix} 0.5(1+\xi) \\ 0.5(1-\xi) \end{bmatrix} = \begin{bmatrix} +0.5 \\ -0.5 \end{bmatrix}. \tag{3.2.8}$$

Back in the 3D example, we need expressions for the approximant of partial displacement $\delta \boldsymbol{u}^h$, the gradient of partial displacement $\nabla \delta \boldsymbol{u}^h$, and the accelerations $\boldsymbol{a}^h$ in (3.2.3) to find $\boldsymbol{u}^h$. In matrix formulation, we can express these in terms of shape functions $\boldsymbol{N}$, B-matrix $\boldsymbol{B}$, the known nodal displacements $\boldsymbol{d}$ at grid vertices, partial displacements $\partial \boldsymbol{d}$ at grid vertices, and accelerations $\ddot{\boldsymbol{d}}$ at grid vertices. Starting with the definition for the approximant for the displacements $\boldsymbol{u}^h_{(e)}$

$$\boldsymbol{u}^h_{(e)}(\boldsymbol{\xi}, t) = \boldsymbol{N}_{(e)}(\boldsymbol{\xi}) \boldsymbol{d}_{(e)}(t), \tag{3.2.9}$$

we find the expressions for the unknowns

$$\delta \boldsymbol{u}^h_{(e)}(\boldsymbol{\xi}, t) = \boldsymbol{N}_{(e)}(\boldsymbol{\xi}) \delta \boldsymbol{d}_{(e)}(t), \quad \boldsymbol{a}^h_{(e)}(\boldsymbol{\xi}, t) = \boldsymbol{N}_{(e)}(\boldsymbol{\xi}) \ddot{\boldsymbol{d}}_{(e)}(t), \quad \text{and} \quad \boldsymbol{\nabla} \delta \boldsymbol{u}^h_{(e)}(\boldsymbol{\xi}, t) = \boldsymbol{B}_{(e)}(\boldsymbol{\xi}) \delta \boldsymbol{d}_{(e)}(t). \tag{3.2.10}$$

The ultimate goal is to update the nodal displacements $\boldsymbol{d}$. Based on these approximations for the kinematic variables the discrete form of the equation of motion can be described inserting (3.2.10), (3.2.7) and (3.2.4) in (3.2.3):

$$\boldsymbol{M} \ddot{\boldsymbol{d}}(t) + \boldsymbol{f}^{\text{int}}(\boldsymbol{d}(t)) = \boldsymbol{f}^{\text{ext}} \tag{3.2.11}$$

with the mass matrix

$$\boldsymbol{M} = \bigcup_{e=1}^{n_e} \left[\int_{\phi(\Omega_e)} \rho \boldsymbol{N}^T \boldsymbol{N} dv \right]_{(e)}, \tag{3.2.12}$$

the internal node forces $\boldsymbol{f}_{\text{int}}$ that are evaluated in the current configuration $\boldsymbol{\sigma} = [\sigma_{11}, \sigma_{22}, \sigma_{33}, \sigma_{12}, \sigma_{23}, \sigma_{13}]^T$

$$\boldsymbol{f}^{\text{int}}(\boldsymbol{d}(t)) = \bigcup_{e=1}^{n_e} \left[\int_{\phi(\Omega_e)} \boldsymbol{B}^T(\boldsymbol{d}(t)) \boldsymbol{\sigma}(\boldsymbol{d}(t)) dv \right]_{(e)}, \tag{3.2.13}$$

and the time dependent outer forces

$$\boldsymbol{f}^{\text{ext}}(t) = \bigcup_{e=1}^{n_e} \left[\int_{\phi(\Omega_e)} \boldsymbol{N}^T \rho \bar{\boldsymbol{b}}(t) dv + \int_{\phi(\Gamma_e)} \boldsymbol{N}^T \bar{\boldsymbol{t}}(t) da \right]_{(e)}. \tag{3.2.14}$$

Note that the B-Matrix and the stresses are evaluated for the current configuration. Damping of the equation of motion can be achieved by adding a viscous damping term $\boldsymbol{C}^s \dot{\boldsymbol{d}}$ to (3.2.2):

$$\boldsymbol{M} \ddot{\boldsymbol{d}}(t) + \boldsymbol{C}^s \dot{\boldsymbol{d}} + \boldsymbol{f}^{\text{int}}(\boldsymbol{d}(t)) = \boldsymbol{f}^{\text{ext}}, \tag{3.2.15}$$

where $\boldsymbol{C}^s$ is the stiffness matrix. Viscous damping can stabilise oscillations. In our particular application oscillations occur during the impact when elements are deleted. Numerical codes offer different element formulations and numerical modifications to solve the equation of motion accurately and stable for the unknown nodal displacements $\boldsymbol{d}$.

3.2.3 Challenges in the FEM to model HVI

HVI includes large deformation, adiabatic heating and fracture. This complex phenomenology requires a robust and accurate method to obtain predictive results. In the following, we discuss selected issues linked to the standard FEM.

Directly related to large deformation is that the behaviour of standard finite elements can get unphysical when the deformation gets too large. For incompressible solids and material with a Poisson's ratio[1] close to 0.5, volume locking occurs as the finite element functions are unable to approximate a volume-preserving strain field accurately [30]. The reason for this is that the displacement approximation is not sufficiently rich to satisfy both the incompressibility condition and the momentum balance. Although steel has a Poisson's ratio of around 0.3 in the elastic regime, it is incompressible in plasticity. The critical assumption of the von Mises plasticity model is that plastic flow is unaffected by pressure. Therefore, the code has to deploy a dedicated element technology to circumvent volume locking. Often, locking is associated with geometrical locking due to the particular geometry, and loading condition, rather than material locking described above [116]. The most prominent example for geometrical locking is shear locking during the bending of a slender beam with linear elements or shells. Shear locking is an error due to the linear nature of the elements that

[1] the Poisson's ratio describes the expansion of material under uniaxial compression in the other directions

can not accurately model the curvature present in the actual material under bending and results in shear stress. However, this kind of locking is not observed in our application.

Another problem related to large deformation is the explicit time step criterion which can get very small for highly deformed elements. The critical time step size Δt_e for solid elements is

$$\Delta t_e = \frac{L_e}{c}\,, \tag{3.2.16}$$

where L_e is the characteristic length and c is the speed of sound. Under compression, the denominator changes to

$$\Delta t_e = \frac{L_e}{\bar{c}}\,, \qquad \text{with} \qquad \bar{c} = Q + \sqrt{Q^2 + c^2} \qquad \text{and} \qquad Q = C_1 c + C_0 L_e |\dot{\bar{\varepsilon}}_p^{vol}|. \tag{3.2.17}$$

Here, Q is a correction term determined by the two bulk velocity coefficients C_0 and C_1 and the volumetric part of the plastic strain rate $\dot{\bar{\varepsilon}}_p^{vol}$ [85]. The characteristic length for an eight-node hexahedral element is $L_e = \dfrac{v_e}{A_{e_{\max}}}$, where v_e is the volume of the element and $A_{e_{\max}}$ is the area of the largest face. For four-node tetrahedral elements, the characteristic length is the minimum altitude. As a consequence, significant deformation of elements leads to a smaller critical time step. A reduced time step can then significantly increase the total run time.

If the plastic deformation is too large, the material loses its load-bearing capacity and fractures. Element fracture is a feature that is not allowed in standard finite elements. The shape functions enforce a continuous solution and, thus, discontinuities like cracks are not part of the approximation space. Instead, numerical techniques such as enrichment of the approximation space can be used to describe cracks in the FEM. In the presence of these discontinuities, stress singularities can occur. The singularities express in the discretisation as follows: the finer the grid, the larger the stress observed in the element at the position of the crack, and the earlier failure occurs. The macroscopic material model can not represent the physics that happens on a microscopic level. Instead, it is optimised to predict the stress correctly at a particular grid size. As a consequence, regularisation of the material model is required such that it is valid for different discretisations.

One last issue with the FEM is not directly related to HVI. It is the difficulty of generating a high-quality hexahedral computational mesh. Hexahedral mesh generation has been considered as the Holy Grail in the mesh generation community for many years and is still not fully solved. In the past years, different researchers improved meshing methods that are not yet commercially available and do only cover a subset of complex geometries (e.g. Jiang [100] or Shang [181]). One main difficulty is the global propagation of hexahedral constraints through the model. These constraints require that the grid does not contain T-nodes, which are nodes that are on the edge of another element. For instance, dividing one element in the discretisation into two can change a large number of other hexahedrons throughout the model. For complex geometries, computer methods can not replace by-hand mesh generation for these elements [175]. However, automatic mesh-generation is a solved problem for tetrahedral elements. An algorithm can generate and connect a user-defined set of node positions with a Voronoi Delaunay tetrahedralization resulting in a mesh of good quality [58, 132]. Other techniques for generating tetrahedral meshes are the advancing front techniques (AFT) (e.g. Lo [135]) and Octree methods (e.g. Schroeder and Shepard [179]).

Whether tetrahedral meshes are a suitable choice for our application and how the number of integration points influences the solution is discussed in the following section.

3.2.4 Element technology to address large mesh deformation

Due to different applications and limitations of the standard FEM, researchers developed variations and modifications to the original FEM. This section first discusses the difficulties of tetrahedral elements and then presents selected element technologies that have been developed to describe large deformation.

Tetrahedral and hexahedral elements

For the sake of readability, we use the terms hexas (hexahedral elements) and tets (tetrahedral elements) in the following. Figure 3.3 shows an exemplary meshing of a cylinder with tets and hexas. Not being able to generate hexahedral meshes automatically is only one reason to elaborate on whether the numerical simulation requires hexas. Another one is the inherited difficulty of investigating convergence, as automatically refined meshes can only divide one element into eight, which leads to a too fast increase in computation cost and memory requirements for our application. There is a long discussion between researchers about which element type is better suited for a particular application. We want to highlight that there are lots of different element formulations for both hexas and tets. Therefore, this brief comparison only relates to specific element technology and is neither complete nor universal.

The linear tet requires no numerical integration, which simplifies assembling the stiffness matrix. However, the stress distribution in this element is constant. This leads to volumetric locking and a too stiff material behaviour [62]. Higher-order tets can improve volumetric locking. Abbas concludes in his comparison that quadratic tets are superior in terms of accuracy, compared to the quadratic and linear hexas he used [1]. Cifuentes [40] and Yoo [219] draw similar conclusions for particular element formulations. The latter reference made the comparison for impact loadings which gives us evidence that these elements can also be a valid choice for our application. Bourdin [29] observes that the major drawback of tets for his application was increased run time, which is however outweighed by the advantages of an automatic meshing approach.

Hexahedral meshes generated by hand have advantages over tetrahedral meshes: Once set up, the modification of the geometry via extrusion or deletion of element layers is much easier compared to tets where the whole geometry has to be remeshed (compare Zukas [231] and Figure 3.3). Clearly, for CFD applications, tets have a disadvantage for mesh refinement in a particular flow direction. There, hexas can be refined more easily [26]. Furthermore, for boundary layer flow, significantly larger elements can be used with hexas. Tets are often preferred in academia, as refinement studies are easier to conduct.

For the particular code *LS-DYNA®*, Schmied and Erhart [178] show that higher-order tets are as accurate as standard hexas for a Taylor bar impact (compare Section 1.2.3). Still, they recommend using hexas whenever possible. They do not recommend mixed meshes in *LS-DYNA®* since they use degenerated tets. These elements collocate the mass of five out of eight nodes of the eight-node element in one node of the tetrahedron element. As we are computing a basic academic example consisting of a cylinder, a sphere and a cuboid, hexa mesh generation can be automated in our application (compare Application II and Application III). Therefore, there is no need for tets. For more complex geometries, higher-order tets can be a legitimate choice to circumvent time-consuming mesh generation.

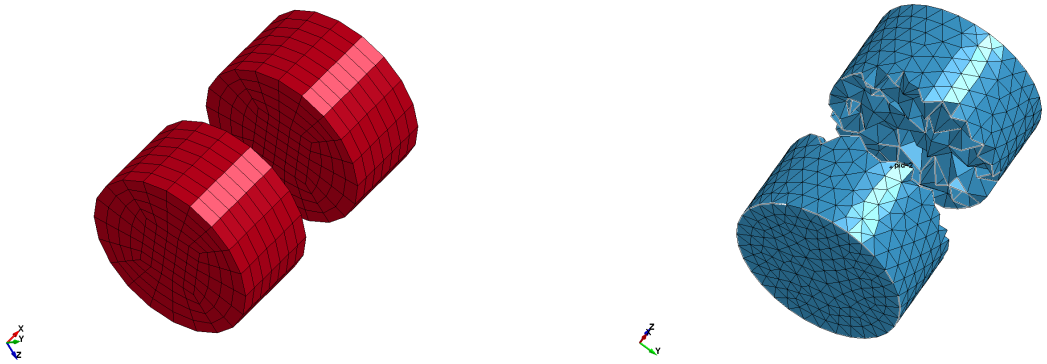

A hexahedral mesh of a cylinder

B tetrahedral mesh of a cylinder

FIGURE 3.3 Comparison of hexahedral and tetrahedral mesh. The inner third is blanked to illustrate the three-dimensional shape of the elements. The aspect ratio can easily be adjusted for hexas but not for tets.

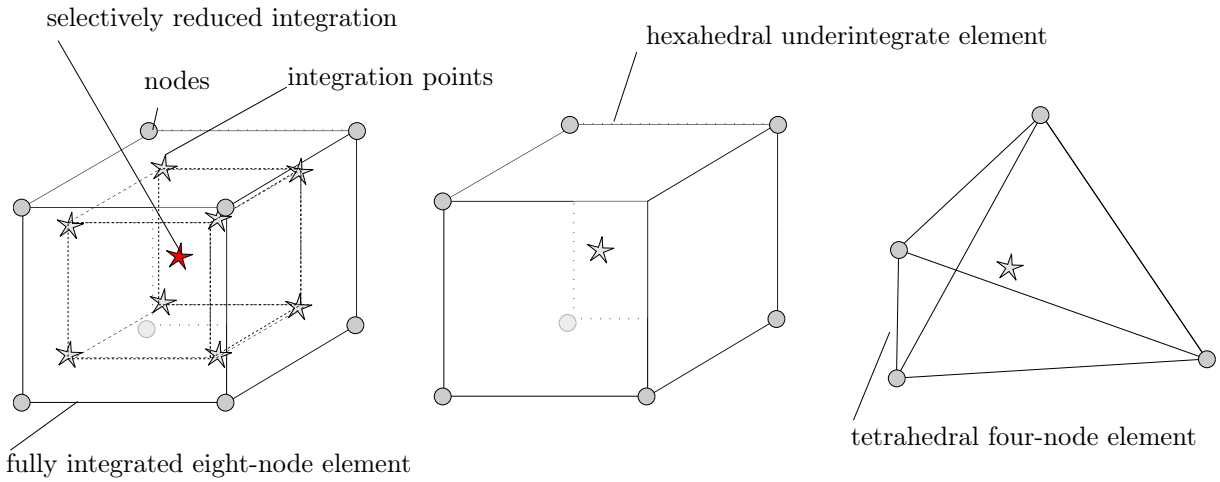

FIGURE 3.4 Different typical element formulations and corresponding integration points. From left to right: a fully integrated eight-node element, a hexahedral underintegrated element with one integration point, and a tetrahedral four-node element with one integration point.

Integration points in elements

The number of integration points of an element determines the accuracy and convergence of the method. Integration points are the spatial positions of the sampling points for the numerical integration in (3.2.2) - (3.2.14). We only discuss hexahedral elements in the following. Figure 3.4 shows different brick elements. In the so-called fully integrated eight-node brick element (first element from the left), the nodal positions of the element are not equal to the integration points. Instead, the integration points are slightly shifted toward the centre of the element. For incompressible or nearly incompressible behaviour (as for von Mises elastoplasticity), locking phenomena can appear when using such elements. These locking phenomena occur when the displacement approximation is not sufficiently rich to satisfy both the momentum balance and the incompressibility equation [25]. To avoid this problem, multi-field elements in which stress and strain are considered as dependent variables can be used [159, 131, 114].

Another approach is to use reduced, or selectively reduced, integration techniques [140]. For the reduced integration technique, only one integration point is used. Besides other shortcomings of this so-called one-point integration in the static analysis, one point integration leads to the well-known hourglass phenomenon. This phenomenon is due to a reduced rank of the stiffness matrix. Stabilisation terms can retain the original rank of the matrix and eliminate zero-energy modes. Since calculation time is directly related to the number of integration points, reduced integration is a very efficient approach.

The selectively reduced integration technique assumes a constant volume change over the element but uses the same integration points as the fully integrated element for the deviatoric part. In principle, we distinguish two approaches to calculate the volume change in selective integration: In the first one, the volume change is calculated at only one integration point at the element centre. The second one, also known as a B-bar method takes the mean value of the volume change over all nodes.

The designer can increase the number of degrees of freedom by adding integration point in the middle of each edge, in the centre of the surfaces, or the brick element centre. These kinds of elements have additional integration points and typically use higher-order shape functions.

3.2.5 Failure and fracture

For the application of HVI, an essential modelling part is failure and fracture. As the shape functions are per definition continuous, additional modelling is required to describe the resulting discontinuities. We distinguish three different methodologies (compare Figure 3.5).

The easiest way to deal with a failed element is to delete it from the simulation. This technique is called element erosion. It is very robust and easy to implement but has two significant drawbacks. Firstly, it deletes mass from the system, which contradicts the principle of mass conservation. Secondly, the deletion of elements can lead to a sawtooth-like contact behaviour and therefore, an incorrect prediction of the impact. To address these issues, different authors propose the conversion of elements to discrete elements or SPH elements.

The second approach is the so-called node splitting. There, elements are not deleted, but the domain is split between two elements that fail. So, the number of nodes increases, since the nodes at the surface that opens up are duplicated. From an implementation point of view, this is challenging as dynamic data structures are required. However, this approach guarantees mass conservation.

The third possibility is the XFEM (eXtended Finite Element Method). The XFEM enables a local enrichment of approximation spaces. More precisely, the enrichment functions are added to the function space

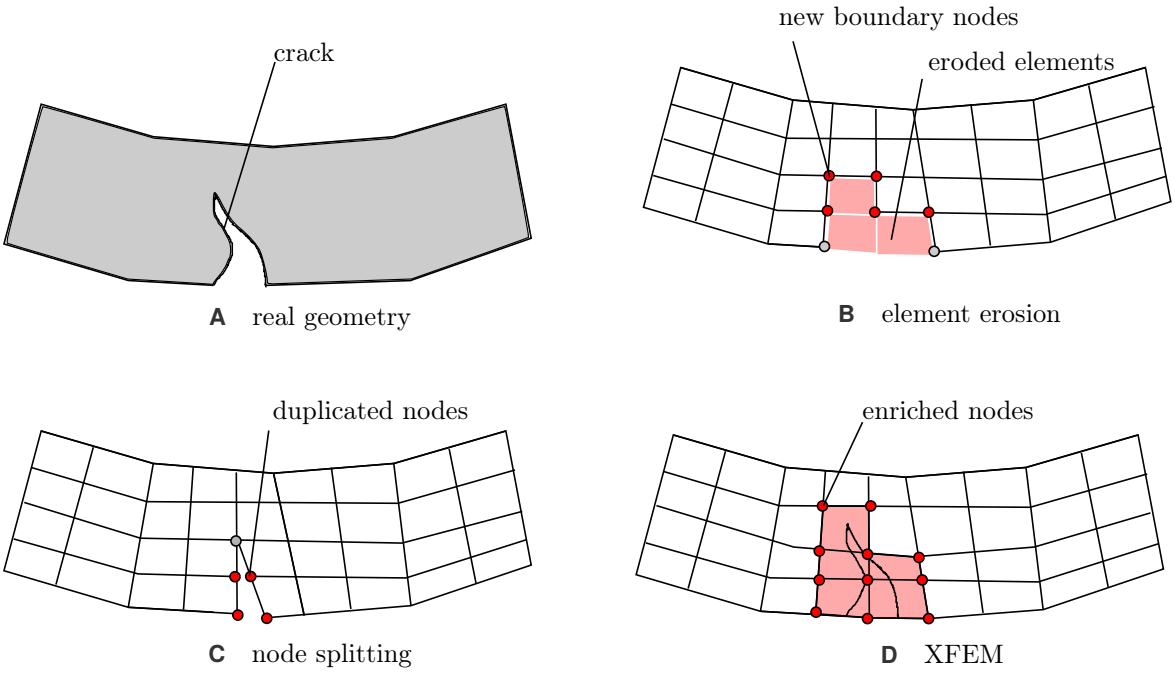

FIGURE 3.5 Three ways to describe fracture in the FEM. **B** element erosion removes elements with material failure from the computation, **C** node splitting retains failed elements but adds additional nodes on the crack surface, **D** XFEM enriches the approximation functions to allow the material density to be zero in the region of the crack.

basis for a subset of the mesh nodes. E.g., for step discontinuities, the enrichment function is the Heaviside step function. The main issues with the XFEM are that the approximation does not have the Kronecker-delta property. Typical applications for the XFEM are quasi-static crack propagation in two dimensions.

To sum it up: There are many possibilities to describe failure and fracture with the FEM. However, we are limited to those methods that are available in the commercial codes that we use. Therefore, the XFEM is not an option for this work. *IMPETUS®* provides a node-splitting algorithm and *LS-DYNA®* deploys element erosion and element conversion to SPH particles or discrete particles to describe fracture behaviour.

3.2.6 Conclusion

This section presented the FEM. Based on our history review, we conclude that the FEM is a methodology which has been used excessively in structural mechanics such as civil engineering, automotive, and beyond for many decades. The basic formulation results in a continuous approximation, which is described by shape functions inside the elements. This continuity requirement is also the limitation of the basic formulation, which is most important for HVI applications. To describe fractures, the model needs to allow discontinuities. We identify element erosion, node-splitting, and XFEM as the three main approaches to overcome the limitations. The second difficulty of the FEM is the description of large deformations. We compare different element technology and identify selectively-reduced elements as a compromise between an accurate integration and little volumetric locking.

3.3 Smoothed-particle hydrodynamics (SPH)

This section presents the mesh-free method SPH as a discretisation method for HVI dynamics, and is structured as follows: In the first section, we outline the history and the development of the method. Furthermore, we describe typical applications and numerical codes that apply it. Next, we derive the basic theory of SPH and make first statements about the accuracy and limitations of the method. Then, we present variations of the SPH method that lead to a final discretisation scheme. Herein, we outline the SPH formulations used for our simulations in detail. Finally, we provide an overview of applications of SPH; in general, and with particular regard to our application in the field of high-strain dynamics.

3.3.1 History and literature review

The SPH method was developed in 1977 by Gingold [70] and Lucy [137] for the simulation of astrophysics problems. Virtual particles are connected with physical properties, and a collocated interpolation method that uses kernel functions describes the interactions between them. This framework can describe arbitrary physical laws, even partial differential equations such as the conservation equations of continuum mechanics. It allowed approximating derivatives without a computational mesh for the first time. In 1991, Libersky and Petchek [127] extended the SPH method to approximate the full stress tensor and, thus, made it capable of simulating problems where material strength is essential. In subsequent work, Libersky and co-workers [128] extended the method to solve three-dimensional problems. However, the SPH method was not only seen as a robust and straightforward scheme for solving partial differential equations. Also, the shortcomings of the method were exposed: The implementation of boundary conditions is one of the difficulties since it is not clear which particles define the boundary. The original SPH method also produces a numerical instability under tension (tensile instability) and is not even 1^{st} order consistent. This property means that it is not capable of approximating constant functions without error. These deficiencies lead to criticism, and researchers doubted the quality of results obtained with SPH. Therefore, techniques were needed to address the deficiencies.

The community found various solutions to overcome the shortcomings: For instance, Randles and Libersky [164] propose a kernel renormalisation approach that restores the consistency, in 1996. Many authors addressed tensile instability. Most approaches can be related to one of the following three ideas: first Dyka [59] proposed a shifted integration technique, the so-called stress-point solution in 1995, second Swegle [188] introduced conservative smoothing in the same year, and thirdly Vignjevic [198] suggested a total Lagrangian formalism in 2006. With these improvements, SPH became a widespread technique in different fields of application. Due to a slightly increased computational cost compared to optimised mesh-based methods, it is applied in particular where classical methods are not further applicable. These applications include problems where significant topological changes occur (such as hydrodynamics, welding, and impact), applications with free surfaces in fluid dynamics (sloshing tank or oil in gearings), and mobile interfaces or complex geometries.

We utilize the SPH implementations of the commercial codes *LS-DYNA®* [208] and *IMPETUS®* [205], and the academic code *MCM* [50]. Besides these SPH codes, universities and software developers implemented several SPH software packages. At the University of Stuttgart, Pasimodo [209] is developed in cooperation with Inpartik [206] as an academic and commercial numerical simulation platform for granular materials, fluids, and largely deformable solids. PySPH [204] is an open-source framework that is implemented in Python and easy to start with. The spheric-community [212] lists a larger, but a non-complete collection of available open-source and commercial solvers.

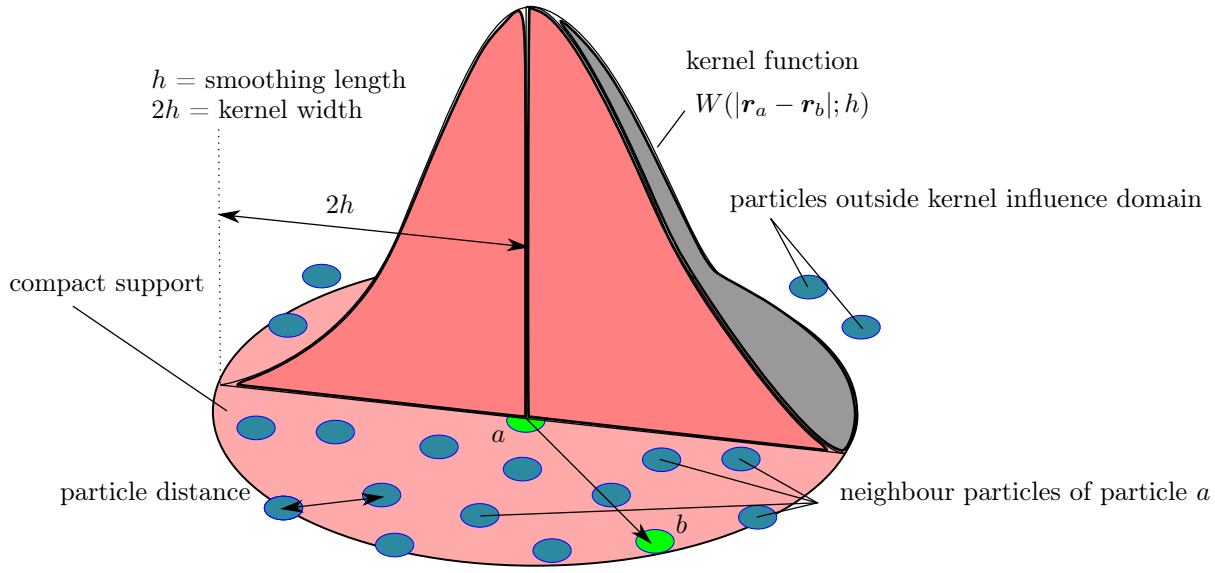

FIGURE 3.6 Sketch of the basic concept of the SPH method: Particles (blue) represent a virtual physical body and particles in a defined neighbourhood (pink) can interact with particle a. Interactions are described based on a kernel function. In the following, the active particle has the index a and all neighbours have indices b.

3.3.2 Basic theory

SPH is a purely meshfree particle method to solve physical problems. Figure 3.6 visualises the basic concept with a set of particles and the shape of the kernel function for one particle. The particles carry physical properties and move in space and time. The kernel function is used to describe interactions between the particles. The underlying theory of SPH is based on the principles of convolution interpolation theory. The following derivation is partly inspired by the work of Kazaz [109]. Let A be a smooth function that only depends on the spatial position. In general, A is also time-dependent but this is omitted to reduce the complexity of the following derivation: The function A can be described as a convolution of itself with Dirac's delta function $\delta(\cdot - \boldsymbol{x})$:

$$\int_{\mathbb{R}^3} A(\boldsymbol{y})\delta(\boldsymbol{y} - \boldsymbol{x})\mathrm{d}\boldsymbol{y} = A(\boldsymbol{x}). \tag{3.3.1}$$

In the approximation approach of SPH, the delta function is replaced by a kernel function $W(|\cdot|; h)\colon \mathbb{R}^3 \mapsto \mathbb{R}$ with smoothing length h (compare Figure 3.6) to obtain compact support (consult the next paragraph for more details on the kernel function). Using the kernel function, we approximate (3.3.1) with

$$A^h(\boldsymbol{x}) := \int_{\mathbb{R}^3} A(\boldsymbol{y})W(|\boldsymbol{y} - \boldsymbol{x}|; h)\mathrm{d}\boldsymbol{y} \underbrace{\rightarrow}_{h \to 0} A(\boldsymbol{x}). \tag{3.3.2}$$

Replacing the integral in (3.3.2) by a quadrature formula with the weights m_b/ρ_b which can be interpreted as a volume, one obtains

$$\langle A^h(\boldsymbol{x})\rangle = \sum_b \frac{m_b}{\rho_b} A^h(\boldsymbol{r}_b)W(|\boldsymbol{x} - \boldsymbol{r}_b|; h), \tag{3.3.3}$$

where the abbreviation $\langle\cdot\rangle$ is used to denote the discrete quadrature-based approximation. The discretisation points for the quadrature rule are called particles. A particle b is a tuple consisting of

$$\begin{aligned} \boldsymbol{r}_b(t) \in \mathbb{R}^3 &\quad \text{position,} \\ m_b > 0 &\quad \text{constant mass,} \\ \rho_b(t) > 0 &\quad \text{density,} \\ \boldsymbol{v}_b(t) \in \mathbb{R}^3 &\quad \text{velocity, and} \\ \boldsymbol{\Phi}_b(t) &\quad \text{other variables.} \end{aligned} \tag{3.3.4}$$

For a finite domain, the approximation quality at the boundary is lower compared to the inner part of the domain. Inside the domain, the convergence of A^h is $\mathcal{O}(h^2)$ for $\mathcal{C}^2$-functions. This property transfers to the sum approximant $\langle A^h(\boldsymbol{x})\rangle$—at least for quasi-regular particle distributions [54]. Various formulations of SPH have been developed based on this theory. In the following, we discuss the three main aspects of SPH that can be modified to obtain a specific SPH discretisation scheme: the formulation of the underlying equations, the choice of the kernel function, and additional stabilisation mechanisms.

Discretisation of the differential operator

We have derived a discrete, quadrature-based approximation for functions. The conservation equations of continuum mechanics that we want to discretise

$$\frac{d\rho}{dt} = \rho\nabla\cdot\boldsymbol{v}, \qquad \frac{d\boldsymbol{v}}{dt} = \frac{1}{\rho}\nabla\cdot\boldsymbol{\sigma} + \bar{\boldsymbol{b}}, \quad \text{and} \quad \frac{dE}{dt} = \frac{1}{\rho}\boldsymbol{\sigma} : \nabla\boldsymbol{v} \tag{3.3.5}$$

do not only contain functions but also gradients of functions. These gradients require special treatment to guarantee a good approximation quality of the solution. There are several possibilities to discretise the gradient or divergence operator. Each of them is leading to a different SPH formulation. The straight forward calculation of the gradient of a function $\langle A^h(x)\rangle$ is

$$\nabla\langle A^h(\boldsymbol{r}_a)\rangle = \sum_b \frac{m_b}{\rho_b} A^h(\boldsymbol{r}_b)\nabla_a W_{ab} \quad \text{with} \quad \nabla_a W_{ab} := \nabla\big(W(|\,\cdot\, - \boldsymbol{r}_b|; h)\big)\big|_{\boldsymbol{r}_a}. \tag{3.3.6}$$

This representation already fails in approximating a constant function for a non-regular particle spacing (compare Figure 3.7). The common approach to improve (3.3.6) is to multiply the function A with a weighting function $f \in C^1$ and calculate the gradient using the product rule as

$$\begin{aligned} \nabla A^h(\boldsymbol{r}_a) &\overset{(3.3.6)}{\approx} \frac{1}{f(\boldsymbol{r}_a)}\left(\langle\nabla\left(fA^h\right)\rangle(\boldsymbol{r}_a) - A^h\langle\nabla f\rangle(\boldsymbol{r}_a)\right) \\ &= \frac{1}{f(\boldsymbol{r}_a)}\sum_b \big(\frac{m_b}{\rho_b} f(\boldsymbol{r}_b)A^h(\boldsymbol{r}_b)\nabla_a W_{ab} - A^h(\boldsymbol{r}_a)\frac{m_b}{\rho_b} f(\boldsymbol{r}_b)\nabla_a W_{ab}\big). \end{aligned} \tag{3.3.7}$$

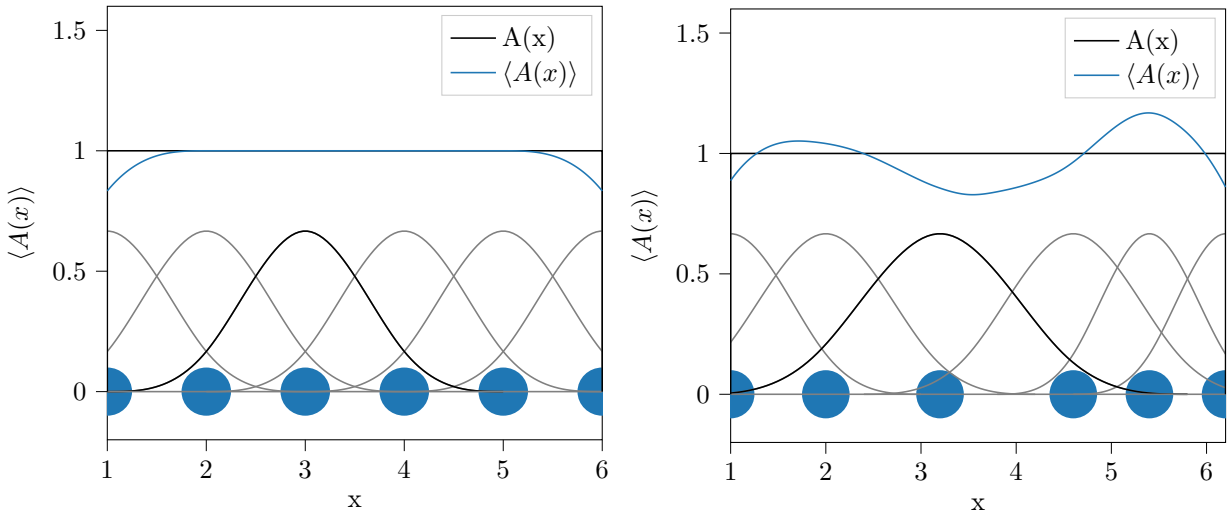

A approximation (uniform) **B** approximation (non-uniform)

FIGURE 3.7 SPH approximation of a constant function: Error in the approximation $\langle A(x)\rangle$ of $A(x)$ in the vicinity of the boundarys **A** and for non-uniform particle distribution in the whole domain **B**.

There are different possibilities to choose f to ensure momentum and rotational momentum conservation. Two very common choices are presented in the following. For the choice $f = \rho$, we obtain

$$\begin{aligned}\nabla A^h(\boldsymbol{r}_a) &= \frac{1}{\rho_a}\sum_b \Big(\frac{m_b}{\cancel{\rho_b}}\cancel{\rho_b} A^h(\boldsymbol{r}_b)\nabla_a W_{ab} - A^h(\boldsymbol{r}_a)\frac{m_b}{\cancel{\rho_b}}\cancel{\rho_b}\nabla_a W_{ab}\Big)\\ &= \frac{1}{\rho_a}\sum_b m_b\big(A^h(\boldsymbol{r}_b) - A^h(\boldsymbol{r}_a)\big)\nabla_a W_{ab}.\end{aligned} \tag{3.3.8}$$

Randles et al. [164] derives the following set of equations also referred to as "conservation laws of continuum dynamics written in the SPH framework" based on this approach:

$$\begin{aligned}\rho_a &= \sum_b m_b W_{ab},\\ \frac{d\boldsymbol{v}_a}{dt} &= -\sum_b \frac{m_b}{\rho_a\rho_b}(\boldsymbol{\sigma}_b - \boldsymbol{\sigma}_a)\cdot\nabla_a W_{ab} + \bar{\boldsymbol{b}}_b W_{ab}, \text{ and}\\ \frac{dE_a}{dt} &= -\sum_b \frac{m_b}{\rho_a\rho_b}(\boldsymbol{v}_b - \boldsymbol{v}_a)\cdot\boldsymbol{\sigma}_a\cdot\nabla_a W_{ab},\end{aligned} \tag{3.3.9}$$

which, according to [164], is more accurate than the symmetric approach derived in the following. In *LS-DYNA®*, this formulation is called fluid-formulation. Choosing $f := 1/\rho$, and applying the following equality

$$\nabla\big(f(\rho(x))\big) = \nabla(\rho(x))^{-1} = -\frac{1}{\rho^2}\nabla\rho \tag{3.3.10}$$

we obtain another formula for the gradient

$$\begin{aligned}\nabla A^h(\boldsymbol{r}_a) &= \frac{1}{f(\rho(\boldsymbol{r}_a))}\nabla\big(f(\rho(\cdot))A^h(\cdot)\big)\big|_{\boldsymbol{r}_a} - \frac{A^h(\boldsymbol{r}_a)}{f(\rho(\boldsymbol{r}_a))}\underbrace{\nabla\big(f(\rho(\cdot))\big)}_{=-1/\rho^2\,\nabla\rho}\big|_{\boldsymbol{r}_a} \\ &= \big(\rho\nabla(\frac{A^h}{\rho}) - \frac{A^h}{1/\rho}\frac{-1}{\rho^2}\nabla\rho\big)\big|_{\boldsymbol{r}_a} \\ &\overset{(3.3.6)}{\approx} \sum_b \frac{m_b}{\rho_b}\left(\frac{A_b^h}{\rho_b/\rho_a} + \frac{A_a^h}{\rho_a/\rho_b}\right)\nabla_a W_{ab}.\end{aligned} \tag{3.3.11}$$

This equation can also be transferred to vector or tensor functions $\boldsymbol{A}^h$. There, the divergence of the tensor is used instead of the gradient, and we can apply (3.3.11) to the momentum equation (3.3.5)

$$\begin{aligned}\frac{\mathrm{d}\boldsymbol{v}_a}{\mathrm{d}t} &= -\frac{1}{\rho_a}\operatorname{div}\boldsymbol{\sigma} + \bar{\boldsymbol{b}} \overset{(3.3.11)}{\approx} -\frac{1}{\rho_a}\sum_b \frac{m_b}{\rho_b}\left(\frac{\boldsymbol{\sigma}_a}{\rho_a/\rho_b} + \frac{\boldsymbol{\sigma}_b}{\rho_b/\rho_a}\right)\nabla_a W_{ab} + \bar{\boldsymbol{b}}_b W_{ab} \\ &= -\sum_b m_b\left(\frac{\boldsymbol{\sigma}_a}{\rho_a^2} + \frac{\boldsymbol{\sigma}_b}{\rho_b^2}\right)\nabla_a W_{ab} + \bar{\boldsymbol{b}}_b W_{ab}.\end{aligned} \tag{3.3.12}$$

This is the symmetric formulation in *LS-DYNA®* notation. Similarly, the equations for the continuity and energy equation can be derived. These are not just evaluated to check the energy loss in the system, like in the FEM, but are a substantial part of the SPH integration cycle. Due to that, SPH conserves energy by definition. The complete set of equations in the symmetric formulation reads (compare [128]):

$$\begin{aligned}\frac{\mathrm{d}\rho_a}{\mathrm{d}t} &= \rho_a\sum_b \frac{m_b}{\rho_b}(\boldsymbol{v}_a - \boldsymbol{v}_b)\nabla_a W_{ab}, \\ \frac{\mathrm{d}\boldsymbol{v}_a}{\mathrm{d}t} &= -\sum_b m_b\left(\frac{\boldsymbol{\sigma}_a}{\rho_a^2} + \frac{\boldsymbol{\sigma}_b}{\rho_b^2}\right)\nabla_a W_{ab} + \bar{\boldsymbol{b}}_b W_{ab}, \\ \frac{\mathrm{d}E_a}{\mathrm{d}t} &= -\frac{\sigma_a}{\rho_a^2}\sum_j m_j(\boldsymbol{v}_a - \boldsymbol{v}_b)\nabla_a W_{ab}.\end{aligned} \tag{3.3.13}$$

From a conceptual point of view, we moved the spatial derivatives from operating on the physical quantities to operating on the interpolation kernel basis functions. This is analogous to the concept of shape functions used in the FEM. However, the strong formulation of the equations is maintained as no integration is required to obtain the discrete equations. For Application I, we compare the solutions with the symmetric (3.3.9) to the standard SPH approach (3.3.13).

Kernel function

A kernel function W is needed to complete the discretisation. It has to fulfil the following properties: positivity, symmetry, unity, compact support, delta function property, decay, and smoothness. Although, different kernel functions have been reviewed in literature, the most common one in numerical codes is the cubic B-spline

kernel that was proposed by Monaghan [147]

$$W(r;h) = \frac{C}{h^D} \begin{cases} (1 - \frac{3}{2}\bar{r}^2 + \frac{3}{4}\bar{r}^3) & \bar{r} < 1 \\ \frac{1}{4}(2-\bar{r})^3 & 1 \le \bar{r} \le 2 \\ 0 & \text{otherwise,} \end{cases} \quad \text{with} \quad C := \begin{cases} \frac{10}{7\pi} & \text{in 2D} \\ \frac{1}{\pi} & \text{in 3D} \end{cases} \tag{3.3.14}$$

where $\bar{r}$ is the normalized distance

$$\bar{r} = r/h, \tag{3.3.15}$$

D is the dimension, and C is a scaling factor which ensures the partition of unity

$$\int_\Omega W(r;h)dv = 1. \tag{3.3.16}$$

One significant advantage of this kernel definition is that the evaluation of the function is much cheaper than a Gaussian kernel, defined as

$$W(\bar{r};h) = \frac{C}{h^D} \begin{cases} e^{-\bar{r}^2} & \bar{r} \le 3 \\ 0 & \text{otherwise} \end{cases} \quad \text{with} \quad C := \begin{cases} \frac{1}{\pi} & \text{in 2D} \\ \frac{1}{\pi^{3/2}} & \text{in 3D,} \end{cases} \tag{3.3.17}$$

because it does not evaluate an exponential function. Alternative kernel functions to these two standard kernels are the Wendland kernel and the quintic B-spline kernel. The Wendland kernel has a positive Fourier transform in three dimensions and is more efficient than the B-spline kernel as fewer case differentiations are required

$$W(\bar{r};h) = \frac{C}{h^D}\left(\max(0, 1-\bar{r})\right)^4 (1+4\bar{r}) \quad \text{with} \quad C := \begin{cases} \frac{7}{4\pi} & \text{in 2D} \\ \frac{21}{16\pi} & \text{in 3D.} \end{cases} \tag{3.3.18}$$

The quintic B-spline kernel has been implemented in *LS-DYNA®* recently to improve the stability for applications [217]. Morris [148] revealed in a stability analysis that higher order kernels that are closer to the Gaussian kernel improve the stability of the method

$$W(r;h) = \frac{C}{h^D} \begin{cases} (3-\bar{r})^5 - 6(2-\bar{r})^5 + 15(1-\bar{r})^5 & \bar{r} < 1 \\ (3-\bar{r})^5 - 6(2-\bar{r})^5 & 1 \le \bar{r} \le 2 \\ (3-\bar{r})^5 & 2 \le \bar{r} \le 3 \\ 0 & \text{otherwise.} \end{cases} \quad \text{with} \quad C := \begin{cases} \frac{7}{478\pi} & \text{in 2D} \\ \frac{3}{359\pi} & \text{in 3D} \end{cases} \tag{3.3.19}$$

3.3.3 Shortcomings in the basic formulation

When used to model a solid body, the primary SPH method has shown four significant problems: (i) inconsistency, (ii) implementation of boundary conditions, (iii) zero-energy modes, and (iv) tensile instability.

(i) In the context of SPH-interpolation, consistency describes the ability of a method to approximate

polynomials correctly. Besides the impossibility to be accurate in the vicinity of boundaries, the SPH method is not even 1^{th} order consistent in the interior if particles are non-regularly distributed (compare Figure 3.7). The inconsistency of the method is the reason why a regular particle distribution is crucial for accurate results with standard SPH. There are two ways to obtain 2^{nd} order consistency: either by modifying the kernel function or by changing the discrete form of the convolution integral (3.3.13). The first of these two approaches is used by Vignjevic [197] and Johnson [104]. As a negative side effect, zero pressure boundary conditions are no longer preserved without additional implementation effort, if we use a corrected kernel.

(ii) In general, the implementation of boundary conditions is a difficult task in SPH. The particles that form the boundary can change, and the algorithm requires ghost particles outside the actual domain as virtual interaction partners for boundary particles. Additionally, sudden changes in the velocity at the boundaries can result in shocks that are challenging for the numerical method. Dissipative mechanisms are required to prevent such behaviour [37].

(iii) An issue not only related to SPH is zero energy modes; these are modes that are not visible to the energy operator and are due to nodal under-integration. Under-integration in SPH is due to the collocation of the field variables. Ambiguity leads to multiple valid solutions, with only one of them being physically correct. For instance, a sinusoidal velocity can be interpolated with a constant field of velocity at the nodal positions, if the particle distance matches the wavelength. Because we seek for a unique and physically correct solution to the problem, it is essential to avoid zero-energy modes. One solution is to evaluate stresses and strains at different positions and, therefore, increase the number of integration points and avoid the collocation of the physical properties. These additional integration points have to be saved separately and moved in space correctly. This procedure requires additional memory and a technique to propagate the stress points in space. It is called the stress point method [165]. Other solutions are a non-local approximation of the strain measure [189] or a least squares stabilisation method [21].

(iv) Swegle [188] and Balsara [9] conducted a von Neumann stability analysis of SPH separately. This analysis revealed that the method suffers from a so-called tensile instability. The observed numerical artefact is that particles are clustering which leads to fracture and fragmentation between clusters. This artefact does not result from the numerical time integration, but a non-physical negative modulus produced by the interaction between the constitutive relation and the kernel-based function approximation [188]. Differently speaking, the kernel interpolation changes the nature of the discretised partial differential equation [197]. This means that changes in effective stress do amplify the perturbations in the strain instead of reducing them. The criterion for stability derived by Swegle requires

$$W''\sigma_{eq} \leq 0 \tag{3.3.20}$$

for stability, where W'' is the second spatial derivative of the kernel function and the equivalent stress σ_{eq} (2.3.21) is defined negative in compression and positive in tension. This is visualized in Figure 3.8 for the B-spline kernel. It shows the transition from a positive to a negative value for the second spatial derivative of the kernel function. In principle, the instability can occur in tension and compression. However, in standard configurations, the particle distance is similar to the smoothing length (compare

Figure 3.6). Thus, standard configurations are unstable in tension. This observation explains why this unstable behaviour got its misleading name "tensile instability".

As mentioned in the introduction, different authors proposed approaches to remedy this problem. Guenther [80] and Wen [213] propose an approach called conservative smoothing. Dyka [59] uses an approach with a non-collocated discretisation of stress and velocity points. A total Lagrangian is used in *MCM* by Vignjevic [198] and a non-collocated discretisation called "quasi-linear reproducing kernel particle method" is implemented in *LS-DYNA®* by Yreux.

The next section presents a set of solutions to the shortcomings that we apply in the numerical experiments.

3.3.4 Advanced formulations and techniques

Variable smoothing length

The smoothing length h determines the support size of the kernel (compare Figure 3.6). In general, the smoothing length is determined based on the distance between neighbouring particles at the beginning of the simulation. Either each particle gets a unique smoothing length, or a uniform smoothing length is computed. For a constant smoothing length in time, particles can numerically lose contact, although they are physically still connected. Therefore, the idea is to adjust the smoothing length in the course of the simulation. In

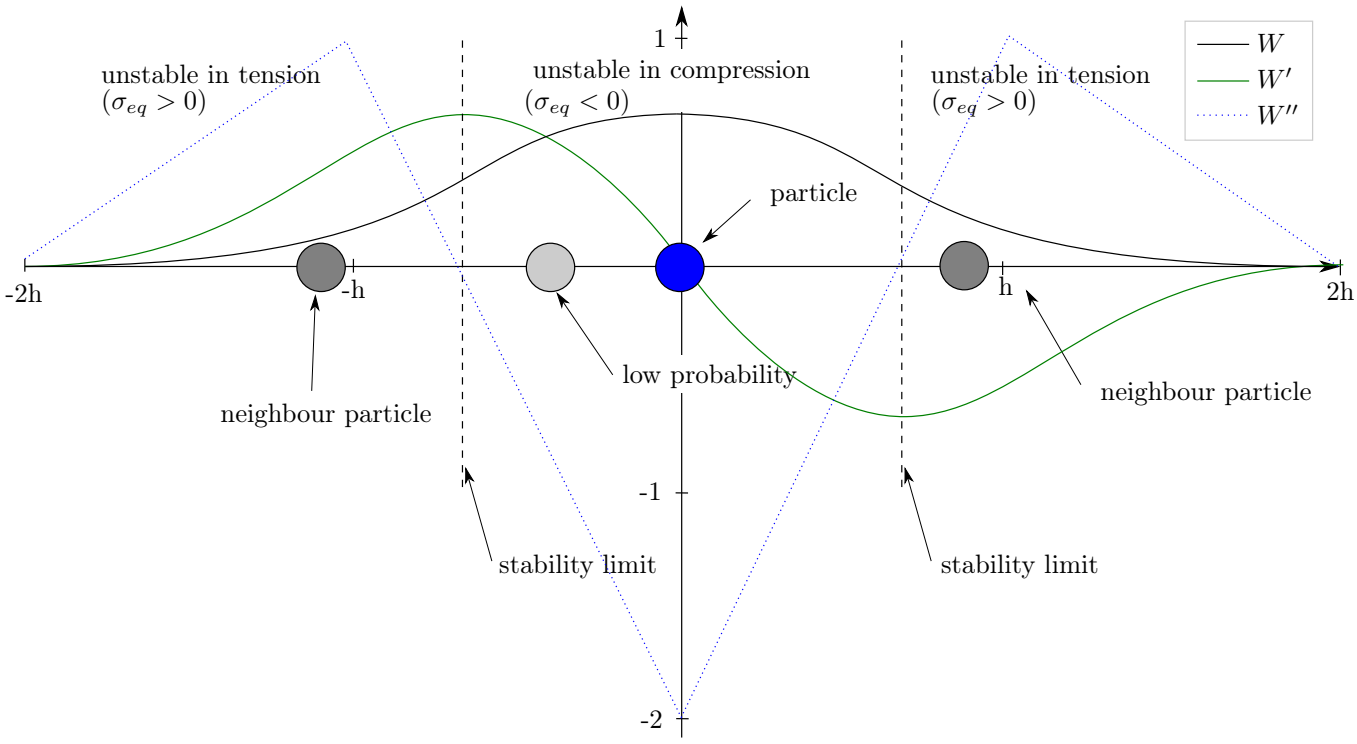

FIGURE 3.8 Numerical instability regimes for the B-spline kernel function in the standard SPH formulation [188]. The kernel function W and the derivatives W', W'' are shown in 1D coordinates for the particle at position 0 (blue). Exemplarly, two neighbours are illustrated (grey) and a position for a neighbour which is unprobable is indicated (light grey). The unprobability of particles in the compression instability region leads to the name "tensile instability".

the following, we differentiate between two loading cases: tension and compression. The loss of contact described above occurs, in particular, under considerable tension. Particles move out of their kernel support and values at one particle are not, or hardly, influencing the evolution of the neighbouring particle through their contribution to the right-hand side of the conservation equations. Under compression, on the other hand, the computation is slowed down as a large number of particles enter the neighbourhood.
Two approaches computing a variable smoothing length are presented in the following. Benz [24] proposes a density-dependent evolution of the smoothing length

$$h = h_0 \left(\frac{\rho}{\rho_0} \right)^{1/D}, \tag{3.3.21}$$

where h_0 and ρ_0 are the initial smoothing length and inital density, and D is the dimension of the problem. Another evolution equation for the smoothing length is based on the conservation of mass and uses the divergence of the velocity as a criterion

$$\frac{\mathrm{d}h}{\mathrm{d}t} = \frac{1}{D} h \, \nabla \cdot (\boldsymbol{v}). \tag{3.3.22}$$

LS-DYNA® uses this evaluation equation to update the smoothing length by default.

Dissipative mechanisms

SPH in the basic form is not stable and, thus, requires a dissipative mechanism [188]. One method to stabilise the solution is to use an artificial viscous pressure term Π_{ab}. The Monoghan-Gingold form [147] is defined by the following equations

$$\Pi_{ab} = \begin{cases} \dfrac{-\alpha \bar{c}_{ab} \mu_{ab}^2}{\bar{\rho}_{ab}} & \text{if } (\boldsymbol{v}_b - \boldsymbol{v}_a) \cdot (\boldsymbol{x}_b - \boldsymbol{x}_a) < 0 \\ 0 & \text{otherwise,} \end{cases} \tag{3.3.23}$$

where

$$\mu_{ab} = \frac{h(\boldsymbol{v}_b - \boldsymbol{v}_a) \cdot (\boldsymbol{x}_b - \boldsymbol{x}_a)}{|\boldsymbol{x}_b - \boldsymbol{x}_a|^2 + \varepsilon h^2}, \qquad \bar{c}_{ab} = (c_a + c_b)^2, \text{ and} \qquad \bar{\rho}_{ab} = (\rho_a + \rho_b)/2. \tag{3.3.24}$$

The parameter α is approximately 1.0 and ε is usually chosen as 0.1. The sound speed of particle a is denoted by c_a and h is the smoothing length.
The artificial viscosity Π_{ab} is added to the pressure terms $\dfrac{\boldsymbol{\sigma}}{\rho^2}$ in the discretised momentum equation (3.3.13) and (3.3.9)

$$\frac{\mathrm{d}\boldsymbol{v}_a}{\mathrm{d}t} = -\sum_b m_b \left(\frac{\boldsymbol{\sigma}_a}{\rho_a^2} + \frac{\boldsymbol{\sigma}_b}{\rho_b^2} + \Pi_{ab} \right) \nabla_a W_{ab} + \bar{\boldsymbol{b}}_b W_{ab}. \tag{3.3.25}$$

Total Lagrangian formalism in SPH

Motivated by the inherited difficulties of the standard SPH approach, Vignjevic and co-workers developed a different formalism [198, 49]. Using the total Lagrangian approach implies the initial state of the domain of interest as the reference state. To distinguish total Lagrangian SPH from standard SPH, the latter is also called updated Lagrangian SPH. The mapping to the initial state $(\cdot)_0$ requires the deformation gradient

$\boldsymbol{F}$ with the Jacobian determinant J in the conservation equations. The three conservation equations of continuum mechanics (3.3.5) in the total Lagrangian formalism read

$$\begin{aligned} \rho &= J^{-1}\rho_0, \\ \frac{\mathrm{d}v}{\mathrm{d}t} &= \frac{\mathbf{1}}{\rho_0}\nabla_0 \cdot \boldsymbol{P} + \boldsymbol{b}, \text{ and} \\ \frac{\mathrm{d}E}{\mathrm{d}t} &= \frac{\mathbf{1}}{\rho_0}\dot{\boldsymbol{F}} : \boldsymbol{P}, \end{aligned} \tag{3.3.26}$$

where the colon denotes the inner tensor product, and $\boldsymbol{P}$ is the nominal Piola-Kirchhoff stress

$$\boldsymbol{P} = J\boldsymbol{F}^{-\mathbf{1}}\boldsymbol{\sigma}. \tag{3.3.27}$$

In the SPH framework of the total Lagrangian formalism, different smoothed equations have to be iterated than for standard SPH. For the density update, only the Jacobian determinant J is needed instead of an explicit kernel interpolation of the continuity equation. Hence, the deformation gradient F is approximated with the kernel function

$$\boldsymbol{F}_a = -\sum_b \frac{m_b}{\rho_b^0}(\boldsymbol{u}_a - \boldsymbol{u}_b)\nabla_a^0 W_{ab}^0 \tag{3.3.28}$$

using the displacements $\boldsymbol{u}$. The conservation of momentum equation becomes

$$\frac{\mathrm{d}\boldsymbol{v}_a}{\mathrm{d}t} = -\sum_b m_b \left(\frac{\boldsymbol{P}_a}{\rho_a^2} + \frac{\boldsymbol{P}_b}{\rho_b^2}\right)\nabla_a^0 W_{ab}^0 + \bar{\boldsymbol{b}}_b W_{ab}^0, \tag{3.3.29}$$

and the energy update reads

$$\frac{\mathrm{d}E_a}{\mathrm{d}t} = \frac{P_a}{\rho_a} : \sum_j \frac{m_j}{\rho_j^0}(\boldsymbol{v}_a - \boldsymbol{v}_b)\nabla_a^0 W_{ab}^0. \tag{3.3.30}$$

This set of equations eliminates the tensile instability [49].

Quasi-linear reproducing kernel particle method

Yreux and Chen [220] suggest a quasi-linear reproducing kernel particle method which improves consistency and stability (implemented in *LS-DYNA®*). In this context, "quasi-linear" means that the method is linear consistent up to a small residuum, that is needed for stability reasons. The method consists of two techniques which Yreux derives in a reproducing kernel particle method (RKPM) framework [134]:

First, to obtain quasi-linear consistency, the SPH kernel functions are replaced by approximation functions that are constructed with a quasi-linear least-squares approach [221]. Second, a stabilisation term is added to the momentum equation to remove tensile instability.

The construction of these approximation functions is based on a vector of monomials multiplied with a normalisation matrix that gives the reproducing property of linear functions. A difficulty of this method is that it cannot guarantee that the momentum matrix is non-singular at all times. As a solution, additional, non-co-planar integration points, which are in a close neighbourhood of the corresponding particle position, are used to calculate the momentum matrix. The following trade-off defines a suitable position of these additional integration points: If these integration points are too far from the original position, the integration

accuracy decreases, while integration points that are too close can lead to unstable behaviour. The authors of the method [221] propose a position that is 10% of the particle distance away from the original particle position.

The RKPM in its original form eliminates the tensile instability by definition, as the same set of particles are neighbours over the entire computation—similar to total Lagrangian SPH. However, this is not the case for the semi-Lagrangian moving least square approach used by Yreux. Therefore, they add a stabilisation term that includes second-order spatial derivatives, second moment of area, and a consistent material tangent to the momentum equation [38]. These two techniques result in a method that has increased accuracy compared to standard SPH and can handle tensile stresses. Yreux and co-authors [220] apply the method to sphere impact and projectile impact at lower velocities of up to 300 m/s. The authors find better accordance with the experiments for the residual velocity, the shape of the plug, and the size of the crater compared to the standard SPH formulation. At the same time, the additional integration points and the more complex approximation functions require more computation time compared to the standard SPH approach.

γ-SPH-ALE

A different approach to overcome the tensile instability is implemented in the *IMPETUS®* SPH solver [44]. It is based on the SPH-ALE formalism by Vila [199] that uses Riemann solvers and significantly improves numerical fragmentation but also adds complexity to the scheme. ALE (Arbitrary Lagrangian-Eulerian) is a way to describe motion with an arbitrary transport velocity. In a purely Lagrangian SPH framework, the transport velocity is equal to the material velocity. The SPH-ALE approach allows the particles to move with a velocity slightly different from the material velocity, similar to XSPH by Monaghan [146]. The continuity conditions are satisfied by exchanging mass flux between particles similar to the finite volume method. As a negative side effect, low-Mach issues are hard to prevent [53]. A finite volume stabilising scheme solves these issues by adding a corrective velocity term to the continuity and momentum equations. This modified SPH formalism is called γ-SPH-ALE. *IMPETUS®* developed the code originally for multi-regime barotropic flows and then extended it to solid body dynamic cases. They evaluated numerical stability thoroughly and proved increased stability and accuracy compared to standard SPH in selected test cases [130].

3.3.5 Failure and fracture in SPH

This section describes how failure is addressed in SPH. In general, failure in SPH sets the stress of the failed particle to zero and removes it from the neighbour list of its neighbours. However, as illustrated in Figure 3.9, this is not wholly accurate. Actually, to be correct, particles c obscured to a particle a by the failed particle b have to be deleted from the neighbour list of particle a as well [49]. Otherwise, the stress state is unphysical—in particular, for a total Lagrangian approach. In the implementation in MCM, a truncated cone is used to determine obscured particles geometrically (compare Figure 3.9). This issue is also essential, but not crucial, for standard updated-Lagrangian SPH, since obscured particles c are likely to move out of the neighbourhood of a. That is because the kernel is defined in the actual configuration. Similar to FEM, continuous damage models can be implemented in SPH without further restrictions. In general, the damage has to be investigated with care to distinguish fracture due to the numerical description (such as tensile instability) from natural fracture.

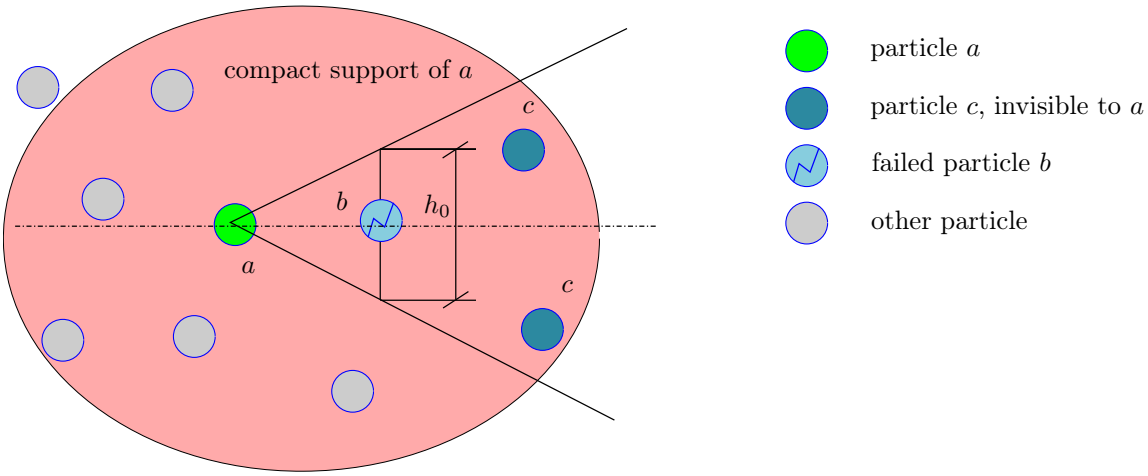

FIGURE 3.9 Visibility criterion based on a truncated cone: Our particle of interest a has a failed particle b in its compact support. Particles c that are on the other side, which is defined by the truncated cone, are not connected with a any more. Therefore, particles c have to be removed from the neighbour list of particle a.

3.3.6 Applications

SPH is a flexible method that is easy to implement in its basic form and versatilely extendable: It does not have geometrical limitations and requires no additional treatment to describe large deformation or the fracture and fragmentation of material. For fluids, SPH can treat free-surfaces without additional effort, and the method can track different fluids and phases in a Lagrangian manner. The significant drawbacks are the discussed numerical artefacts and a decreased accuracy compared to FEM. Based on this analysis of strength and weaknesses, a lot of different research areas applied SPH:

Apart from our application, SPH is applied in microfluidics and micro-drop dynamics [93], in coast hydrodynamics and offshore engineering, and environmental and geophysical flows [133]. We discuss different applications of the SPH method in the context of high-strain hydrodynamics with material strength in the following.

The term hydrodynamics can be misleading, as it is also used in terms of fluid dynamics. However, here it only expresses, that, at certain loading conditions, the material starts to flow and inherits fluid-like properties. These applications require to model shock waves, localised material response, and impulsive loadings accurately. Due to its properties as a meshfree, Lagrangian approach, researches have used SPH intensively for simulating high-strain hydrodynamics. A lot of research and development of the SPH method focuses on impact and penetration [162, 156, 150, 124, 32, 103, 95, 196]. Most of these applications are in the defence and aerospace field. SPH simulations of defence applications range from Taylor tests for material characterisation to projectile impact and shaped charge jets. In aerospace, beyond others, hypervelocity impacts on space bumpers and satellite collisions are examples for applications of SPH. For civil aircraft engineering, bird strike impacts and high-fidelity analysis of collisions with buildings are investigated with SPH. The latter has been used to design nuclear power plants or to understand the failure of the World Trade Center under the September 11 attack [193]. During this research, several aspects of SPH have been developed. Solutions to the tensile instability, or the use of a variable smoothing length, has already been

presented. Others include the coupling to different numerical methods such as DPD (dissipative particle dynamics) or MD (molecular dynamics) as well as an adaptive SPH (ASPH) formulation that describes a methodology with an anisotropic kernel operating on an ellipsoidal influence domain.

3.3.7 Concluding remarks

This section gave a state-of-the-art overview of SPH. The history and literature review of SPH showed that it attracted a lot of researchers of different fields and has seen decent development in the last years. In the next part, we derived the basic theory and identified four basic shortcomings: (i) inconsistency, (ii) boundary conditions, (iii) zero-energy modes, and (iv) tensile instability. These deficits are not present in every application, and so solutions have been proposed to each of them. We highlight the solutions which are relevant for our thesis and discuss the difficulty of obscured particles in the fracture description. There we draw attention to carefully evaluate whether a fracture is physical or not. In the final paragraph, we give an overview of applications that have been addressed with SPH and concluded that it had been extensively used for hydrodynamic behaviour and beyond.
Therefore, SPH is a well-advanced and well-suited method to predict the behaviour of terminal ballistics.

3.4 Comparison of the FEM and SPH

This section compares FEM and SPH in terms of (i) discretisation, (ii) degrees of freedom, (iii) variations, (iv) typical applications, (v) limitations, and (vi) advantages of each method.

The most fundamental difference between FEM and SPH lies in the discretisation. While the FEM uses a mesh-based discretisation that divides the computational domain into elements, SPH describes the domain with particles. The degrees of freedom for the FEM are the displacements at the mesh nodes. A standard 8-node element uses eight integration points in the element. The SPH method, on the other hand, evaluates the approximation at the particle positions itself (collocation method). Kernel functions exchange momentum and thermal properties in SPH, and the FEM uses shape functions. In the FEM, the delta-function property is satisfied for the shape function in the formulations used here, while the kernel function, in SPH, has compact support but no delta-function property.

For both methods, scientists developed different implementations. An element can be hexahedral or tetrahedral and can have one or multiple integration points. Selectively reduced integration evaluates only some properties at all integration points. In SPH, the formulation of the discretised equations and kernel interpolation describes the approximation property of the method. There, advanced methods provide stabilisation mechanisms and improved consistency.

If we look at applications, the FEM mainly predicts structural mechanics in civil engineering and crash tests. The SPH method, on the other hand, was developed initially for star collision and is used mainly for fluid applications and hypervelocity impacts. Our application lies between crash test and hypervelocity impact in terms of the strain rate and material behaviour. The material exceeds the yield conditions, but material strength is still relevant to predict the behaviour correctly.

From a theoretical point of view, we can identify the following difficulties in the two frameworks. The FEM, in its basic form, has a locking problem and cannot describe fracture. Furthermore, creating a hexahedral

computational mesh is a complex task. Under-integrated elements with hourglass-control can be used to avoid locking. Node-splitting, element-erosion and XFEM are techniques to describe fracture in the FEM.

The drawback of the SPH method, as an interpolation method, is that it is not even 1^{st} order consistent. Furthermore, when used with material strength, a tensile instability gives incorrect results [188]. SPH can retain consistency with an advanced formulation and address tensile instability with additional integration points, for instance. In contrast to the FEM, fracture description requires no additional methods in SPH. There, particles are not connected in a grid and discontinuities are allowed. Without the use of element erosion mass conservation is satisfied. The preprocessor can automate the particle generation with simple algorithms even for complex geometries.

FEM seems to be superior for problems with small deformation since well-known error estimates exist. Furthermore, FEM experienced much more interest and more extensive development. However, researchers developed sophisticated formulations for SPH as well. As the focus of this thesis lies in an accurate description of the fracture behaviour, SPH seems to be a serious alternative to the classical FEM.

3.5 Conclusion

This theoretical chapter discussed numerical approaches to solve partial differential equations described in Chapter 2. First, we looked at a wide spectrum of mesh-based and meshfree methods and determined that FEM and SPH are suitable choices for our purpose. For each of these methods, we gave a literature overview, outlined the theory with respect to the equations we have to solve, discussed limitations and shortcomings, and presented solutions. The last section summed up these findings in a conclusive comparison between FEM and SPH. Based on our theoretical findings, there is not one method that is particularly better than the other for our application. Instead, each method has its own advantages and difficulties, and only numerical experiments can show which approach is better suited for our application.

4

Application-specific modelling

This chapter explains application-specific modelling techniques with particular regard to a terminal ballistic (TB) template for numerical simulations. These techniques include specific material models, a suited contact description, numerical coupling methods and a tailor-made discretisation of the geometries. A python software combines the techniques in a template and generates an input deck for arbitrary HVI problems. The findings with the investigated applications determine the actual settings that are used as default by our black-box model. In the last section, we suggest two methodologies to detect fragment in the postprocessing of numerical simulations.

4.1 Materials

In our applications, we model different metals and an explosive. This section outlines models for the hardening rule in plasticity and damage models to describe the fracture of metal. Furthermore, we describe a constitutive model to describe an explosive.

4.1.1 Metal plasticity

In Section 2.3.3, we described the von Mises plasticity flow rule (2.3.20) and how it is combined with a hardening rule (2.3.24). The choice of the hardening rule is of high importance for the application of HVI as a broad range of loading conditions occur. Here, we present three advanced plasticity models that account for the change in hardening depending on temperature and loading. The Johnson-Cook (JC) model is an empirical model that determines five modelling parameters to fit the given experiments best. It has been proposed on the IBS[1] by Johnson and Cook [105] and is since then the standard model to describe materials under highly dynamic impacts. Cowper and Symonds propose a different relation for the strain rate hardening

[1] International Ballistics Symposium

[48]. This can be implemented in the original JC model, and we call this modified JC model "CS model" for simplicity. In contrast to the empirical JC model, the Rusinek-Klepacko (RK) model [173] is based on physical assumptions that describe new immobile dislocations and thermal activation. The resulting model is more complex, but requires only one modelling parameters more than the JC model.

Johnson-Cook (JC) model

The JC model expresses the hardening in (2.3.20) in terms of three internal variables

$$q(\bar{\varepsilon}_p, \dot{\bar{\varepsilon}}_p, T) = \left(\sigma_y + B\bar{\varepsilon}_p^n\right)\left(1 + C\ln(\dot{\varepsilon}^*)\right)\left(1 - (T^*)^m\right), \tag{4.1.1}$$

where $\bar{\varepsilon}_p$ is the effective plastic strain, $\dot{\bar{\varepsilon}}_p$ is the plastic strain rate, and T is the current temperature. Furthermore, σ_y is the yield stress at standard conditions,

$$\dot{\varepsilon}^* = \frac{\dot{\bar{\varepsilon}}_p}{\dot{\varepsilon}_0} \tag{4.1.2}$$

is a normalization of the effective plastic strain rate with test strain rate $\dot{\varepsilon}_0$, and

$$T^* = \frac{T - T_c}{T_m - T_c} \tag{4.1.3}$$

is a homogenized temperature regarding the melting temperature T_m and the critical or room temperature T_c. The other variables B, C, n, and m denote material-specific input constants. In addition to the hardening law, the temperature has to be updated as plastic work is converted to heat according to the Quinney equation [192]

$$T = T_0 + \frac{\beta}{\rho C_p}\int_0^{\bar{\varepsilon}_p} \sigma_{eq}\left(\bar{\varepsilon}_p, \dot{\bar{\varepsilon}}_p, T\right) d\bar{\varepsilon}_p, \tag{4.1.4}$$

where σ_{eq} is defined as in (2.3.21), ρ is the density, T_0 is the initial temperature, C_p is the specific heat coefficient and β is the Taylor-Quinney coefficient. Some scientific contributions report that β varies with plastic deformation (e.g., Macdougal [138] or Zaera [222]), but we use the constant default value of $\beta = 0.9$ instead (e.g., [33]), since we do not have according data.

JC model with Cowper-Symonds (CS) modification

According to experimental results that were published by Meyers [144] and Lee et al. [123], the original JC model underestimates the hardening for large strain rates. The CS model replaces the strain rate term $(1 + C\ln(\dot{\varepsilon}^*))$ in (4.1.1) with a polynomial relation

$$1 + \left(\frac{\dot{\varepsilon}^*}{\overline{C}}\right)^{\frac{1}{p}} \tag{4.1.5}$$

that uses the modelling parameters $\bar{C}$ and p. With them, the non-linear hardening observed in experiments can be modelled with higher accuracy. The final model reads

$$q(\bar{\epsilon}_p, \dot{\bar{\varepsilon}}_p, T) = \left(\sigma_y + B\bar{\epsilon}_p^n\right)\left(1 + \left(\frac{\dot{\bar{\varepsilon}}^*}{\bar{C}}\right)^{\frac{1}{p}}\right)\left(1 - T^{*m}\right). \tag{4.1.6}$$

Rusinek-Klepacko (RK) model

The RK model expresses the plastic flow in an additive form

$$q(\bar{\varepsilon}_p, \dot{\bar{\varepsilon}}_p, T) = \frac{E(T)}{E_0}\left(\sigma_\mu(\bar{\varepsilon}_p, \dot{\bar{\varepsilon}}_p, T) + \sigma^*(\bar{\varepsilon}_p, \dot{\bar{\varepsilon}}_p, T)\right), \tag{4.1.7}$$

where the internal stress σ_μ describes how the creation of new immobile dislocations influences strain hardening (4.1.9), the effective stress σ^* models the thermal activation process (4.1.10), and E models the temperature and damage-dependent evolution of Young's modulus (4.1.8). The latter is based on the value E_0 at initial conditions, [113] and reads

$$\frac{E(T, C_d)}{E_0} = C_d\left(1 - \frac{T}{T_m}\exp\left(\frac{T^{ch}}{T_m}\left(1 - \frac{T_m}{T}\right)\right)\right), \tag{4.1.8}$$

where the temperature is normalized differently than in the JC model using the characteristic temperature T^{ch}. C_d defines a coupling with the damage evolution and scales the yield modulus according to (2.3.27) which is not part of the original RK model. Originally, E is only a function of T. The two stress components are described with the following equations

$$\sigma_\mu = B(\dot{\bar{\varepsilon}}_p, T)(\varepsilon_0 + \bar{\varepsilon}_p)^{n(\dot{\bar{\varepsilon}}_p, T)} \tag{4.1.9}$$

and

$$\sigma^* = \sigma_0^*\left[1 - D_1\left(\frac{T}{T_m}\right)\log\left(\frac{\dot{\varepsilon}_{\max}}{\dot{\bar{\varepsilon}}_p}\right)\right]^m \qquad \sigma^* \geq 0, \tag{4.1.10}$$

where D_1 is a material constant, $\dot{\varepsilon}_{\min}$ and $\dot{\varepsilon}_{\max}$ are case specific lower and upper bounds of the strain rate, and σ_0 is the effective stress with no loading applied. The constant D_1 is no modelling parameter but can be determined from

$$D_1\left(\frac{T_c}{T_m}\right)\log\left(\frac{\dot{\varepsilon}_{\max}}{\dot{\varepsilon}_{\min}}\right) = 1, \tag{4.1.11}$$

since the stress component vanishes for $T = T_c$, where T_c is the critical temperature. In practice, T_c equals the room temperature. In terms of physical background, the second stress term describes the kinetics of thermally activated processes similar to the Arrhénius equation [157]. For the internal stress σ^*, we further define the plasticity modulus B and strain hardening n as

$$B(\dot{\bar{\varepsilon}}_p, T) = B_0\left[\left(\frac{T}{T_m}\right)\log\left(\frac{\dot{\varepsilon}_{\max}}{\dot{\bar{\varepsilon}}_p}\right)\right]^{-\nu} \tag{4.1.12}$$

and

$$n(\dot{\bar{\varepsilon}}_p, T) = n_0 \left(1 - D_2 \left(\frac{T}{T_m}\right) \log\left(\frac{\dot{\bar{\varepsilon}}_p}{\dot{\varepsilon}_{\min}}\right)\right) \quad \text{for} \quad n(\dot{\bar{\varepsilon}}_p, T) \geq 0, \quad n = 0 \quad \text{otherwise,} \tag{4.1.13}$$

where the subscript 0 denotes ambient conditions, D_2 is a modelling parameter, and ν is a constant that describes the temperature sensitivity of flow stress. The hardening n is set to 0 if it has a negative value. Similar to the JC model, the RK model updates the temperature with the Quinney equation (4.1.4). The RK model does not consider the effects of strain-rate and temperature history. Tanimura and Duffy investigated history effects but did not find a conclusive result on how it affects the material behaviour [190]. In terms of material fitting we have to determine the static parameters B_0 and n_0, and the dynamic parameters $\bar{\nu}$, σ^*, m and D_2. All other parameters are material specific constants.

4.1.2 Damage

Section 2.3.4 presented the framework of accumulative damage models (compare (2.3.25)). In this section, we give examples for f that are relevant to our application and model the damage accumulation, according to

$$\int_0^{\bar{\varepsilon}_p} f(\cdot) d\bar{\varepsilon}_p = D_c, \tag{4.1.14}$$

where $\bar{\varepsilon}_p$ is the plastic strain and D_c is the critical value where the material is fractured. Most of the models proposed in the following use $D_c = 1$. The Johnson-Cook, the Lemaitre, and the Rittel model are described first as they are the damage models that were implemented during this thesis. Next, we describe the Cockcroft-Latham failure criterion, which is used with *IMPETUS®*. Finally, we outline the Hosford-Coulomb damage model, which models the whole fracture surface but has not been applied in this work. However, it is used frequently in similar applications and is therefore presented for completeness. Whilst Rittel and Cockcroft-Latham describe an energy-based failure criterion; all other models describe a strain-based failure criterion.

Johnson-Cook damage model

The Johnson-Cook damage model is a popular fracture model for HVI [106]. It calculates the damage function f in (2.3.25) as

$$f = \Big(\big(D_1 + D_2 \exp(D_3\eta)\big)\big(1 + D_4 \ln(\dot{\varepsilon}^*)\big)\big(1 + D_5 T^*\big)\Big)^{-1}, \tag{4.1.15}$$

where D_1, D_2, D_3, D_4, D_5 are modelling parameters, $\dot{\varepsilon}^*$ is the effective plastic strain rate, η is the stress triaxiality, and T^* is the normalized temperature. The approach uses the same ideas as the JC strength model (4.1.3). Instead of defining a critical damage D_c (compare (2.3.25)), the JC model uses $D_c = 1$ as threshold for failure and scales $D_1 - D_5$ accordingly.

Lemaitre damage model

Lemaitre [125] suggests the following damage accumulation function

$$f = \left(-\frac{Y}{S} \right)^t \tag{4.1.16}$$

with

$$-Y = \frac{\sigma_{eq}^2}{2E(1-D)^2} \left(\frac{2}{3}(1+\nu) + 3(1-2\nu) \left(\frac{-p}{\sigma_{eq}} \right)^2 \right), \tag{4.1.17}$$

where ν is the Poisson's ratio, and D, E, S and t are modelling parameters. The material fails at $D_c = 1$.

Rittel energy failure criterion

Dolinski and Rittel propose a criterion based on a plastic strain energy density (PSED) rather than a critical strain [57, 155, 169, 56]. First, they define a critical PSED W_{crit} as

$$W_{crit} = \int_0^{\alpha} \sigma_{eq} d\bar{\varepsilon}_p, \tag{4.1.18}$$

where α is the plastic strain $\bar{\varepsilon}_p^{\text{crit}}$ at which the material begins to lose its structural strength. Although we can define this for the other damage models as well, the Rittel model includes gradual element failure already in the model

$$\sigma_{eq}^* = \sigma_{eq}(1 - D^b). \tag{4.1.19}$$

The current flow stress σ_{eq}^* is described by the damage D and an exponent b. According to Rittel, b should be set to one. The damage is calculated as

$$D = \begin{cases} 0 & W \leq W_{\text{crit}} \\ \dfrac{W - W_{\text{crit}}}{W_{\text{frac}} - W_{\text{crit}}} & W > W_{\text{crit}} \end{cases}, \tag{4.1.20}$$

where W_{frac} is the second modelling parameter that describes the PSED where the material fails, and

$$W = \int_0^{\bar{\varepsilon}_p(t)} \sigma_{eq}^* d\bar{\varepsilon}_p \tag{4.1.21}$$

is the current PSED. In terms of the complexity, this model is very descriptive, and only two parameters, critical strain $\bar{\varepsilon}_p^{\text{crit}}$ and W_{frac}, have to be provided. However, the model's main criticism lies in its simplicity.

Cockcroft-Latham failure criterion

The criterion by Cockcroft and Latham [43] first came up with the term "true ductility", which is the natural strain at fracture in an idealised test with uniaxial tension. The criterion is directly related to the workability of a material - namely the maximum deformation before fracture during rolling, extrusion, and other processes. One main benefit of their description is that results obtained during tension tests can be directly transferred

to torsion tests. The original paper restricts the model to conditions at ambient temperature, which is a simplification not valid for HVI where high temperatures occur. The idea is that the integrated value of the first principal stress σ_1 determines when fracture occurs. It only occurs if σ_1 is positive:

$$f = \frac{1}{W_c} \max(0, \sigma_1), \tag{4.1.22}$$

or in other words that no damage accumulates under compression ($\sigma_1 < 0$).

Hosford-Coulomb damage model

The Hosford-Coulomb damage model is considering the experimental findings for the relation between Lode angle, triaxiality and fracture. The following definitions are written based on Marcadet [141]. The Lode angle is defined as

$$\Theta = \frac{1}{3} \arccos\left(\frac{3\sqrt{3}}{2} \frac{J_3}{(J_2)^{3/2}} \right), \tag{4.1.23}$$

where J_i are the invariants of the stress deviator. For the Mohr-Coulomb model, the first Lode angle parameter

$$\bar{\Theta} = 1 - \frac{2}{\pi} \Theta \tag{4.1.24}$$

is required to define the Lode angle dependent trigonometric functions

$$f_1(\bar{\Theta}) = \frac{2}{3} \cos\left(\frac{\pi}{6} (1 - \bar{\Theta}) \right), \quad f_2(\bar{\Theta}) = \frac{2}{3} \cos\left(\frac{\pi}{6} (3 + \bar{\Theta}) \right), \quad \text{and} \quad f_3(\bar{\Theta}) = -\frac{2}{3} \cos\left(\frac{\pi}{6} (1 + \bar{\Theta}) \right). \tag{4.1.25}$$

The fracture criterion in mixed strain-stress space is then

$$f = b(1+c)^{-1/n} \left(\left(\frac{1}{2} \left((f_1 - f_2)^a + (f_2 - f_3)^a + (f_1 - f_3)^a \right) \right)^{1/a} + c(2\eta + f_1 + f_3) \right)^{1/n}, \tag{4.1.26}$$

where η is the triaxiality and a, b, and c are the material specific parameters. Unlike most other fracture models, this approach captures the reduction of strain to fracture for triaxialities between 1/3 and 2/3.

4.1.3 Modelling of the explosive

The explosive is modelled with an equation of state (EOS) (compare Section 2.4), a high explosive burn constitutive material model, and explosive related material parameters. We model the explosive with the JWL-EOS proposed by Jones, Wilkens and Lee [118, 119]. It defines the pressure as

$$p_{\text{EOS}} = A\Big(1 - \frac{\omega}{R_1 \tilde{V}}\Big) e^{-R_1 \tilde{V}} + B\Big(1 - \frac{\omega}{R_2 \tilde{V}}\Big) e^{-R_2 \tilde{V}} + \frac{\omega E}{\tilde{V}}, \tag{4.1.27}$$

where, A, B, R_1, R_2, ω and E are material specific constants and $\tilde{V} = \rho_c / \rho$ is the ratio between the density of the explosive ρ_c and the density of the detonation products ρ. The parameters A, B, and E have units of pressure, and all other parameters are dimensionless.

The explosive used in Application I of this work is a Composition B cast explosive (65% RDX, 35% TNT). Literature data of Elek et al. [60] and Dobratz [55] provide parameter sets for the JWL-EOS for this composite

TABLE 4.1 Literature data for the JWL-EOS of Elek [60] and Dobratz [55] for Comp B explosive. The parameter set of Elek was chosen since the experiments for obtaining the data were closer to our application. A, B, R_1, R_2, ω and E are material specific parameters.

	A [GPa]	B [GPa]	R_1 [-]	R_2 [-]	ω [-]	E [GPa]
Elek	497	3.42	4.04	0.78	0.346	9.35
Dobratz	524	7.67	4.20	1.10	0.340	8.7

(see Table 4.1). This study uses the data provided by Elek, who validated his model with explosive rings and used the same composition. The initial relative volume $\tilde{V}_0 = \dfrac{\rho_0}{\rho}$ is set to 1.0.
The material behaviour can be modeled with a high-explosive-burn material model where the pressure is defined as

$$p = F\ p_{\mathrm{EOS}}(\tilde{V}, E), \tag{4.1.28}$$

where F is the burn fraction and p_{EOS} is the pressure determined by the equation of state (4.1.27). *LS-DYNA®* offers two different *BURN* options. One of them considers only volumetric compression and the second describes the behaviour of undetonated material. Detailed information about the burn fraction is given in the *LS-DYNA®* user manual [85], the model has been presented by Wilkins [214] and Giroux [71]. The explosive is further characterised by the density of the explosive ρ, the detonation velocity D, and the Chapman-Jouget pressure p_{CJ}. The density ($\rho = 1.73$ g/cm^3) and detonation velocity ($D = 8250$ m/s) were determined in-house. Similar values can be found in the literature. Dobratz documents a 3% smaller detonation velocity ($D = 8000$ m/s). The Chapman-Jouget pressure was estimated by Deal [52] as $p_{\mathrm{CJ}} = 292$ kBar $= 29.2$ GPa.

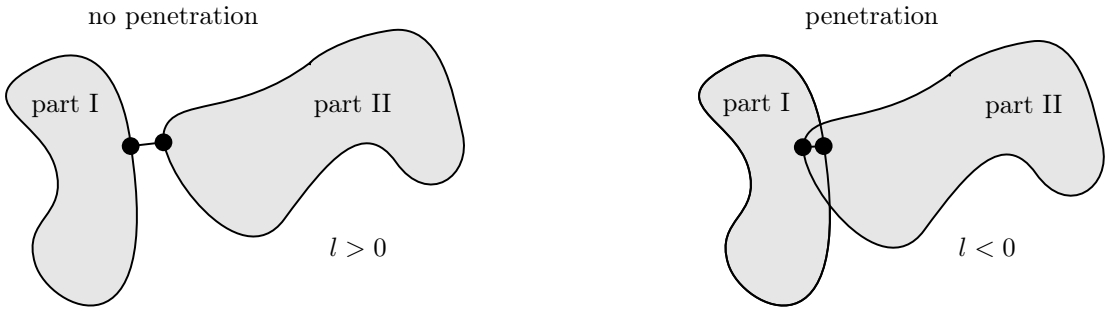

FIGURE 4.1 Contact between two bodies (part I and part II). If the penetration l is positive the parts are not in contact, if it is negative the penetration condition is fulfilled and the two parts are in contact.

4.2 Contact

For the modelling of dynamic impact events, a correct treatment of the interaction between two moving, deformable bodies, is of high importance. Since there is no prior knowledge of the exact behaviour, the contact must be correctly identified and described from both a mechanical and a numerical point of view. This section presents an overview of how contact can be modelled in general and points out particular methods in the FEM and SPH. The tied contact that is applied for a hybrid FEM-SPH meshing is presented in the subsequent section and further outlined in the black-box HVI model Section 4.4. Furthermore, we present particular techniques to improve the contact description in HVI applications.

4.2.1 Modelling contact

Contact in numerical simulations is present in four different situations: (i) self contact, (ii) two-body contact, (iii) contact between a body and a rigid boundary, and (iv) contact between two rigid bodies (compare Popp [161]). Without loss of generality, the following explanations are regarding two-body contact:
Let part I and part II be two bodies called "slave" and "master" approaching and getting in contact (compare Figure 4.1). In a numerical description, these bodies consist of a set of nodal positions. In terms of FE, these nodes are part of the computational grid. In terms of SPH, these nodes represent the particles of the body. The classical contact definitions check a penetration condition for each node of the slave part into the master body. As illustrated in Figure 4.1 the penetration depth l of a node can be measured. If the non-penetration condition

$$l < 0 \tag{4.2.1}$$

is violated, a correction has to be applied since two bodies can not occupy the same space at the same time. This correction can be defined by different means:

- A penalty contact adds a repellent force, depending on the magnitude of penetration and the material properties.
- A constraint-based contact applies a constraint on the global equations (2.5.1) by transforming the displacement of the nodes along the interface to ensure the impermeability condition.

For the temporal discretisation, the problem can be separated in a contact-independent and contact-dependent

part. From an algorithmic point of view, the solving procedure of a contact algorithm in an explicit time integration is straightforward: First, the dynamic equilibrium is calculated for each body independently ignoring the contact. Then, the contact interfaces are detected using a sorting algorithm. Finally, a correction term is added that is supposed to eliminate the penetrations. This correction term is a contact-induced movement which is determined by one of the above-described procedures. A more detailed description of contact modeling during explicit, transient dynamics is given by Hallquist et al. [84], Belytschko and Neal [23], Anderheggen [4], Rust [174], or Heinstein et al. [88].

4.2.2 Contact options in LS-DYNA® and IMPETUS®

This section discusses the contact-impact algorithms relevant to the application of HVI. First, we explain the contact options in the FEM and justify the decision for a penalty-based contact. Next, we discuss the two different SPH contact formulations: a kernel-interpolation-based technique and a penalty-based approach. In the last paragraph, we discuss contact damping. These contact settings are thoroughly compared in the numerical experiments of Application II. Tied contact, which links together two different parts, e.g., elements and particles for a hybrid-meshed domain, is described not in this, but as part of the following section.

Contact formulations in the FEM

The FEM implementation in *LS-DYNA®* offers three contact algorithm classes: (i) the kinematic constraint method, (ii) the distributed parameter method, and (iii) the penalty method.

(i) The kinematic constraint method is mainly used to tie interfaces, as for the hybrid FEM-SPH formulation of the target (compare Section 4.4.2). There, constraints are imposed by a modification of nodal displacement components of slave nodes at the contact interface. Impact and release conditions were initially imposed to obtain momentum conservation but were removed for efficiency. For TB, the correct treatment of impact and release is fundamental. Thus, this kind of contact is not suitable for describing an impact event correctly.

(ii) The distributed parameter method distributes mass and pressure between slave and master nodes. It then imposes constraints on the slave node acceleration and ensures non-penetration with a "put back on" logic. It was initially used in DYNA2D, and in the "sliding only" option in DYNA3D [85].

(iii) The penalty method is one of the most common approaches to describe contact numerically and is also applied in this work to describe the impact event. The main idea is to introduce virtual springs between nodes that cause penetration of object boundaries otherwise. Based on the spring stiffness, boundary forces are added on the right-hand side of the momentum equation for penetrating nodes. Three different implementations for the penalty contact are available in *LS-DYNA®*: a standard formulation (*SOFT=0*), a modified formulation (*SOFT=1*), and a segment-based penalty formulation (*SOFT=2*).

We explain method (iii) in the following in more detail using the notation of Figure 4.2. If a slave node S penetrates the master surface, an interface force $\boldsymbol{f}_S$ between S and contact point R is applied in terms of an

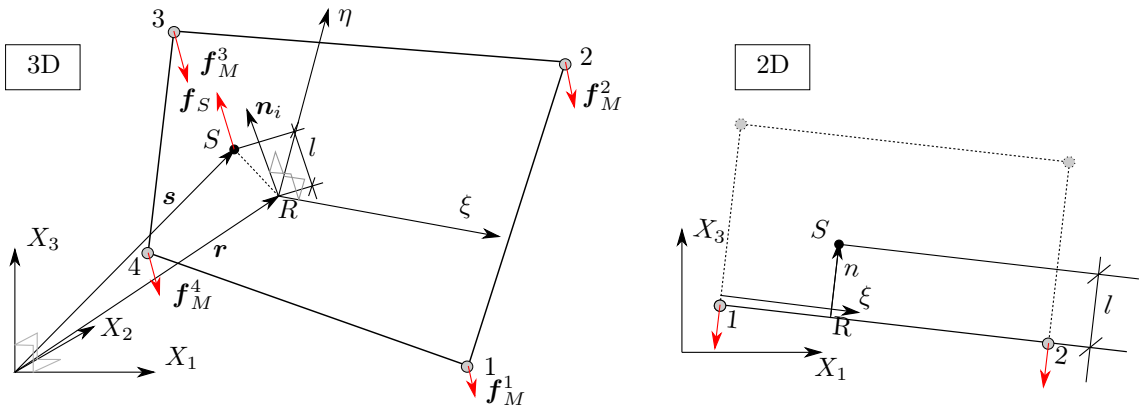

FIGURE 4.2 Penetration of a slave node S into a master segment M at the contact point R and with a depth of penetration l. A 2D visualisation of the 3D contact is depicted on the right for clarity. The forces acting on the master segment nodes $\boldsymbol{f}_M^j$ and slave nodes $\boldsymbol{f}_S$ are highlighted in red colour. The two coordinate systems are the local master segment coordinate system (η, ξ) and the global coordinate system (X_1, X_2, X_3).

interface spring with a magnitude proportional to the amount of penetration l and spring stiffness k_i.
In the following, we derive expressions for (i) the magnitude of penetration l, (ii) the interface force acting on the slave node $\boldsymbol{f}_S$, and (iii) the force transferred to the nodes of the master surface $\boldsymbol{f}_M^j$.
The amount of penetration is

$$l = \boldsymbol{n} \cdot (\boldsymbol{s} - \boldsymbol{r}) < 0, \tag{4.2.2}$$

where $\boldsymbol{n}_i$ is normal to the master segment at the position R of S on the segment, $\boldsymbol{s}$ is the coordinate of S, and $\boldsymbol{r}$ is the coordinate o R in global coordinates (compare Figure 4.2). The force acting on S is then

$$\boldsymbol{f}_S = -lk\boldsymbol{n}, \tag{4.2.3}$$

where k is the spring stiffness factor of the master segment, which is defined by (4.2.5). The force component which has to be added in (2.5.1) to each node ($j = 1, 2, 3, 4$) that comprise this master segment is

$$\boldsymbol{f}_M^j = \phi_j(\xi_c, \eta_c)\boldsymbol{f}_S \quad \text{if} \quad l < 0, \tag{4.2.4}$$

where ϕ_j are the corresponding shape functions of node j. The stiffness factor k in (4.2.3) is formulated in terms of the bulk modulus κ, element volume V, the element face area A, and a stiffness scaling factor f_{sf} as

$$k_{SOFT=0} = \frac{f_{\text{sf}}\kappa A^2}{V}. \tag{4.2.5}$$

This is the stiffness factor for the standard penalty contact, which is defined by the keyword *SOFT=0* in *LS-DYNA®*. In the above formulation, the contact stiffness k is of the same magnitude as the stiffness of the interface element. Therefore, the time step size is unaffected, but for considerable interface pressures, unacceptable penetration can occur (compare [85]). To counteract this problem, we have to increase the scaling factor of the stiffness artificially. This increase, however, is likely to induce instabilities. Thus, a smarter approach is to take into account the mass of the master and the slave node to calculate the stability

contact stiffness k_{cr}:

$$k_{cr}(t) = 0.5\ f_{\text{sf}}\ m^* \left(\frac{1}{\Delta t_c(t)} \right)^2, \tag{4.2.6}$$

where m^* is a renormalized mass of the master node and the slave node, and $\Delta t_c(t)$ is an updated initial time step size. When the solution time step grows, Δt_c is updated to prevent unstable behaviour. In a final step, the algorithm compares k_{cr} to k computed with (4.2.5) and takes the larger of the two

$$k_{SOFT=1} = \max\{k_{cr}, k_{SOFT=0}\} \tag{4.2.7}$$

to compute the contact stiffness for $SOFT = 1$. $SOFT = 2$ uses a segment-based penalty formulation. In contrast to the two methods explained above, a "slave-segment master-segment" implementation is used instead of a traditional "slave-node master-segment" approach. The calculation of the spring stiffness reads

$$k_{SOFT=2} = 0.5\ f_{\text{sf}} \left\{ \begin{array}{c} f_{\text{sf},SFS} \\ \text{or} \\ f_{\text{sf},SFM} \end{array} \right\} \left(\frac{m_1 m_2}{m_1 + m_2} \right) \left(\frac{1}{\Delta t_c(t)} \right)^2, \tag{4.2.8}$$

where $f_{\text{sf},SFS}$ and $f_{\text{sf},SFM}$ are user defined scaling factors for the stiffness of the slave, and the master, respectively. The masses m_i in (4.2.8) are segment masses rather than nodal masses, which are defined as half of the corresponding element mass. $\Delta t_c(t)$ is the same time step used for $SOFT = 1$. However, t_c is only updated if the time step grows more than 5%.

All contact types ($SOFT$=0, $SOFT$=1, and $SOFT$=2) are used in the context of a symmetric surface to surface contact. Symmetry means that the algorithm is called twice, once for part I being master and once for part II being master (compare Figure 4.1). The resulting penalty forces are the average of both values.

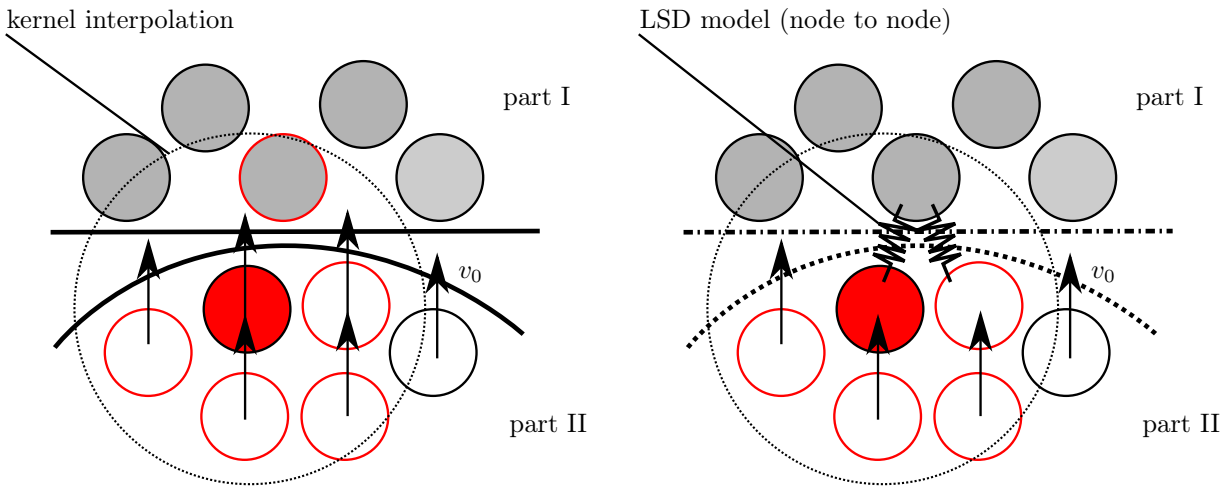

A standard formulation using kernel interpolation **B** penalty contact using a LSD model

FIGURE 4.3 SPH contact formulations in *LS-DYNA®*: For the standard formulation two parts are treated as one part and the contact is calculated during the kernel interpolation. For the penalty contact a LSD-model (linear spring-dashpot—compare Figure 4.4) between particles of different parts is transferring the repulsive force. Particles which are considered in the kernel interpolation are visualized with a red outline.

Contact formulations in SPH

For SPH, two different contact options are implemented in *LS-DYNA®*: The standard contact formulation is based on kernel interpolation in SPH, and the penalty contact formulation adds repulsive forces similiar to the FEM [218, 102] (compare Figure 4.3).

In the standard formulation, particles from a different body are included in the interpolation (3.3.13) if they are in the particles' support domain, and the resulting repulsive force adds directly to the right-hand side of the momentum equation. This contact treatment does not include a release condition, which means that different bodies that are in contact experience strong adhesive forces and stick together [96].

The second contact option is a node to node penalty contact which calculates a contact force $\boldsymbol{f}_c$ proportional to the displacement or overlap $\delta = d - 2h$ between particles ([102], Figure 4.4)

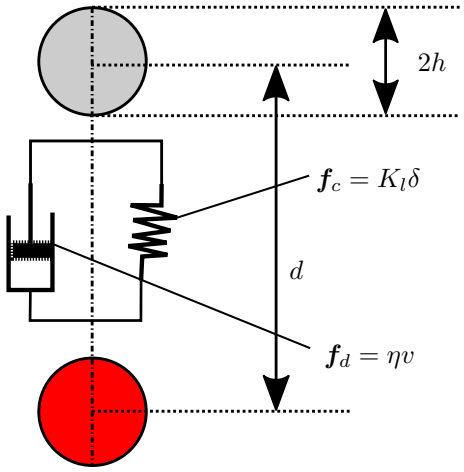

FIGURE 4.4 LSD (linear spring-dashpot) used in the contact formulation in *LS-DYNA®*.

$$\boldsymbol{f}_c = k\ \delta\ PFACT \qquad \text{if} \quad d < (d_c\ SRAD), \tag{4.2.9}$$

where $PFACT$ and $SRAD$ are modelling parameters explained below and d_c is the critical distance below which two particles are in contact. To account for energy loss due to friction, a damping force

$$\boldsymbol{f}_D = \eta\ \boldsymbol{v}_{12}\ DFACT \tag{4.2.10}$$

is implemented, which is proportional to the relative velocity $\boldsymbol{v}_{12} = \boldsymbol{v}_1 - \boldsymbol{v}_2$ and controlled with a damping coefficient η. Four parameters control this advanced contact description. The first parameter (*PFACT*) defines a penalty scale factor, which, according to the manual, should be between 0.01 and 1×10^{-4} for high-velocity events [85]. The second parameter (*SRAD*) determines the range d_c in which nodes are in contact. The size must be chosen large enough, such that the contact is detected before the impact, to guarantee an accurate description of the impact. There are two different definitions for the minimum distance, based on the sign of *SRAD*. For a positive sign, the distance is defined in terms of the mean smoothing length $(h_i + h_j)/2\ |SRAD|$. For a negative sign, the radius of the particles is considered instead $(\sqrt[3]{V_i} + \sqrt[3]{V_j})/2\ |SRAD|$. Since the kernel-width is defined dynamically, the option with the particle radius is used in this study for repeatability. The third parameter (*DFACT*) scales the damping coefficient η in (4.2.10), and the last parameter (*ISOFT*) enables the *SOFT*-option similar to the FEM-contact, which changes the calculation of the stiffness factor k in (4.2.9) according to (4.2.7).

Contact in IMPETUS® (FEM)

The contact in *IMPETUS®* is a symmetric surface to surface penalty contact. Similar to *LS-DYNA®*, a penalty factor defines the contact force. However, this factor is multiplied with the area where the contact is active. It can be user-defined or automatically calculated based on the loading condition

$$k/A = \frac{k_0/A}{L_{\min}} \ \min\left(1 + \left(\frac{\boldsymbol{v}_{\max}}{100}\right)^2, 100\right) \ [\text{Pa/m}], \tag{4.2.11}$$

where k_0 is the stiffness factor below the hydrodynamic domain, $\boldsymbol{v}_{\max}$ is the highest initial velocity in the model, and $L_{\min}$ is a characteristic length of the smallest element. In the study in Application II, a fixed value for k/A is chosen to improve the repeatability of the scenarios. By default, the contact damping—explained in the damping paragraph below—is 10% of the critical damping.

Contact damping

Contact damping is often beneficial for reducing high-frequency oscillations in crash or impact simulations [66]. Forsberg recommends $20\% - 40\%$ of critical damping for viscous damping with the segment-based contact in *LS-DYNA®* [66]. Viscous damping is a technique adapted from engineering systems, e.g., instruments such as balances or electrical meters and shock absorbers. It applies a damping force proportional to the velocity across the damper, which is opposed to the direction of motion. The term critical damping describes the amount of damping which is necessary to provide the quickest approach to zero amplitude for a damped linear oscillator [11]. Thinking about engineering design, this is a desirable outcome for damped oscillators such as door-closing systems. In a damped harmonic oscillator, the critical value for the damping $\tilde{D}_{cr}$ is

$$\tilde{D}_{cr} = 2\sqrt{km}, \tag{4.2.12}$$

where k is the spring stiffness and m is the mass of the oscillator. For our application of numerical simulations, this gives us a metric of the damping coefficient, which can be used independently of the loading case. In *LS-DYNA®* and *IMPETUS®*, the viscous damping is a user-defined percentage of critical damping.

4.3 Coupling between FEM and SPH in LS-DYNA®

LS-DYNA® offers two adaptive options based on the FE model where the simulation is initialised with finite elements only. As soon as elements are too distorted or eroded, they transform adaptively into SPH particles via *FEM2SPH* or discrete elements via *FEM2DEM*. This approach allows to use state of the art FEM as long as possible and change the discretisation only when required. The advantage is that computational resources are saved and, at the same time, mass and energy are better conserved. However, this approach is of interest, in particular for application where little element erosion is present. If considerable element erosion occurs, the amount of overhead from transferring particles outweighs the run time advantage, which is due to a non-decreasing time step. In our application, up to 50% of elements are eroded. Therefore, the element conversion does not give any run time advantages and, in terms of accuracy, it is similar to a pure SPH simulation in the fracture region.

Therefore, for the application of HVI, we propose the solution with a hybrid meshing instead. For this approach, a tied contact with offset is required that ensures the correct force transmission between SPH particles and FE mesh. Offset, in this context, means that the algorithm does not move tied particles onto the nearest point on the FEM surface but keeps them with an offset at their original position. Our model uses a constraint-based tied contact with an offset. *LS-DYNA®* offers constraint-based and penalty-based contact for the tied contact. A constraint-based contact instead of a penalty contact proved to be more stable for our application. This result might be because SPH particles do not have rotational degrees of freedom, and the penalty contact tries to enforce a translational and a rotational constraint [85]. Defining an offset is required to ensure that SPH particles are not projected onto the surface and, thus, destroying the particle distribution. The algorithm updates each tied interface independently. The nodal force and nodal mass of each slave node are distributed to the master nodes, defining the segment which contains the contact point. Further details on technical aspects are given in the *LS-DYNA®* theory manual [85]. The proposed hybrid FEM-SPH discretisation is explained in the subsequent section in detail.

4.4 Black-box HVI model

A terminal ballistic (TB) template is a geometrical model that can be used as an input for a simulation software and includes two components: the impactor and the target. Furthermore, it consists of all relevant settings of the numerical model, such as impact and contact settings.

The impactor is in most cases a rotationally symmetric body or can be simplified to a rotationally symmetric equivalent. For example, the wings of larger projectiles are only relevant to stabilise the flight-trajectory and do not influence the TB behaviour. Small calibre projectiles consist of multiple subparts with different materials. The template needs to describe this kind of setup as well. Furthermore, the user defines the numerical resolution in the template.

The target in TB real-world experiments is mostly substituted by a plate made of the same material and with similar thickness, as used in the real application. The main challenge, in particular for small calibre projectiles, is the size difference between impactor and target. At the same time, the resolution of impactor and target has to be similar in the impact region to guarantee an accurate prediction of the interaction. Computing the approximation for the whole geometry with this resolution is not possible as the resulting number of

integration points is not feasible. From a modelling point of view, there are two solutions to this.

- First, the size of the target can be reduced in the numerical model. If the material is brittle enough and the bending of the plate is negligible, this is legible.
- Second, a bias mesh can be used to account for plate bending with larger elements close to the boundary and a fine resolution in the impact region to capture the interaction correctly.

As we want to be predictive for ductile materials as well, we implement the second option. Besides the discretisation, our template defines the boundary conditions. The target can be clamped in for v50 tests with small calibre projectiles or placed in front of a concrete wall for DOP tests (compare Section 1.2.3). Therefore, the boundary conditions have to be defined at the top, bottom, left, right and back. For the v50 tests, the plate is clamped in one or two directions. For the DOP tests, the ground and the concrete wall at the back are modelled with rigid boundary conditions. Also, for a hybrid discretisation of the target, a tied contact has to be defined between SPH and FEM.

To finalise the ballistic template, we have to define the velocity and angle of the impactor. A separate file provides the material properties (baseline input deck). So, we need to specify which unit-system in *LS-DYNA®* is used. With this information, case-specific settings such as simulation time and the SPH-box[2] are defined. Finally, the user can also provide additional manipulations of flags in the input-deck (e.g., a different end-time for the simulation, or a different SPH or contact formulation), which shall be applied whenever a new case is generated. This way, neither the baseline nor the final input-deck for the simulation must be modified, and reproducibility is guaranteed.

In the following, we give further details about the discretisation: The discretisation is a central component of numerical simulations. Fortunately, the geometries considered in this work are elementary. Therefore, it is possible to investigate different discretisation techniques. Automatic mesh generation has several advantages over hand-made mesh generation and is one of the key ingredients for the success of this work. First, automatic mesh generation allows us to easily compare different grid resolutions and evaluate convergence. With little effort, we can determine whether the solution is converged or not. Second, we can define design criteria for our discretisation and use these criteria consistently throughout numerical studies. Third, we can automatically define boundary conditions, as the program knows the node positions.

For SPH, we discuss different approaches to populate particles in a projectile shape. For FEM, we propose a bias mesh for a large target plate and automated meshing of the projectile.

[2]only particles that are still inside the SPH-box are considered in the computation

4.4.1 Particle distributions in SPH

Initially, the need for an in-house particle preprocessor was implied by the fact that the preprocessor of *LS-DYNA®*[3] had limited capabilities to generate SPH particle distributions. The available option was to generate the particle positions based on an existing FE mesh (compare Figure 4.6). The problem with this approach is that the design criteria for the FEM and SPH are different: For SPH, the design criteria are:

(i) that the distance between all particles is similar;

(ii) that all particles occupy a similar volume;

(iii) and that the geometry occupied by particles is approximated well.

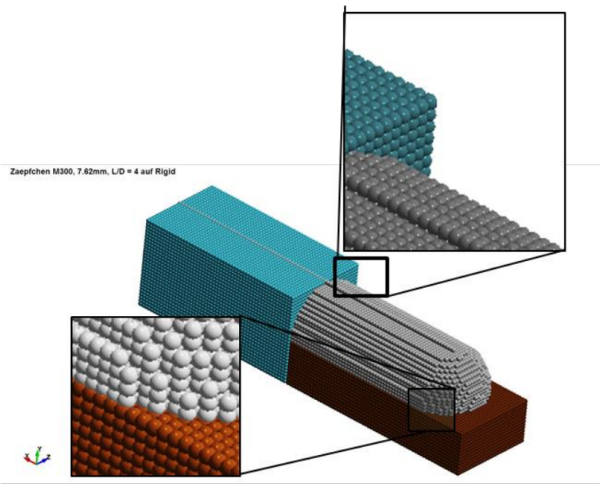

FIGURE 4.5 Cut from block of particles.

In particular, (i) and (ii) are not necessarily required for the FEM. Therefore, simulations with a particle-distribution which is based on node positions of the FE mesh (see Figure 4.9A) lead to a poor approximation.
A simple solution which is only flawed in terms of design criterion (iii) is shown in Figure 4.5: particles are positioned on an equidistant lattice that is fully covering the geometry to discretise. Then, particles that are outside the body are removed from the particle distribution (compare Figure 4.9B). Numerical simulations are showing that this regular discretisation triggers instabilities (compare Application III in Section 8.2.1). If a crack opens up perpendicular to the symmetry axis of the impactor, the tensile instability propagates the crack through the whole geometry along the plane between two particle layers. These layers do not exist for more random distributions and avoid this kind of unphysical behaviour. Thus, we designed a particle positioning algorithm that adds irregularity and improves the fulfilment of criterion (iii) as presented in Figure 4.7 and 4.9C. Instead of a rectangular lattice, particles are distributed on cylindrical coordinates. Similarly, a spherical object, such as the tip of the impactor investigated in Application III, can be discretised with spherical coordinates (see Figure 4.8 and 4.9D). However, this is more complex and, for generality, we propose a different solution: assuming that the body is rotationally symmetric, the geometry is expressed with the diameter as a function of the axial coordinate. To improve the quality in term of criterion (iii), the size of the particles is kept variable in a small range. By this, nearly arbitrary rotationally symmetric bodies, including spheres, can be discretised well. The application of the method is limited for very sharp bodies such as cones with very small diameter.

[3] *LS-PREPOST* V4.5

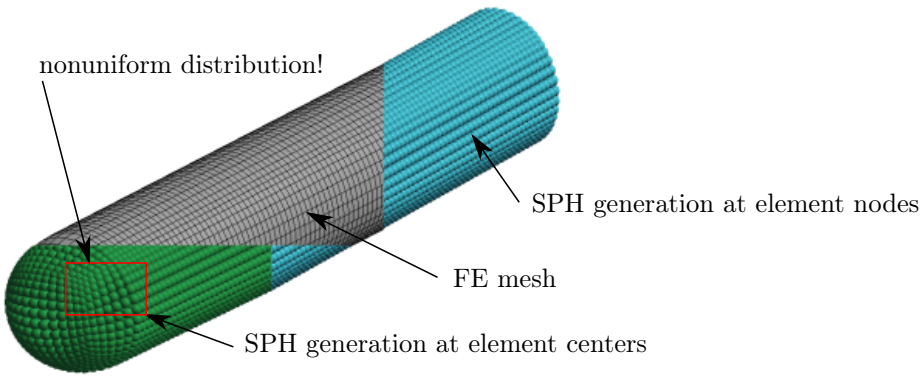

FIGURE 4.6 Particle distributions in SPH: Illustration of the conversion from finite elements to SPH particles. There are two options: (green) placing the nodes at the element centers; (blue) placing the nodes at the element nodes.

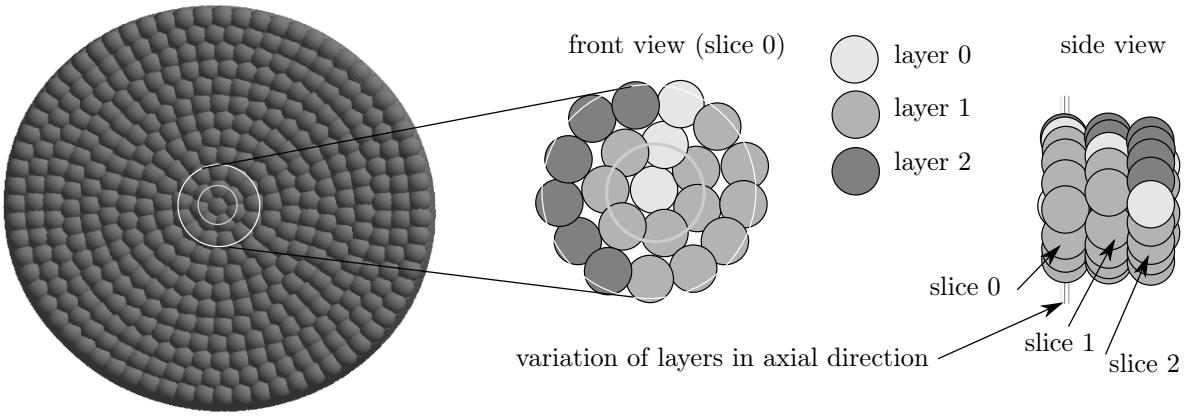

FIGURE 4.7 Particle distributions in SPH: To discretise the cylinder we distribute particles on cylinder slices first. Each slice consists of several layers. Each layer has six more nodes than its adjacent inner layer. The layers are slightly shifted to avoid instabilities for a regular distribution. This is indicated by the vertical lines in the side view.

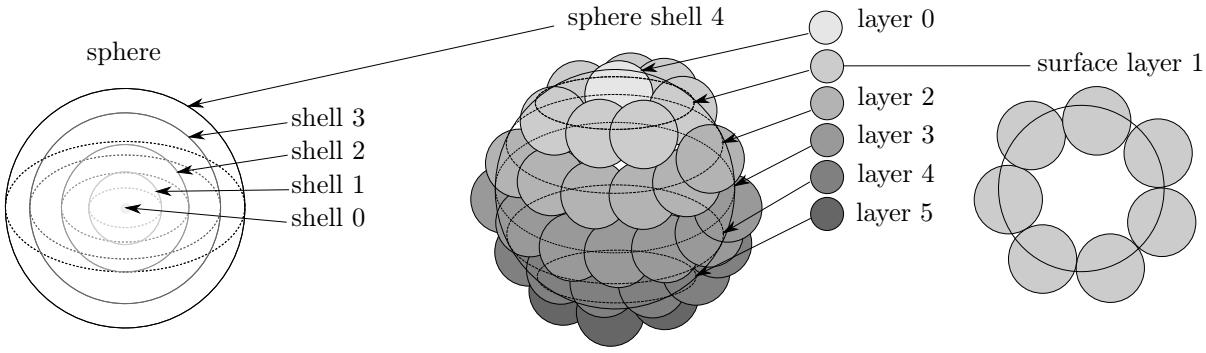

FIGURE 4.8 Particle distributions in SPH: The discretisation of a sphere is complex if all design criteria have to be fulfilled. We divide the sphere in spherical shells and distribute particles on each sphere shell. This distribution itself consists of separate layers.

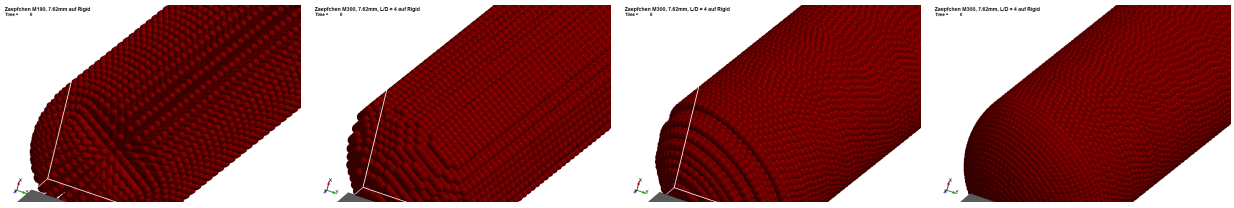

A FEM to SPH **B** cutout **C** cylinder **D** sphere

FIGURE 4.9 Particle distributions to mesh the impactor for SPH. **A** is the standard approach in *LS-PREPOST* **B-D** have been developed in the scope of this work. The positioning are explained in Figure 4.6, Figure 4.5, Figure 4.7, and Figure 4.8.

4.4.2 Finite element meshing of the plate for hybrid meshing

In our hybrid HVI-model, we need FE meshing for the region outside the impact region to save computation time and to account for a correct propagation of shock waves. We furthermore developed a FE meshing algorithm for a simplified impactor, as used in Application III. Since meshing of a sphere and a cylinder are well-documented [83], this is not described here. From a numerical point of view, we have the following constraints to our hexahedral elements

- the shape of each element should be as close as possible to a cube;
- for a bias mesh, the difference in size between neighbouring elements should be moderate.

From a technical point of view, meshing is more difficult than the particle distribution as

- we have to preserve elements and connectivity of nodes;
- if we connect different subparts to one part, we have to eliminate duplicate nodes;
- we have to detect boundary nodes and surfaces for applying boundary conditions.

The geometry to be discretised for the hybrid FEM-SPH target with finite elements is a plate with a hole (SPH particles fill the hole). Due to symmetry, the discretisation in the plate thickness direction can be regular. Thus, we face a two-dimensional problem in the remaining directions, which is a rectangle with a circular hole. The idea is to define straight lines in the radial direction first, which have approximately the same angle between each other. As a constraint, this distribution must contain lines which end at the four corners of the plate surface. Next, we distribute a user-defined number of grid points along each line, starting at the cylinder and ending at the plate boundary. Our discretisation ensures that the first segment length is similar to the SPH-particle diameter and that the element size continuously grows towards the outer boundary. This way, we have a smooth transition between the FE and SPH domain. This two-dimensional mesh can be extruded into the axial dimension with a user-defined amount of layers.

As an addition, this approach can also be used for a pure FE model of the plate as the cylindrical geometry of the hole can be automatically meshed with finite elements. This approach generates, with little effort, a high-quality and computational-efficient mesh for the application of HVI, where the plate size is considerably larger than the size of the impactor.

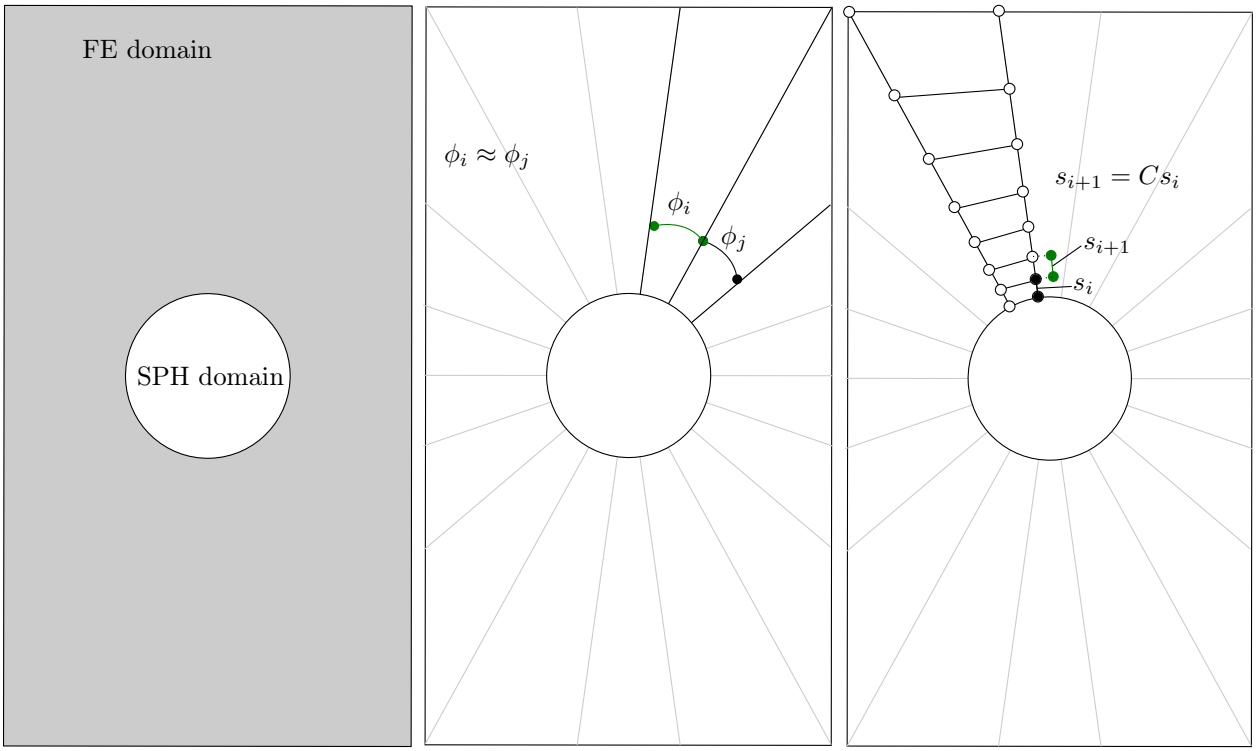

FIGURE 4.10 FE meshing approach for the target: **A** shows the domain which has to be discretised; **B** shows how the radial lines are defined; **C** shows how the bias discretisation towards the boundary is constructed. For visualization the number of discretization points is significantly smaller than in the experiments.

4.5 Fragment detection in numerical simulations

This section is based on the contribution to the 8th GACM Colloquium on Computational Mechanics [14]. The motivation for developing a fragment detection algorithm is that the applied postprocessing software Paraview [3] and *LS-PREPOST* [83] have no possibility to identify separated parts. The manual workaround is time-consuming and error-prone, in particular when evaluating the mass and average velocity of the resulting fragments.

There is only little literature available on this particular application, but the problem can be abstracted from graph theory. If the nodal positions are known, a suitable criterion determining the graph connectivity is needed. We compare two criteria: First, we propose an approach that uses a regular grid to sort the nodes and determine the neighbours. Second, we apply a density-based clustering algorithm to the point cloud, which was first proposed by Ester et al. [63]. As the number of nodes in a three-dimensional simulation is large, an efficient algorithm and a fast implementation are indispensable. A further technical challenge is the incorporation of the fragment information back into the visualisation data.

This section first describes the two algorithms and then applies them to two exemplary applications. In our comparison, we discuss the difference in terms of accuracy and run time.

4.5.1 Problem definition

The simulations for which the algorithm is applied contain between 50,000 and 1,000,000 particles. The input for the algorithm is the nodal position of these particles. If the particles are closer together than a threshold distance, they are considered connected and belong to the same fragment. Let S be a set of points in $\mathbb{R}^3 \times \mathbb{R}$, then two particles $(\boldsymbol{x}_i, t) \in S$ and $(\boldsymbol{x}_j, t) \in S$ are referred to as neighbours at time t if and only if

$$||(\boldsymbol{x}_i, t) - (\boldsymbol{x}_j, t)|| < \varepsilon, \tag{4.5.1}$$

where $||\cdot||$ denotes the Euclidean norm in $\mathbb{R}^3$ and ε is the threshold distance. Besides special criteria, we have to consider the time component. Particles which have not been connected can get sufficiently close and satisfy (4.5.1). The particles are called connected neighbours if and only if they are neighbours at all times t. A fragment is a set of nodes that form a connected graph in terms of this criterion. For our application, it is improbable that particles connected in the beginning disconnect and connect again since the fragments can move in arbitrary directions. Therefore, we only consider the initial and final time step. For other applications, it might be necessary to consider the intermediate time steps.
If we compared all particles to each other in a naive approach, we would have a complexity of $\mathcal{O}(n^2)$. In particular, if the problem size grows to the upper limit of 10^6 nodes, we would require 10^{12} comparisons and reach the limits of current desktop computers to calculate the result without considerable waiting times. This motivates the use of a smarter algorithm that can reduce complexity.

4.5.2 Classical grid-based approach

The classical grid-based approach performs the following four steps:

1. Divide the computation domain into uniform pixels (2D) or voxels (3D).

2. Assign each node to one of the voxels.

3. Determine the neighbours (according to (4.5.1)) in a connectivity graph.

4. Determine the fragments from the connectivity graph.

For step 1, the size of the voxels has to be chosen carefully. If the voxels are too large, too many nodes are in the same voxel, and the number of comparisons is significant. On the contrary, if they are too small, more voxels have to be considered in the comparison. A good compromise is to choose the edge length of the voxel identical with the threshold distance. Then, only the surrounding 27 voxels have to be considered for each node. In step 3, the connections are saved in a connectivity graph which is leaner and easier to analyse than a linear data structure—particularly for this application. The following algorithm describes the implementation of step 4, which is the part where the fragments are finally identified:

```
1  loop over all vertices of the connectivity graph;
2  while vertices do
3      pop the next vertice;
4      start = vertices.pop();
5      get all connected neighbours of the start vertice;
6      fragment = nGraph.dfs(start);
7      fragment = set([start]) | (fragment & vertices);
8      crop particles which are not in vertices any more;
9      vertices = vertices - fragment;
10     check if the fragment is larger than the threshold size;
11     if len(fragment) > fragmentMin then
12         increase the fragment ID;
13         fragmentID += 1;
14         for particle ∈ fragment do
15             assign particle to fragmentID;
16             fragmentNPart[particle] = fragmentID;
17         end
18     else
19         for particle ∈ fragment do
20             assign particle to dust if the fragment is below threshold size;
21             fragmentNPart[particle] = 0 ;
22         end
23     end
24 end
```

Algorithm 1: Assigning the particles to the fragment-based on the connectivity graph.

A solution would be to build the graph at the initial time step and only update the edges in each time step. This also leads to $\mathcal{O}(N)$ comparisons in each time step and the equal distribution in the first time step is guaranteed by construction. Such an approach is of particular interest if the temporal crack evolution is required.

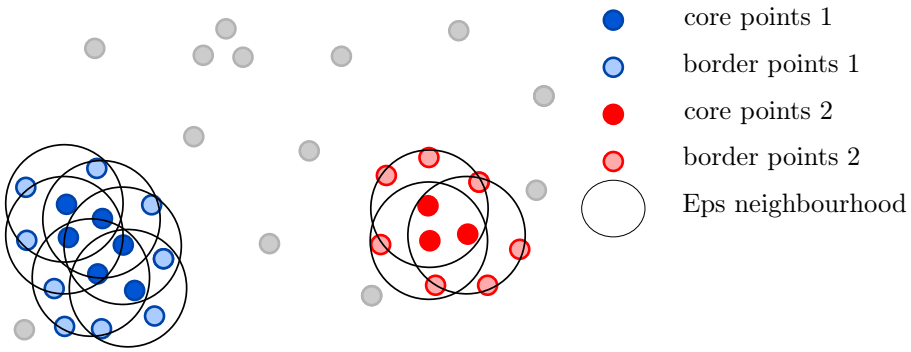

FIGURE 4.11 DBSCAN clustering example using random 2D data points. First, all core points are identified which have at least four points in their Eps neighbourhood. Next, all border points are added to the cluster. All other points are noise points.

4.5.3 Density-based spatial clustering of applications with noise (DBSCAN)

The second approach which we apply to verify our results is the DBSCAN algorithm. The idea of DBSCAN is illustrative: Visually, one distinguishes clusters by their density (compare Figure 4.11). Clusters are areas of high density separated by areas of small density. To define the term density in a point cloud, DBSCAN uses the distance to neighbouring points in a so-called Eps neighbourhood. This distance can be an arbitrary distance function - we use the Euclidian distance. Density is defined by the number of points which are within the described Eps neighbourhood. In the next step, the algorithm distinguishes between core points, border points and noise points. Core points are points which are satisfying the density criterion. Border points are points which are density reachable by core points. Density reachable means that they are within the Eps neighbourhood of core points. All other points are noise points. Core points which are density connected, and the corresponding border points, form clusters. These clusters define the fragments for our application. The algorithm uses a R^* tree [19], which is a balanced tree that uses rectangles as bounding boxes (in 2D) as a data structure. The modification to R trees is that the query complexity is reduced by using reinsertion while initialising the tree. The tree structure is used to query the nearest neighbours of each point. This is needed to identify core and border points and their connectivity. Each query requires $\mathcal{O}(\log(N))$ comparisons leading to an overall complexity of $\mathcal{O}(N \log(N))$. Compared to the proposed solution above, DBSCAN is slightly more complex. However, the constant in $\mathcal{O}(N)$ is large as all particles in 27 neighbouring voxels have to be considered. The main advantages of this algorithm are that it can detect noise, outliers and arbitrarily shaped clusters. The limitations are applications with a varying density as one global threshold density is used. Furthermore, for some applications, the choice of the tuning parameters can be demanding. For our application, these limitations are not relevant as all particles are of the same size.

4.5.4 Results

In this section, we show results for two applications. Application I investigates the natural fragmentation of explosively driven cylinder rings. Here we visualise the fragments from the final state in different time steps. In Application III, we investigate the crack development of the impactor.

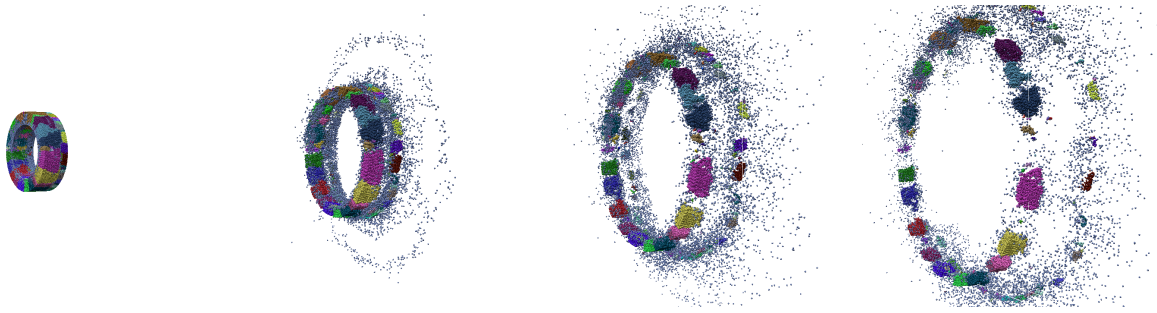

A $t = 0\ \mu s$ **B** $t = 50\ \mu s$ **C** $t = 100\ \mu s$ **D** $t = 150\ \mu s$

FIGURE 4.12 Visualization of natural fragmentation with *MegaMol* [79]. Each color represents a different fragment. Due to a large amount of fragments similar colors might appear.

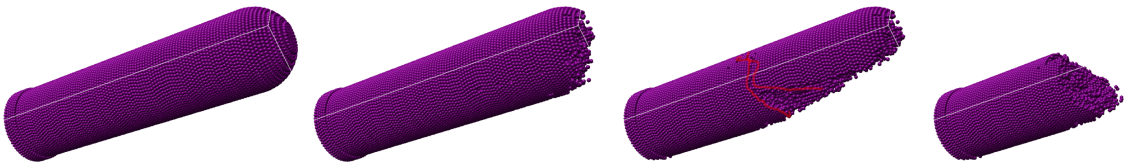

A $t = 0\ \mu s$ **B** $t = 40\ \mu s$ **C** $t = 80\ \mu s$ **D** $t = 120\ \mu s$

FIGURE 4.13 Temporal evaluation of projectile-breakup during oblique impact. The red line shows the development of a crack.

Natural fragmentation (Application I)

For the evaluation of Application I, we require visual and statistical information about fragment size, fragment velocity, and visualisation of crack patterns. While the fragment size distribution can be tested a posteriori in the experiment, the physical mechanisms can only be revealed with numerical simulation: Due to the large deformations of the fragments during the ring expansion, the ring can not be reconstructed in experiments. Simulations, in combination with fragment detection, on the other hand, allow visualising fragments in their original position in the intact cylinder ring. To argue that the simulation is reproducing the experimental behaviour well, the fragment-size-distribution can be compared as a measure of accuracy. Since there is no direct postprocessing option for this task, the proposed algorithm fills the gap to obtain the distribution and visualise the crack patterns (compare Figure 4.12). The particle visualization software *MegaMol* [79], is used for the three-dimensional visualization of particles.

High-velocity impact (Application III)

The temporal crack evolution, or crack formation, of fragments, can only be investigated using the numerical results processed with this methodology (see Figure 4.13). Furthermore, the approach can blank disconnected particles to obtain a clearer picture compared to the visualization with *LS-PREPOST*.

4.5.5 Conclusion and comparison of classical approach and DBSCAN

In this section, we proposed two algorithms to detect fragments from point clouds, such as the final particle distribution of an SPH simulation. Both algorithms detect the same fragments except for statistical differences. Therefore, the run time and range of applications evaluate the algorithms. In terms of the range of applications, DBSCAN is much more flexible as it can work with an arbitrary node distribution in space. The classical method has to define the voxels accordingly to the geometry filled with nodes. If a different application is used, no modification is required for DBSCAN. The run time of both algorithms for our applications is only a few seconds and not relevant since the IO is more critical for the overall run time. An application where the classical method outperforms DBSCAN is crack evolution. There, the difference between two subsequent time steps has to be evaluated, which means for the classical method that only the existing connectivities have to be updated, whereas DBSCAN generates the clusters from scratch. However, this is not of interest for our application, and we apply DBSCAN in this work.

4.6 Conclusion

This chapter extended the general numerical framework with particular techniques used for our applications. In terms of the material model, we presented (i) three hardening rules for the von Mises plasticity introduced in Chapter 2, (ii) selected accumulative damage models, and (iii) an EOS for the explosive with the respective parameters for Application I. In terms of contact, we outlined the numerical description of contact and discussed different options in FEM and SPH. For the FEM, we identified the soft option as essential for our modelling and in SPH, we identified the penalty contact to be better adjustable than standard contact. Moreover, we outline the contact implementation in *IMPETUS*® and coupling options which are needed for our black-box model.

Our black-box model determines the preprocessing of the numerical simulations with particular regard to the coupling and the discretisation. Here, we compare different techniques to generate the initial particle distribution for the impactor and outline how the hybrid FEM-SPH discretisation of the target is generated. The final section describes the postprocessing of particle simulations and evaluating the fragments. We identify DBSCAN as a suitable clustering algorithm for this task. If the crack development is of interest, classical methods might be superior.

5

Real-world experimental methods

This chapter describes the experimental methods used in our applications. First, we show different imaging techniques, pendulum tests to investigate flight stability of projectiles, and methods to recover fragments. Then, we give an overview of the software we implemented to extract residual fragment velocities from X-ray images of impact events and explain the required image processing algorithms. There, we compare different implementations and investigate the corresponding parameters.

5.1 High-speed camera

Standard cameras can not be used in TB-experiments as the required exposure times are orders of magnitudes smaller than what these cameras can capture, and a very high frame rate is necessary. Thus, specialised high-speed cameras have to be used. In our experiments, we use a SIMD16 camera from Specialized Imaging depicted in Figure 5.1. Similar to the HSFC Pro from PCO, which is used in Section 5.2.2, this camera is an image intensifier camera. An image intensifier consists of a photocathode that converts photons in electrons, a multi-channel plate which multiplies the number of electrons, and a phosphor plate that back converts the multiplied electrons to photons such that the high-speed camera can detect visible light and capture the digital image.

FIGURE 5.1 SIMD 16 high speed camera (image `https://www.specialised-imaging.com/products/framing-cameras/simd`).

The sensor of the SIMD16 has a resolution of 1360×1024 pixels, and single exposures have a cropped resolution of 1280×960 pixels with a 12-bit greyscale. The incident photons to create

an image can be amplified by a factor of up to 7000. Theoretically, the camera can take up to 1 billion frames per second with a minimum exposure time of 3 ns. The main advantage of this technique is that images do not have parallax—which describes a displacement in the apparent position of an object due to different lines of sight—and the number of images per experiment is not as restricted as with X-ray. Therefore, this is the first choice for the v50 experiments presented in Application III where we use an exposure time of 1 μs and an interframe time of $t_{\text{if}} = 10 - 50$ μs, which is defined as

$$t_{\text{if}} = 1/\text{fps}, \tag{5.1.1}$$

where fps is the framerate. Furthermore, a high-speed camera is used in the setup of the multi-anode X-ray cinematography (see Section 5.2.2).

5.2 Flash X-ray (FXR)

Due to the eroded material during an oblique impact, a high-speed camera is not able to observe what is happening for a ricochet. Instead, FXR images are taken, which can see through the dust and foam. FXR uses the discharging of high voltage pulsors to generate highly energetic short X-ray pulses and create a shadow image without motion blur. Furthermore, this technology allows us to use additional material around the setup to protect the camera and to recover fragments for later analysis.

5.2.1 Multi-exposed X-ray

Multi-exposed X-ray uses multiple separate and linear aligned X-ray flashes to register up to four exposures on one image plate. The X-ray flashes have a finite distance between each other. Therefore, the images contain a parallax (described in Section 5.1). All exposures are saved on the same film as it is not possible to change the film within the short interframe time between the exposures. The result with this technique is one image which contains several shifted exposures. Regarding the analysis, the shift is corrected using distinctive reference points in the exposure. Due to the three-dimensionality, these points should be located in the flight axis and in the vicinity of the object to be tracked, so that the image alignment error is small. Only large fragments can be tracked with this analysis, as it is hard to assign small spots on the image to the corresponding exposure.

5.2.2 Multi-anode X-ray cinematography

Since this approach was mainly used during our experiments, we (i) explain the methodology, (ii) argue why it is advantageous for our application, and (iii) describe the setup in the real-world experiments of Application III. The recently installed multi-anode X-ray setup is state of the art and allows to capture up to eight images per experiment. In contrast to the X-ray described before, the radiation is not saved on an image plate but is converted to visible light and captured with a high-speed camera (compare Figure 5.2). This allows generating separated images with a high framerate. To secure the high-speed camera from highly energetic radiation, we place it slightly shifted to the plane of observation. A high-quality mirror redirects the light to keep the absorption and distortion of the image as small as possible.
One advantage compared to FXR is that the number of exposures is not limited to four and, therefore, increases

the possibilities of observing the dynamics of the impact. However, the most significant advantage of the multi-anode setup over FXR is that single images are obtained similar to a high-speed camera. Therefore, the post-processing does not require a separation of images. Instead, only the parallax of the images has to be resolved. When a fracture occurs, this separation can be very complicated or even impossible. Regarding parallax error, a dedicated python software addresses this problem with an affine transformation using reference points in the images (see Section 5.5). Due to a circular instead of a linear arrangement of the X-ray flashes, the parallax is smaller than for the standard FXR setup. The main drawback of the multi-anode X-ray is low image quality. Due to the conversion of X-ray radiation into visible light and redirection of the light to the lens of the high-speed camera, the number of incoming photons is small. Therefore, the camera requires an image intensifier, to increase the number of photons and output a human-visible image. However, this component also increases noise. The second difficulty is that the exposure time needs to be very small for our application. Therefore, it requires a widely opened objective shutter for more light. The sensitivity of the camera sensor needs to be very high as well. In the end, there is significant noise in the image that has to be fixed. One approach for reducing the fixed-pattern-noise of the images is to subtract a dark-image. A fine-tuning of the exposure parameters can also improve image quality. In particular, a spectral fitting between image intensifier and scintillator screen turned out to be of high importance [64].

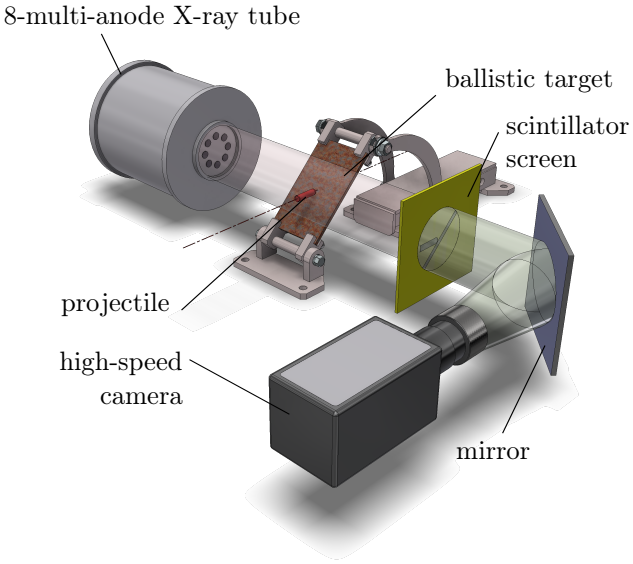

FIGURE 5.2 Setup of multi-anode X-ray: Eight anodes can be activated within a very short delay. The electrons induced by the X-rays are converted to visible light with a scintillator screen. This can be captured by a high-speed camera producing up to eight separate images.

In our experiments, only six out of eight anodes were available; thus, six images could be captured for each experiment. The recording time in our application is 150 to 200 μs. Accordingly, the images are taken with an interframe time between 30 and 40 μs. The exposure time was set to 3 μs, and the image intensifier used 85% of the maximum amplification to avoid ghost images. Ghost images are low opacity artefacts that occur when the luminosity of the previous image has not entirely faded. There was no real-time setup available which would trigger the X-ray flashes depending on the actual velocity of the projectile. Thus, the exposure times had to be calculated depending on the estimated velocity. Therefore, a direct comparison of images between different experiments is not possible. For a large oblique angle, there is also a distinct uncertainty about where the projectile hits the target. Thus, for these cases, the longer interframe time of $t_{\mathrm{if}} = 40$ μs was used to capture a more considerable duration; for the smaller oblique angles $t_{\mathrm{if}} = 30$ μs is used to obtain a higher time resolution during the impact.

5.3 Pendulum tests

For reproducibility and comparability between real-world and numerical experiments, the aim is to have no yaw of the projectile during the impact. However, it occurred that sometimes there was yaw. To investigate the pendulum behaviour, we place paper stripes at various positions in the trajectory. Examination of the hole shape, cut in these stripes by the projectile, reveals the magnitude of the yaw. Here, no distinction between pitch and yaw, which initially described the difference to perpendicular impact in a horizontal and vertical direction, is made. Instead, we compute the total deflection angle to the perpendicular flight direction. A sharp circular hole shows that the projectile has no yaw. A blurred nonsymmetrical shape indicates that there is yaw. In Application III, the results with yaw are used for sensitivity analysis. The yaw angle can be estimated from the size of the hole in the principal directions (compare Figure 5.3 and Figure 5.4). This estimation is dependent on the length to diameter ratio (L/D) of the impactor. We present the analysis for the surrogate used in Application III which is a cylindrical impactor with $L/D = 4$ and a spherical nose (compare Figure 5.4): Let C be the ratio between the diameter of the hole in the first principal direction d_1 and the second principal direction d_2 and γ be the yaw-angle. Then, the relation between d_1 and d_2 is

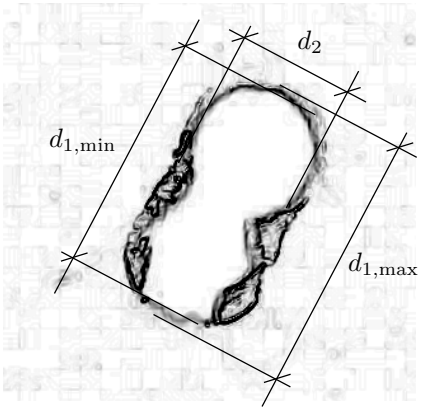

FIGURE 5.3 Example cut-hole and estimation of yaw.

$$d_1/d_2 = C = \left(3.5\sin(\gamma) + 0.5\cos(\gamma) + 0.5\right). \tag{5.3.1}$$

Using trigonometric equivalences, we can solve this equation for γ:

$$\gamma = 2\left(\tan^{-1}\left(\frac{7 \pm \sqrt{-4C^2 + 4C + 49}}{2C} + (\pi n)\right)\right) \qquad n \in \mathbb{N}. \tag{5.3.2}$$

The uniqueness of γ is given by the requirement $0 \leq \gamma \leq 45°$. The edge detection of the hole yields no sharp edges; thus, the mean of the inner and outer distance for the principal diameter is taken to estimate the yaw. Hence, the uncertainty range is resulting from the inner and outer distance and is visualised with error bars in Chapter 8.

5.4 Soft recovery of fragments

The soft recovery of fragments is a challenging task during TB experiments. Depending on the application and test site, different materials can be used for the recovery. For Application I, a water basin is placed underneath the experimental setup. In TB, fragments can fly in all directions, and water is difficult to use in an indoor lab. Therefore, other soft materials such as wood, cardboard or polyethene have to be applied. Our observations showed that the most suitable material is cardboard since fragments can easily be extracted from it, and the material can be reused. At first, it was not clear in which direction fragments spread, and

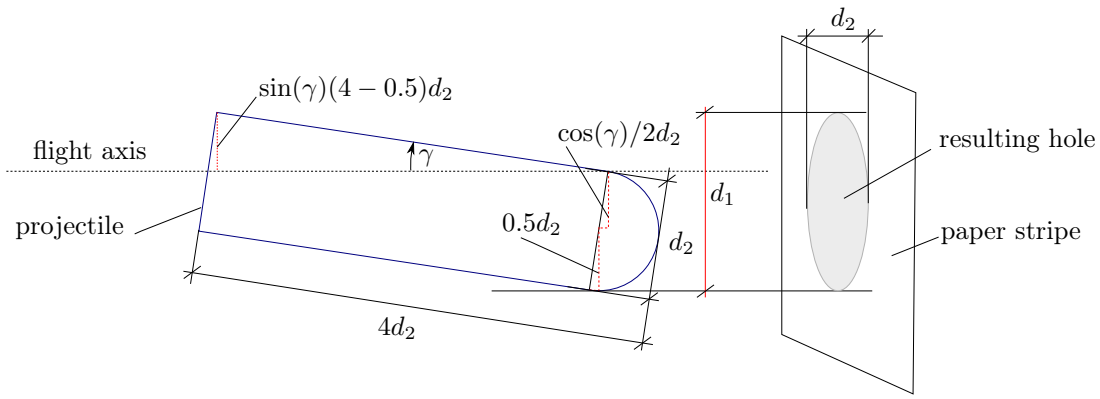

FIGURE 5.4 Experimental estimation of the yaw based on the hole diameters d_1 and d_2 extracted from the paper stripes (compare Figure 5.3). The length d_1 can be calculated as a function depending on d_2 and γ. This equation can then be solved for γ (compare 5.3.2).

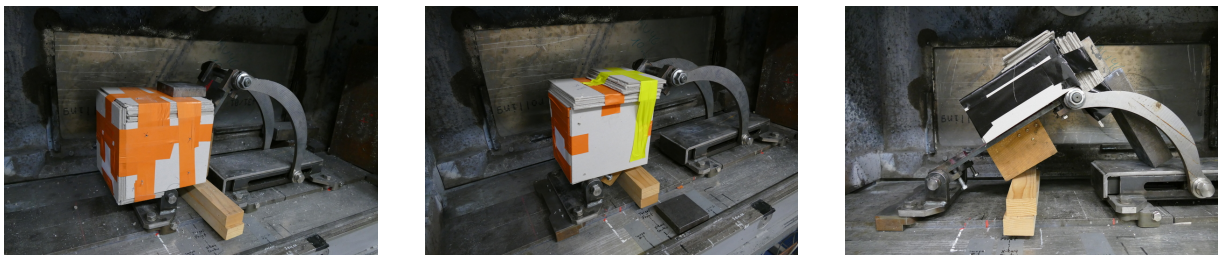

A 30° **B** 45° **C** 60°

FIGURE 5.5 Experimental fragment detection: The images show the shape of card-boxes installed to catch the fragments depending on the obliquity of the shot.

cardboard was placed all around the target plate (compare Figure 5.5). At that point, the cardboard not only served to recover the fragments but also to protect the experimental setup. For each impact angle, a different box had to be created, which was time-consuming. Furthermore, the usage of the box reduced the contrast of the image. Based on experience, the fragments stayed in the plane described by the flight axis and the vector perpendicular to the plate. This result was verified by further experiments in which Styrofoam hemispheres were placed on the target so that the entry and exit positions could be precisely determined. Therefore, in the following experiments, the cardboard was only placed where fragments were expected. This approach reduced the noise and simplified the experimental setup.

5.5 Computer-aided evaluation of FXR images of HVI-experiments (FXRIP)

Since the multi-anode X-ray has been installed recently at ISL, our experiments presented in Application III are among the first applying it. Besides standard image processing tools such as *Photoshop®* and *gimp®*, no postprocessing possibilities have been available yet. In particular, the parallax of the different images has to be eliminated in order to evaluate quantitatively physical properties from the images. While for older, horizontally arranged flashes (compare Section 5.2.1), the parallax error could be reduced to a shift of the images, a more complex algorithm has to be considered for the circular aligned flashes of the multi-anode

setup. Therefore, we developed a python software using the *OpenCV* image processing library [31] and a *TK* front-end. In general, the front-end is kept simple, and the user can access all options directly via one of the implemented buttons (compare Figure 5.6). The software reads in X-ray images and includes tailor-made image processing techniques. It addresses in particular, (i) noise reduction and edge detection, (ii) image alignment, and (iii) physical property extraction.

- For (i), the user can define the strength of enhancement with graphical sliders or load settings from previous experiments. The software processes the images in real-time and different settings can be applied to each image as the sensor sensitivity can change significantly in TB-experiments.
- For (ii), the user can select the reference points, and the software performs the alignment. To improve accuracy, the user can zoom into the image. These points can also be saved and reloaded from ASCII files. Saving the points increases efficiency, as the alignment only needs to be redone if the experimental setup changes. The aligned and improved images are saved in the folder of the experiment.
- For (iii), the user can select the fragments that shall be tracked. If the image quality is sufficient, the user only needs to select one point on the outline, and the algorithm detects the fragment automatically. For the selected fragments, the software computes the correct translational and rotation velocity and outputs it to an ASCII file. The curves can also be visualised in our software directly.

The implemented functionality addresses all requirements for TB experiments with regard to image processing and velocity extraction. HTML user documentation is available through the program for a complete explanation. Before the software can be applied, the experiment has to be prepared such that reference points are visible on the image details to align the images.
In the following, we explain and compare different solutions for (i), (ii) and (iii).

5.5.1 Noise reduction and edge detection

The images obtained with X-ray cinematography (compare Section 5.2.2) contain a considerable amount of noise. Our software aims to eliminate the noise and enhance the general image quality. Furthermore, we implement edge detection in order to semi-automate fragment detection. Edge detection is sensitive to noise in the image, which also demands to reduce the noise first.
This section consists of two parts: First, we discuss two different noise reduction approaches and investigates the tuning parameters. Second, it explains the edge-detection and analyses the modelling parameters.

Noise reduction of raw X-ray images

Different methods can realise denoising. We compare a Gaussian filter with a non-local means denoising proposed by Buades et al. [34]. The Gaussian filter computes the smoothed value by summing up values from pixels in a particular neighbourhood, weighted by a Gaussian function. The non-local means denoising searches for patterns or patches within a given search block around each pixel. The denoised value of the pixel is the average of all pixel values which are surrounded by the same pattern. Initially, this method has three input parameters: the strength of denoising, the size of the patch, and the size of the search block. In our software, the user only defines the strength of the noise reduction. The other two parameters are derived from the strength as proposed in [34]. Figure 5.7, compares the results of the Gaussian blur to the non-local

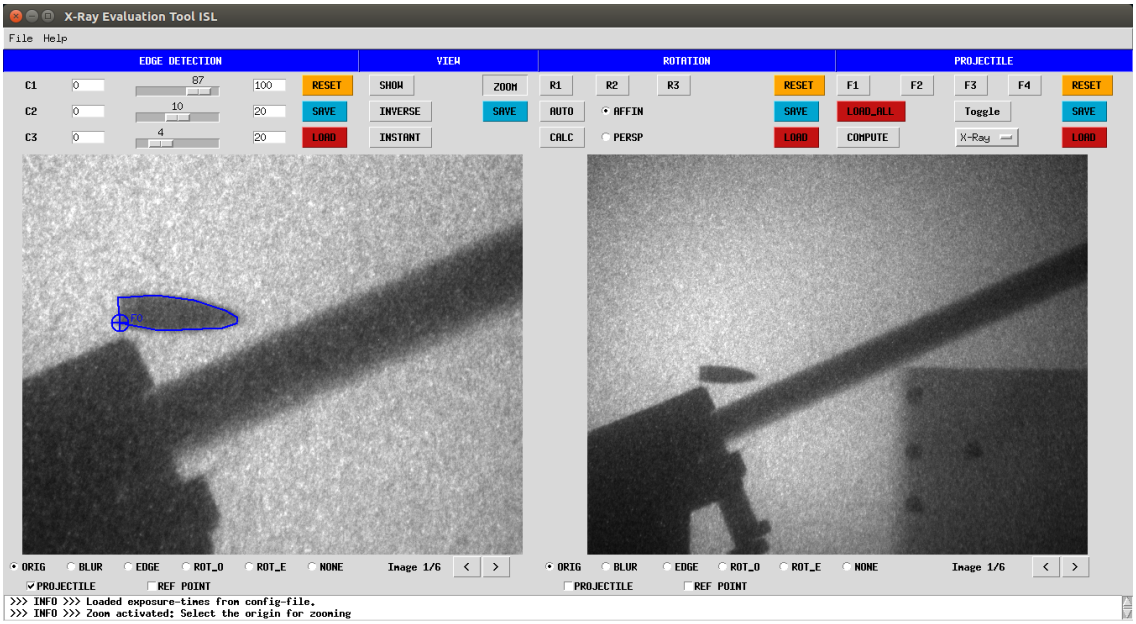

FIGURE 5.6 Screenshot of the FXRIP software. The program contains all necessary options to deal with the challenges in evaluating multi-anode X-ray images. Edge detection can be performed, and the images are aligned. If one selects the fragments, physical properties can be extracted and used for numerical validation.

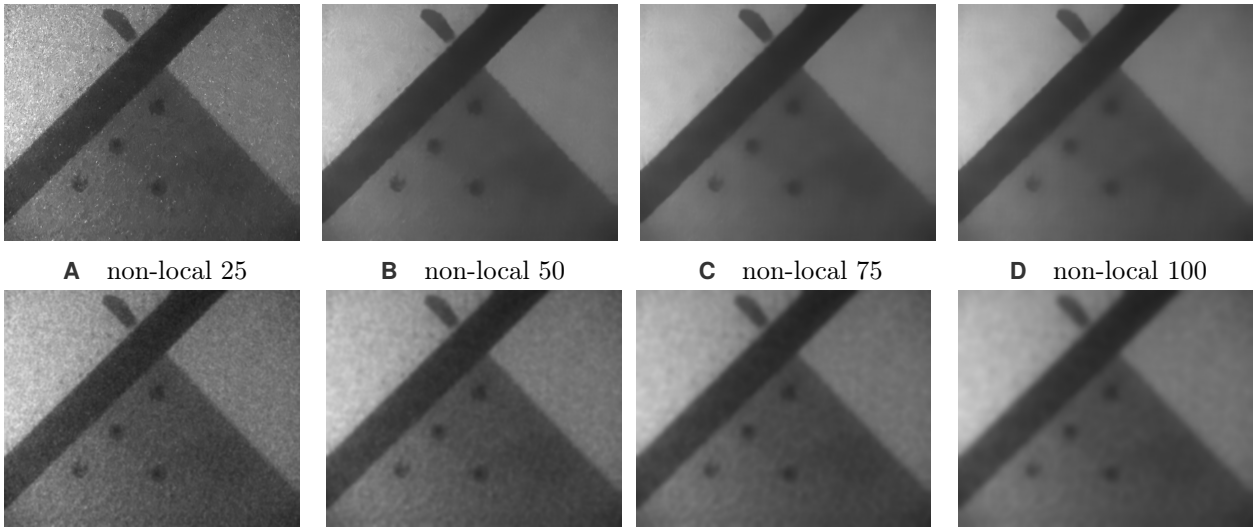

FIGURE 5.7 Non-local denoising compared to Gaussian denoising for an exemplary X-ray image (an inclined metal plate and nails determine the material density and, therefore, the brightness of the pixels).

denoising method. For the non-local method, we vary the strength between 0 and 100, and for the Gaussian blur, we change the filter size between 0 and 40 pixels using the same relative variance of the smoothing kernel. The aim is to delete the random noise, without blurring the details of the contours. The non-local method almost eliminates the noise with a noise reduction level of 50. The contour details remain visible even for the strongest denoising. The Gaussian method, on the other hand, still shows random noise patterns for the strength of 40, although the contour details are already blurred. For our application, the Gaussian filter removes too much detail from the images. Therefore, we use the non-local method in our software. If there is only one fragment, much more noise reduction can be applied than for an image with multiple and smaller fragments. The actual choice for the denoising strength has to be chosen case-specific.

Canny edge detection for fragment identification

Regarding edge-detection, we apply the Canny edge detection algorithm [36] which is implemented in the *OpenCV* library [31]. This algorithm processes four steps: (i) noise reduction, (ii) determining the intensity gradient of the image, (iii) non-maximum suppression, and (iv) hysteresis thresholding.

(i) In the first step, a Gaussian blur with a strength of five is applied. This step affects our image only very little as we already reduced the noise.

(ii) The second step filters the image with a Sobel kernel[1] in both directions that calculates the first derivative to determine the edge gradient.

(iii) Step three scans the entire image for pixels that are local maxima in the direction of the gradient. This step already provides a binary image which contains an image with "thin edges".

(iv) The final image is calculated with the threshold values c_1 and c_2. These values define which edges are relevant and which are not. All edges which have a gradient norm larger than c_2 are so-called "sure edges". Edges with a gradient norm above c_1 are only added to the relevant edges if they are connected to a sure edge. The larger c_1 and c_2 are, the fewer details are captured with the edge detection.

Figure 5.8 compares different values for c_1 and c_2 for an exemplary X-ray image which is denoised with non-local = 50 (compare previous paragraph). The function flips c_1 and c_2, if c_1 is larger than c_2. This flip results in symmetric behaviour for some image pairs (e.g., the couple 30-10 and 10-30 are the same). We still present the images twice for completeness of the image grid.
In the following, we aim to determine an appropriate choice for c_1 and c_2 from this image grid. First, we analyse the influence of c_1 exemplarily in the third column. A few details which were visible in **C** are gone in **O**. However, in general, the influence of c_1 is negligible. On the other hand, the choice of c_2 has a large impact. Comparing images **E**–**H** in row two, we observe that each increase of c_2 reduces the number of detected edges significantly. Therefore, regarding our software, we use only c_2 as a user defined parameter and define $c_1 = 0.5\ c_2$. Figure 5.9 shows the edge detection only for c_2 between 0 and 100 and the respective c_1. For $20 \leq c_2 \leq 50$, the largest fragments are well distinguishable, and not many unnecessary edges are detected. For $c_2 > 50$, smaller fragments are not detected any more and for $c_2 < 20$, many obsolete edges are classified as relevant edges. Therefore, c_2 should be defined between 20 and 50.

[1] 3x3 kernel that convoluted with the image calculates approximates of the derivatives [177]

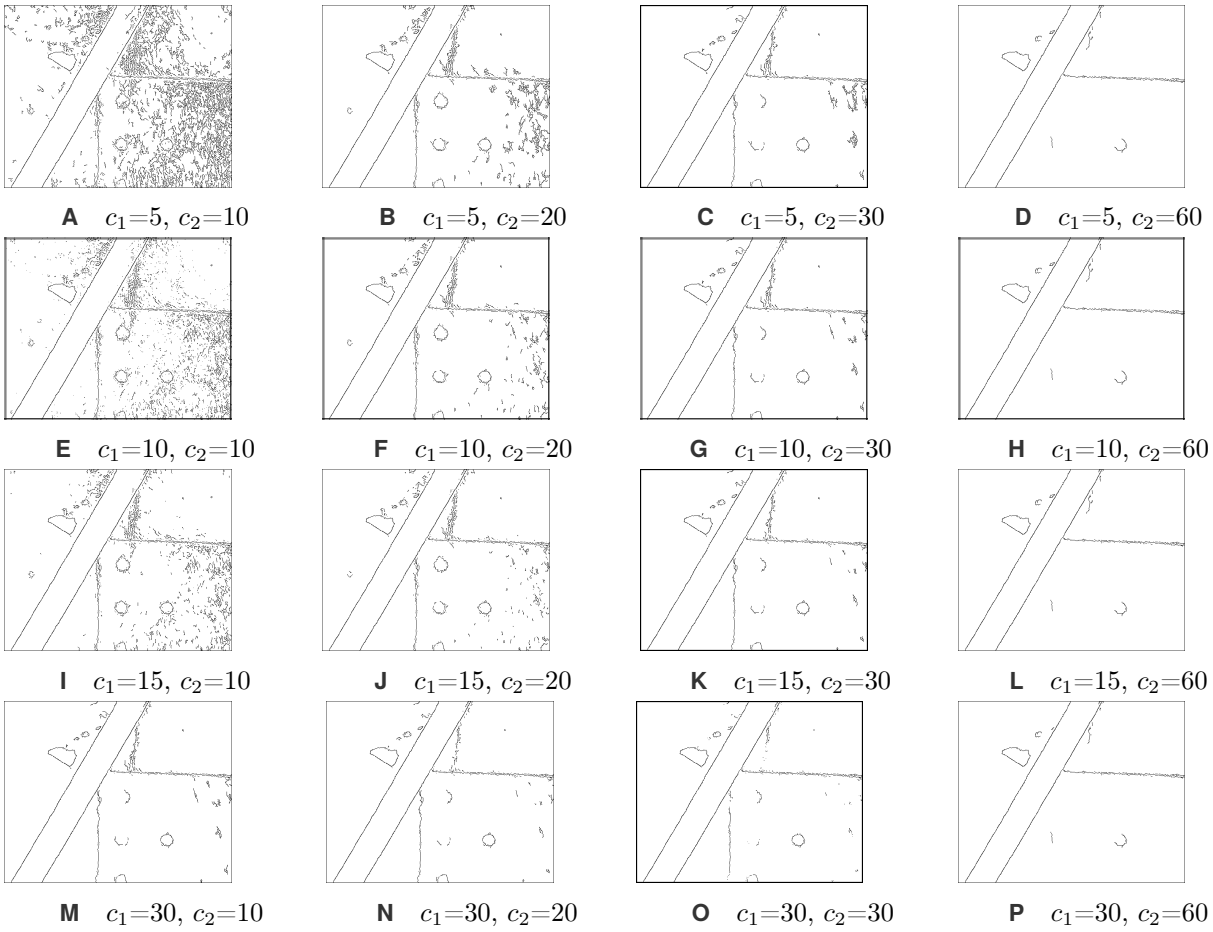

FIGURE 5.8 Canny edge detection for different parameter choices. The image has been treated with non-local noise reduction with a denoising level of 50 in a preprocessing step.

In summary, the given edge-detection is suited for our application and we found a suitable relation between c_1 and c_2 to simplify it to one parameter which can be user-defined in our software.

5.5.2 Image alignment

The images of the real-world experiments are aligned by an affine transformation that maps reference points in two images. The question that this section answers is how inaccuracy in determining the reference points affects the solution. Therefore, we first give a motivation why we need image alignment. Then, we describe the affine transformation. Next, we explain how the uncertainty quantification is calculated and conclude whether or not the error is acceptable.

The image alignment is required for two purposes: First, the real dynamics of the experiment are not recognisable before the images are correctly aligned. Second, it is a central part of correctly estimating the physical properties of interest from the X-ray images (described in Section 5.5.3). The images are aligned with the aid of reference points. Two fundamental transformations can do the alignment. An affine transformation requires three reference points, and a perspective transform requires four of them. A perspective transform is

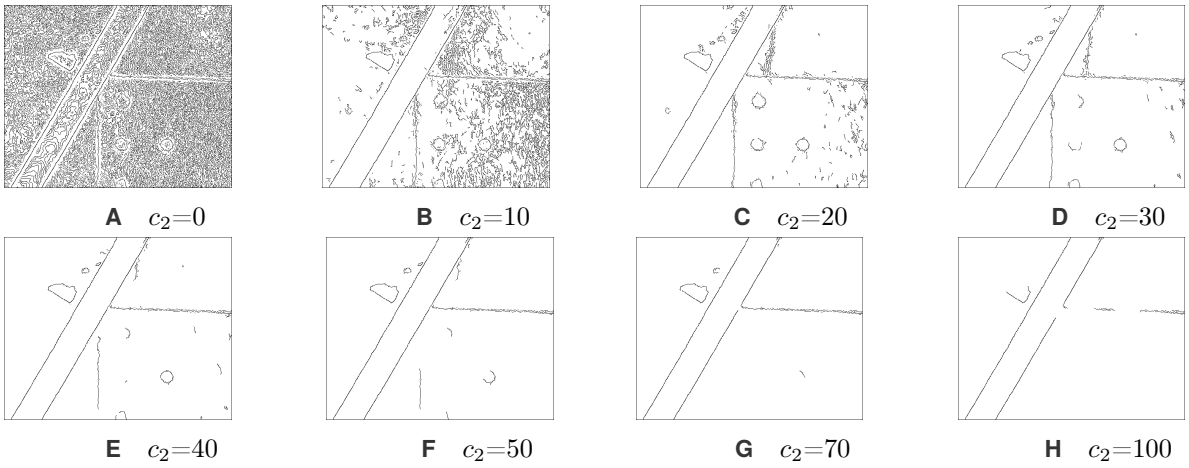

FIGURE 5.9 Canny edge detection results as a function of c_2 and $c_1 = 0.5\ c_2$—like it is implemented in FXRIP. c_2 should be selected between 20 and 50.

only needed if the image was captured non-perpendicular. Since this is not the case for the X-ray setup used in this work, we focus on the affine transform in the following.

An affine transformation is a linear transformation (rotation and scaling) which is expressed by a matrix multiplication and a translation which is vector addition. The position of transformed points $\boldsymbol{x}'$ is described with the algebraic equation

$$\boldsymbol{x}' = \boldsymbol{A}\boldsymbol{x} + \boldsymbol{B}, \tag{5.5.1}$$

where $\boldsymbol{x}$ are the original positions, $\boldsymbol{A}$ is the 2×2 transformation matrix and $\boldsymbol{B}$ is the translation vector. The six unknown coefficients of $\boldsymbol{A}$ and $\boldsymbol{B}$ are described by the linear system of equations resulting from the three reference points where (5.5.1) is satisfied. The user selects the reference points for the affine transformation. Due to noise and an imprecise selection, the chosen points are inaccurate. Therefore, the transformation matrices, which are based on these points ($\tilde{\boldsymbol{A}}$ and $\tilde{\boldsymbol{B}}$), are inaccurate as well, and so are the transformed pixels

$$\tilde{\boldsymbol{x}}' = \tilde{\boldsymbol{A}}\boldsymbol{x} + \tilde{\boldsymbol{B}}. \tag{5.5.2}$$

The alignment error ε of each pixel x is defined as

$$\varepsilon(\boldsymbol{x}) = ||\tilde{\boldsymbol{x}}' - \boldsymbol{x}'||. \tag{5.5.3}$$

The estimation of the alignement error is not trivial as we do not know the true positions. Therefore, we suggest the following simplification: Figure 5.10 visualizes how the affine transformation can be decomposed to simplify the analysis: In principle, image I and image II have to be aligned. If we could determine the reference points of both images exactly, we can calculate the "perfect alignment". This is only a theoretical intermediate state as we can not select the points in both images exactly. In reality, there is a difference between the selected reference points resulting in the "actual alignment". The goal of this study is to quantify the error (5.5.3) between "actual alignment" and "perfect alignment" (image II and image II distorted), but this is not possible. Instead, we compute the translation of each pixel for the "mismatch alignment". This transformation is the affine transformation from the exact reference points in image II (which we can define)

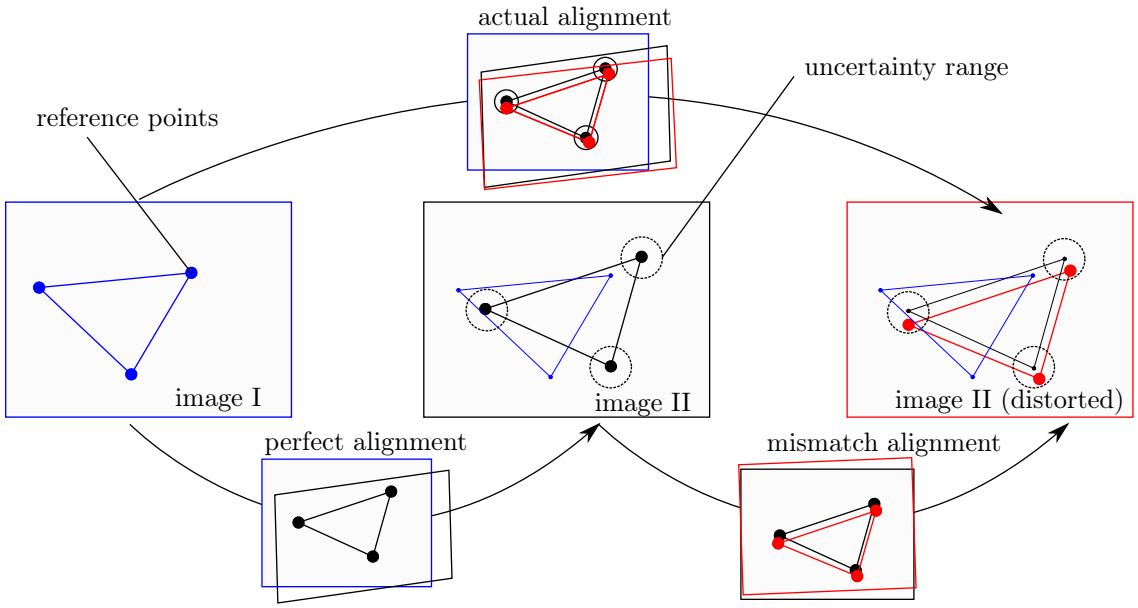

FIGURE 5.10 Image alignment: Quantification of the effect of inaccurate reference point selection on the image alignment results: Decomposition of "actual alignment" in "perfect alignment" and "mismatch alignment". In our uncertainty quantification we limit ourself to the "mismatch alignment".

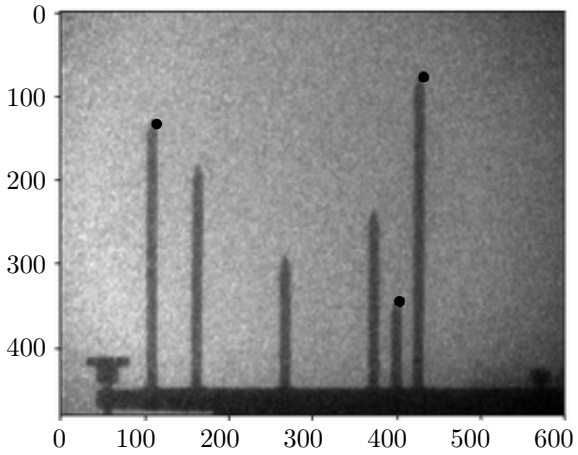

FIGURE 5.11 Image alignment: X-ray image which is used for alignment with the corresponding reference points highlighted in black. The three points which inscribe the largest area are supposed to give the most accurate transformation.

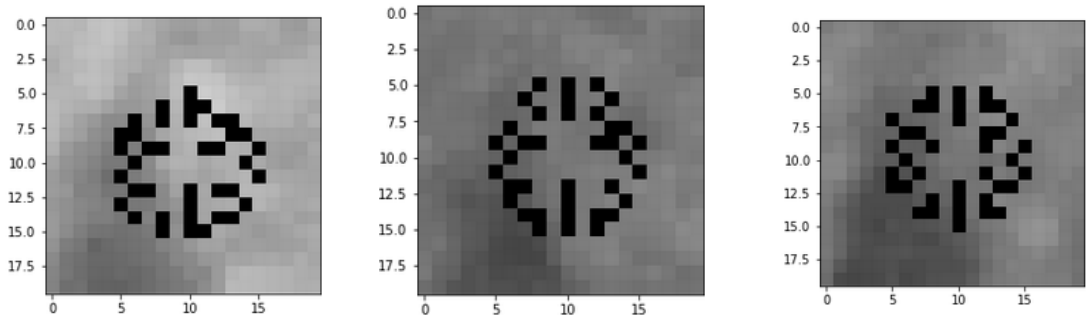

FIGURE 5.12 Image alignment: For each alignment-point, 40 points in a local neighbourhood are used to estimate the uncertainty during the point selection process.

to distorted reference points in image II (which we can define based on our defined exact points). Due to the linearity of the affine transformation, this modified analysis is equivalent to the original one.

For our study, we (i) select randomly disturbed reference points, (ii) apply the affine transformation to all pixels in image II from the correct reference points (black) to the distorted reference points (red), (iii) compute the difference between the disturbed and the original position for each pixel, and (iv) repeat this for a sufficient number of samples to estimate the statistical error properties for each pixel.

By experience, we assume that the accuracy of the point selection for (i) is less or equal to five pixels. Figure 5.12 shows the selection of reference points in the surrounding of five pixels that are used for this analysis. These points are picked randomly without any statistical assumptions about the probability density. To be as close to the application as possible, we use an X-ray image from our experiments for the analysis, which contains several marker points (Figure 5.11). Since the result is highly depending on the choice of reference points, we choose them such that the inscribed area of the three points is as large as possible. This choice should give the smallest errors.

In the following comparison, we investigate the error during the affine transformation of pixels due to an inaccurate selection of the reference points. In a first comparison (see Figure 5.13A), we analyse the influence of each reference point individually and in the second comparison (see Figure 5.13B), we investigate the results from the different combinations (of distorting all reference points at once). All values in the following analysis are given in pixels. In 5.13A, we observe, as expected, that the error is zero on the line defined by the two undisturbed reference points. In normal direction to this line, the error increases linearly. The last plot in 5.13A is a superposition of the values from the three points, resulting in an upper bound for the mean error. Figure 5.13B is the more realistic approach, as all combinations of distorted reference points are tested. Due to a large number of combinations, the resolution is reduced compared to 5.13A. In the plots of Figure 5.13B, we present the mean error, the standard deviation and the maximum error. For the mean error, we observe that the minimum is precisely the maximum distortion of the reference point (5 pixels). In the area of interest, the mean value is less than seven pixels with a standard deviation of about three pixels. These values indicate that the error in average scales with a factor between one and two regarding the selection uncertainty of five pixels. In terms of maximum error, not significantly more than three times the user uncertainty (15 pixels) is observed in the relevant region. Outside the triangle described by the reference points a more significant error can occur, both in mean (10 pixels) and maximum error (24 pixels).

In conclusion, the inaccuracy in point selection is feasible regarding the resulting error for the aligned pixels. In particular, in the inscribed triangle of the three reference points the error is small. This is exactly

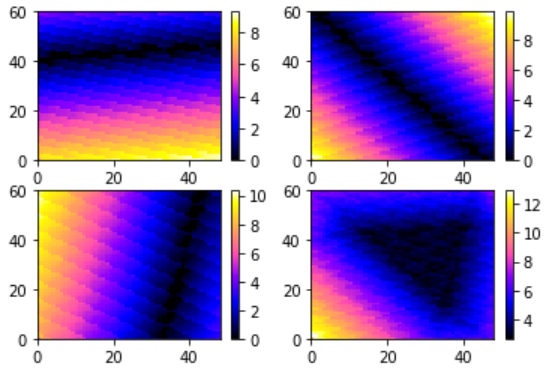

A mean error if only one alignment point is changed (1-3) and superposition of the error in (4)

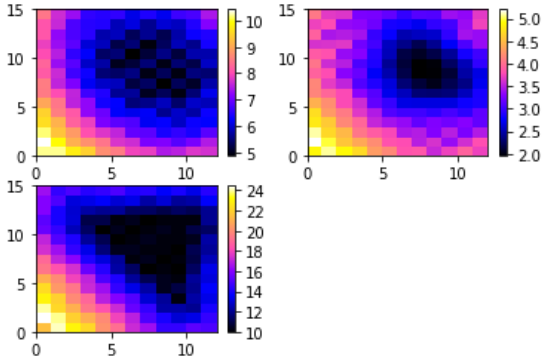

B (1) mean error, (2) standard deviation, (3) max error, for combinations using a subset of 12×15 points

FIGURE 5.13 Quantification of image alignment error in terms of accuracy of the chosen reference points. Each plot shows the mismatch error of each pixel position. In **A**, 50×60 pixels are observed and in **B**, 12×15 pixels are included in the analysis. In total, 64,000 combinations are investigated and for the proposed position of alignment points the error does not amplify significantly in the region of interest.

where it is relevant for the extraction of physical properties from fragments, described in the next section.

5.5.3 Extraction of physical properties

In the last two sections, we detected the fragments and aligned the X-ray images. The last step to track the fragments is the extraction of the motion based on subsequent images. This section describes how the fragment motion can be tracked. It first gives a brief motivation and a general illustration of motion tracking. Then it describes error norms which are essential for the analysis and proposes two classes of algorithms and variants of it. Finally, it compares them regarding run time and accuracy.

In terms of motion tracking, we aim to determine the translational and rotation velocity. These values are a central component in the quantitative comparison of the real-world experiments with numerical simulations. The translational velocity is proportional to the distance between the positions of the centre of the area ($\boldsymbol{x}_0$) of each fragment in two subsequent images divided by the interframe time. Extracting the rotation of an object from two images is not as straight forward as the object can change its shape due to off-axis rotation. In the following, the object is denoted as A in the first time step and B in the second time step. In principle, we match them by first applying a translational correction mapping to $\bar{B}$ and then a rotation correction mapping $\tilde{B}$ (see Figure 5.14). The latter step reveals an approximate for the rotation angle. The image of the fragment is defined by a set of points on the fragment outline, i.e., a polygon can describe the outline mathematically. We suggest two algorithms to compute the rotation angle. The first algorithm is called point matching algorithm (PMA) and minimises the distance between points on the outline of A and $\tilde{B}$. The second algorithm minimises the distance between points of A and the polygon outline of $\tilde{B}$ (nearest neighbour algorithm). We suggest three different methods to minimise the distance between A and $\tilde{B}$ in the second algorithm. Therefore, we compare four different approaches in total.

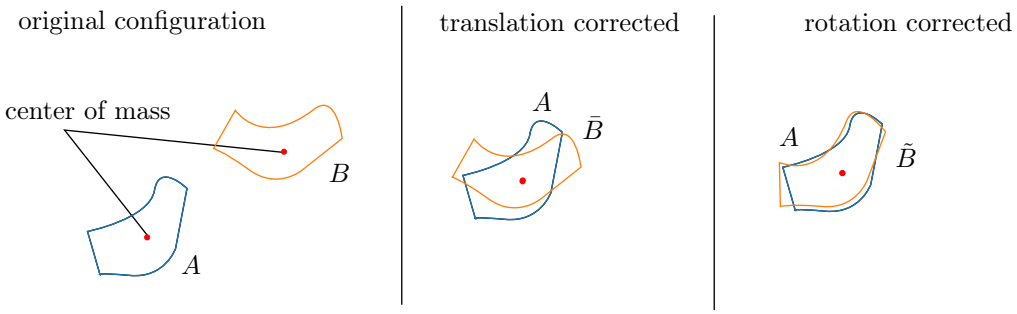

FIGURE 5.14 Extraction of physical properties: Illustration of fragment A and B in original position, translation corrected ($\bar{B}$), and translation and rotation corrected ($\tilde{B}$).

Error estimation for the fragment tracking

We define three error estimates for this application: (i) a matching error ε_m, (ii) an approximation error ε_a, and (iii) a discretisation error ε_d.
The algorithms minimise error (i), which is defined differently for both algorithms and measures the differences between A and $\tilde{B}$. In general, it can be described as

$$\varepsilon_m = \sum_{j=1}^{N} \frac{||A_j - \tilde{B}_j||}{N}\,, \tag{5.5.4}$$

where A_j and $\tilde{B}_j$ are the positions of point j on the outline of A and $\tilde{B}$, respectively. For the PMA, $\tilde{B}_j$ is the coordinate of the point geometrically corresponding to A_j, and for the nearest neighbour algorithm, it is the point which is closest to A_j on the outline of $\tilde{B}$. The (ii) error

$$\varepsilon_a = |\varphi - \varphi_{\text{actual}}| \tag{5.5.5}$$

is the difference between the angle φ estimated with the algorithm compared to the actual angle φ_{actual}. The latter is only known for the validation data of the numerical simulation and is unknown for the real-world experiments. This error determines the accuracy of the algorithm. The (iii) error

$$\varepsilon_d(N) = |\varphi(N) - \lim_{n\to\infty} \varphi(n)| \tag{5.5.6}$$

describes the error of the solution for a finite discretisation N compared to a converged solution. We use a fine discretisation to approximate the converged solution as the run time of the matching algorithm is small enough to achieve a negligible discretisation error. (5.5.4) requires point pairs A_j and $\tilde{B}_j$. We describe the algorithms to generate those in the following: (i) the point matching algorithm and (ii) the nearest neighbour algorithm.

Point matching algorithm (PMA)

The idea of our point matching algorithm is that there exists a bijection of points $\boldsymbol{x}$ describing the outline of the fragment in each corresponding image pair. The input for the algorithm is a set of points on the outline. These points have to be in rotational order but can start from different positions, and the distance can vary

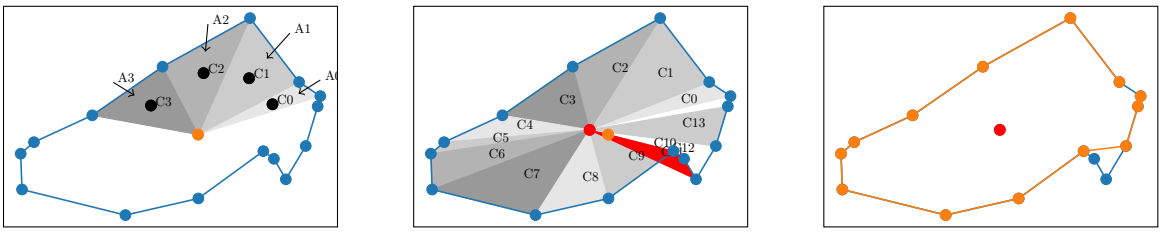

A calculate A and c **B** simplification **C** simplified polygon

FIGURE 5.15 Step 1 of our point matching algorithm for two subsequent images of a fragment: **A** An initial triangulation C_i is generated using the original points at the outline of the fragment and the centroid of these points; **B** the new center (red) is calculated as mean of the centers of the triangulation C_i and the triangulation is updated accordingly; **C** all nodes with negative corresponding triangle volume are removed from the discretisation. The remaining outline is a simplified star-domain (orange) approximating the original polygon (blue).

as well. The algorithm consists of three steps:

1. Simplification of the geometry of both fragments to a star-convex domain.
2. Discretisation of the outline of both fragments.
3. Determination of the rotation angle by aligning the two point sets while first applying a rotation, and second computing the error for all possible starting points.

In step 1, the outline is simplified to a star domain S with respect to the centre of the polygon $\boldsymbol{x}_0$. A star domain describes a domain, in which all points $\boldsymbol{y}$ on a connection line between any point $\boldsymbol{x} \in S$ and $\boldsymbol{x}_0$ are also in S

$$\forall \boldsymbol{x} \in S \;\Rightarrow\; \boldsymbol{y} = c\,(\boldsymbol{x} - \boldsymbol{x}_0) \;\in S \quad \forall c \in (0;1]. \tag{5.5.7}$$

This does not only simplify and accelerate the algorithm but also enhances the quality of the estimation as the material points can be better distributed. Figure 5.15 illustrates the three steps to determine a star-convex domain. In 5.15A, the centroid of points is computed and used to set up an initial triangulation. With this triangulation the center of area $\boldsymbol{x}_0$ is defined as the area-weighted centroid of all triangle centres $\boldsymbol{c}_i$:

$$\boldsymbol{x}_0 = \frac{1}{A} \sum_i \boldsymbol{c}_i A_i, \tag{5.5.8}$$

where A_i is the area of each triangle i. An alternative to the described approach is using the *polygon* class from the *sympy* package[2] to compute $\boldsymbol{x}_0$. In terms of performance, our lean implementation, not using *sympy* is superior and consequently used. In 5.15B a new triangulation is set up with respect to $\boldsymbol{x}_0$. All nodes where the adjacent triangle has a negative orientation do not satisfy the criterion (5.5.7). The corresponding nodes on the fragment outline are removed resulting in the desired star convex domain 5.15C.

In step 2, the outline of the fragment is re-discretised. The criterion for the discretisation is the equality of the areas of the triangles in the respective new triangulation. The following paragraph elaborates on how to realise such an area-weighted discretisation. The idea is that the inscribed area of $\boldsymbol{x}_0$ and the outline between

[2] `https://docs.sympy.org/latest/modules/geometry/polygons.html`

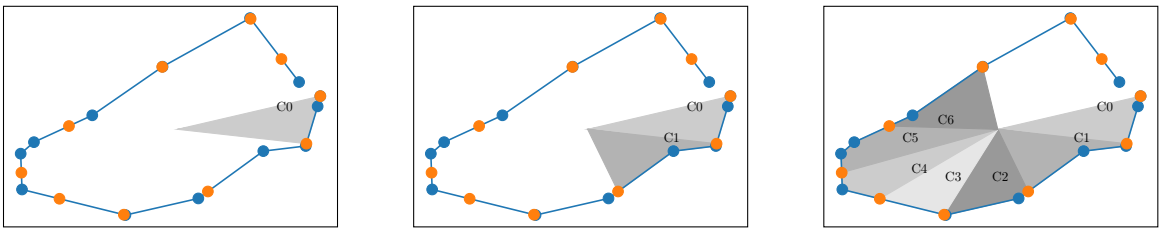

A first triangle **B** second triangle **C** further iteration

FIGURE 5.16 Step 2 of our point matching algorithm computes the point pairs for our point matching algorithm: The points on the outline (orange) are distributed on the polygon (blue) such that the inscribed area of each triangle (shades of grey) is constant. Small resolution ($N = 10$) for visualization.

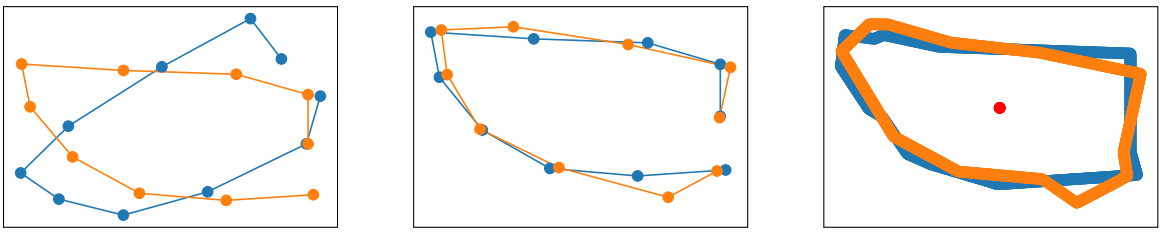

original orientation **A** coarse fit **B** fine fit

FIGURE 5.17 Step 3 of our point matching algorithm computing the rotation speed: The Kabsch algorithm computes the optimal rotation angle to fit the two point sets (orange and blue). We compare **A** a discretisation with 10 points and **B** a discretisation with 1000 points.

two adjacent discretisation points is constant in the whole fragment. Figure 5.16 depicts this process. First, the algorithm computes the target area from the total fragment area and the predefined number of triangles. Then, given a start point, the next discretisation point is chosen such that the inscribed area matches the target area. The algorithm processes all discretisation points in this way. The resolution of this discretisation is not necessarily higher than the original resolution. However, a higher resolution describes more features and might be superior in terms of accuracy.

In step 3, this discretisation is used with the Kabsch algorithm [108][3] to compute the optimal rotation angle. Since it is not clear a priori which points of A and $\tilde{B}$ coincide, our algorithm considers all possibilities and chooses the one with the smallest error. The proposed distribution of nodes on the outline guarantees that the centroid of the nodes and the centre of the polygon are identical. Thus, the distribution fulfills the requirement of the Kabsch algorithm.

In the following, we are looking at the results for a different number of discretisation points ($3-1000$), first, qualitatively in Figure 5.17, and then quantitatively in Figure 5.18. Figure 5.17 depicts the fit between the blue and orange polygon. The coarse fit uses only 10 points, and the fine fit uses 1000 points in the discretisation. The coarse fit already shows a good match and little difference compared to the fine discretisation. Figure 5.18 investigates the results obtained with the Kabsch algorithm quantitatively. In Figure 5.18A, we present the error as a function of the starting point with a resolution of 1000 points. In terms of the matching error (5.5.4), two local minima exist. This fact is due to the symmetric shape of the geometry. However, as long as

[3] `https://github.com/charnley/rmsd`

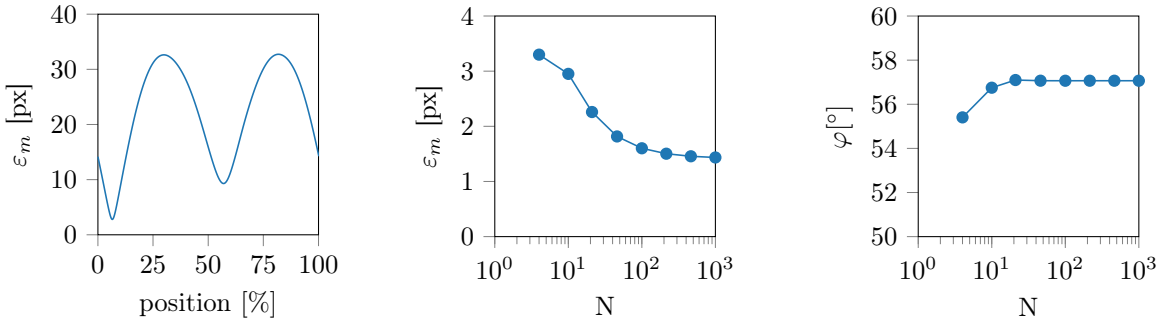

A error starting point **B** Kabsch error **C** rotation angle

FIGURE 5.18 Step 2 and 3 of our point matching algorithm computing the rotation speed for the geometry in Figure 5.17. ε_m is the matching error according to (5.18A) in pixels. Investigation of the approximation error as a function of starting points **A** and number of discretisation points **B**. **C** shows the corresponding angle to **B**.

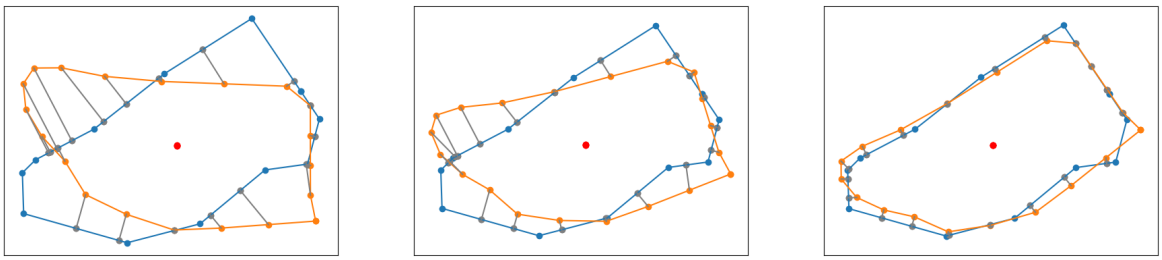

A original orientation **B** angle #1 **C** angle #2

FIGURE 5.19 Explanation of the error estimation of the nearest neighbour algorithm. The length of the grey connection lines between the two images quantify the matching error.

distinct nonsymmetric features exist, the algorithm predicts the correct rotation. Otherwise, we can exclude the second solution as only one of them is physically correct. Figure 5.18B investigates the matching error for different discretisations of the geometry. The error is discretisation dependent, and the rotation angle converges (see Figure 5.18C). The estimated angle itself changes only little when the discretisation has more than ten points. More complex geometries might require more discretisation points.

Nearest-Neighbour Algorithm (NNA)

The major drawback of the PMA is the treatment of geometry changes from one time step to the other. This change of geometry is mainly due to the rotation of the fragment in 3D space. In case of such change, the corresponding points do not match any more, and the algorithm predicts a different rotation angle. We propose a more robust algorithm based on the nearest-neighbour approach, which minimises the symmetric difference between both areas (compare Figure 5.19). In other words, the algorithm maximises the overlapping area of the two polygons. This algorithm consists of three steps:

1. Simplification of the geometry of both fragments to a star-convex domain.

2. Discretisation of the fragment of $\tilde{B}$ with points similar to the point matching algorithm, and determination

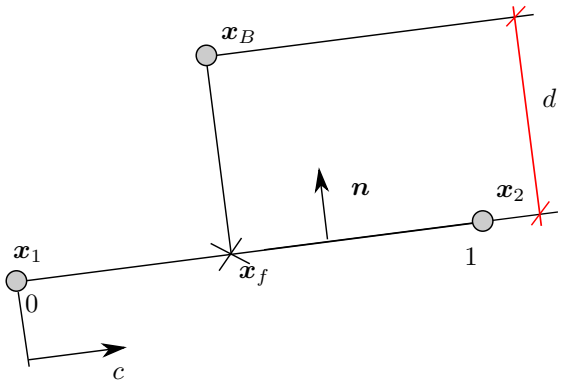

FIGURE 5.20 Determination of the distance d between point $\boldsymbol{x}_b$ to edge $\boldsymbol{x}_1$-$\boldsymbol{x}_2$ and x_f denotes the foot point and $\boldsymbol{n}$ is normal to $\boldsymbol{x}_1$-$\boldsymbol{x}_2$.

of the star-convex polygon for A.

3. Determination of the correct angle while calculating the matching-error for different angles (three variants):

   (a) Uniform bracket minimum search: Calculation of the matching error for a finite number of angles and determination of the angle with the smallest error.

   (b) Newton-Raphson: Selection of a starting angle (e.g., 0°) and iterative calculation of the next angle based on the Newton algorithm minimising the matching error.

   (c) Newton-Raphson+: Usage of foreknowledge about the starting angle (e.g., the angle of the last computation or the result of a coarse bracket minimum search estimation).

The crucial part for the matching error estimation in this algorithm is to determine the distance d between a polygon and a point $\boldsymbol{x}_B$ efficiently. The problem can be simplified to the search of the minimum distance between every edge of the polygon and the point (illustrated in Figure 5.20). Starting with the definition of the foot point $\boldsymbol{x}_f$ of a point $\boldsymbol{x}_b$ on a straight line through the points $\boldsymbol{x}_1$ and $\boldsymbol{x}_2$, where

$$\boldsymbol{x}_b = \boldsymbol{x}_f + \boldsymbol{n}d = \boldsymbol{x}_1 + c\,(\boldsymbol{x}_2 - \boldsymbol{x}_1) + \boldsymbol{n}d \tag{5.5.9}$$

with $c, d \in \mathbb{R}$, $\boldsymbol{n} \perp \boldsymbol{x_2} - \boldsymbol{x_1}$, and $||\boldsymbol{n}|| = 1$. This constitutes a linear system for c and d. d is the required distance between the line and the point $\boldsymbol{x}_b$. If $0 \leq c \leq 1$ the foot of the perpendicular is on the line and the distance is $|d|$, otherwise the distance is $\min\left(||\boldsymbol{x}_b - \boldsymbol{x}_1||, ||\boldsymbol{x}_b - \boldsymbol{x}_2||\right)$. Without further modification, each point $\boldsymbol{x}_b$ on $\tilde{B}$ has to be compared with all edges. Then, the computational effort is scaling with the number of points in A times the number of nodes of the polygon B. Aiming for fast performance, we compute the distance to all edges only for the first point. For all other points, it is then sufficient to calculate the distance only to the next edges in each direction, starting from the closest edge of the last point. This simplification creates no additional error if the point discretisation is at least as fine as the smallest edge length of the polygon. For robustness three edges in each direction are considered instead of one. In terms of run time, this is still advantageous to comparing every node $\boldsymbol{x}_b$ with all edges.

(a) Uniform bracket minimum search (BMS)

There is no a priori knowledge of whether the matching error ε_m (5.5.4) has a local minimum and, therefore, whether an iterative algorithm can be applied. Instead of such an algorithm, we first implement a uniform bracket minimum search without hierarchical refinement using a finite number of linearly distributed angles with $\varphi_i = \varphi_{beg} + id\varphi, \quad d\varphi = (\varphi_{end} - \varphi_{beg})/(N-1)$. The precision of the approximation is then $d\varphi$ or, for assuming that in a local neighbourhood the function is linear, it is $d\varphi/2$. We aim to keep the approximation uncertainty as low as possible (e.g., $d\varphi = 0.4°$) such that it plays no role in the overall uncertainty quantification. The rotation angles that we investigate are between $-180° \leq \varphi \leq 180°$, as otherwise, the result is not unique any more. In general, we observe angles between 0° and 45° for our experiment. For the desired approximation uncertainty, this means that 450 function evaluations for ε_m are required, in total.

(b) Newton-Raphson iterative solver (NR)

The Newton-Raphson algorithm is a well-known approach for finding the zero point of a function and has quadratic convergence. However, it is only locally convergent, which means that the starting point has to be chosen carefully. Finding the minimum of the error function is similar to finding the zero point of $d\varepsilon_m/d\varphi$ with the constraint $d^2\varepsilon_m/d\varphi^2 > 0$. The algorithm requires a starting point $\boldsymbol{x}_0$ and then calculates the next position recursively

$$x_{n+1} = x_n - c\frac{f(x_n)}{f'(x_n)}\,. \tag{5.5.10}$$

In our case $x = \varphi$, $f = d\varepsilon_m/d\varphi$ and $f' = d^2\varepsilon_m/d\varphi^2$. Additionally, we use a relaxation factor of $c = 0.5$ for more robustness. The numerical description of the first and second derivative is implemented with standard central differences,

$$\varepsilon'_m(x_n) = \frac{\varepsilon_m(x_n+\delta) - \varepsilon_m(x_n-\delta)}{2\delta}, \quad \varepsilon''_m(x_n) = \frac{\varepsilon_m(x_n+\delta) - 2\,\varepsilon_m(x_n) + \varepsilon_m(x_n-\delta)}{\delta^2}, \tag{5.5.11}$$

and requires three function evaluations for each iteration. To avoid finding a maximum instead of a minimum, we set $c := -1/c$ if the second derivative is negative to go back in the direction of the minimum. The numerical parameter δ, to determine the numerical derivative, is set to 0.05 for accurate but robust results. Since five iterations are sufficient for obtaining the same accuracy as the first algorithm, fifteen function evaluations are required in total, and the method is thirty times faster in the end. Due to the fast convergence, we do not consider other approaches such as multigrid methods.

Since the Newton-Raphson algorithm is only locally convergent, we implemented two options for estimating the starting point (in the following abbreviated with NR+). The first one assumes that the rotation velocity changes slowly and takes the last rotation angle as a starting point. The second one is more general and applies the bracket method with a very coarse resolution for a first guess, and then, starts the iterative approach with the guess as starting value.

Validation with the numerical test case

In this paragraph, the performance and accuracy of the algorithms are investigated in two tests: first, the postprocessing images of a numerical experiment; second, the X-ray images of a real-world experiment. The tests represent a typical TB-application, which will be presented as Application III and contains a small-calibre

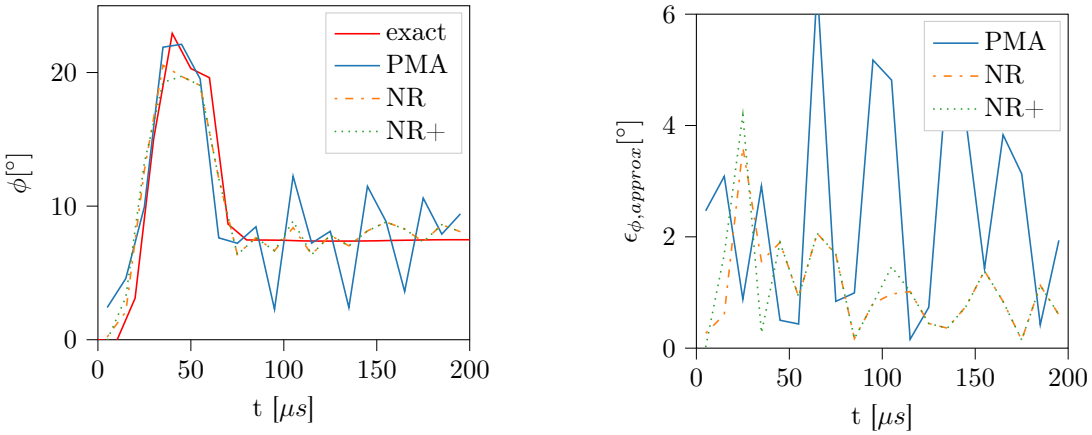

A approximation rotation angle

B absolute difference in rotation angle

FIGURE 5.21 Comparison of approximation quality for PMA, NR and NR+: **A** rotation angle over simulation time and **B** difference between exact solution and approximation over simulation time.

surrogate that impacts a metal plate. The surrogate impacts with a velocity of 800 m/s on a target plate under an oblique angle of 60°.

In this first test, we trace the largest fragment for 200 μs and apply the algorithm to images of the fragment that were extracted from the simulation. The software reads the outline of these fragments automatically to exclude uncertainty due to human interaction. The computed rotation angle is then compared to data which is directly extracted from the simulation output. Figure 5.21A shows the approximation of the rotation angle φ for all time steps (e.g., all image pairs) for a sufficiently fine discretisation of the fragment outline. Figure 5.21B depicts the corresponding approximation error. While all methods are well capable of estimating the peak rotation angle, the slow rotation of constant velocity, happening afterwards, is not captured well by the point matching algorithm. For the nearest neighbour approaches (NR, NR+), the error is fluctuating around 1°. The difference is because the algorithm assumes that the fragment is only moving in one axis and behaves like a rigid body. In reality, inner tensions in the fragment lead to temporal changes in the geometry which are not captured in 2D. Furthermore, the movement is more complex and not perfectly symmetric, initiated by small asymmetries of the FEM discretisation.

In the following, we investigate the average error of the approximation. In Figure 5.22 we look at the convergence and run time regarding the number of discretisation points on the outline N. Therefore, we discretise the outline of the fragments with 10, 30, 100 and 300 points. This method is implemented providing a graphical user interface (GUI); thus, the results should be fast computable. Figure 5.22 shows the run time and the approximation error of the different algorithms as a function of the resolution. In Figure 5.22A we investigate the average absolute error in the rotation angle as a function of N for the PMA, BMS, NR and NR+ algorithm. Only the coarsest resolution of $N = 10$ does not converge for the NR+ method. All other discretisations and algorithms are consistent. We assume that the wrong approximation is due to a too little amount of points on the outline and derive the requirement of $N > 10$. We suggest $N = 30$ to ensure a correct approximation as a further increase in the number of discretisation points does not affect the solution anymore. The nearest neighbour approaches (BMS, NR, and NR+) give more accurate results (approximately 1° of error in average), compared to the PMA (3°). On the other hand, due to simplicity, the

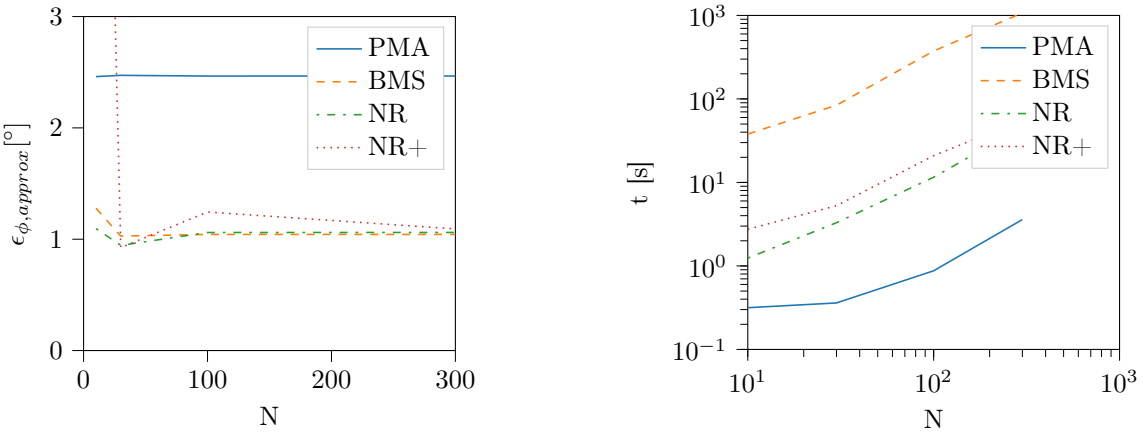

A average absolute approximation error

B run time

FIGURE 5.22 Comparison of error and run time for the different algorithms (solid line: point matching algorithm, dashed: bracket minimum search, dash-dotted: Newton-Raphson, dotted: Newton + bracket).

PMA is by far the fastest algorithm (compare Figure 5.22B). The longest run time is observed for the BMS. Both variations using the Newton-Raphson method are fast enough for the application with the required resolution of 30 points and provide better accuracy than the PMA. The computational costs increase linearly with the discretisation.

In conclusion, the nearest neighbour algorithm combined with the Newton-Raphson method and either pre-conditioning with a bracket minimum search for an appropriate starting point, or using the last computed angle is the way to be efficient and accurate. However, scenarios might exist where the Newton-Raphson method does not converge. If accuracy is not the highest priority, the point matching algorithm can be used. When the run time does not matter, the bracket-search algorithm is also a safe choice. It is crucial for the success of the algorithm that the fragments do not change too much in size and shape.

Application to a real-world example

In this second comparison, we apply the algorithm to data obtained from a real-world experiment. The X-ray images from which the data is extracted have been aligned to exclude parallax error. The user identifies the points for the outline of the fragment, and there is no ground truth we can compare the results to. So, this is a qualitative, rather than a quantitative comparison.

Figure 5.23A shows the input data for the algorithm which are obtained from the experiment. The projectile moves from left to right, hits the target, and ricochets off. The blue outlines depict the fragment at the six time steps captured during the impact. For each step, the blue line shows the fragment at time step i and the orange line the rotated fragment at time step $i + 1$. Qualitatively, no mistake of the software can be observed for the matching. In particular, for the last time step, the shape changes considerably, but the algorithm is still stable in predicting the rotation. The run time for all images is below the desired threshold of one second.

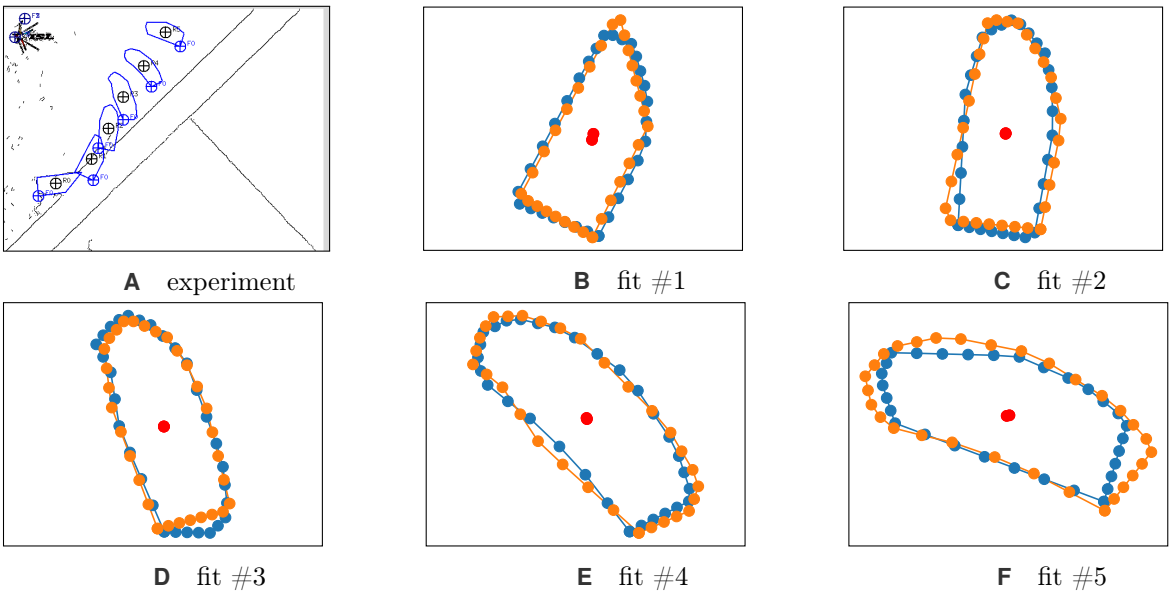

FIGURE 5.23 Impact of a surrogate against a 30° inclined plate (Application III): Result of the Newton-Raphson algorithm ($N = 30$) total run time (0.8 s) for experimental results. Each image showes the match of two consecutive images.

5.6 Conclusion

This chapter presented four different observation techniques for TB-experiments: (i) using a high-speed camera, (ii) X-ray, (iii) pendulum tests, and (iv) soft recovery of fragments. For (iii), a geometric analysis to determine yaw in the experiments is developed. For (ii), a software was implemented with which the translational and rotation velocity of fragments can be extracted from X-ray images. Regarding the software, the three main components of noise reduction, image alignment, and physical property extraction are discussed, and a suitable setup is determined. Herein, different algorithms are proposed and compared to real-world experimental data. The tests proved that our algorithms are working well for this application. The software is required to process the X-ray images presented in Application III and significantly helps during the evaluation of TB-experiments.

6

Application I: Natural fragmentation of explosively driven cylinder rings

Before looking at our main application, the high-velocity impact of a projectile, we have to understand which model best describes the fracture behaviour during highly dynamic events. Since fracture occurs only under certain circumstances during the oblique impact of a projectile, it is difficult to use these experiments as a benchmark case for evaluating fracture models. Instead, we use a tailor-made application to investigate ductile fracture in highly dynamic events. During the natural fragmentation of simple objects such as cylinder rings, spheres, and plates, we can analyse different fracture mechanisms. Moreover, the size distribution of the resulting fragments is a stable metric to compare numerical and real-world experiments. Mott [149] was one of the pioneers to investigate the natural fragmentation of cylinder rings. In particular, he proposes an exponential distribution of the size distribution. The natural fragmentation can be provoked with fast compression or expansion. This is realised by pressure forces due to explosive charges or electromagnetic forces by discharging a capacitor. In our experiments, an explosive is used due to simplicity. This approach has also been frequently used in literature to study the fracture under high strain rates for ductile material [18, 172, 223, 224, 107]. Grady and Benson, and de Vuyst et al. [75, 49] investigated the electromagnetically driven variant of expanding ring experiments. Olovsson et al. investigated electromagnetically driven ring compression [154].

The range of strain rates is comparable to what we observe in high-velocity impact, and due to simple geometries, the problem is easy to set up. From a numerical point of view, we can also investigate which model triggers tensile instabilities by deploying no fracture model. As mentioned before, there are two different approaches to initiate radial expansion. In our study, we look at the natural fragmentation of explosively driven cylinder rings. De Vuyst et al. [51] published the real-world experiments we use among with numerical results. We studied different SPH-formulations and material parameters in *LS-DYNA®* [16].

This chapter is structured as follows:

- In the experimental part, we describe the problem and derive metrics from two observation techniques (X-ray imaging and fragment collection in a water basin). Next, we use existing material testing data and suggest an approach to determine the parameters for the applied material models. Herein, we show an analytical model to determine the fragment velocity of finite cylinder rings.
- In four conclusive studies we investigate (i) different model setups (SPH formulation, uncertainty quantification of material parameters, fracture descriptions) in *LS-DYNA®*, (ii) variations we implemented in the academic code *MCM*, (iii) different plasticity and fracture models in *MCM*, and (iv) compare the final models of *LS-DYNA®*, *MCM*, and *IMPETUS®*.
- In our conclusion, we summarise the findings from this study that are relevant to our main application (Application III).

6.1 Real-world experiments

In this section, we argue which metrics are suitable to compare to the results of numerical experiments. The real-world experiments were conducted by ISL [207] and first published by De Vuyst et al. [51]. In principle, there are two difficulties: first, the number of values that can be extracted from the real-world experiments is limited. Second, the metric should be robust, repeatable, and easy to compare.

In the following, we first discuss the experimental setup, then the results of X-ray imaging and finally the fragment collection in a water basin. For X-ray imaging, we present a digression on how to estimate the fragment velocity of finite cylinder rings.

6.1.1 Setup

Our conference contribution [16] inspires the following description: In the experiments, an explosive charge (Comp B, RDX/TNT 65/35) is placed inside a hollow steel cylinder. As soon as the charge is detonated, the detonation pressure accelerates the ring in the radial direction. The ductility of the material limits the enlargement of the ring. When the material is not able to withstand the outer forces, voids start to grow, and the coalescence of them ultimately lead to fractures. The study includes cases with two different materials (grade EN 34CrNiMo6 / EN30CrNiMo8—both similar to 4340 steel), and four different height to width (h/w) aspect ratios (1:1, 2:1, 3:1, 10:1). Similar to the study by the preceding papers [51, 16], we limit ourselves to a single material and study the different aspect ratios. These aspect ratios are realized by modifying the cylinder length h and fixing the wall thickness w (compare Figure 6.1). The dimensions of the explosive are scaled such that the explosive length protruding on both sides remains constant.

For the evaluation of the experiments, two measurement methods are utilised: (i) X-ray reveals the qualitative behaviour and gives an estimate for the fragment velocity of the fastest fragment (compare Figure 6.3), (ii) a water basin is installed below the setup for recovery of the fragments (compare Figure 6.2). In the following, we first discuss the X-ray images and explain how we obtain the fragment velocity. After that, we investigate the recovered fragments and discuss how we can use the fragment statistic to evaluate the accuracy of the numerical results.

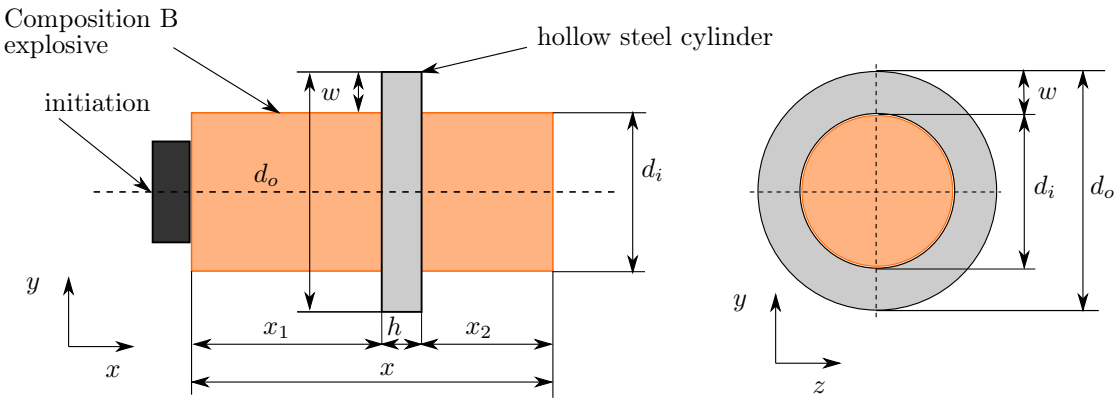

FIGURE 6.1 Charge dimensions of the experiment. Constant for all cases: The inner diameter ($d_i = 38.1$ mm), the outer diameter ($d_o = 57.2$ mm), the charge extension left ($x_1 = 45$ mm), the charge extension right ($x_2 = 32$ mm), and the wall thickness of the cylinder ($w = 9.5$ mm). (Image similar to [51])

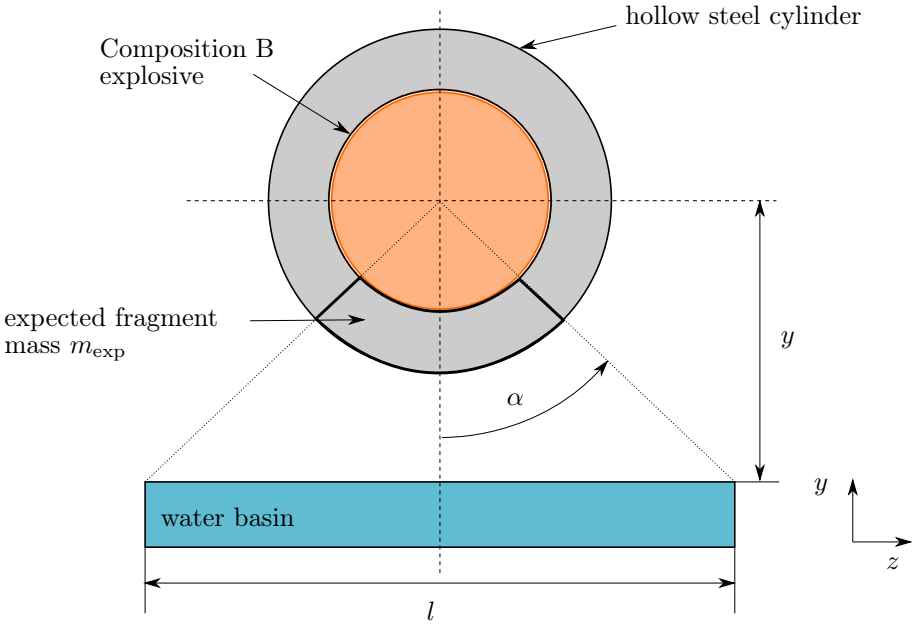

FIGURE 6.2 Charge position and fragment recovery in a water basin. The charge is placed 700 ± 20 mm above the water basin (y). The length of the basin (l) is 1200 mm. This results in an angle of $\alpha = 98 \pm 1°$, or $m_{\text{exp}} = 27.2\%\ m_{\text{cyl}}$. (Image similar to [51])

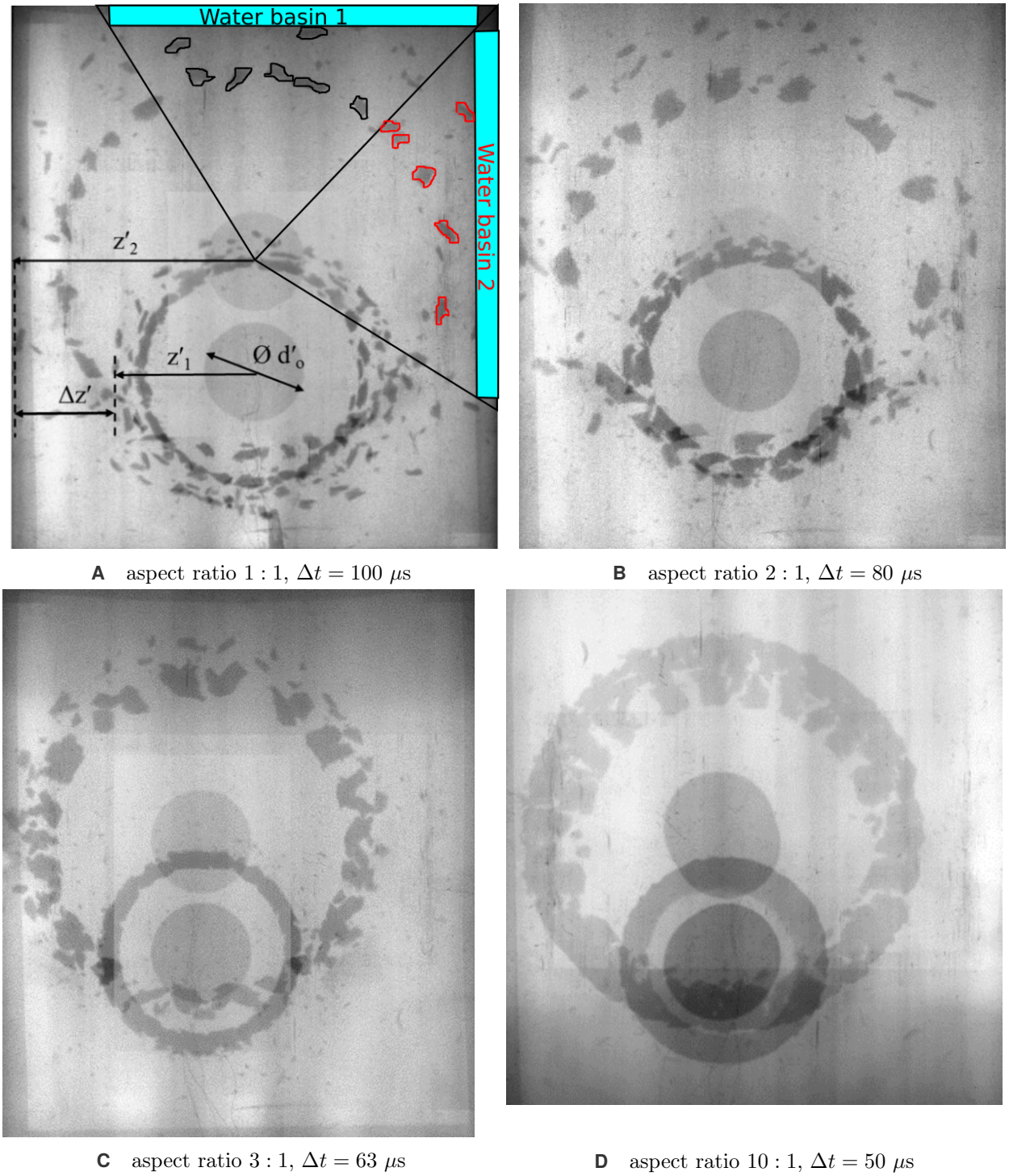

A aspect ratio $1:1$, $\Delta t = 100\ \mu$s

B aspect ratio $2:1$, $\Delta t = 80\ \mu$s

C aspect ratio $3:1$, $\Delta t = 63\ \mu$s

D aspect ratio $10:1$, $\Delta t = 50\ \mu$s

FIGURE 6.3 Double exposed X-ray images for aspect ratio 1:1 and 10:1. The exposure times are chosen to visualize the behaviour best. Images at the initial position are required to determine the fragment velocity v ($v = \Delta z/\Delta t$ and $\Delta z = \Delta z' \cdot d_o/d'_o$ and $\Delta z' = z'_2 - z'_1$) (compare **A**). The influence of a discrete fragment distribution is visualized with two imaginary water basins. (Image similar to [16])

6.1.2 X-ray imaging

Double-exposed X-ray images freeze the dynamics with a time resolution of 50 μs for (10:1), 63 μs for (3:1), 80 μs for (2:1), and 100 μs for (1:1). As described in Section 5.2.1, the two time-delayed exposures result in a single image and can neither be separated, nor aligned. The camera position is outside the cylinder in its axis (normal to the radial expansion), and the images show the two-dimensional projection of the fragments (compare Figure 6.3). For the experiments with small aspect ratios, this method creates clear images that are easy to interpret. The larger the cylinder height h is, the longer is the resulting fragment and, thus, three-dimensional effects become evident. Therefore, the interpretation of the images becomes difficult.

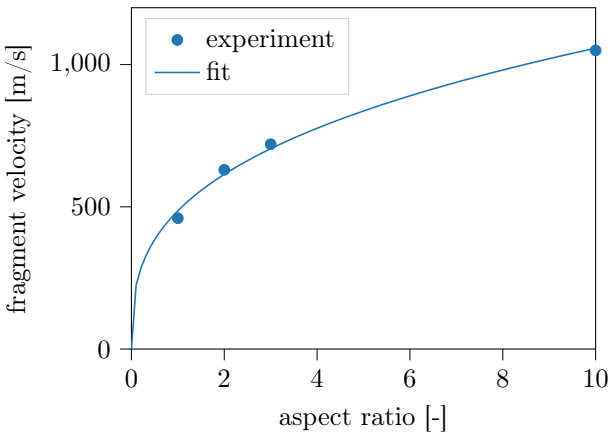

FIGURE 6.4 Upper limit for fragment velocity extracted from experiments and nonlinear fit ($f(x) = (x^{1/3})$).

In Figure 6.3A we can distinguish two separate rings of fragments: an inner ring with larger fragments and an outer ring with smaller fragments. The size and shape of the fragments are random: therefore, we must recover a considerable amount of fragments to capture a representative sample. For 10:1 (Figure 6.3D), we observe that the circumferential fracture patterns are similar to 1:1. However, not only circumferential but also axial fractures occur, according to the measured length of the recovered fragments. For 10:1, we can not clearly distinguish secondary debris as for 1:1. Based on the increased height of the fragment ring, we conclude that either extensive bending occurs or the axially aligned fragments move with different velocity. For all experiments, it is neither manually, nor with state of the art tracking methods, possible to track a single fragment from one image to the other. The fragments are rotating, appear different on the exposures, and overlap. Further development in computer vision could be able to detect corresponding fragments in the two exposures and track them. However, we can still measure the overall ring expansion that gives an estimate for the fragment velocity. Since it is most reliable to use the outermost fragments for this analysis, the estimate gives an upper limit for the fragment velocity. Figure 6.3A illustrates the approach. We use the image coordinate system in both exposures to measure the distance z_i' between the centre of the explosion and the outer boundary of the fragment ring. The difference between these two distances $\Delta z_i'$ can be converted into the real values Δz using the known outer diameter d_o of the static image. We use this procedure for all experiments and obtain the following results: Figure 6.4 shows the velocity range of fragments for different height to width ratios. The velocities range between 400 m/s and 1100 m/s. In a short digression, we derive a simplified model from estimating the fragment velocity for finite cylinder rings filled with explosive based on fundamental energy considerations.

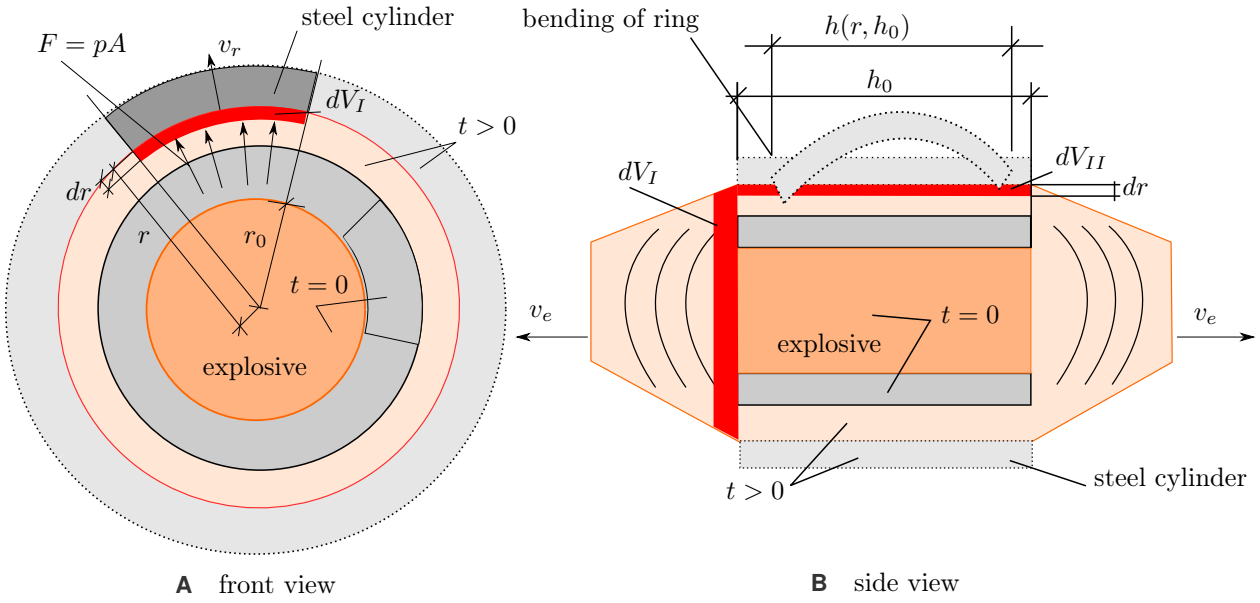

FIGURE 6.5 Illustration of the theoretical cylinder expansion and all relevant parameters for a simplified model. In particular: Estimation of the explosive volume dV_I and dV_{II}. (initial radius r_0, velocity of explosion v_e, velocity of the ring v_r, radial increment dr, incremental volume increase in axial direction dV_I, incremental volume increase in radial direction dV_{II}, current height of the cylinder due to bending h, pressure force F)

Digression: Simplified model to estimate the fragment velocity of finite cylinder rings under explosive loading

Literature provides some analytical models to estimate the fragment velocity due to explosive loading [225, 126, 76]. Most prominent, Gurney derived an analytical model to estimate the residual velocity of plates (1D), infinite cylinder (2D), and spheres (3D) [81]. He used two assumptions:

1. The whole chemical energy of the explosive is transferred to the material.
2. The energy loss due to fracture is negligible.

The cylinder-rings of our application are too small to be approximated infinite. Instead, a different model is derived using the pressure from the JWL-EOS (Jones-Wilkins-Lee equation of state) to estimate the transferred energy. We use three slightly different assumptions for the derivation:

1. The whole pressure force is transferred to the material.
2. The energy loss due to fracture is negligible.
3. The cylinder ring expands up to an ultimate strain.

We express the following derivation for the expansion of the cylinder with its current radius r that is discretised with an incremental dr (compare Figure 6.5). Let E_e be the energy of the explosive transferred to the steel cylinder

$$E_e(r) = \int_{r_0}^{r} p(V(r))A(\tilde{r})d\tilde{r}, \tag{6.1.1}$$

where r is the current radius of the cylinder ring, r_0 is the initial radius, $\tilde{r}$ is the integration variable, p is the pressure, and A is the area. The pressure p is a function of the expansion factor $\tilde{V} = V_e/V_0$, where V_0 is the volume of the explosive and V_e is the volume of the explosion products. It is calculated based on the JWL-EOS (compare (4.1.27)):

$$p(\tilde{V}) = \tilde{A}(1 - \frac{\omega}{R_1\tilde{V}})e^{-R_1\tilde{V}} + B(1 - \frac{\omega}{R_2\tilde{V}})e^{-R_2\tilde{V}} + \frac{\omega\tilde{E}}{\tilde{V}}\,, \tag{6.1.2}$$

where, $\tilde{A}$, B, R_1, R_2, ω and $\tilde{E}$ are material specific constants and described in more detail by Kury et al. [118] and Lee et al. [119]. The area A where the pressure affects is the inner surface of the cylinder ring, and can be approximated with the current radius r

$$A(r) = 2\pi h_0 \max(r, r_{\max}), \tag{6.1.3}$$

where h_0 is the initial height of the cylinder ring and $r_{\max}$ is the maximum radius of the ring until fracture. To account for the axial bending of the ring, that is observed during the experiments, we propose a modification of (6.1.3) with a non-constant length of the cylinder

$$A(r) = 2\pi\ h(h_0, r)\ \max(r, r_{\max}) \qquad \text{and} \qquad h(h_0, r) = h_0 \min\left(1, 1.5r_0\sqrt{\frac{1}{h_0(r - r_0)}}\right). \tag{6.1.4}$$

Next, to update the pressure in (6.1.2), an accurate estimation of the expansion factor $\tilde{V}$ is required in the model. As the ring expands, the volume of the explosive increases in two directions: (I) in the radial direction with expansion velocity v_r and (II) in the axial direction with detonation velocity v_e. Before giving an expression for the volume expansion, we need an expression to compute the radial expansion velocity v_r: Assuming all energy of the explosive transferred to the cylinder E_e is kinetic energy, we find

$$E_e = E_{\text{kin}} = \frac{1}{2}\, m v_r^2 \tag{6.1.5}$$

and the expansion velocity can be expressed as a function of E_e

$$v_r(r) = \sqrt{\frac{2E_e(r)}{m}}\,. \tag{6.1.6}$$

The volume expansion of the explosive

$$\tilde{V} = 1 + \frac{1}{V_0}\int_{r_0}^{r} \underbrace{\pi\tilde{r}^2\frac{v_e}{v_r}}_{I} + \underbrace{2\pi\tilde{r}\ h(\tilde{r})}_{II}\, d\tilde{r}, \tag{6.1.7}$$

closes the system of equations. Typically, one would rewrite the equations and integrate over the time $dt = dr/v$, however, due to the singularity at $t = 0$ where $v_r = 0$, we implemented the integration regarding the radial increment of the ring dr. The algorithm then updates ring expansion $r = r + dr$, pressure p (6.1.2), area A (6.1.3), energy E_e (6.1.5), velocity v_r (6.1.6), and expansion of the explosive $\tilde{V}$ (6.1.7) until a static velocity is reached. This problem is solved with integration, and accuracy is achieved by a high spatial

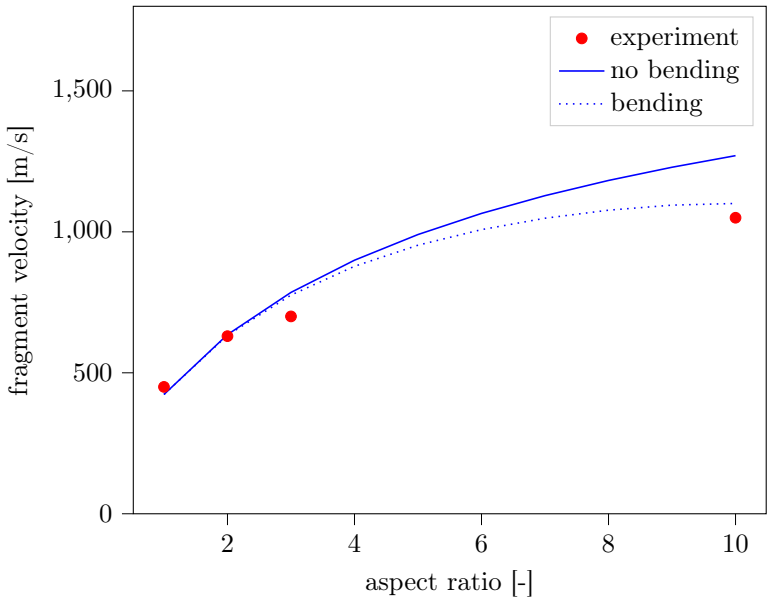

FIGURE 6.6 Result of our model to estimate the fragment velocity. The dotted line shows an empirical approximation of the area reduction of the cylinder due to bending.

resolution of dr. The problem converges for $dr < 0.001\ r_0$. The integration is done until the expansion of the steel ring r has reached a cut-off value $r_{\max} = 10\ r_0$. The acceleration at that point is already close to zero. Figure 6.6 shows the approximation of the fragment velocity with our model and the velocity measured during experiments. The solid line shows the result without accounting for bending, which is an upper limit for the fragment velocity. The dotted line shows the result with the proposed modification and describes the real-world experimental results better. To apply the model for a different material, we have to know how much the material bends and adjust the modelling of $h(h_0, r)$ accordingly. If the material differs significantly from our material, the model might be inaccurate otherwise.

As shown in the digression, the fragment velocity is decoupled from material properties of the ring—except for density. This is an important finding as it is sufficient to check the fragment velocity once to make sure the explosive is modelled correctly. In summary, we use the X-ray images as an additional, qualitative validation of the numerical experiments, besides the fragment size distribution, we introduce in the next paragraph. For most studies comparing the fragment size distribution is sufficient for the validation.

6.1.3 Fragment collection in water basins

With the setup of the water basin, depicted in Figure 6.2, only a fraction of the generated fragments is recovered. We assume that these fragments are appropriate representatives in the size and shape of the characteristic fragments due to symmetry conditions. From those fragments recovered in the water basin, an average of 67% of the expected mass was recovered. The remaining 33% is pulverised or very small fragments that were not found. Therefore, the number of fragments must be normalised with the expected, and not with the recovered, mass [16]. Only the number of small fragments might be larger. This was mistaken in the original publication, and therefore the curves differ compared to [51]. The recovery of fragments of the largest

ring was not ideal. Due to the immense kinetic energy, the water basin was considerably deformed, and it is not clear whether all fragments stayed intact after hitting the basin wall or the water surface. Therefore, experimental results obtained with 10:1 ratio have to be taken with caution.

After recovering, the fragments in the water basin they were weighted, and the larger fragments were collected and photocopied for further investigation. Since we cannot reconstruct the position of the fragment in the initial state, it is difficult to make a qualitative comparison. Exemplarily, we used 3D scanning to compare the three-dimensional shape of characteristic fragments. We processed 3D scans for the case 2:1 (see Figure 6.7), but the main focus lies on the X-ray images regarding a qualitative comparison. The main challenge of publishing results using the 3D scans is that the data has to be shown from different angles. For primarily qualitative comparison, and for analysing the angles of the fragment, it improved the measurement accuracy since the physical fragments are more difficult to measure than their digital twin. Due to the randomness of the breaks, analysing particular fragments is less suitable for our application.

Instead, we can use the fragment mass extracted from the water basin observation for statistical comparison. A common approach is to compare the accumulated size distribution of the fragments, as shown in Figure 6.8. This is our central database to validate and tune our numerical models in the studies of this chapter. Based

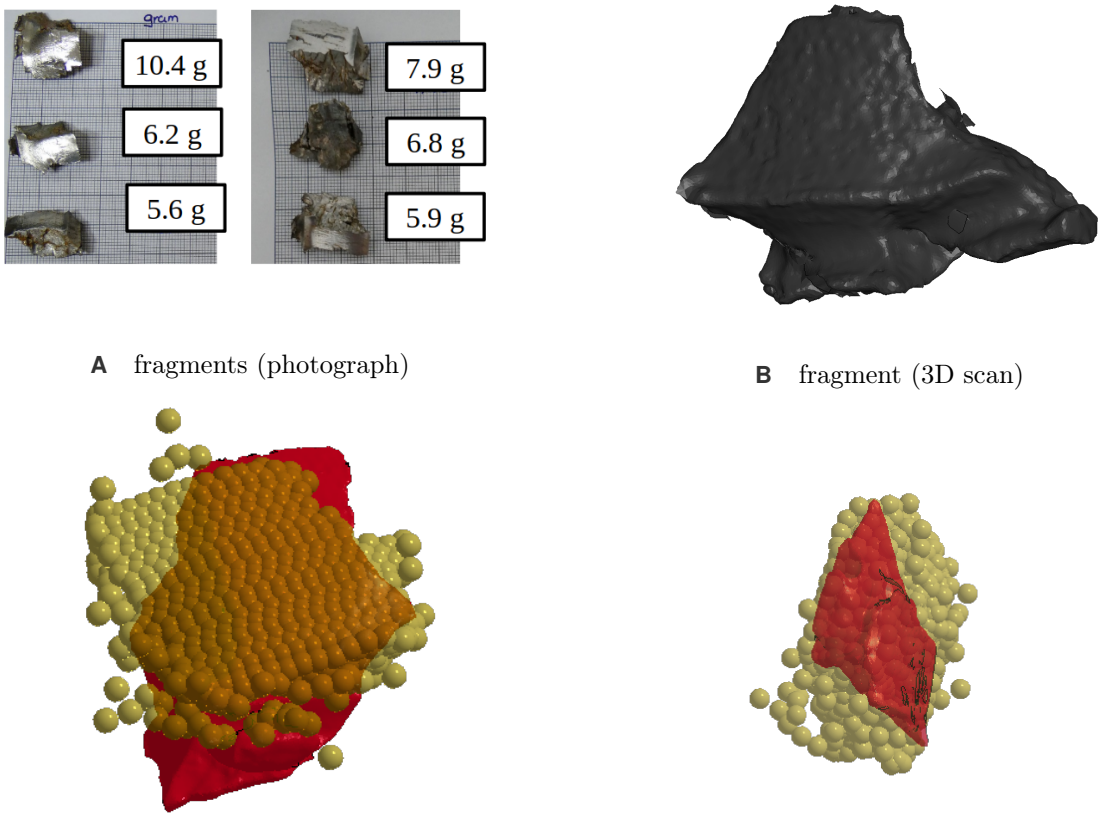

A fragments (photograph)

B fragment (3D scan)

C 3D scan vs. SPH: front view

D 3D scan vs. SPH: side view

FIGURE 6.7 Natural fragmentation of cylinder ring with $h/w = 2{:}1$: Analysation of recovered fragments with photocopy **A** and 3D scan **B**. **C** and **D** comparison of one of the fragments computed with the SPH simulation to the 3D scan.

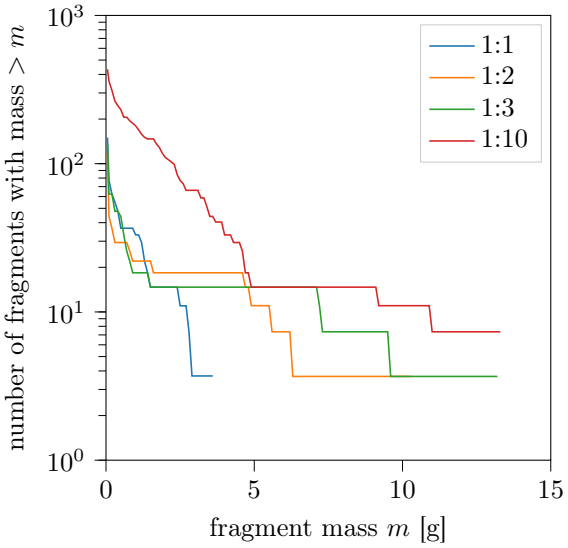

FIGURE 6.8 Fragment size distribution extracted from experiments. Each curve shows the result of a different aspect ratio.

on the experiments we can already see, that for aspect ratios up to 3:1, the number of small fragments is nearly identical. Only the size of the larger fragments increases with an increased cylinder height. On the other hand, the size of the largest fragment does not increase further for the 10:1 case. Instead, the number of small fragments increases by a factor of approximately five. We expect that this transition is difficult to represent with numerical simulations.

6.1.4 Conclusion

In this section, we presented the setup and outlined the difficulties in recovering fragments from the experiment. We analyse two experimental methodologies:

First, we showed X-ray images which can be used to estimate an upper limit of the fragment velocity. However, this velocity is independent of the steel grade. We showed this by presenting a simplified numerical model to approximate the fragment velocity from basic physical assumptions and the pressure force from an EOS.

The second method deals with the recovery of fragments. Since the fragmentation is random, 3D scans are difficult to use in the validation. Instead, we evaluate the fragment mass statistics. The data of Figure 6.8 will be essential in the following validation.

6.2 Material calibration

Before running the numerical simulation, we determine the properties of our steel in terms of the modelling parameters. We use the Johnson-Cook (JC), the Cowper-Symonds (CS) and the Rusinek-Klepacko (RK) plasticity model (compare Section 4.1.1) with selected fracture models (Johson-Cook, Lemaitre, and Rittel) in the simulation.

We distinguish four types of input parameters of the material model: (i) material constants (ii) numerical parameters, (iii) static modelling parameters for plasticity, and (iv) dynamic modelling parameters for plasticity. Parameters (i) are found in the literature (e.g., [171] for the RK-model), and parameters (ii) are user-defined values which describe the application (e.g., the range of strain rates). Accordingly, we have to determine the parameters (iii) and (iv).

A common approach is to use stress-strain curves obtained by material testing to fit the parameters. We described typical material tests in Section 1.2.3. Due to the number of parameters, we decouple the determination of (iii) and (iv). As part of the HVIS paper [51] quasi-static experiments were conducted. These curves are used to fit (iii). Because no dynamic material characterisation experiments were conducted for exactly our material, we use stress-strain curves obtained by Lee and Yeh [123] for a similar 4340 steel to fit (iv). We conclude that our material and the material investigated by Lee and Yeh is similar since the extrapolation of the yield stress to the strain rate of our quasi-static tests is similar. For the static fit, we only need an initial guess of some dynamic parameters. Therefore, we simplify the hardening rules ignoring the dynamic part. For the JC model, (4.1.1) becomes

$$q(\bar{\varepsilon}_p) = \big(\sigma_y + B\bar{\varepsilon}_p^n\big), \tag{6.2.1}$$

where q is the flow stress, $\bar{\varepsilon}_p$ is the plastic strain, and $\sigma_y,\ B,\ n$ are the three static modelling parameters. The RK hardening rule (4.1.7) becomes

$$q(\bar{\varepsilon}_p) = B_0\ 2^{-\nu}(\varepsilon_0 + \bar{\varepsilon}_p)^{n_0}, \tag{6.2.2}$$

where B_0 and n_0 are the static modelling parameters, and ν is the dynamic parameter needed for initialization. Not only for the RK model but also for the JC model, a dynamic guess is needed.

- For the JC model the parameters are usually defined for a strain rate of $\dot{\varepsilon_0} = 1.0\ 1/s$. Since our experimental data with quasi-static tests is obtained at a strain rate of $\dot{\varepsilon}_{\text{exp}} = 10^{-6}\ 1/s$, we need an initial estimate for the strain rate hardening to recompute

$$q^* = q\Big(1 + C \ln\left(\frac{\dot{\varepsilon}_{\text{exp}}}{\dot{\varepsilon_0}}\right)\Big). \tag{6.2.3}$$

  The reference strain rate of $1\ 1/s$ is not obligatory for the JC model, but it is convenient for comparison, as most materials are calibrated for this strain rate. For us, this means that we can use the JC damage parameters for 4340 steel from Johnson [106] without the need to recalibrate.

- For the RK model, the modelling parameter ν has to be considered during the evaluation of static parameters. The value for the static fit is taken from the literature [171] and is approximated during

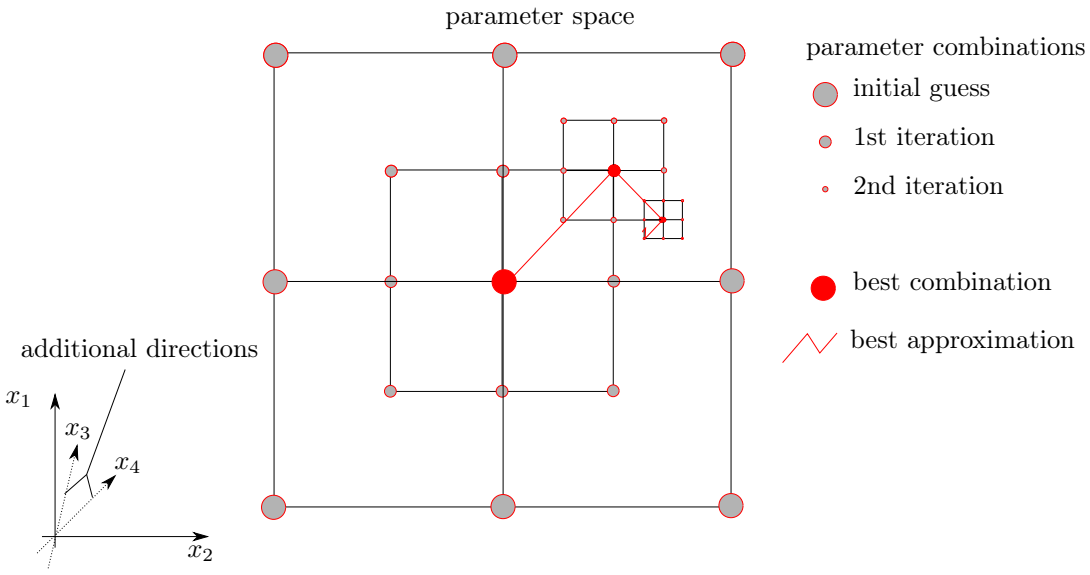

FIGURE 6.9 Parameter approximation with an hierarchical approach for high-dimensional parameter space. We show only two dimensions to simplify the visualization. (Image published in [15])

the dynamic fit.

After q^* and ν are defined, the determination of the static parameters is straight forward: For the JC model, we use the value estimated by Johnson and Cook [105] for 4340 steel as a first estimate and adapt them until the curves match. As there is only one curve to fit, we do not need a hierarchical approach. For simplicity, we use the same static parameters with the CS modification (see Section 4.1.1). For the RK model, we similarly iterate B_0 and n_0 (compare Figure 6.10A).

Lee and Yeh [123] conducted Split-Hopkinson pressure bar (SHPB) tests to determine dynamic stress strain curves (compare Section 1.2.3). The SHPB method is developed by Kolsky [115] based on the early work of Hopkinson [92] and is used to estimate material parameters at very high strain rates. Figure 6.10B to 6.10D show the experimental curves as well as the corresponding curve fit. We use a least-squares regression on a hierarchical grid, for the calibration. Due to the decoupling of static and dynamic parameters, the number of dimensions is feasible on a regular grid (compare Figure 6.9). In terms of data that describe our "truth", we have 12 experiments discretised with 10 points each, resulting in 120 evaluation points. Our hierarchical approach assumes that there is only one local minimum and a grid refinement around the minimum of the parent grid monotonically improves the parameter estimation. With this approach, we can find a parameter combination that approximates all curves nicely. The only uncertainty is, how the parameter set fits data at strain rates observed in our application that are $10 - 1000$ times larger than in SHPB tests. In terms of a fit of fracture parameters, we can not use this data set. Besides the reduced amount of fitting points (only the point where the fracture occurs can be used), triaxiality is essential for fracture and was not investigated with the SHPB tests. Furthermore, localisation effects result in higher strain rates and temperatures in the area of a crack are not documented. Therefore, instead of using the SHPB tests, the fracture model is calibrated with the cylinder ring tests.

Tables 6.1, 6.2, and 6.3 present the final material parameters for the applied plasticity and fracture models. This contains not only the parameters (ii) and (iii) obtained by material fitting, but all necessary information.

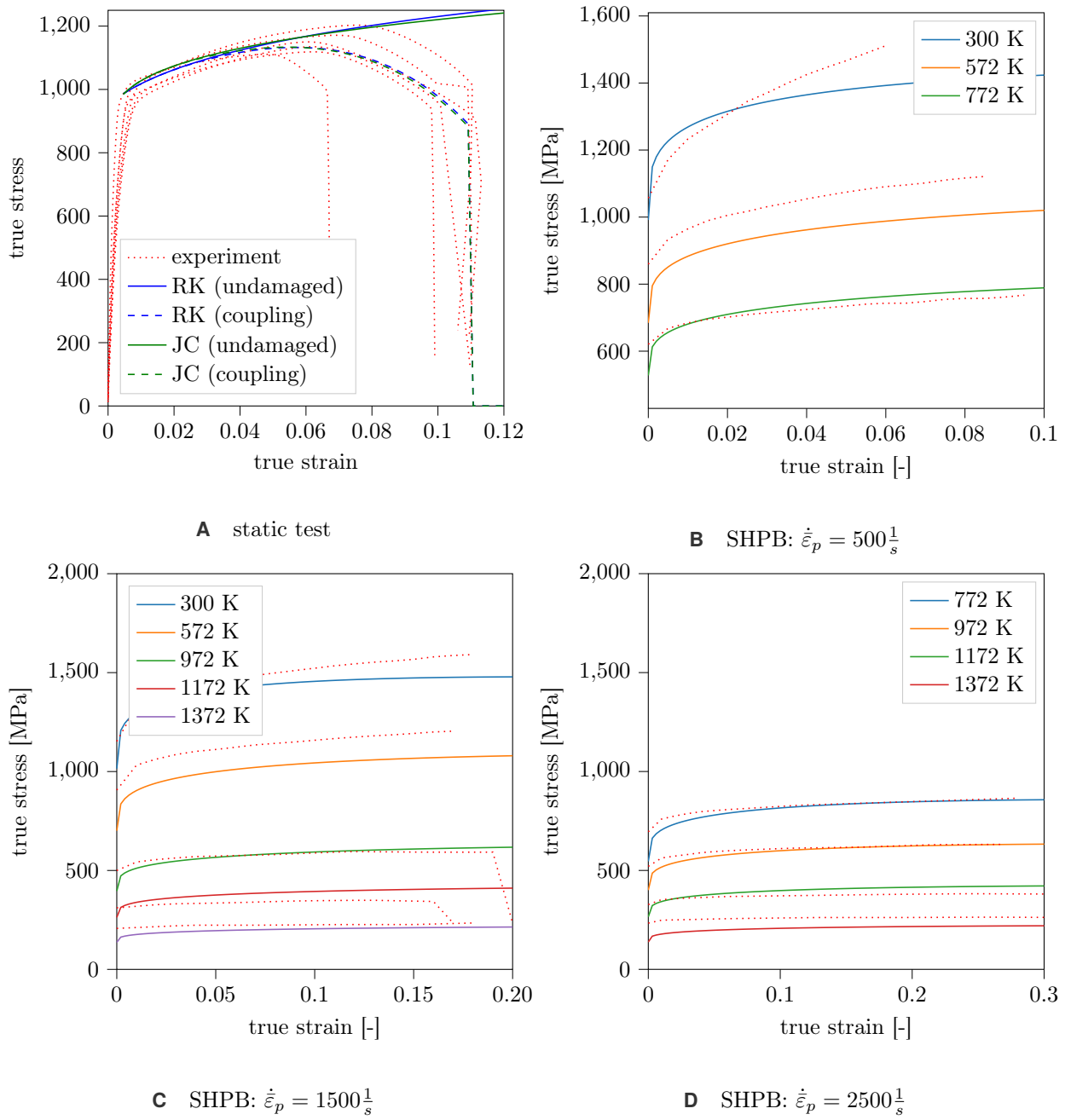

A static test

B SHPB: $\dot{\bar{\varepsilon}}_p = 500\frac{1}{s}$

C SHPB: $\dot{\bar{\varepsilon}}_p = 1500\frac{1}{s}$

D SHPB: $\dot{\bar{\varepsilon}}_p = 2500\frac{1}{s}$

FIGURE 6.10 Material calibration. **A**: static fit of JC and RK model (solid line). A constant damage accumulation is assumed and coupled with the yield strength to model necking (dashed line) (see Section 2.3.4). **B**– **D** dynamic fit of JC and RK model for different strain rates using literature data by Lee and Yeh [123]. Each line represents a different temperature (in Kelvin). Exemplarily, we show the fit for the JC model. The experimental results are visualized with red dotted lines. (Image published in [15])

TABLE 6.1 Parameters for the RK plasticity model. (i) material constants (ii) numerical parameters, (iii) static modelling parameters for plasticity, and (iv) dynamic modelling parameters for plasticity. (Table published in [15])

Parameter	Value	Comment
B_0 [MPa]	1,600	(iii) scaling of static curve
n_0 [-]	0.12	(iii) curvature of static curve
ε_0 [-]	1.8×10^{-2}	(ii) minimum plastic strain
D_1 [-]	0.49	(i) modelling parameter
ν [-]	0.225	(iv) modelling parameter
σ_0^* [MPa]	352	(iv) activation stress at ambient conditions
m [-]	1.10	(iv) temperature sensitivity
D_2 [-]	0.0108	(iv) modelling parameter
E_0 [GPa]	212	(i) Young's modulus
θ^* [-]	0.59	(i) T_{ch}/T_m normalized characteristic temperature
T_m [K]	1,600	(i) melting temperature
$\dot{\varepsilon}_{\max}$ [s^{-1}]	10^7	(ii) maximum strain rate
$\dot{\varepsilon}_{\min}$ [s^{-1}]	10^{-5}	(ii) minimum strain rate
C_p [J kg^{-1} K^{-1}]	470	(i) heat capacity
β [-]	0.9	(i) Taylor-Quinney coefficient
ρ [kg m^{-3}]	7800	(i) density
α [K^{-1}]	10^{-5}	(i) thermal expansion factor

TABLE 6.2 Parameters for JC and CS plasticity model (converted to testing strain rate of 1 $1/s$). To match the strain rate dependence with CS better an exponent of $1/5$ is chosen despite a better set of parameters with respect to temperature for $p = 1/8$. (iii) static modelling parameters for plasticity, and (iv) dynamic modelling parameters for plasticity. (Table published in [15])

Parameter	JC paper	JC fit	CS fit	Comment
A [MPa]	792	880	880	(iii) scaling of static curve
B [MPa]	510	833	830	(iii) strain hardening (scaling)
n [–]	0.26	0.26	0.26	(iii) strain hardening (curvature)
m [–]	1.05	0.75	0.75	(iv) thermal softening
C [–]	0.014	0.025	$9 \times 10^6 1/s$	(iv) strain rate hardening JC
p [–]	-	-	5	(iv) strain rate hardening CS

TABLE 6.3 Parameters for damage models. The JC parameters are fitted with the ring experiment and compared to literature data [106]. The Lemaitre and Rittel parameters fitted with the ring experiments are compared to the parameter fit with the SHPB fit [123]. (Table published in [15])

JC	JC Paper	Ring fit	**Lemaitre**	SHPB fit	Ring fit	**Rittel**	SHPB fit	Ring fit
D1	0.05	0.05	Dc	0.55	0.35	eps	0.03	0.06
D2	3.44	0.8	S	0.20 MPa	60 MPa	Wcrit	91 MPa	250 MPa
D3	-2.12	-0.44	t	0.28	0.75	b	1.0	
D4	0.002	-0.046						
D5	0.61	-2.9						

6.3 Numerical experiments

This section presents the numerical experiments with *MCM*, *LS-DYNA®* and *IMPETUS®*[1] and is structured as follows: First, we describe the numerical model in detail. Next, we give an overview of the cases and present four different studies:

- STUDY I compares different settings in *LS-DYNA®* for the SPH formulation, the material parameter set, and the fracture description.
- STUDY II investigates selected implementation aspects in *MCM* for the plasticity and fracture modelling.
- STUDY III uses the findings of STUDY II to systematically compare different plasticity and fracture models in *MCM*.
- STUDY IV uses the best choice of STUDY I and STUDY III and compares them to the results obtained in the third code *IMPETUS®*.

6.3.1 Setup of the model

The natural fragmentation of explosively driven cylinder rings is fully modelled with SPH in all codes. In particular, the explosive is not described by a pressure boundary condition but is explicitly simulated. The explosive and the cylinder ring are discretised with the same particle size to improve the approximation quality and avoid artefacts due to the resolution. The same resolution is used throughout different cases. The material parameters for the steel were derived in the previous section (Tables 6.1, 6.2, and 6.3). Besides the plasticity model, a Grüeneisen EOS is used for the steel ring (speed of sound $c = 4570$ m/s, linear shock parameter $S_1 = 1.4$, and Grüeneisen parameter $\gamma_0 = 1.67$), and a JWL-EOS (Jones-Wilkins-Lee equation of state) describes the pressure of the explosive. In addition to the EOS the Chapman-Jougot pressure ($p_{CJ} = 292$ Mbar), the detonation velocity ($v_d = 8250$ m/s), the bulk viscosity coefficients ($Q_1 = 1.5, Q_2 = 2.0$), and the initial density of the explosive ($\rho_0 = 1740$ kg/m^3) are described with a high explosive (HE) material model. The details of the SPH-solver itself vary on the code used. All codes use standard contact and a B-spline interpolation kernel. For *LS-DYNA®*, we investigate the quasi-linear SPH formulation (compare Section 3.3.4) with a fixed kernel width and a velocity cutoff of $10,000$ m/s. In *MCM*, we select the standard Eulerian SPH kernel with Monaghan bond viscosity and *IMPETUS®* uses the stabilized γ-SPH-ALE solver with reduced bulk viscosity ($Q_1 = 0.5,\ Q_2 = 0.1$) [44].

6.3.2 Overview of cases

In this chapter, our main objective is to quantify the influence of model components, parameter choices and numerical methods on the fracture behaviour. This is done in terms of four numerical studies described in Tables 6.4 to 6.7. The generated insights are used to select a fracture model for our HVI-model. In the commercial code *LS-DYNA®*, we are restricted to investigate input parameters with existing approaches and to compare different SPH formulations. Thus, with *LS-DYNA®*, we investigate numerical approaches, strength values, and fracture options for one ring size (2:1) (STUDY I). *MCM* is a non-commercial code where

[1] numerical solvers described in Section 1.2.4

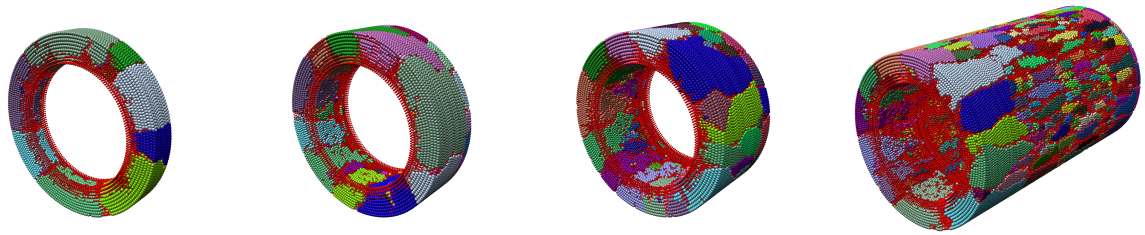

FIGURE 6.11 Fracture distribution in initial position for different aspect ratios obtained with the *MCM* code. We compare three hardening rules JC, CS, and RK, and three fracture models JC, Lemaitre (LE) and Rittel (RI). (Image published in [15])

we can add and modify arbitrary material models. Therefore, the study with *MCM* compares specific choices of numerical solver components (STUDY II), again for 2:1, and plasticity and fracture models for different ring sizes (STUDY III), see Figure 6.11. *IMPETUS®* provides an algorithm with improved energy conservation and dedicated stabilisation schemes for highly dynamic impact. Furthermore, the highly parallelized and efficient GPU implementation allows running models with higher resolution. The question in the last comparison is how the results with *IMPETUS®* compare to our *LS-DYNA®* and *MCM* model (STUDY IV).

As described in the material calibration, we have to adjust the fracture parameters to our application. For this calibration, we use the 2:1 rings. Thus, the findings for the numerical experiment used to fit the parameters (2:1) are of secondary interest as they are the best fit by construction. Instead, the other ring-sizes are used to evaluate the limitations of the model with our chosen parameters. As the loading conditions change considerably between the different aspect ratios, this is a coherent approach. Considering the findings in Section 6.1, we mainly use the fragment size statistics to compare the different experiments.

TABLE 6.4 STUDY I: **LS-DYNA®**—three parameter studies investigating (i) the numerical SPH formulation, (ii) the influence of material strength, (iii) different fracture criteria. These studies are all investigating 2:1 rings. In addition, the simulations were conducted for all aspect ratios with the most accurate model, to compare in STUDY IV.

id	study	formulation	σ_y [MPa]	plasticity model	damage criterion	aspect ratio
101	(i)—(iv), (VI)	Quasi-Linear	1000	CS	spall + JC damage	2:1
102	(i)	Standard	1000	CS	spall + JC damage	2:1
103	(i)	Renormalized	1000	CS	spall + JC damage	2:1
104	(i)	Symmetric	1000	CS	spall + JC damage	2:1
111	(ii)	Quasi-Linear	700	CS	spall + JC damage	2:1
112	(ii)	Quasi-Linear	1400	CS	spall + JC damage	2:1
113	(ii)	Quasi-Linear	1000	CS	spall + JC damage	2:1
121	(iii)	Quasi-Linear	1000	CS	none	2:1
122	(iii)	Quasi-Linear	1000	CS	JC damage	2:1
123	(iii)	Quasi-Linear	1000	CS	spall	2:1
131	(VI)	Quasi-Linear	1000	CS	spall + JC damage	1:1
132	(VI)	Quasi-Linear	1000	CS	spall + JC damage	3:1
133	(VI)	Quasi-Linear	1000	CS	spall + JC damage	10:1

TABLE 6.5 STUDY II: **MCM**—five independent preliminary studies investigating (i) initial damage with three different threshold values, (ii) coupling between plasticity and damage model, (iii) use of a Newton-Raphson plasticity corrector, (iv) modification of the Lemaitre fracture model, (v) modification of the Rittel and the Johnson-Cook fracture model. All simulations use an aspect ratio of 2:1 and the CS model.

id	study	initial damage	coupling	Newton-Raphson	Fracture model	Modification
201	(i)—(iv)	0.0	0.0	False	Lemaitre	both
202	(i)	0.1	0.0	False	Lemaitre	both
203	(i)	0.3	0.0	False	Lemaitre	both
211	(ii)	0.1	0.0	False	Lemaitre	both
212	(ii)	0.1	1.0	False	Lemaitre	both
221	(iii)	0.1	0.3	True	Lemaitre	both
231	(vi)	0.1	0.3	True	Lemaitre	none
232	(vi)	0.1	0.3	True	Lemaitre	triax
233	(vi)	0.1	0.3	True	Lemaitre	threshold strain
241	(v)	0.1	0.3	True	Rittel	none
242	(v)	0.1	0.3	True	Rittel	triax
243	(v)	0.1	0.3	True	JC	none
244	(v)	0.1	0.3	True	JC	triax

TABLE 6.6 STUDY III: **MCM**—plasticity and fracture models: five different combinations for all different aspect ratios. This study determines the most accurate model to describe the real-world experiments. Simulation 301-304 are compared in STUDY IV.

id	STUDY	plasticity model	fracture model	aspect ratio
301-304	II, IV	CS	Lemaitre	1:1, 2:1, 3:1, 10:1
311-314	II	CS	JC	1:1, 2:1, 3:1, 10:1
321-324	II	CS	Rittel	1:1, 2:1, 3:1, 10:1
331-334	II	RK	Lemaitre	1:1, 2:1, 3:1, 10:1
341-344	II	JC	Lemaitre	1:1, 2:1, 3:1, 10:1

TABLE 6.7 STUDY IV: **IMPETUS®**—final comparison of *LS-DYNA®*, *MCM*, *IMPETUS®* with real-world experiments. The most accurate solution of all codes is compared against each other four all cylinder sizes. In this study, also qualitative comparisons to the experimental results are considered.

Aspect ratio	*IMPETUS®*	*MCM*	*LS-DYNA®*
1:1	401	301	101
2:1	402	302	141
3:1	403	303	142
10:1	404	304	143

6.3.3 STUDY I: formulation of SPH equations, material strength, and fracture mechanisms in LS-DYNA®

The parameter study in *LS-DYNA®* was published and presented during the Light-Weight Armor Group (LWAG) Symposium in 2019 [16]. Here, we give a summary of the results during this study and derive the optimal parameters in *LS-DYNA®*. We investigate three different influence factors: the SPH formulation, the material strength and different fracture mechanisms. The default settings are the quasi-linear formulation, the JC plasticity model with $A = 1000$ MPa and the CS modification, combined with the JC damage model with a spall criterion (compare Figure 2.6).

(i) Influence of the SPH formulation

In *LS-DYNA®*, there are more than ten different formulations of the SPH equations; four of them are of interest for our application. First, the standard formulation that we also use in *MCM*; second, a renormalised version of the equations; third, a symmetric approach; and last, the quasi-linear description (described in Section 3.3.4). The aim of this comparison is to see the differences to the other formulations rather than to determine the best-suited formulation. The quasi-linear approach is the only one which is unconditionally stable under tensile loads in *LS-DYNA®*.

The results are presented in Figure 6.12: all formulations predict two axial layers of fragments like in the experiment. The standard and the symmetric formulation predict a similar behaviour regarding fragment

A *MCM* **B** quasi-linear **C** standard **D** renormalized **E** symmetric

FIGURE 6.12 Different numerical formulations of the conservation equations in SPH (*LS-DYNA®*). (Published in [16])

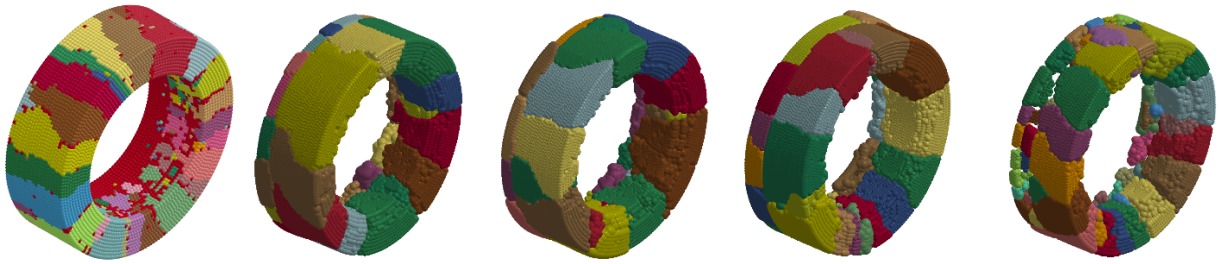

A *MCM* **B** $\sigma_y = 1000$ MPa **C** $\sigma_y = 700$ MPa **D** $\sigma_y = 1400$ MPa **E** $\sigma_y = 1000$ MPa, JC

FIGURE 6.13 The influence of yield strength σ_y and strain rate dependence in the hardening law on the fragmentation behaviour. The choice of the strain rate dependence is predominant. The results are not very sensitive to the yield strength in the numerical model. (Published in [16])

size, which also correspond to the results observed in *MCM* with the 2017 model setup [51]. The fragment sizes simulated with the quasi-linear formulation are considerably larger than the sizes obtained by all other formulations. A large amount of erosion is observed with the renormalised formulation. Although the standard formulation is more accurate in terms of fragment size, we use the quasi-linear formulation in the following studies (ii) and (iii), as it is the only one which is stable under tensile loads.

(ii) Influence of material strength

Based on uncertainty quantification of the modelling parameters, we identified the yield strength σ_y to have the most extensive influence among the input parameters in the JC plasticity model. Therefore, the investigation of material strength, with *LS-DYNA®* focuses on this parameter and is done by comparing the CS results with three different values for the yield strength to the JC model in Figure 6.13.

In our study, σ_y influences the width of the second fragment layer but is not affecting the circumferential fractures. The linear strain rate dependency of the standard JC model results in considerably more erosion.

(iii) Influence from fracture model

The last study is also purely numerical and answers the following question: What happens if we do not apply a spall criterion, only a spall criterion, or no fracture criterion at all? Directly linked to this question is: Is

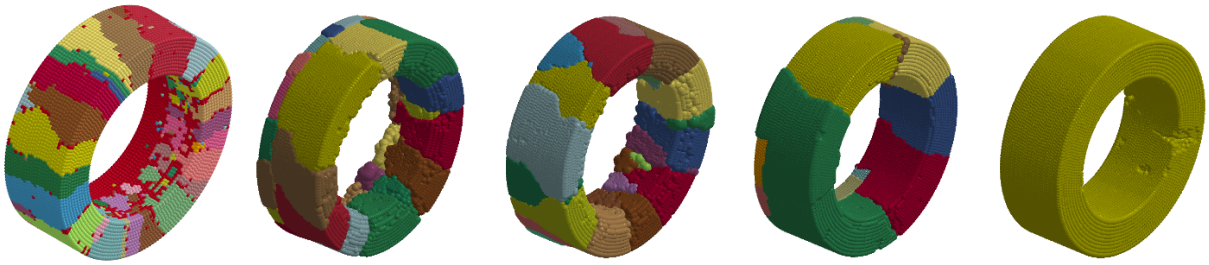

FIGURE 6.14 Different fracture mechanisms in the model. Only the combination of the damage model with a spall criterion leads to the behaviour observed in real-world experiments. Without a spall criterion, no second debris ring is predicted. The figure on the right shows that our model is stable in tension. (Published in [16])

the model stable if no failure model is used?

As a first result, Figure 6.14 shows that the spall criterion is required to predict the second debris ring. The second debris ring develops in the early stage upon the explosive detonation where the reflecting pressure wave interacts. This generates a pressure above the spall strength which tears the material apart. The second result of this comparison is that the chosen numerical model is stable in tension. If no damage is used, the cylinder does not fracture when the quasi-linear formulation is applied. On the other hand, in the standard formulation in *LS-DYNA®*, the particles experience tensile stresses which trigger tensile instabilities and the ring breaks in small fragments.

Summary and parameter choice for the final comparison

We have identified the numerical description to have a massive impact on fracture formation. Although the standard SPH-formulation shows better accordance with the experiments, we apply the quasi-linear version that is more stable in tension and avoids numerical fractures. The yield strength σ_y is of small importance and, therefore, small differences in the implementation of the strength model of *MCM*, *LS-DYNA®*, and *IMPETUS®* have a negligible impact on the results. We observed a strong correlation of the fracture formation and the strain rate hardening formulation. We suggest the CS model for this case. It represents the macroscopic material behaviour in highly dynamic events more realistically than the standard JC strain rate hardening [144]. Regarding fracture, we use both fracture criteria, damage and spall in *LS-DYNA®*.

In the following section, we present an improved version of the *MCM* results, which was already used as a reference for this comparison. This includes different plasticity models, fracture models, and other modifications. The aim is to design advanced models that can be refactored into commercial codes and improve the accuracy in predicting fracture during highly dynamic events.

6.3.4 STUDY II: initial damage, coupling plasticity and fracture, iterative solvers and damage accumulation in MCM

In this first of the two studies with *MCM*, we evaluate the following modifications of the model:

(i) a randomized initial damage distribution to describe material imperfections;

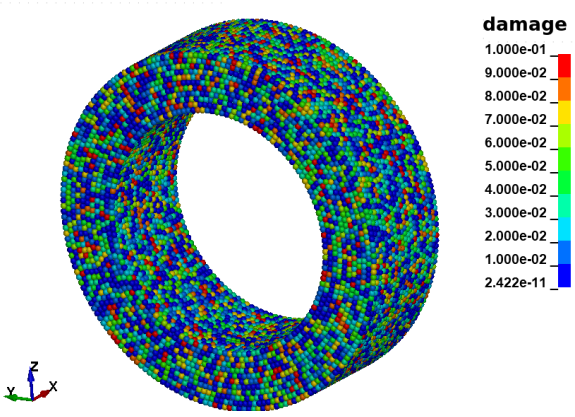

FIGURE 6.15 Initial damage distribution (2:1). (Image published in [15])

(ii) coupling the fracture criterion with the plasticity model to describe the reduced yield strength due to damage in the material;

(iii) an iterative solver to improve the overall accuracy of the plasticity algorithm:

(iv) the effect of a damage cutoff criterion.

All studies are conducted for the 2:1 rings with the CS hardening rule, and, except for (iv), all use the Lemaitre damage model.

(i) Distribution of the initial damage

We model the material imperfections with a randomised value of initial damage D_0 at each SPH-particle (see Figure 6.15). We further assume that imperfections are little $D_0 < 1$ and affect only a small number of particles (mean$(D_0) << 1$). Accordingly, we model the initial damage of particle i as

$$D_0(i) = D_{0,\max}\ \text{rand(i)}^2; \qquad \text{rand} \in [0,1], \tag{6.3.1}$$

where $D_{0,\max}$ models the upper limit of initial damage and the random value rand(i) is equally distributed between 0.0 and 1.0. For comparability, we use the same random seed for all aspect ratios. The modelling parameter $D_{0,\max}$ should be smaller than 1.0, such that no particles are nearly fully damaged during initialisation.

Figure 6.16 compares the fragment size distribution for different values of initial damage (0.0, 0.1, 0.3, 1.0) with the experimental results (red). Here, (0.1) is the default value, and (0.0) is no initial damage. In terms of the number of fragments up to 5 g, the numerical experiments agree with the real-world observations. For heavier fragments ($m > 5$ g), a higher number is predicted with all numerical models. In general, we observe that more large fragments are found with a randomised initialisation. Using no initial damage corresponds better with the real-world data. Still, we choose to include randomisation in order to make sure that the particle positioning does not influence fractures. Thus, we have to assert that the value for $D_{0,\max}$ is not too large such that it is not provoking earlier cracks. According to the plot, there is little change between (0.1) and (0.3). A further increase of $D_{0,\max}$ leads to a considerable difference in fragment statistic. Therefore, 0.1

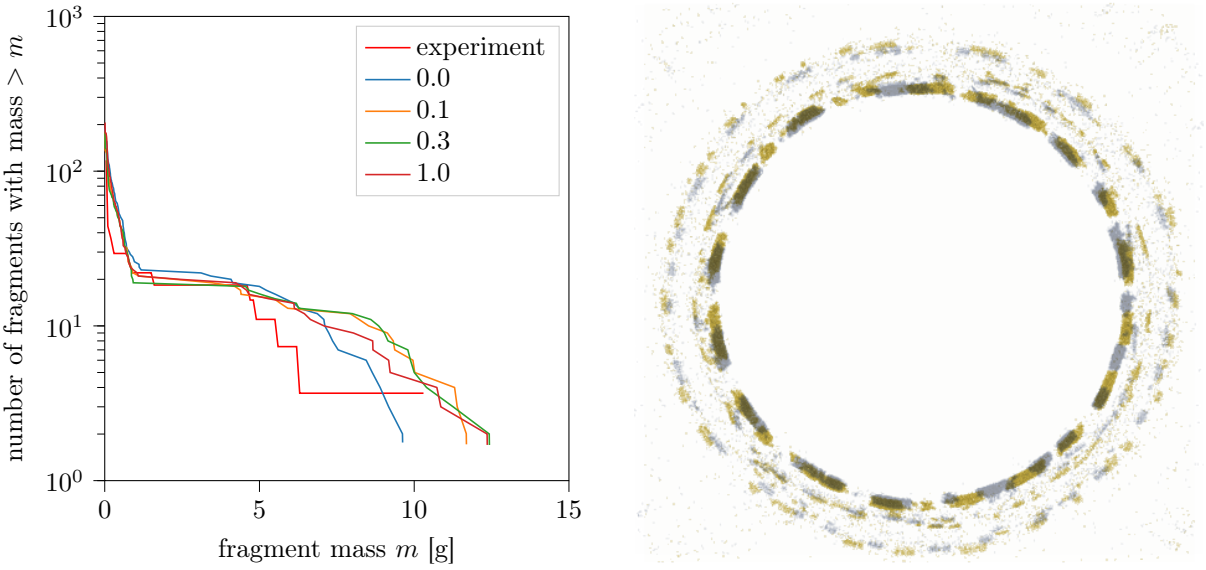

A size distribution **B** qualitative difference: 0.1 (blue), 0.0 (yellow)

FIGURE 6.16 Influence of an initial damage distribution in the numerical model. Each run is described by the amount of maximum damage $D_{0,\max}$ during the initialization (0.0—1.0). (Image published in [15])

is chosen as the default value for damage initialisation. To have a more qualitative comparison Figure 6.16B compares the fragmentation patterns with pre-damage in blue, to no pre-damage in yellow. The differences between the two results are, as we could expect based on the fragment statistic, very small. Solely, some fragments that remained uncracked with damage initialisation were split into two fragments in the simulation without pre-damage. This does not follow the intuition that with pre-damage particles fail earlier. We conclude that introducing pre-damage has a small but observable influence on the fragmentation. Furthermore, it is numerically reasonable as it leads to more randomisation of crack patterns. We use a value of $D_{0,\max} = 0.1$ as default in all following model setups.

(ii) Coupling of plasticity and fracture model

We have seen in the static experiments (compare Figure 6.10A) that if the yield strength is reduced depending on the amount of damage, the real-world stress-strain curves can be approximated better. We recall the coupling function (2.3.27):

$$\sigma_y = C_D \sigma_y^0, \qquad C_D = (1 - D^{1/c}), \tag{6.3.2}$$

where the yield strength reduction σ_y due to damage $D \in [0, 1]$ is defined by the factor C_D. The coupling is modelled with c, and the initial yield strength is σ_y^0. The parameter c was adjusted according to static experiments ($c = 0.3$) in Section 6.2.

Figure 6.17A analyses three different values for c between 0 and 1. No coupling is equivalent to $c = 0.0$, the value which matches the experiments is $c = 0.3$, and Dolonski and Rittel [57] propose $c = 1.0$ which we denote as strong coupling. Again, the influence on the size distribution is negligible. Only a small increase in the size of the larger fragment is observed. This can be explained by the fact that the material is softer for significantly damaged material. Then, if the coupling is deactivated, these particles, which loose contact for

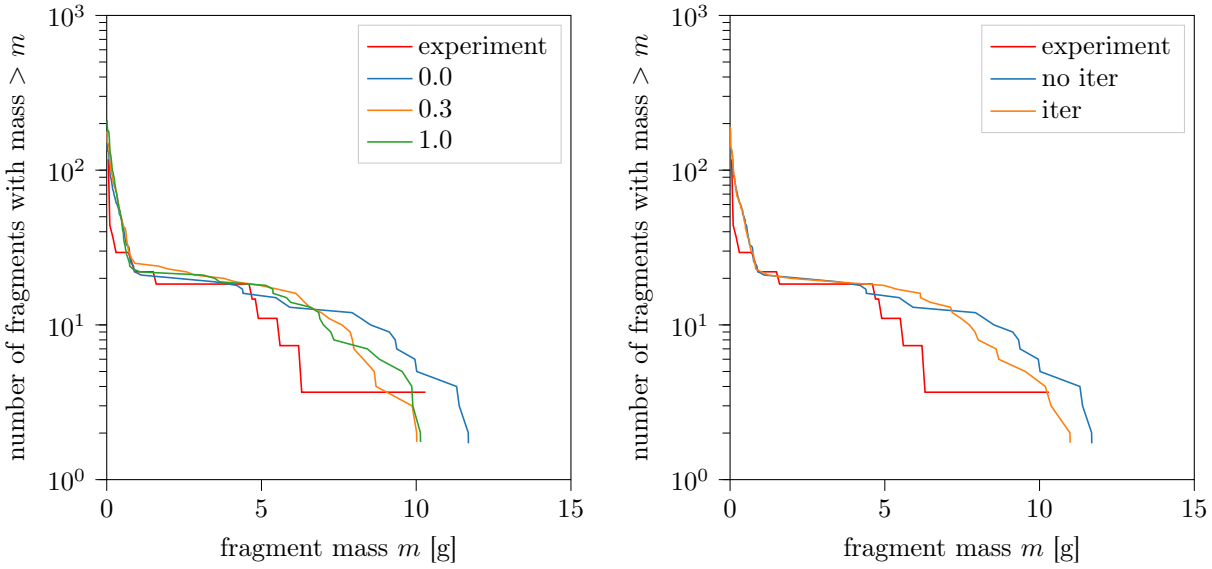

A coupling damage and plasticity **B** Newton-Raphson vs single-step evaluation

FIGURE 6.17 Analysis of **A** different damage-plasticity coupling parameters and **B** the influence of Newton-Raphson iterations with the radial return algorithm in the plasticity model.

a softer material, stay attached if the coupling is deactivated. We conclude that the coupling suggested by the experimental data is slightly improving the general behaviour. Therefore, it is enabled in all following experiments.

(iii) Newton-Raphson iterative solver in the plasticity algorithm

In the stress update of the plasticity algorithm, the stress state is projected back onto the yield surface. The residual of the resulting non-linear system of equations can be minimised with an iterative approach, such as the Newton-Raphson algorithm. This improvement to a one-step prediction that is used generally requires additional run time. For most applications, the strain increment is small enough to cause no significant error with the standard computation. In our application, we face large strain increments since the whole process is highly dynamic. There, it is assumed that an iterative solver can improve the precision of the solution.

Figure 6.17B investigates whether an iterative solver actually influences the solution. We observe that the solution with the iterative solver is not significantly influencing the result but is tending towards the experimental result. This small influence can have different causes. First, the material strength, in general, has only a small impact on fracture patterns. Second, the error for not using the iterative solver is probably only present in a few particles, which do not influence the overall result significantly.

(iv) Modifications of the fracture criterion

The previous studies have shown that damage initialisation, coupling, and a modification of the plasticity algorithm do influence the result only a little. Although this seems to be obvious, we now have evidence that we only have to focus on the damage model as this consequently is the primary driver of the fractures. This paragraph shows precisely that, and investigates empirically reasoned modifications of the damage models.

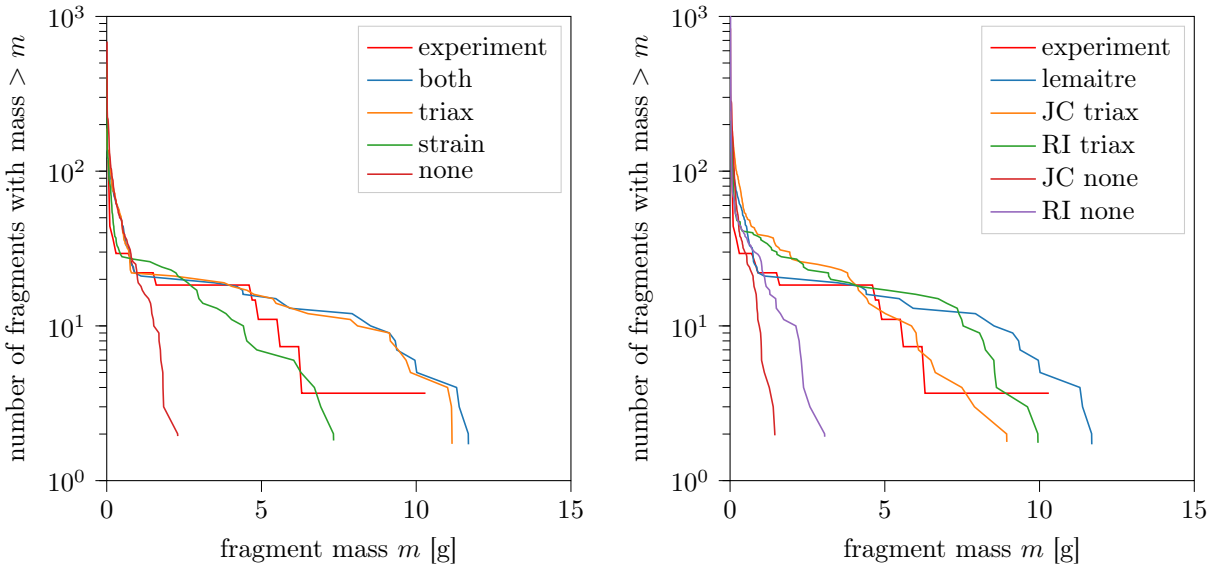

FIGURE 6.18 Modifications of fracture criteria for Lemaitre, JC and Rittel damage model. (Published in [15])

The paragraph is split into two parts: First, we analyse a plastic strain and a triaxiality cutoff criterion with the Lemaitre damage model. Second, we apply the triaxiality criterion to the JC and Rittel damage model. The triaxiality criterion means that under compression ($\eta < -1/3$) no damage is accumulated. The other criterion accumulates no damage if the plastic strain is below a threshold strain ($\bar{\varepsilon}_p < \bar{\varepsilon}_p^t$).

Figure 6.18A investigates four cases: both criteria (*both*), only triaxiality criterion (*triax*), only plastic-strain criterion (*strain*), and without modification (*none*). The pure fracture model (*none*), is not well describing the behaviour as the ring scatters already as a result of the first pressure wave of the detonation. The best accordance between the numerical and the real-world experiment is observed when using only the plastic strain criterion (*strain*).

The other two cases, *both* and *triax*, predict nearly the same statistical distribution. In general, more large fragments are predicted as in the real-world experiment, but the results correspond better regarding the size of the largest fragment. Since the two cases are identical, we conclude that the triaxiality criterion is more restrictive than the strain criterion. We assume that this is related to our application: First, the ring expands due to the pressure of the explosive (*triax* is not satisfied). Then, as soon as the ring is accelerated, tensile and shear stresses arise in the ring and dominate the pressure. There, the threshold strain is already reached for most particles.

Without the triaxiality criterion, we observe the same scattering for both, JC and Rittel model, as with the Lemaitre model (red and purple curve in Figure 6.18B). Since we did successfully improve the results for the Lemaitre damage model using the triaxiality criterion, we are optimistic about applying it to the JC and Rittel model, as well. Again, applying the triaxiality criterion solves the scattering problem and is better predicting the experimental findings. Therefore, a triaxiality criterion enhances the applicability and is used with all fracture models in *MCM* in all subsequent studies.

TABLE 6.8 Qualitative comparison of curves in Figure 6.19 (small/medium/large) fragments (small: $m < 0.2\, m_{\max}$, medium: $0.2\, m_{\max} \geq m \geq 0.5\, m_{\max}$, large: $m > 0.5\, m_{\max}$), where $m_{\max}$ is the size of the largest fragment observed in the corresponding real-world experiment.

h/w	JC_LE	CS_JC	CS_LE	CS_RI	RK_LE
1:1	o/+/-	++/+/+	o/+/-	+/+/o	o/+/o
2:1	++/+/o	-/+/++	++/+/o	++/+/o	++/+/o
3:1	++/+/++	-/-/-	++/+/++	++/+/++	++/+/++
10:1	++/-/+	o/o/-	++/-/+	++/-/o	++/-/+

6.3.5 STUDY III: plasticity and fracture models in MCM

In the previous studies, we identified the basic setup in *MCM*. In this study, we use these settings to compare a combination of different material models. We analyze three hardening rules (JC (blue), CS (green), and RK (purple)), and three fracture models (JC (orange), Lemaitre (green), and Rittel (dark red)) for different aspect ratios (compare Figure 6.19). Based on the findings in STUDY II, we expect that the fracture models have the largest impact. Figure 6.19 presents a different aspect ratio in each plot **A**—**D**. Despite uncertainties and fluctuations in the experiment, we compare our numerical model to the experimental results (red). However, we are more interested in describing the data qualitatively than in matching each data point. The qualitative evaluation is summarised in Table 6.8. In general, we observe that the numerical model predicts slightly more fragments than recovered in the experiment.

We observe a significant difference between the effect of plasticity and fracture model. On the one hand, the differences between the three plasticity models are relatively small; only for an aspect ratio of 3:1, the JC-model deviates from the other two plasticity models in terms of the largest fragment. On the other hand, there are significant differences between the three damage models; while the results for 1:1 and 2:1 are similar, there are huge differences for the cases 3:1 and 10:1. Since the fracture model should be predictive independently of material and geometry, we conclude that the JC model is either not able to capture some of the fracture mechanisms or needs further tuning. For an aspect ratio of 3:1 and 10:1, only the Lemaitre and Rittel model predict the size of the largest fragments correctly. The maximum fragment size with the JC model is almost identical for all ring sizes. In the laboratory experiments the fragment size was increasing upto 3:1 ring size. For the larger ring only the amount of fragment increased. Therefore, the JC model was slightly better align for the small rings 1:2 and 1:3 but not for larger aspect ratios. Throughout the experiments the number of small fragments is better corresponding to the laboratory experiments. As we are more interested in large fragments which are critical to protective structures, this result is only of theoretical relevance. In terms of the parameters, we fitted for our fracture models with the ring experiment, and we conclude the following.

The Lemaitre and Rittel model are overpredicting the fragment size consistently in all cases, but are much closer to the experimental results and applicable to all aspect ratios. Due to the consistency in the deviation, we are confident that we can match the results better with fine-tuning. In terms of the plasticity model, we could not identify a clear advantage for one of the three models.

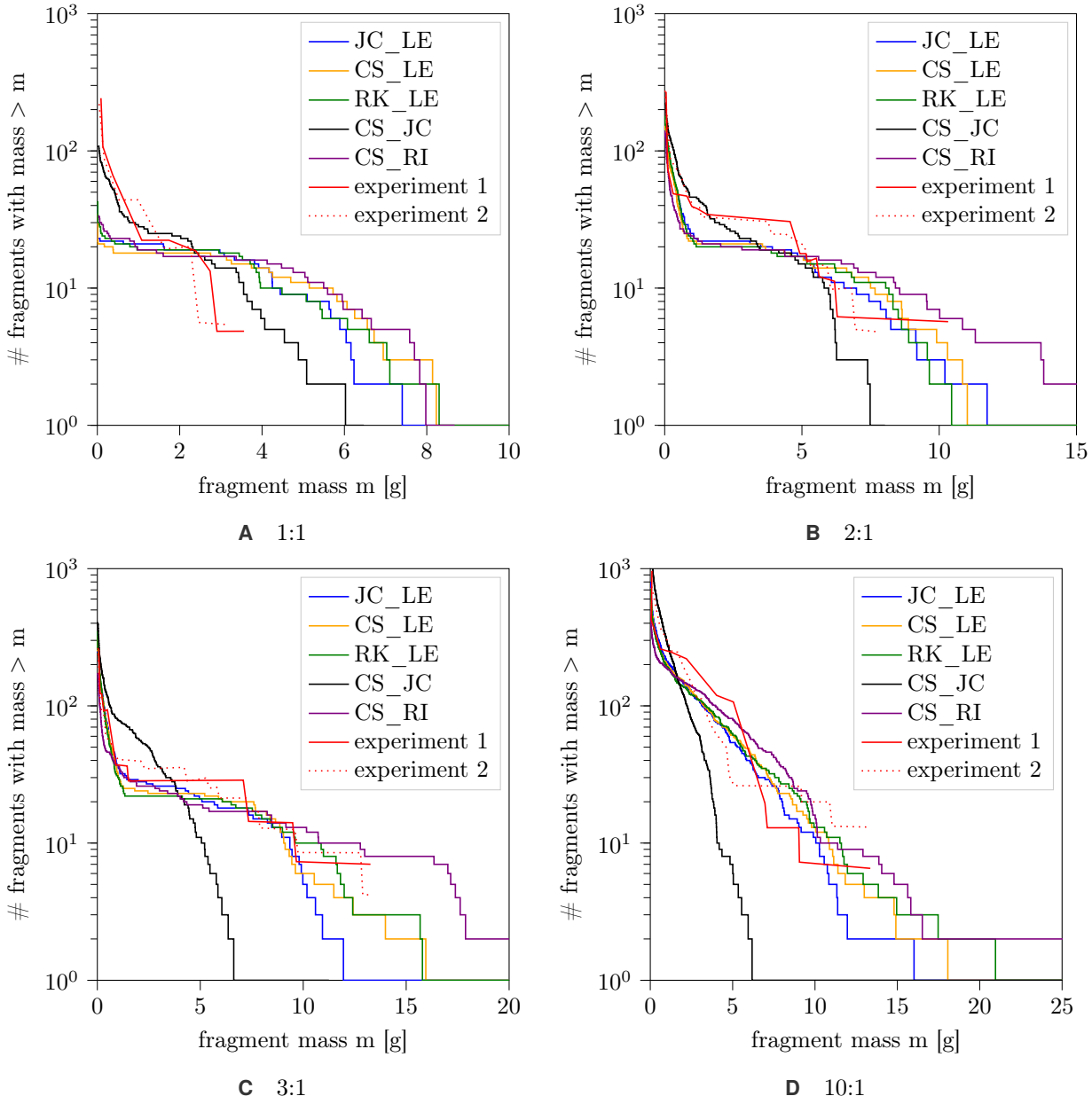

FIGURE 6.19 Fragment size distribution for different ring sizes and different combinations of hardening rule and damage model: JC-LE = JC hardening and Lemaitre damage, CS-JC = CS hardening and Johnson-Cook damage, CS-LE = CS hardening and Lemaitre damage, CS-RI = CS hardening and Rittel damage, RK-LE = RK hardening and Lemaitre damage. Qualitative evaluation in Table 6.8. (Figure published in [15])

6.3.6 STUDY IV: final comparison between MCM, LS-DYNA®, and IMPETUS®

We have tuned our numerical model in *LS-DYNA®* and *MCM* in the previous studies. Similarly, *IMPETUS®* provided us with a model for this application that uses their tailor-made SPH solver, which uses state of the art stabilisation and is much more efficient regarding the run time per degree of freedom. Hence, the *IMPETUS®* model can use approximately ten times more particles within the same computation time on comparable hardware platforms. Considering that a numerical model converges with finer discretisation, we should see a better approximation. In the range of the possibilities, differently discretised cylinder rings were tested in *MCM* and *LS-DYNA®* and showed consistent results. Based on this refinement-study, we believe that a higher resolution does not significantly change the findings in *MCM* and *LS-DYNA®*. Three validation approaches have been used in our previous studies: (i) a fragment visualisation in the initial configuration, (ii) an X-ray like visualisation, and (iii) a comparison in terms of fragment statistics. We provide the fragment statistic for all cases and exemplarily showcase the X-ray like visualisation for an aspect ratio of 3:1, and the initial fragment visualisation for an aspect of ratio 2:1.

- Figure 6.20 shows the fragment statistics of each ring size in a separate plot. For the 1:1 case, the *IMPETUS®* solution is closest to the experiment. In particular, the number of small fragments is well described. This might be attributed to the higher resolution where the material has more possibilities to fracture. All models represent the second case (2:1) well. In particular, *MCM* and *IMPETUS®* show good accordance with the experimental data. The third case (3:1) is best described with the *LS-DYNA®* model. *IMPETUS®* and *MCM* overpredict the number of fragments and underpredict the amount of dusting. Similar to the (2:1) case, both codes are nearly identical in their prediction. For the last case (10:1), *MCM* is closest to the experimental case. As discussed, for this case, the fragment recovery was not optimal. The fragments deformed the water basin significantly. It is not clear if they broke while impacting the basin and if all fragments were recovered. Therefore, results are interpreted with caution. If the fragments cracked while impacting the basin, the prediction with *IMPETUS®* might be best. Otherwise, *MCM* is more accurate.

- For the comparison with the X-ray images depicted in Figure 6.21, we select the ring size of 3:1. The ring is visualized at $t_1 = 64$ μs and $t_2 = 128$ μs. In the X-ray image, the background noise was manually cropped. The first time step shows that all models do not fracture too early as the rings are still intact in the real-world and the numerical experiment. In the second time step, we can see how the fragments open up in the experiment. They are not only accelerated in the radial direction but also experience rotation or bending in an axial direction. *LS-DYNA®* and *IMPETUS®* describe this rotation, which might be due to the asymmetric initiation, or the interaction of shockwaves inside the cylinder ring as well. The second debris ring, consisting of smaller fragments, can be observed with all three codes.

- Figure 6.22 shows the position of the fragments in initial conditions for an aspect ratio of 2:1. This can not be reconstructed for real-world experiments. Therefore, this comparison is purely numeric. In the initial position, the fragments look very similar for the chosen ring size. The fractures are mainly normal to the circumferential direction. The second debris ring is observed for all codes on the opposite side to the initiation of the explosive. *LS-DYNA®* predicts the largest and *MCM* predicts the smallest fragments in the circumferential direction. The size of the fragments predicted with *IMPETUS®* lies in between the size observed for *LS-DYNA®* and *MCM*.

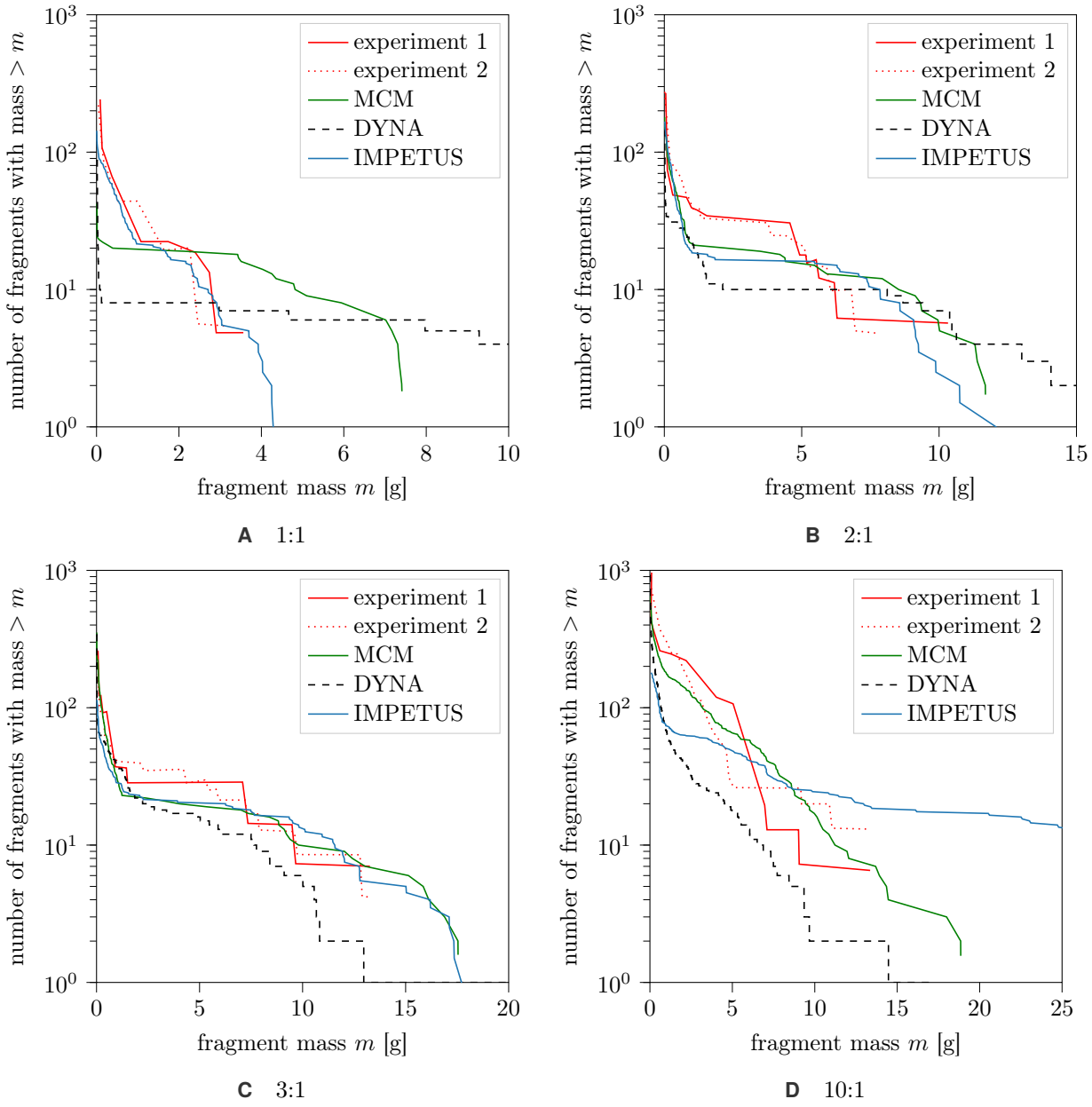

FIGURE 6.20 Natural fragmentation of explosively driven cylinder rings: fragment size distribution for different ring sizes and three numerical models in *MCM*, *LS-DYNA®* and *IMPETUS®*.

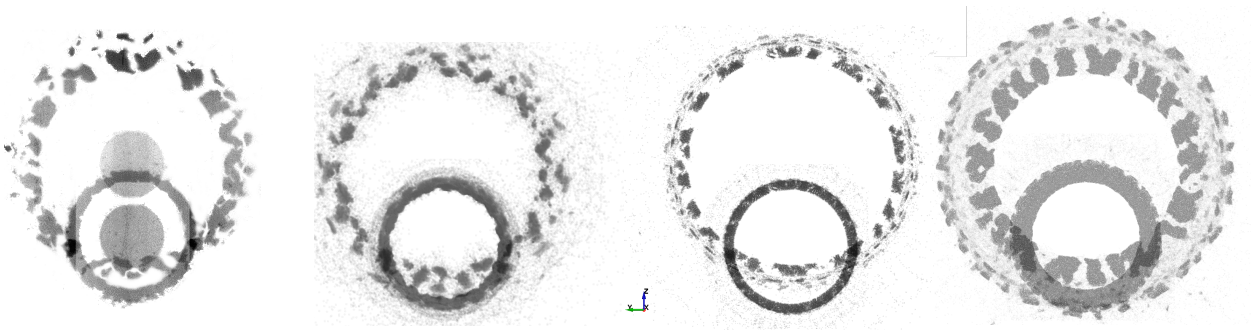

A experiment **B** *LS-DYNA®* **C** *MCM* **D** *IMPETUS®*

FIGURE 6.21 Comparison of X-ray images with corresponding experimental results. *LS-DYNA®* and *IMPETUS®* predicts the rotation of the fragment and give a better qualitative representation (ring size 1:3).

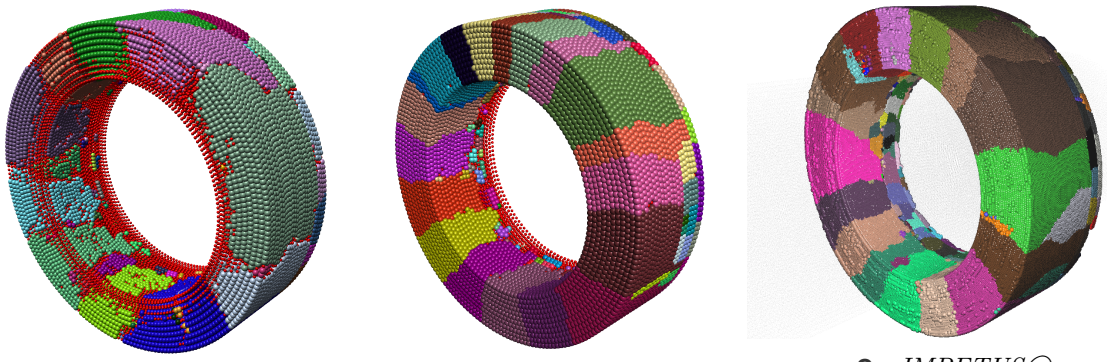

A *LS-DYNA®* **B** *MCM* **C** *IMPETUS®*

FIGURE 6.22 Fragments mapped in initial configuration. Each color represents a unique fragment. Dust particles are visualized red in *LS-DYNA®* and *MCM*, and light blue in *IMPETUS®*.

6.4 Conclusion

We used the SPH model of three simulation codes (*LS-DYNA®*, *MCM* and *IMPETUS®*) in four studies to evaluate the natural fragmentation of explosively driven cylinder rings numerically:

- **STUDY I** investigated three aspects of the numerical model in *LS-DYNA®*: (i) the numerical formulations of SPH, (ii) material strength, and (iii) fracture model settings. First, to avoid numerical fractures, the quasi-linear SPH formulation is suggested, although other formulations were closer to the experimental results. Second, we showed that the Cowper-Symonds modification of the strength model has a distinct impact and improves the representation of the results. Third, we observed that a spall criterion has to be implemented in the fracture model to reproduces the second debris ring—as seen in real-world experiments.

- In **STUDY II** we investigated four modifications that we implemented in *MCM* on top of the original numerical model: (i) randomised damage initialisation, (ii) coupling between fracture and damage

model, (iii) a Newton-Raphson iterative plasticity algorithm, and (iv) modifications of the damage models. Random fracture patterns were improved by using (i), and only minor changes to the results were observed when modifying (ii) and (iii). Applying the triaxiality criterion, such that damage is only accumulated for $\eta > -1/3$, was a game-changer for all damage models. Instead of predicting a scattering of the ring for larger aspect ratios, the fragmentation was accurately described.

- The settings of **STUDY II** are then applied in **STUDY III** to three different plasticity models and three damage descriptions—again with *MCM*. As expected, all hardening rules predicted similar results, whereas the choice of the fracture model has a large impact. Only the Lemaitre and Rittel model describe the increased fragment size for larger aspect ratios. On the other hand, the Johnson-Cook fracture model predicted a constant fragment size for all cases. This was only closer to the laboratory experiments for 1:1 and 2:1 rings. Also, the JC fracture model was better predicting the amount of small fragments. Still the performance of JC and Rittel model is better, as the amount of large fragment is a more critical criteria than the amount of small fragments.

- In **STUDY IV**, we investigated all three final numerical models: *MCM*, *LS-DYNA®* and *IMPETUS®*. Each of them has advantages and disadvantages in different parts of the problem. However, the results do not aim to benchmark the codes for this application. In particular, because each code uses a unique SPH formulation and a different fracture model. Instead, we wanted to see (i) whether another SPH-code is better suited to model highly dynamic events (ii) if we would need another fracture model in *LS-DYNA®* and (iii) where the limitations of our models are.

Based on our findings, it is not necessary to use a different code to predict fracture during high-velocity impact. Instead, it is essential to set up the fracture model of choice with the available data, use a sophisticated numerical formulation, validated material parameters, and verify remaining modelling parameters. For us, this means the following for using SPH in *LS-DYNA®* for highly dynamic simulations: We (i) have to use the quasi-linear formulation if significant tensile stresses occur, (ii) can stick to the JC plasticity model with CS modification, (iii) use the Johnson-Cook damage model, in the way it is already implemented. In particular, we do not rely on other fracture models, where we do not have more accurate damage parameters for the material we use. From the modelling part, we now have to verify the contact description in *LS-DYNA®*, to complete the modelling setup for HVI. The contact description is, besides numerical formulation and material description, the third component that dominates the impact behaviour.

7

Application II: Contact investigation using an impacting sphere

To evaluate the influence of different contact modelling techniques, a simplified, purely numerical test-case is defined where a sphere is impacting a thick plate (compare Figure 7.1). Spherical geometries are typical for hyper-velocity impacts as they are used as representatives for space debris [112]. The different contact options are evaluated for this test case using three necessary metrics which assess the impact and release description. We discuss the advantages and disadvantages of the different contact techniques in FEM and SPH and recommend a suitable choice concerning the application of high-velocity impact. The model has only been tested for the velocity range of interest and might be unsuitable for lower velocities (e.g., car crash $\approx 10 - 20$ m/s). Furthermore, we did not investigate other geometries such as sharp or flat impactors.
This chapter presents the numerical experiments and is structured in six parts:

- A general case description, including material description and dimensioning of the experiment.
- A discussion on suitable measures, apart from the contact force.
- Preliminary studies on contact options in FEM, with particular regards to the *SOFT*option.
- Preliminary studies on contact parameters in SPH; in particular, input parameters for the SPH penalty contact in *LS-DYNA®*.
- The comparison between FEM and SPH with the determined settings, including results with *IMPETUS®*.
- A conclusion on how to set up the numerical contact for other impact applications.

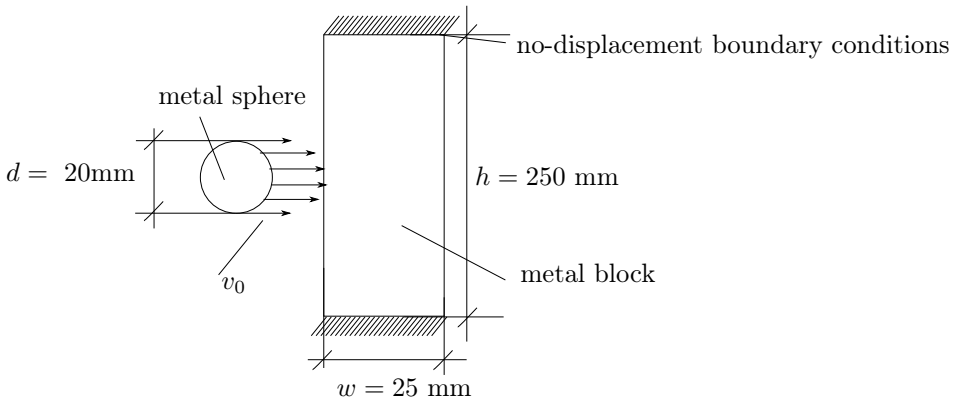

FIGURE 7.1 Setup for evaluating the contact description. A metal sphere is impacting a thick armor steel plate.

7.1 Case setup

A simplified impact case is designed for the experimental evaluation of afore mentioned contact options in *LS-DYNA®* (compare Section 4.2.2). The setup is depicted in Figure 7.1: a spherical impactor with a radius of 10 mm is impacting a plate with a size of 250 mm × 250 mm × 25 mm ($l \times h \times w$) with different impact velocities. In the following, we explain (i) why we chose a spherical impactor, (ii) how we chose the plate dimensions, and (iii) how we determined the relevant velocities.

For (i), a sphere is chosen because the projectile surrogate we investigate in Application III has a hemispherical nose, too. Choosing a spherical impactor instead of the surrogate has multiple reasons: The main objective during the design of this case was to isolate the contact algorithm, as good as possible, from other effects such as material erosion. A spherical impactor has a small depth of penetration and, thus, causes less mesh deformation at the target. Furthermore, we simplified the material such that the case can be used in any other simulation code to validate the contact algorithm. In the plastic-kinematic material description, only the yield stress ($\sigma_y = 1$GPa), Young's modulus ($E_0 = 210$ GPa), and the Poisson's ratio $\nu = 0.33$ are prescribed. Launching spheres is possible in real-world experiments, and contact forces can be measured. So, real-world data can be obtained in the future.

For (ii), the plate size is chosen so that there is little influence from shockwaves reflected at the boundaries. Similar to the typical HVI experiment setup, the plate is clamped at two opposite plate edges. Elastic shock waves travel at a speed of

$$c_{\text{el}} \approx \sqrt{\frac{E}{\rho}} = \sqrt{\frac{2.1 \times 10^{11}\ \text{Pa}}{7800\ \text{m/s}}} = 5200\ \text{m/s} = 5.2\ \text{mm}/\mu\text{s}. \tag{7.1.1}$$

This means that it takes

$$t = \frac{h - d}{v_0} = \frac{250\ \text{mm} - 20\ \text{mm}}{5.2\ \text{mm}/\mu\text{s}} = 48\ \mu\text{s} \tag{7.1.2}$$

for the wave to reach the boundary and return, which corresponds to the length of the impact event.
For (iii) and in order to observe the limitations of the contact algorithms, a velocity range between 200 m/s and 1600 m/s is investigated. Friction is neglected in the contact.

7.2 Metrics to evaluate contact

When two bodies collide, a repulsive force ensures that they do not interpenetrate. This repulsive force is calculated by the contact algorithm and applied to the surfaces of the collision partners. Therefore, we call it the *surface force*. In order to compare multiple impact scenarios, it is reasonable to compare the *maximum surface force* instead of the time course, which, however, contains considerable fluctuations. To ensure that the maximum value is physical and contains no numerical fluctuation, we use the percentile to smooth the data: Let $\boldsymbol{f}_t$ be the vector containing the temporal course of the surface force at a constant time interval and $p_n(x)$ be the n%-percentile of a vector x. Then, we define the smoothed maximum

$$f_{\max,s} = \min(\max(\boldsymbol{f}_t), 1.05\ p_{95}(\boldsymbol{f}_t)). \tag{7.2.1}$$

Assuming a linear distribution of values, we use a correction factor of 1.05 to account for the cut-off and limit the smoothed value to the original maximum. For the FEM simulation, the surface force is a direct output that can be evaluated. For the SPH contact, the surface force between SPH parts is not accessible in *LS-DYNA®*. As a workaround, the surface force between the SPH and the FEM part of the hybrid FEM-SPH target is used (compare Section 4.4.2). For small velocities, little energy is dissipated in plastic deformation, and the force at the interface is the same as at the actual contact. For large velocities, differences might occur due to plastic energy dissipation.
We summarize the following two definitions:

- the *surface force* $\boldsymbol{f}_t$ is a vector containing the sum over all incremental surface forces of elements which are in contact for each time step, and
- the *maximum surface force* $f_{\max,s}$ is the smoothed maximum of the *surface force* according to (7.2.1).

During the deceleration of the sphere, the kinetic energy is partially transferred to an elastic potential. When the plate stops the impactor, this elastic potential is released and reconverts into kinetic energy. We call this the elastic rebound of the sphere. Two properties characterise this rebound:

- the *release velocity* v_{rel} is the sphere velocity after the rebound, and
- the *release time* t_{red} is the time when the normal velocity of the sphere changes its sign.

Only elements and particles that are still connected to the deformed sphere determine the release velocity. In terms of protective design, we evaluate the following integral values, which are also influenced by the contact description:

- the *bending of the plate* b_{plate} is the bulging thickness due to plastic deformation, and
- the *depth of penetration* d_{P} describes the crater depth minus the bulging thickness,
- the *length reduction of the sphere* l_{red} is the difference between initial and final length in the direction normal to impact.

Besides scalar, quantitative metrics, we do also compare the qualitative impact behaviour with 3D visualisation.

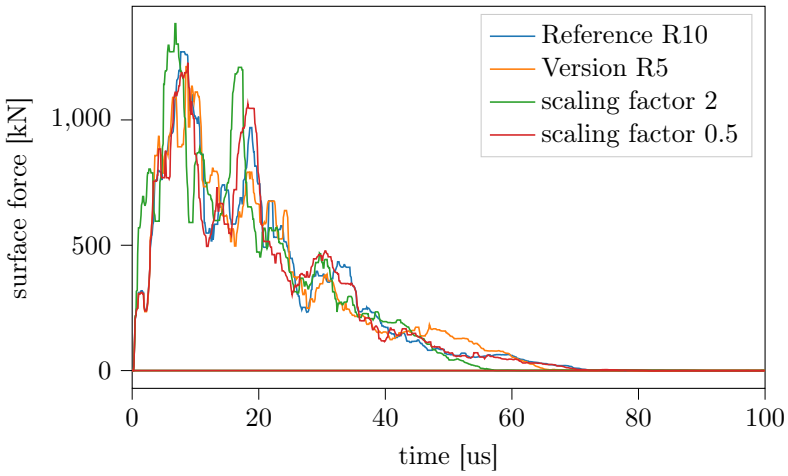

FIGURE 7.2 Impact of a sphere: investigation of a modification of the penalty scaling factors. Median filter (width = 11 time steps) applied to damp oscillations. Solution with *LS-DYNA®* version (release 5) quantify the differences.

7.3 Preliminary studies with FEM

As described in Section 4.2, *LS-DYNA®* offers three implementations for the computation of the contact stiffness k. k determines the repulsive force during the contact and is therefore of substantial interest. The three implementations can be selected by the *SOFT* parameter: 0, 1, or 2 (compare Section 4.2.2).

To exclude influence from the penalty stiffness, we present results for different penalty stiffness scaling factors in Figure 7.2. The difference between the two versions of *LS-DYNA®* is more significant than a difference due to the penalty stiffness. This result underlines that the influence of the stiffness factor can be neglected.

Figure 7.3 compares the contact behaviour of three different configurations in *LS-DYNA®*. Since the standard stiffness computation (*SOFT*=0) is not able to detect the contact correctly, we compare (i) *SOFT=1*, (ii) *SOFT=2*, and (iii) *SOFT=2* with viscous damping. Figure 7.3 consists of six plots which cover different aspects of the contact: plots 7.3A and 7.3B investigate the grid convergence for (i) and (ii), plots 7.3C and 7.3D show the converged solution for different impact speeds for (i) and (ii), and plots 7.3E and 7.3F investigate the influence of viscous damping (iii).

For the grid convergence shown in plots 7.3A and 7.3B, the surface force is plotted over the simulation time for an impact velocity of $v_0 = 800$ m/s and three different grid resolutions. The grid resolutions are chosen so that the number of elements doubles with each refinement step. While the *SOFT*=1 contact shows fast and large oscillations for all refinements, the *SOFT*=2 contact seems to be much smoother and already converged at the "mid"-resolution. The magnitude of the maximum surface force, and also when the surface force reaches zero, is similar in both configurations.

Plots 7.3C and 7.3D have the same layout, but instead of different refinement levels, different initial velocities are compared. We observe that the most considerable difference between the two configurations occurs for the highest velocity of $v_0 = 1600$ m/s. There, the segment-based algorithm predicts a surface force approximately twice as large as the surface force predicted for 800 m/s. The corresponding results for

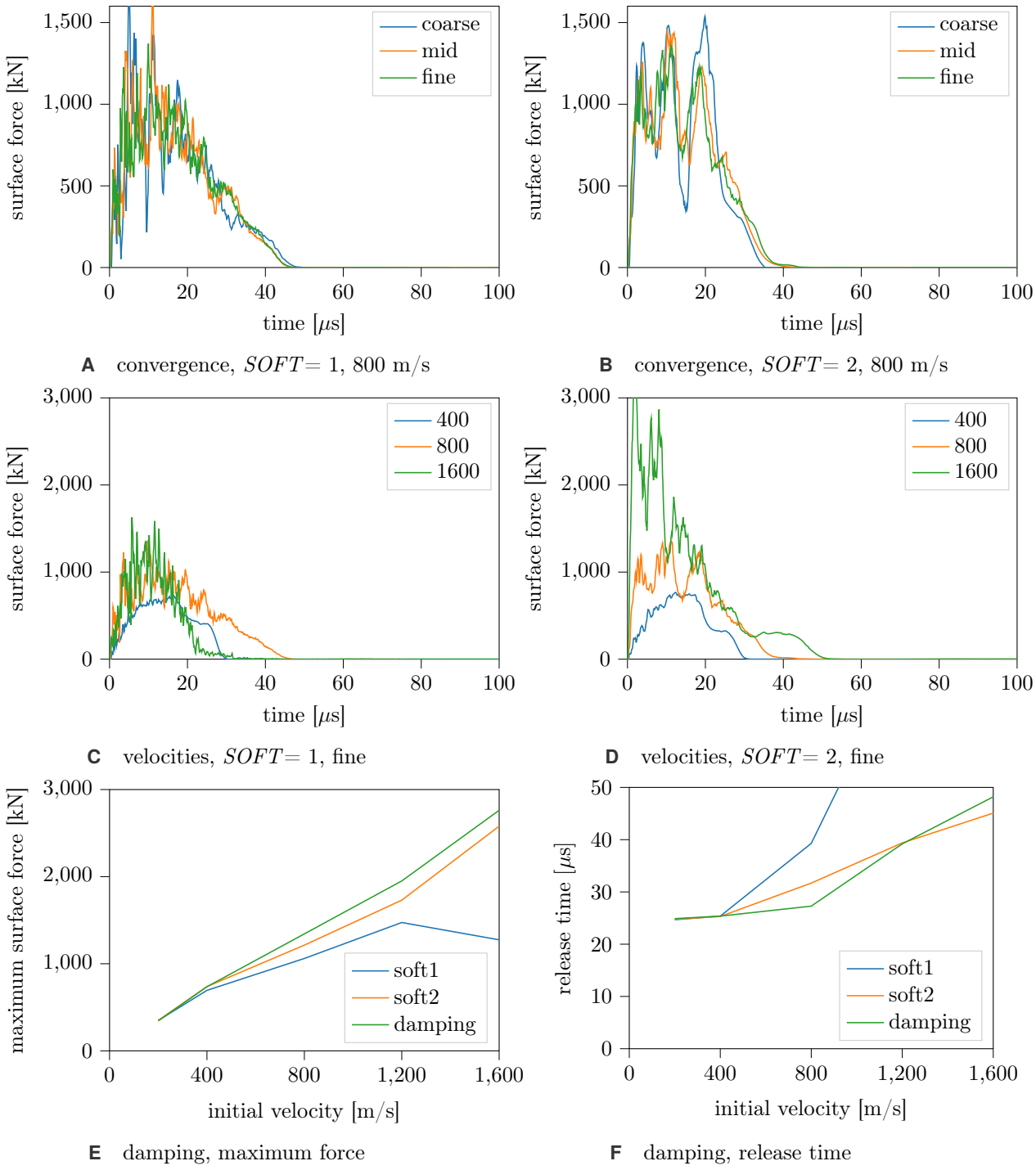

FIGURE 7.3 Investigation of the $SOFT$=1 and $SOFT$=2 contact algorithm in FEM for the application of high-velocity impact of a sphere (compare Figure 7.1). The first row compares three different refinement levels for 800 m/s; the second row compares different velocities between 200 m/s and 1600 m/s; the third row investigates the influence of viscous damping. Against intuition the surface force is larger with damping.

400 m/s and 800 m/s are similar concerning the peak values and release time. Hence, $SOFT = 1$ predicts a limit for the surface force, whereas $SOFT = 2$ predicts linear growth. The question is whether the surface force is physically limited or not, to decide which of the simulation results is more accurate.

This question is elaborated in the digression below. Lastly, plots 7.3E and 7.3F compare the results to the configuration with damping. Instead of the temporal progression, we compare the smoothed maximum surface force (7.2.1) and the release time as a function of the initial velocity. This metric is the best way to compare the key features identified in plots **A-D**. By this, we can better compare the information which showed to be most relevant in the previous plots. For both properties, the influence of adding viscous damping to the model is smaller compared to the difference between the two *SOFT*-options. Against our intuition, damping leads to an increase in the surface force. For the release time, no trend can be identified. The *SOFT*=1 option fails in predicting both values for the highest velocity. For small velocities of 200 m/s and 400 m/s, all models are almost identical.

We conclude that the only model which can predict the impact behaviour for the whole velocity range is the *SOFT*=2 configuration. Enabling viscous damping influences the result only slightly for large velocities, and is therefore not necessary. The general behaviour of $SOFT = 2$ looks much smoother in general. Furthermore, the contact force is already well converged for the medium resolution. In contrast, the results with $SOFT = 1$ are less consistent and show a lot of local peaks. These local peaks or shark-teeth-profile is accounted to the erosion criteria. Whenever an element is eroded, no contact between the two parts is detected until the next element layer impacts, and the contact is enabled again.

7.3.1 Digression: theoretical aspects of the maximum surface force

Depending on the setup of the simulation, we observed two different characteristics of the contact force. Either the contact force is limited at $v_0 = 800$ m/s (e.g., $SOFT = 0$), or the contact force is not limited in the velocity range observed (e.g., $SOFT = 2$ and *Impetus* in Section 7.5). Hence, the question is which of the two is true: is the contact force theoretically limited due to the material strength, or is the limitation artificial? Even if the contact force is limited, it might still be necessary from a numerical point of view to exceed the physical limitation in order to maintain the non-penetration condition.

For our theoretical analysis, we assume similar to Taylor [191] a uniaxial stress state on the surface of the contact area. Thus, we consider the projected contact area A_{proj}, which is for a sphere

$$A_{\text{proj}} = \pi r^2. \tag{7.3.1}$$

Due to deformation, the projected radius r is larger compared to the initial radius r_0. The measured radial expansion of the sphere is approximately $r = 1.2\ r_0$. For the sphere with $r_0 = 10$ mm, the upper bound for the projected area is $A_{\text{proj}} = 4.52 \times 10^{-4}\ m^2$. For the material, we assume that failure occurs at a yield stress of $\sigma_{\max} = 2.95 \times 10^9$ Pa. Assuming uniaxial stress the resulting maximum force is

$$f_{\max} = \sigma_{\max} A_{\text{proj}} = 4.52 \times 10^{-4}\ \text{m}^2\ \times 2.95 \times 10^9\ \text{Pa} = 1.33 \times 10^6\ \text{N} = 1330\ \text{kN}. \tag{7.3.2}$$

This derivation gives evidence that the limitation observed in the numerical simulation is not artificial but can be related to the geometry and material properties. However, the contact force is a parameter which is of academic rather than industrial interest. Thus, if our model predicts the integral quantities correctly, this

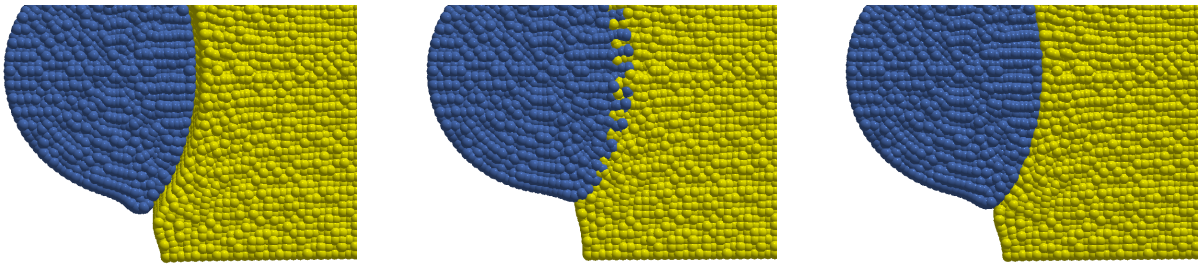

A $SRAD = -3.0$, included void **B** $SRAD = -1.5$, interpenetration **C** $SRAD = -2.2$, correct contact

FIGURE 7.4 Impact of a sphere on a plate: qualitative influence of the *SRAD* parameter on the simulation result. Contact is detected too early **A** or too late **B** for an unsuited choice of *SRAD*.

result can be ignored.

7.4 Preliminary studies with SPH

As described in Section 4.2.2, there are two different contact algorithms in SPH: the standard interpolation method and a node to node penalty contact. With the standard contact, the interacting bodies stay in contact after impact as the adhesive forces are too large to trigger the release after impact. Based on our experience in similar real-world experiments, and based on the results obtained with the FEM, this behaviour is unphysical. Since the standard contact type can not be modified, this section investigates only the penalty based contact to find a parameter configuration that gives physical results. There is little published on this new methodology in *LS-DYNA®* [102]. So, the aim is to identify the relevant parameters and to assess how they influence the solution. The following four parameters are investigated independently:

1. *SRAD* (the minimum distance for two particles to be in contact),
2. *DFACT* (the damping of kinetic energy),
3. *PFACT* (the penalty factor, which influences the contact forces), and
4. *ISOFT* (the *SOFT* contact option similar to the FEM).

Each study is repeated with the determined parameters of the other studies as a default value. Therefore, the order of the studies is irrelevant. To ensure that the choice of parameters does not depend on the velocity, we examine two representative velocities (200 m/s and 800 m/s). A larger velocity adds further difficulties to a consistent comparison, and results are presented in the final study in Section 7.5. Similar to the last section, we compare the maximum surface force, defined by (7.2.1), and the release properties.

7.4.1 SRAD: the minimum distance for two particles to be in contact

The *SRAD*-parameter determines the minimum distance below which the contact algorithm is activated (compare Figure 4.4 and (4.2.9)). Figure 7.4 depicts the qualitative behaviour: If the magnitude of *SRAD* is too large (Figure 7.4A), a void with no particles remains between the two bodies. This void transfers the contact force but has no physical meaning. For a too small value, such as $SRAD = -1.5$ (Figure 7.4B), the

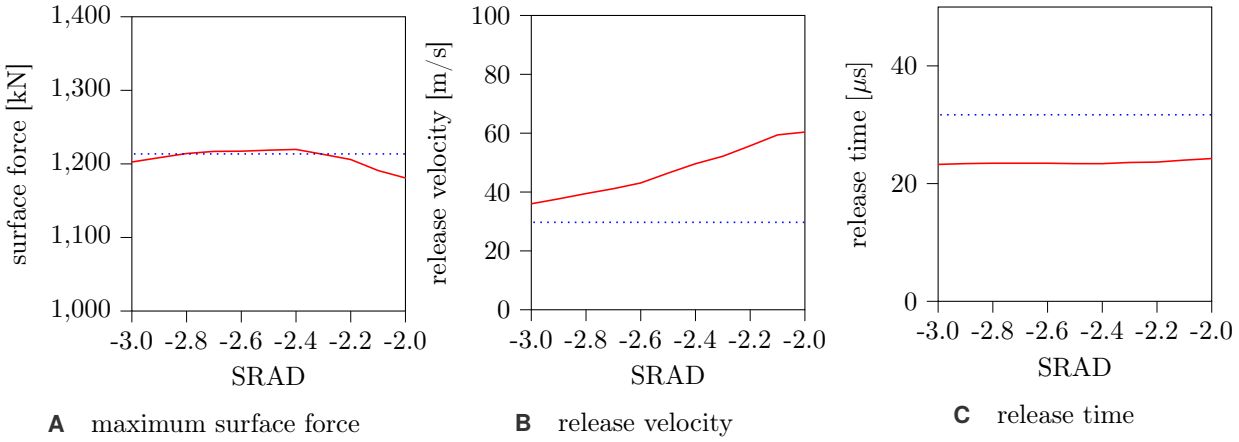

A maximum surface force **B** release velocity **C** release time

FIGURE 7.5 Impact of a sphere on a plate: influence of the SPH parameter *SRAD* on the contact force and release parameters for values between $-3.0 \leq SRAD \leq -2.0$. Comparison between SPH (solid line) and FEM results (dotted line).

contact stays undetected and the bodies interpenetrate. Thus, only a value between $-3 \leq SRAD \leq -2$ is physical (e.g., $SRAD = -2.2$ in Figure 7.4C). Figure 7.5 compares the influence of *SRAD* on the surface force, the release velocity, and the release time. The contact force is little affected, and all values lie between $\pm 3\%$ of the solution obtained with the FEM. The curve shows a local maximum for $SRAD = -2.4$. The release velocity is strongly dependent on the *SRAD* parameter. The larger the parameter is, the slower is the release velocity. For a value of -2.0 and -2.1, the slope of the curve is close to zero, which indicates that this is a correct choice. However, there the release velocity is twice as large as the release velocity measured with the FEM, which we assume to be already a good representation of the real behaviour. In contrast to the strong dependence between release velocity and the contact parameter, the release time is not affected and on average 8 μs or 26% earlier compared to the FEM. As we do not have reference values from experiments or analytical models, we select $SRAD = -2.2$ which does not create a void in Figure 7.4 and is very close to the FEM result in terms of the surface force.

7.4.2 DFACT: the damping factor, which determines the damping of kinetic energy

In contrast to the description in the manual [85], the damping factor is only a binary switch which is enabled for $DFACT = 1.0$. No partial damping is possible in the version we used mpp – double-precision – Release 11 – Version 132007, so we can only compare the two binary cases of damping or no damping. Enabling damping increases the surface force by 79 kN or 7.2% of its undamped value, which is closer to the FEM result than without damping. The return time is 1 μs earlier, and the return velocity is slightly larger (3 m/s). This behaviour is contradictory to intuition: The damping describes the velocity-dependent force and is supposed to add stickiness. Thus, it should increase the return time and decrease the return velocity. Due to the unexpected behaviour, we ignore the *DFACT* parameter in our model.

7.4.3 PFACT: the penalty factor, which influences the contact forces

In the FEM, the penalty factor is often used to change the contact behaviour artificially [28]. It changes the spring stiffness and is supposed to be an essential parameter for the SPH contact as well. The default value for this parameter is 1.0, but the manual encourages the user to define much smaller values between 0.01 and 1×10^{-4} for high-velocity applications. However, we experienced that a penalty stiffness below $PFACT \leq 1$ has the same effect like setting $SRAD \leq 2$: The contact is partly undetected, and the bodies interpenetrate. Although the manual does not recommend a value above one, we compare values up to ten. For our evaluation, we have to consider two things: First, the solution obtained with the FEM is good for a rough comparison—but not the reference. Therefore, we are more interested in general trends in order to find a proper setting. Second, the contact force measured in the SPH is not precisely the same as in the FEM as it is evaluated at the contact between the SPH and the FEM discretisation in the hybrid mesh.

Figure 7.6 shows the results for both, 200 m/s and 800 m/s, to ensure the results are generalisable to a larger velocity range as we expect a high sensitivity for this parameter. For 800 m/s, the surface force predicted with SPH is smaller than with the FEM for all configurations. We identify a local maximum for $PFACT = 3$. For 200 m/s, the surface force increases monotonically and intersects with the FEM result for $PFACT = 1$. For a value of $PFACT = 0.01$, as suggested in the manual, the surface force is 30% below this value. In general, the difference between the FEM and the SPH is acceptably small otherwise. In the following, results of $PFACT < 1$ are therefore removed from the analysis. For the release values, we can make the following observation: While the release velocity is strongly dependent on the penalty factor, the release time is little affected—similar to what was observed for $SRAD$. With an increasing penalty factor, the release velocity decreases. For an initial velocity of $v_0 = 800$ m/s, v_{rel} decreases from 60 m/s to 16 m/s and for $v_0 = 200$ m/s, v_{rel} decreases from 65 m/s to 35 m/s. The corresponding, unaffected release times are 26.7 ± 0.5 m/s and 24.8 ± 0.6 m/s.
Based on our observations for the surface force and the release velocity, a value between $1 < PFACT < 3$ is a reasonable choice for HVI.

7.4.4 ISOFT: the SOFT contact option similar to the FEM

Exemplarily, the study of the penalty factor was repeated with $ISOFT = 0$ to see how the $ISOFT$ option influences the result. In contrast to the FEM, where it results in a significant difference, no change was observed for all cases in the SPH. We can not say whether there is a velocity, discretisation, or geometry, where the $SOFT$-option changes the contact behaviour, but for our case, it does not. Thus, we do not investigate this parameter any further.

7.4.5 Conclusion and final parameter choice

We investigated the four relevant tuning parameters of the SPH contact in *LS-DYNA®*. While $SRAD$ and $PFACT$ are crucial to obtain a physically correct solution, $DFACT$ and $ISOFT$ have little or no influence for our application. A contact-distance of approximately two times the particle diameter ($SRAD \approx -2$) proved to be large enough to prevent interpenetration and small enough to not result in voids between the bodies. This value was also giving similar results than the FEM in terms of surface force and release properties. Therefore, it is a suitable choice for our application. Despite the recommendation of a small stiffness factor (1×10^{-4} to

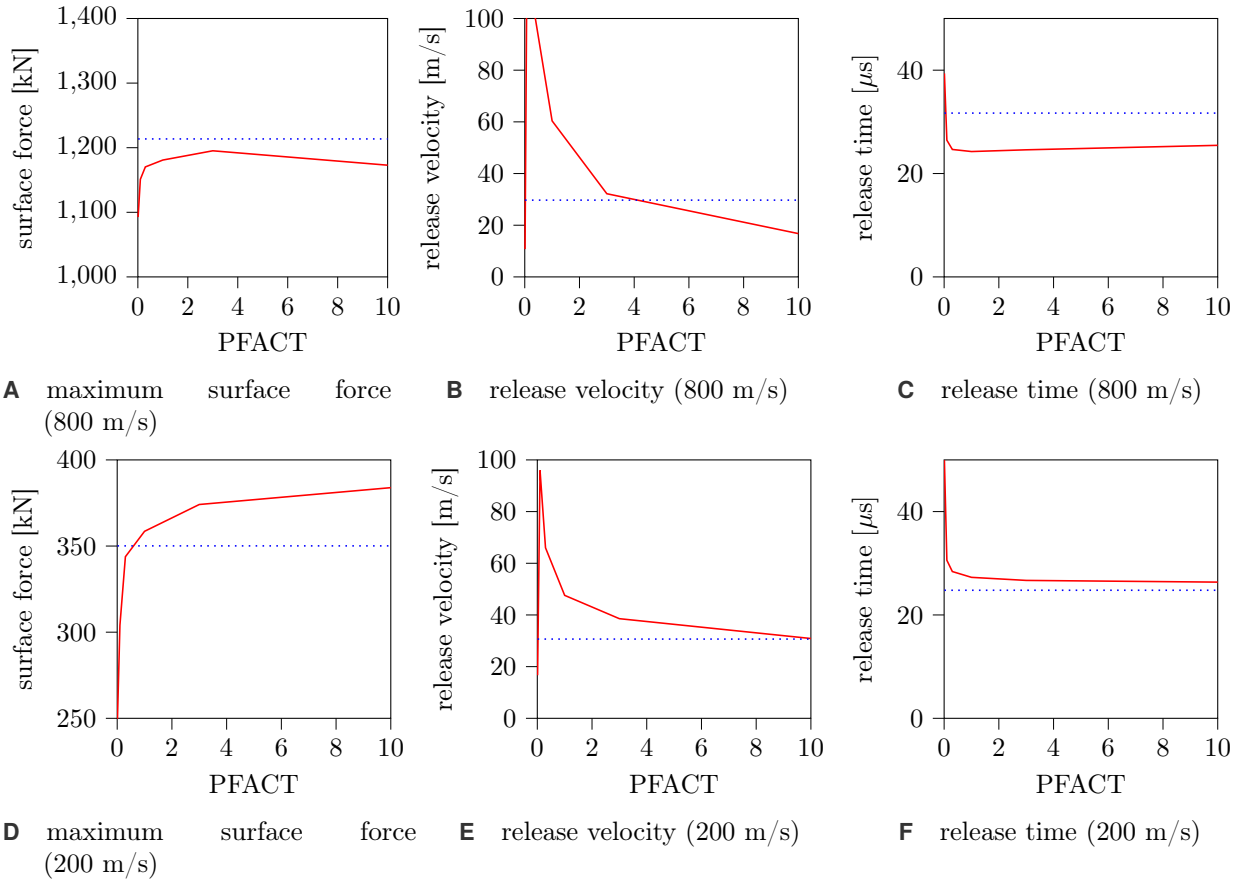

A maximum surface force (800 m/s) **B** release velocity (800 m/s) **C** release time (800 m/s)

D maximum surface force (200 m/s) **E** release velocity (200 m/s) **F** release time (200 m/s)

FIGURE 7.6 Impact of a sphere on a plate: Influence of the SPH parameter *PFACT* on the contact force and release parameters for values between $0.01 \leq PFACT \leq 10.0$. Comparison between SPH results (solid line) and FEM results (dotted line).

0.01) in the user manual, it requires a stiffness factor of 1.0 or higher to prevent the interpenetration of the impacting bodies. A value of *PFACT* between $1.0 \leq PFACT \leq 3.0$ matches the FEM results best regarding the release velocity and surface force. No influence on the release times can be observed for both, *SRAD* and *PFACT*. The *SOFT*-option and the contact-damping have little influence on the results. Furthermore, similar to the observations with FEM, we observe a contradictory behaviour for enabling the damping: the surface force and release velocity are amplified and not damped.

7.5 Final comparison of FEM and SPH

In the last two sections, we identified the optimal contact settings for FEM and SPH in *LS-DYNA®*. In this section, we compare these two simulation approaches with another SPH formulation in *LS-DYNA®* and a FE model in *IMPETUS®*. Furthermore, the aim of this section is to extend the study for different impact velocities v_0. The quasi-linear SPH formulation (compare Section 3.3.4) uses the same contact settings determined for the standard SPH, and the *IMPETUS®* solver has an optimised contact formulation for the HVI which does not require further adjustment. Since the *IMPETUS®* solver is target-made for impact applications, we consider the solution with *IMPETUS®* as the reference solution. The quasi-linear SPH results are included to quantify the difference towards a more accurate SPH formulation. Thus, we compare the following four cases:

- *FEM* denotes the *LS-DYNA®* solution with FEM, *SOFT*=2, and no damping,
- *SPH* denotes the *LS-DYNA®* solution with the standard SPH formulation and the penalty contact,
- *F12* denotes the *LS-DYNA®* solution with the quasi-linear SPH formulation and the penalty contact, and
- *Impetus* denotes the *IMPETUS®* solution with third-order finite elements and standard contact.

Besides comparing the primary contact properties, which are investigated in the previous sections, we compare the qualitative behaviour, the depth of penetration d_P, and the bending of the plate b_plate. These properties are not only influenced by the contact definition but also the numerical method. Nonetheless, the transferred contact energy is one of the primary mechanisms which provokes the bending and deformation of the plate. Comparing these characteristics has the advantage of smoothing local peaks of contact energy by comparing the final state of the simulation. Furthermore, d_P and b_plate are the properties that define a protective structure. It is essential to know which attributes are more related to the contact definition and which of them are more related to the numerical method. We identify the length reduction of the sphere l_red as a parameter which is mainly determined by the numerical description as it is mainly related to the stiffness of the elements. We use it to quantify the influence of the different methodologies applied. This approach is the only way to give a conclusive statement about the accuracy of the contact algorithms.

7.5.1 Qualitative behaviour

Figure 7.7 shows the postprocessed simulation results for an impact velocity of $v_0 = 800$ m/s, 30 μs after impact. The time corresponds approximately to the release time, and the velocity is similar to the original

use-case of rifle ammunition. In the following, some characteristics of the different simulation approaches are discussed. Image 7.7A shows the result obtained with *FEM*. The elements of both the impactor and the target are eroded in the contact area. The erosion influences d_P and b_plate, which is further investigated in the following sections. Image 7.7B shows the results obtained with *Impetus*. The higher-order elements can handle the deformation and are not relying on erosion. Therefore, we expect that d_P is smaller than for standard FEM, and the remaining sphere is larger than for the other results. The *SPH*, in image 7.7C, shows a more hydrodynamic behaviour of the particles. The original sphere transforms in a disc-like object with a larger diameter compared to *FEM* and *Impetus*. A second aspect which influences our results is tensile instability of the standard SPH method (*SPH*). This can be seen when comparing *SPH* and *F12* at the fastest test speed of 1600 m/s (compare Figure 7.8). There, the plate stays intact only with the improved formulation *F12*. Based on the FE approximations an intact rather than a fractured target is expected.

7.5.2 Contact force

Figure 7.9A shows the maximum surface force, according to (7.2.1), for the four different cases. No significant differences are observed for impact velocities of $v_0 \leq 800$ m/s. For $v_0 = 1200$ m/s, both FEM solutions predict the same results and the two SPH solutions are similar as well. The surface force predicted with *FEM* and *Impetus* is larger compared to *SPH*. The higher value might be attributed to the impossibility of measuring the contact force directly at the contact, and partial energy dissipation for larger velocities. For the highest velocity, all approaches predict a different force. For the *FEM* solution, the difference to *Impetus* might be due to more erosion at the target. The *SPH* solution shows a tensile instability for this velocity (compare Figure 7.8), which might explain the reduced contact force for 1600 m/s.

In conclusion, all methodologies are consistent for impact velocities below 1000 m/s. For larger velocities, differences occur that might not only be related to the contact description.

7.5.3 Release properties

As introduced in Section 7.2, there are two properties which characterize the release behaviour: the release time t_rel and the velocity v_rel. While t_rel is a relatively stable measure, v_rel is difficult to predict. We expect a large spread for the sphere rebound if the material behaviour is dominated by plastic flow and only a small

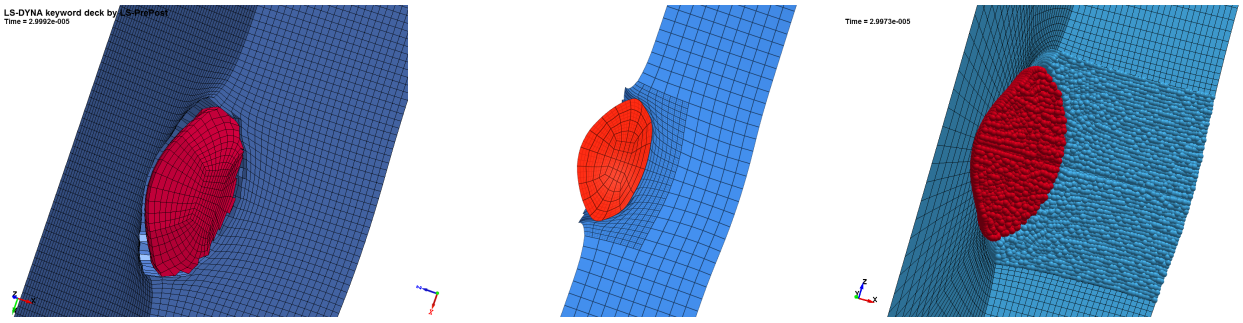

A *FEM* **B** *Impetus* **C** *SPH*

FIGURE 7.7 Impact of a sphere on a plate: General behaviour 30 μs after impact; predicted with the different simulation approaches for an initial velocity of $v_0 = 800$ m/s.

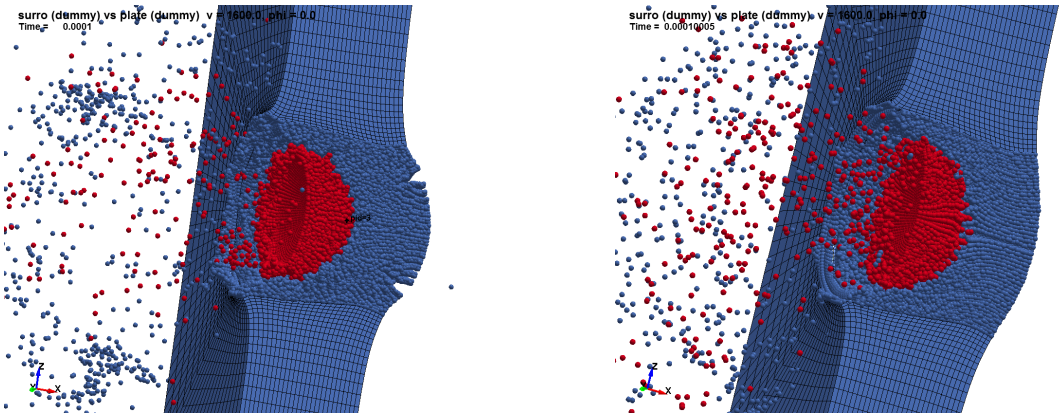

A standard SPH (*SPH*) **B** improved SPH (*F12*)

FIGURE 7.8 Impact of a sphere on a plate: Tensile instability of the standard SPH method at $v_0 = 1600$ m/s, 100 μs after impact. The tensile instability reveals as cracks opening up at the opposite side of the plate.

elastic deformation. However, here the goal is to see a general trend and verify that all methods predict the release of the sphere. The latter is fulfilled, and we observe the following trends for the release velocity (compare 7.9B): Both *FEM* and *Impetus*, predict a smaller release velocity of 15 m/s $\leq v_{\text{rel}} \leq$ 35 m/s, which is fluctuating for different initial velocities v_0. The release velocity predicted with all approaches, but *Impetus* is, on average, 10 m/s larger compared to *Impetus*. Except for 1600 m/s, *SPH* and *F12* are nearly identical. Large fluctuations between 20 m/s $\leq v_{\text{rel}} \leq$ 70 m/s are observable for the two SPH solutions compared to the consistent results with the FEM. All four approaches predict a similar value for a velocity of 1200 m/s. In connection with the further results, this is likely a coincidence.

For the release times in 7.9C, we can distinguish two behaviours: (i) *FEM* predicts a monotonic increase of the release time, and (ii) the other simulation methods predict a local minimum for an initial velocity of 800 m/s. *SPH* and *Impetus* are similar, except for the highest impact velocity. This similarity indicates that the release time is a quantity that is not significantly affected by the numerical description. Only for the highest velocity, the standard SPH method predicts a more than 50% increased release time.

7.5.4 Length reduction of the impactor

Three properties determine the length of the sphere after impact in 7.9D: the erosion criteria, the material, and the contact algorithm. Since the material is unchanged, it reduces to two properties: the erosion criteria and the contact algorithm. Similar to previous investigations, there are no significant differences between FEM and SPH for impact velocities of up to 800 m/s. For higher velocities, a smaller residual length of the sphere is observed with the *FEM*. We attribute the difference to the element-erosion which occurs in particular for higher velocities $v_0 \geq 800$ m/s. The length reduction predicted with *Impetus* is align with *SPH*. As discussed in the introduction of Section 7.5, l_{red} is not an attribute of the contact algorithm but the numerical problem description. This result confirms the statement. The *FEM*, as implemented in our model, is not able to predict the large deformation. Instead, higher-order FEM or SPH are required to describe the contact for this velocity range (here: *Impetus*, *SPH* and *F12*).

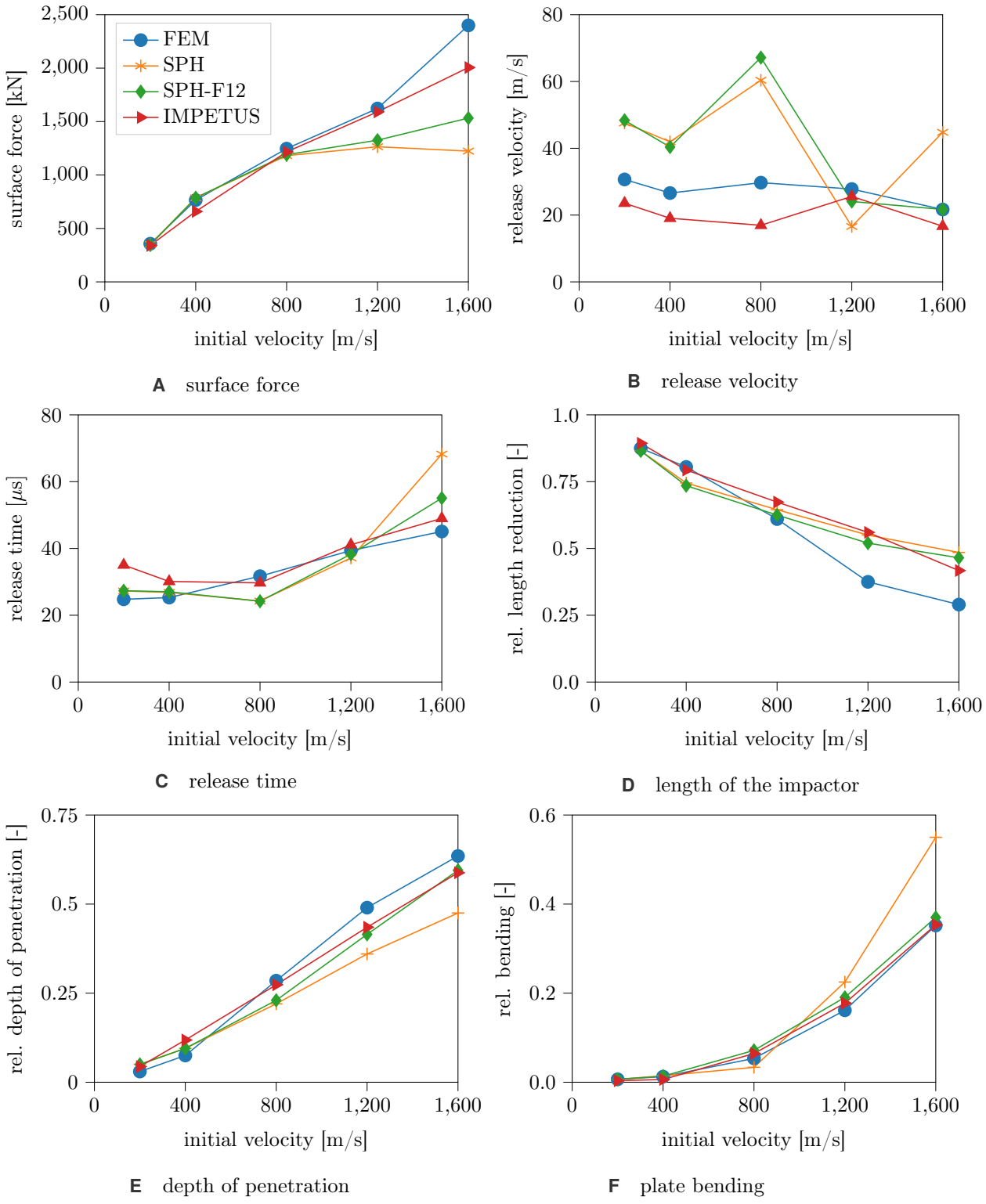

FIGURE 7.9 Impact of a sphere on a plate: Summary of all results *LS-DYNA®* (*FEM* (blue, sphere), *SPH* standard formulation (orange, plus), *F12* quasi-linear formulation (green, diamond) and *Impetus* (red, triangle). **A** maximum surface force extracted from the simulations according to (7.2.1); **B** – **C** release properties; **D** – **F** effect of the contact force onto the target.

7.5.5 Depth of penetration and plate bending

The depth of penetration d_{P} and the plate bending b_{plate} are essential metrics to assess the protection level of a structure. Both properties increase for higher velocities. While d_{P} increases linearly (compare 7.9E), b_{plate} increases polynomially (compare 7.9F). All results are consistent for velocities below 1000 m/s. Above this velocity we observe two different behaviours for d_p: First, *FEM* predicts a larger d_{P}, which is probably due to element erosion and not contact related. Second, *SPH* predicts a considerably smaller value for d_{P} and a more extensive bending. This is attributed to the numerical description since the *SPH* is unstable in tension (compare Figure 7.8).

7.6 Conclusion and recommended settings

Isolating the contact description in a simulation and finding a proper metric to evaluate and compare the contact behaviour in FEM and SPH with different contact algorithms is not straight forward. In this chapter, we propose a purely numerical, simplified example of a sphere impacting a steel plate at a high-velocity.

The geometry and the velocity range are chosen similar to our main interest Application III. The simplified geometries (sphere impactor and cuboid plate) have the advantage that the meshes can be generated automatically with the preprocessing software described in Section 4.4. As a further simplification, a simple material model is used which assumes linear hardening after yielding and which initiates fractures at a user-defined strain. Two different numerical codes are compared: *IMPETUS®* and *LS-DYNA®*. While the first of them provides an optimised contact algorithm for this application, different contact options were compared to set up *LS-DYNA®* for the given application and velocity range.

In this context, six metrics were introduced to evaluate the results: First, a metric which is directly related to the impact description: the transferred *contact force* f; Second, the contact algorithm is responsible for the release behaviour, which is quantified with the two metrics *release velocity* v_{rel} and *release time* t_{rel}. The latter proved to be a more stable metric. Third, the resulting damage is investigated, according to the requirements for a protective structure. This includes three metrics: the *depth of penetration* d_{P}, the *bending of the plate* b_{plate}, and the *length reduction of the impactor* l_{red}.

As mentioned, not only the contact description but also the numerical discretisation of the underlying equations influences the result. We propose the following approach to distinguish influences from the numerical description and the contact description: We compare different properties which are influenced to a different amount by the numerical description and the contact description. Then, we investigate these properties separately and combine the findings.

The preliminary studies identify segment-based contact ($SOFT = 2$)—combined with a fine computational grid and optionally viscous damping enabled—as a stable setup for the whole velocity range with the FEM in *LS-DYNA®*: . In the SPH framework in *LS-DYNA®*, a penalty contact has to be defined instead of the standard contact to correctly capture the release condition ($SRAD \approx 2$, $PFACT \approx 1 - 3$).
Having found suitable setups in *LS-DYNA®*, we compare four approaches: the linear FEM in *LS-DYNA®*, the third-order FEM in *IMPETUS®*, the standard formulation of SPH in *LS-DYNA®*, and the improved quasi-linear implementation of SPH in *LS-DYNA®*. The latter was included in the analysis since the standard SPH method is not stable in tension. Still, the standard SPH is used in Application III as it is more reliable

than the improved implementation, where we often experienced run time errors. Furthermore, it is more efficient with our work station. Therefore, it was important to test it in this analysis, to see at which velocities the instability gets unfeasible. The following results were obtained for this final comparison:

For up to 800 m/s impact velocity, all four simulations predict similar contact forces. Only for higher velocities, differences were observed: In general, the SPH predicts a smaller contact force than the FEM. For the release properties, the FEM in *LS-DYNA®* predicts a monotonically increasing release time. In contrast, the other methods predict a local minimum at $v_0 = 800$ m/s. Especially for the highest initial velocity ($v_0 = 1600$ m/s), the results differ. The investigation of the depth of penetration d_P confirms the observation above, where the largest difference occurs at velocities above 800 m/s. The linear FEM predicts the largest d_P and is, thus, most conservative. However, this can be attributed to erosion, which is significant for these velocities. The standard SPH method, predicts a significantly lower value for d_P for $v > 800$ m/s. One reason for this is accounted to the tensile instability, which becomes noticeable and leads to less penetration, more shearing, and, thus, more bending. Regarding the length of the impactor, we observe that the FEM solution in *LS-DYNA®* deviates for large velocities from all other results. This deviation is attributed to erosion which is needed to stabilise the simulation. The FEM solution with *IMPETUS®* is in good accordance with the results with SPH for the whole velocity range.

Since the velocity of Application III is 800 m/s and little affected by tensile instability and erosion, we can use the following setup in our next chapter: for FEM we can use the contact with *SOFT*=2; for SPH we can use the penalty contact setup derived here—with standard SPH.

8

Application III: High-velocity impact of a projectile surrogate

This work aims to understand ricochet, fracture, and fragmentation during oblique high-velocity impact. The first two applications investigated contact, different constitutive models, and damage models for similar applications. Similar is meant in this context regarding the material, the magnitude of the strain rate, and the dimension of the geometry.

In this chapter, we propose a surrogate of a small calibre projectile that has reduced complexity regarding material and geometry compared to real small calibre ammunition. We investigate internal and external ballistics to prove that our surrogate is suited for this purpose. Our main focus, however, lies on the terminal ballistics (TB) properties. We conduct two kinds of experiments regarding TB: first, we investigate the ballistic limit of the surrogate for different plate thicknesses; second, we analyse the impact for different oblique angles with particular regard to fracture and ricochet behaviour. Ricochet as a protective mechanism is for example of particular interest for helmet design [180]. Helmets are designed, such that they enhance a ricochet which is fatal to the soldier in fewer cases.

This work develops a numerical model which in the future can be applied to helmet design as well. Here, we compare three numerical approaches: FEM, SPH, and a mixed approach using both models (HYBRID). The mentioned TB real-world experiment with the surrogate is used as a validation case. This validation shows how well each of the numerical models can predict fracture and the projectile motion after impact. In terms of real-world data, we compare residual length, mass, deflection angle, and velocity of the largest fragment as well as the qualitative match. This chapter is structured in two parts:

- The first part shows the real-world experiments. Here, we explain how we designed the experiment and the surrogates internal, external and terminal ballistic properties. The main focus lies on the TB results, which are used in the second part.

- The second part shows the validation of our three numerical models with the TB experiments presented in the first part. We investigate three modelling aspects: (i) the influence of the improved contact description determined in Application II, (ii) different particle distributions that were introduced in Section 4.4.1, and (iii) the run time advantages of the HYBRID model we developed in Section 4.4.2. In a final comparison, we present the results of the optimised FEM and HYBRID model.

8.1 Real-world experiments

The first part presents the real-world experiments that were carried out with the projectile surrogate and is structured as follows: First, we explain the design of the validation experiment, which includes the surrogate and the experimental setup. There, we detail in particular the choice of the surrogate geometry and material (Section 8.1.1). Next, we investigate two properties of the internal ballistics. First, we investigate the transfer of the rotation from the barrel groves. Second, we discuss the relationship between powder mass and muzzle velocity (Section 8.1.2). Regarding external ballistics, we study the yaw of the projectile using paper stripes in the flight axis (Section 8.1.3). For the perpendicular impact tests, we determine the ballistic limit curve of the surrogate and select the plate thickness for the oblique impact tests (Section 8.1.4). The final tests, which are used for the validation of our numerical model in the next section, are the oblique impact tests. There, we study the ricochet and fracture behaviour for different impact angles and analyse the motion after impact as well as the size of the largest remaining fragment (Section 8.1.5).

8.1.1 Design of the validation experiment

An armour-piercing small calibre projectile consists, in general, of three components: (i) the armour-piercing hardened steel core, (ii) a lead to increase kinetic energy, and (iii) a brass jacket. The latter sustains high temperatures during the acceleration and is soft enough to transfer rotational momentum from the barrel groves without eroding them. The rotational momentum spin-stabilises the projectile. In terms of FE meshing, these sub geometries are complex. Regarding the numerical model, different materials and contact interfaces increase the amount of uncertainty. Therefore, we chose to develop a simplified surrogate for the bullet, which resembles the projectile in size and material. This development includes (i) designing a simple geometry, (ii) ensuring stable flight of it, and (iii) choosing a sufficiently brittle material, such that it fractures under an oblique impact.

In terms of (i), we select a cylinder with a spherical tip (compare Figure 8.1). The spherical tip reduces the effect of yaw during impact compared to a blunt projectile, as it does not impact on an edge in case of yaw. The length to diameter ratio of four is chosen similar to a typical small calibre ammunition.

In terms of (ii), a projectile can be spin or fin-stabilised. Fin-stabilisation requires a longer flight distance and a dedicated sabot for launching. Therefore, it is not realisable for our application, and we have to find a way to spin-stabilise the surrogate. Here, the challenge is to transfer the momentum from the barrel groves to the projectile. This process is not straight forward, as for (iii) we require a high-hardness material, which would erode the groves from the barrel if a too large surface area is in contact. At the same time, we want to avoid using a different material for momentum transfer as it adds another component to our model. Thus, the idea is to reduce the contact area and transfer the momentum without changing the geometry significantly. The tail of the impactor has the smallest impact on the TB behaviour. Therefore, we decided to add a nose

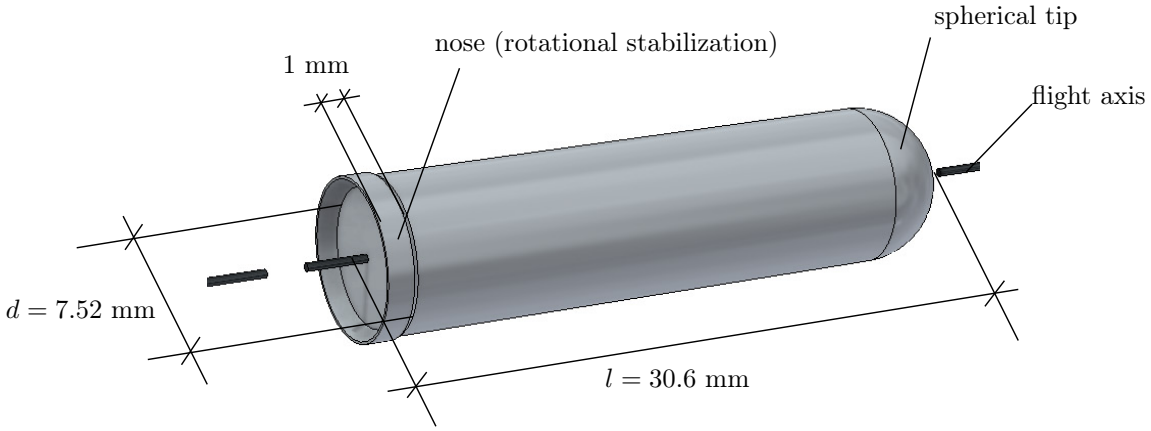

FIGURE 8.1 Surrogate used in Application III: The surrogate is designed for numerical validation. The simple geometry (cylinder with spherical tip) is extruded from a metal block.

at the end of the surrogate to transfer the rotational momentum. This final design is an excellent compromise to satisfy all design criteria.

To verify the flight stability, we performed a six degrees of freedom flight analysis with *PRODAS*[1] [65]. For a spin-stabilised projectile, the gyroscopic stability factor is computed according to

$$S_g = \frac{2\ I_x^2\ p^2}{\pi\ I_t\ \rho\ C_{m\alpha}\ d^3\ V_m^2}\,, \tag{8.1.1}$$

where I_x is the projectile polar moment of inertia, p is the projectile spin rate [rad/s], ρ is the density at the gun muzzle, I_t is the projectiles transverse moment of inertia, $C_{m\alpha}$ is the projectiles pitching moment coefficient derivative, d is the projectile reference diameter, and V_m is the muzzle velocity. For a spin-stabilised projectile, S_g should be above 1.1 for stability in standard conditions. If the external conditions deteriorate (e.g., altitude increases and air density decreases), the critical stabilisation factor is 1.4 [65]. The surrogate has a stability factor of $S_g = 1.52$, which means that it is unconditionally stable if the momentum is correctly transferred. In preliminary experiments, we measured the rotation with a high-speed camera. According to these experiments, the rotation is successfully transferred from the groves to the surrogate. In later experiments, we observed that some specimens developed a yaw angle during flight. We changed the distance between barrel and target since this behaviour appeared only after a few meters of flight.

In terms of (iii), we had to choose between existing materials that were already characterised as material characterisation is out of the scope of this work. The requirements for the material are that (1) it is not too hard to destroy the barrel groves and still processable, (2) it fractures in a wide range of impact angles, and (3) it is well-characterised to use it in the numerical model. With regard to (3), we compare two materials: the RHA (rolled homogeneous armour) steel MARS®190 and the UHHA (ultra-high hardness armour) steel MARS®300. The difference between RHA, HHA (high-hardness armour), and UHHA steels are discussed by Cimpoeru [41]. To ensure (1), we first investigated MARS®190 which has a smaller Brinell hardness (< 360 HB) than MARS®300 (630 HB). However, MARS®190 was too ductile and did not result in fractures during an oblique impact. Thus, we switched to the more rigid MARS®300, which proved to be acceptable

[1] Projectile Rocket Ordnance Design and Analysis Software

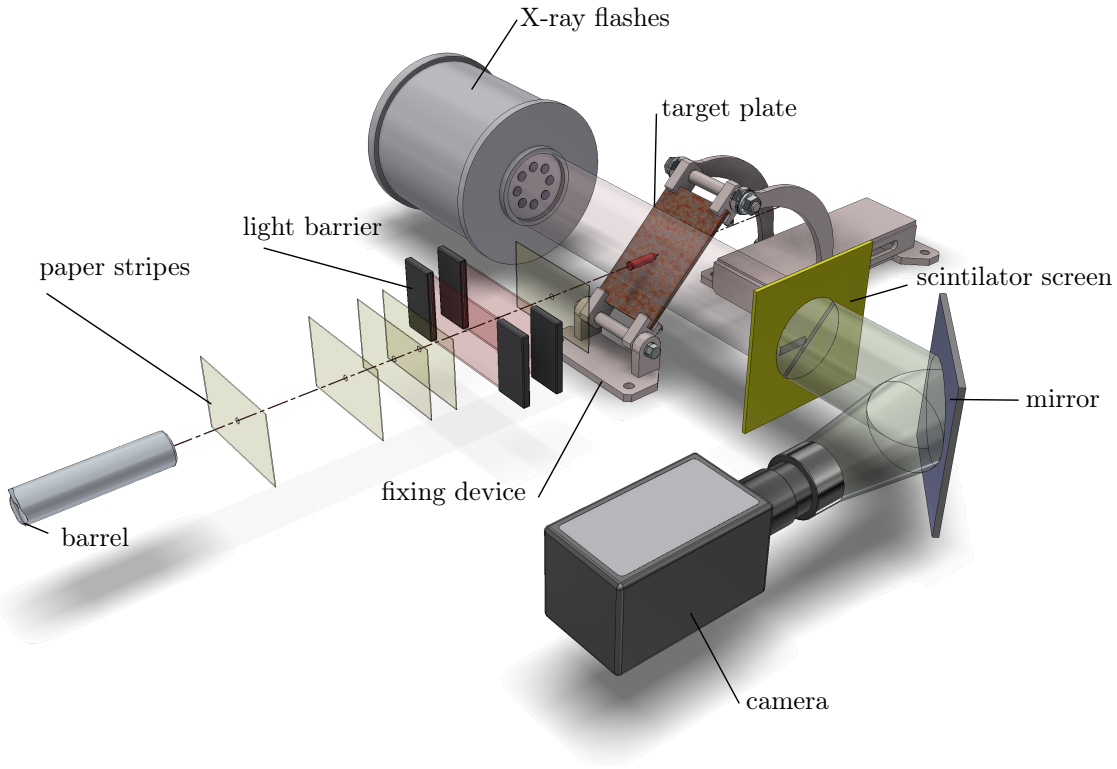

FIGURE 8.2 Setup of the TB experiments in Application III. From left to right: The projectile is accelerated in the barrel; the paper stripes are used to track the yaw; the light barrier measures the velocity; the target is fixed to a desired angle; the fragments are recovered with card; the flashes of the multi-anode X-ray setup are perpendicular behind the point of impact.

in terms of (1) and behaved as desired regarding (2). Each specimen is made in the internal workshop at ISL, which extruded the specimens within a tolerance of 0.01 mm.

The target plate consists of the same material as the surrogate, and the thickness is determined in perpendicular impact experiments to guarantee the projectile would not penetrate ($d = 10.5$ mm). A high-hardness target which bends little has the advantage that it can be simplified in numerical simulations by using a rigid wall. Besides the definition of impactor and target, the experimental setup contains several observation techniques. In the following, we describe the parts of the experimental setup, depicted in Figure 8.2, along the flight-axis from left to right: First, the surrogate is accelerated in the barrel of the static powder gun (internal ballistics). The impact velocity is measured with a light barrier close to the target, and investigated in Section 8.1.2 and Section 8.1.4. For yaw measurement, paper stripes are installed in suitable positions of the flight axis, and the yaw is investigated in Section 8.1.3. The impact on the target plate itself (terminal ballistics) is captured with the multi-anode X-ray setup (consisting of X-ray flashes, scintillator screen, mirror and camera—further explained in Section 5.2.2 and needed for the evaluation in Section 8.1.5) The remainder is captured with card plates and investigated in Section 8.1.4 and Section 8.1.5. The card plates are excluded in the figure to not hide other relevant parts. They are illustrated and described as part of the experimental chapter (compare Section 5.5).

8.1.2 Internal ballistics

Internal ballistics (also interior ballistics (IB)) is a subfield of ballistics that studies the propulsion of a projectile. For powder guns, it covers the time from the ignition of the propellant until the projectile exits the barrel. We are interested in two properties of IB: the transfer of rotational momentum and the resulting muzzle velocity. For a fully developed ammunition, the jacket material and geometry is optimised to guarantee that the rotation from the spiral barrel groves is entirely transferred so that there is little friction and the muzzle velocity is reproducible. Since these experiments are the first of its kind, we do not know the IB properties. Neither do we know whether the rifling transfers the rotation to the surrogate or how much powder it requires to obtain a given target velocity. In the following, we discuss these two properties in two separate paragraphs.

Transfer of the rotation from the barrel groves

For investigating the transfer of rotation, we track a marker on the surrogate with a high-speed camera and compare the actual rotation to the theoretical rotation based on the rifling (compare Figure 8.3). According to the images, a rotation of 90° requires a flight distance of approximately 60 mm; therefore, a full rotation requires about 240 mm. The theoretical rotation speed is 40 calibres per revolution, which corresponds to $7.62\,\text{mm} \times 40 = 305\,\text{mm}$. Since the rotation in real-world can not exceed the theoretical value, we conclude that the rotation is successfully transferred to the impactor and the difference is due to measurement inaccuracy.

Relationship between powder mass and muzzle velocity

For investigating the relationship between powder mass and muzzle velocity, we tracked the powder mass for all perpendicular impact experiments with respect to the resulting muzzle velocity (compare Figure 8.4). The muzzle velocity was measured not precisely at the muzzle, but two meters after. According to the *PRODAS* calculation, the deceleration due to drag is 2.4 m/s per meter of flight. The deceleration is negligible for a flight distance of two meters and not considered in the following analysis. The measurement accuracy of the scale is 0.001 g; therefore, correlated uncertainties are negligible as well (< 1 m/s). Although the measurement points spread considerably, a linear relation between muzzle velocity and powder mass is found. From an energetic point of view and neglecting friction, the muzzle velocity should show a root-like course. However, IB

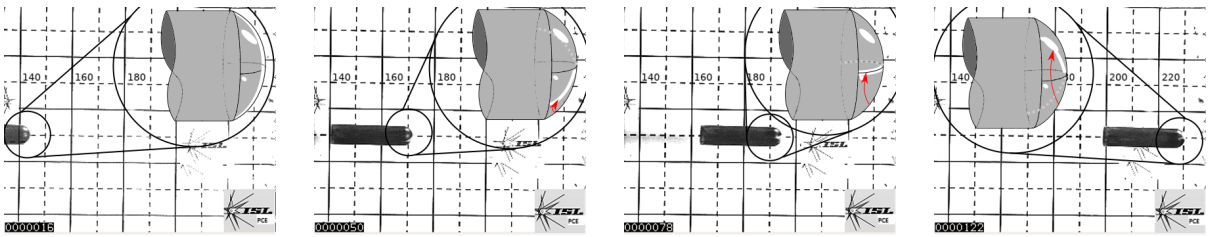

A 0 deg **B** 45 deg **C** 90 deg **D** 135 deg

FIGURE 8.3 Internal ballistic evaluation for Application III: Projectile rotation. A white marker visualizes the rotational position: **A** no marker, **B** marker inclined downwards, **C** marker in the middle, **D** marker upward inclined. According to these angles and the axial position in the images, the surrogate rotates once per 240 mm of flight. Images are horizontally flipped—rotation direction is the other way round.

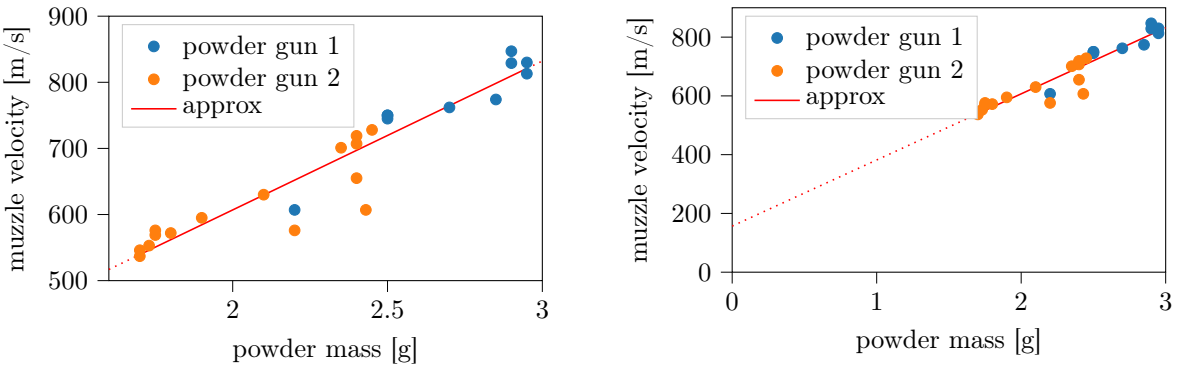

FIGURE 8.4 Internal ballistic evaluation for Application III: Achieved muzzle velocity for different amount of powder. The values obtained with two different powder guns are colored differently. Four shots are outliers. All others are less than 40 m/s, and in average 15 m/s from the linear regression.

is more complex: not all powder releases its full energy; thermal effects due to pressure differences, supersonic effects and friction occur. Thus, a linear least-square regression of all measurement points is calculated to quantify the difference (15 m/s mean deviation). This spread is considerably more than observed for a standard projectile (STANAG requirement: maximum ±10 m/s spread [77]), complicates the experiments, and gives a clue that there is a optimisation potential regarding the IB of the surrogate.

8.1.3 External ballistics

External ballistics describes the projectile behaviour during flight from the exit of the barrel until impact. The goal in external ballistics armour design is good aerodynamics and flight stability to obtain high accuracy. In terms of external ballistics, we study the yaw of the surrogate, which is related to flight stability. According to the stability factor of 1.52 calculated with (8.1.1), the projectile flies unconditionally stable. Based on our real-world experiments, this is not the case (compare Figure 8.5). This instability can have different causes: the groves of the barrel were slightly eroded after some experiments, and the rotation was not correctly transferred; the exit of the surrogate at the muzzle is not perfect, and a small perturbation aggravates. According to visual inspection, the grooves were still intact, but we have no data that the rotation was transferred in every experiment.

To obtain a better understanding, we performed yaw measurements with paper stripes. Exemplarily, we present four experiments: two experiments with and two experiments without yaw. Figure 8.5 shows the yaw angle, estimated according to the procedure described in Figure 5.3, as a function of the distance to the barrel. The examination papers had to be placed in suitable positions of the setup and are therefore not equidistant. The required diameters to estimate the yaw with (5.3.2) are measured in the contour plots of the cutting holes (compare Figure 5.3 and Figure 8.5A).

Having a look at the two first experiments where yaw occurred, it clarifies that the yaw amplifies during flight. For the two last experiments without yaw, the extracted values always lie below 3°; however, with a considerable uncertainty range due to the blur of the edges. Without changing the experimental setup, this self-amplifying behaviour could only be observed in some of the experiments, while no yaw amplification was observed for the other experiments. Therefore, the yaw is found to be chaotic and self-amplifying—possibly due to an initial instability. The only possibility to avoid yaw during impact is to reduce the distance between

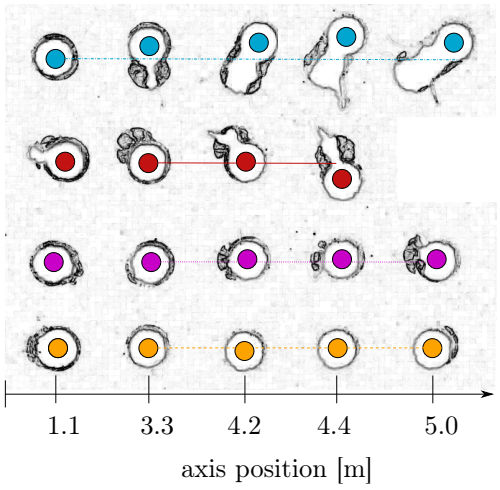

A raw data obtained from experiments

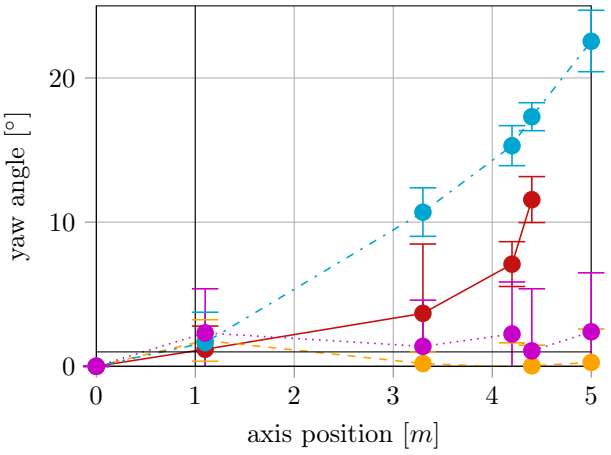

B evaluated yaw angle from **A**

FIGURE 8.5 External ballistic evaluation for Application III: Yaw extracted from four pendulum tests (blue, red, purple, yellow). An amplification of yaw can be observed three meters behind the barrel for the blue and red experiment. The amplification increases to a significant yaw at the impact position.

the barrel and the target to a minimum. This has been done for the terminal ballistic experiments presented in the following.

8.1.4 Terminal ballistics I: perpendicular impact

In ballistics, perpendicular impact tests are used to characterise the protective specifications of armour systems in terms of the v_{50}—or ballistic limit (compare Section 1.2.3). During the perpendicular impact, the complexity of the experiment is reduced compared to general impact tests, which are done under an angle. The setup is rotationally symmetric, and instead of several different cases (ricochet, fragmentation, fracture), only the binary information whether there is a perforation or not is relevant. Therefore, we performed these tests before investigating the more complex oblique impact. Perpendicular impact tests are easily reproducible and estimate the worst-case scenario. Depending on the impact velocity and the plate thickness T, the failure mechanism changes [170, 229]. Therefore, it is demanding for a numerical model to predict the ballistic limit correctly for a wide range of plate thicknesses. From another perspective, this means that if a model predicts all cases correctly, it is probable that it also describes the physics correctly. Thus, it is a targeted and suitable validation experiment for the description of the target plate in a TB numerical model.

We study three TB properties in Figure 8.6: (i) the ballistic limit, (ii) the mass of the residual projectile, and (iii) the mass of the extruded plug. The ballistic limit velocity (i) is estimated for each plate thickness using the perforation information of the experiments (compare Figure 8.6A). For the 6.5 mm plate, the v_{50} lies at 560 m/s, for the 8.5 mm plate, it is 710 m/s and for 10.5 mm, it is 770 m/s. Based on these values, we extrapolate the ballistic limit curve (compare Figure 8.6A). According to Zukas [230], the shape of this curve is not necessarily polynomial. Depending on the fracture mechanisms, it can change its shape for different thickness ranges. We did not consider normalisation of T. The usual approach is normalisation with the diameter D of the impactor, which means that we investigate the range of $0.85 \leq T/D \leq 1.38$. For the mass

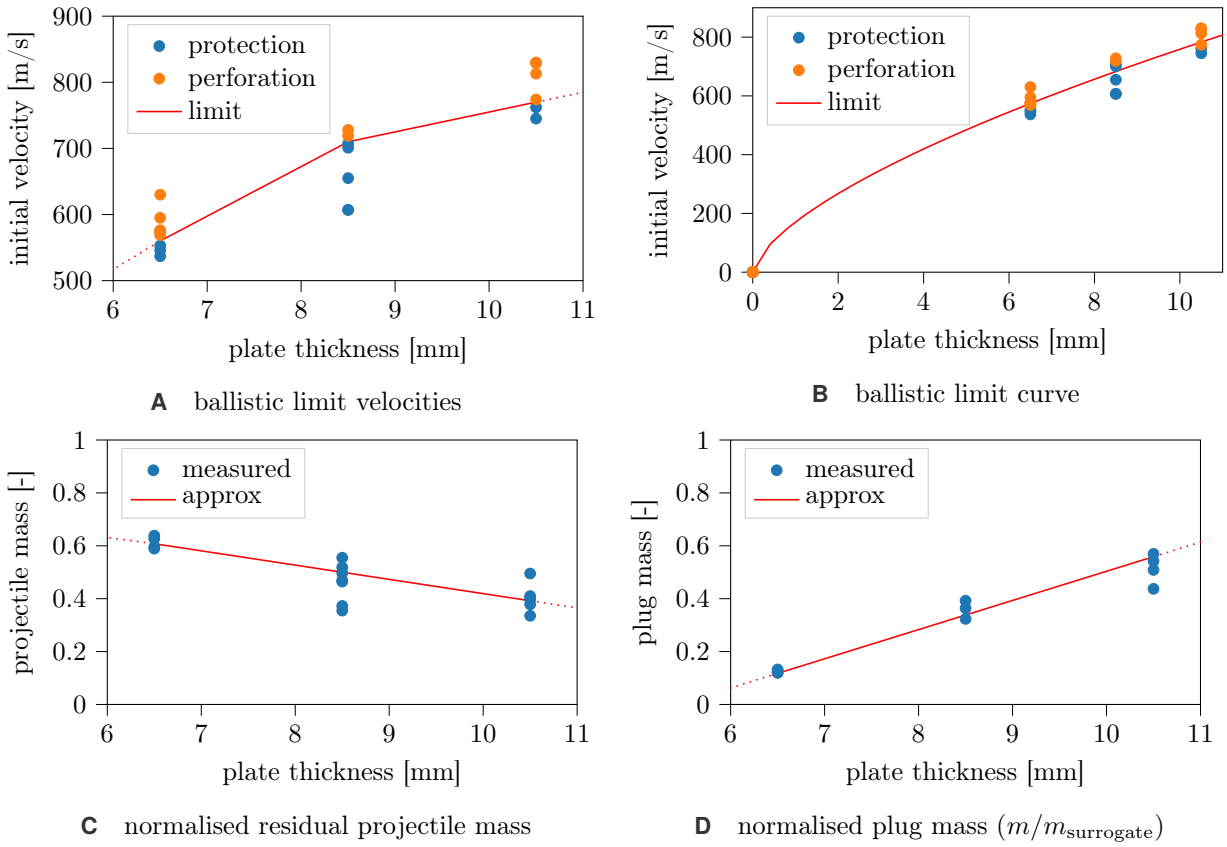

FIGURE 8.6 Application III: Evaluation of perpendicular impact experiments. Linear and non-linear regression is shown in red. **A** shows the ballistic limit and the velocity of each shot that perforated or was stopped. **B** is the extrapolation of **A** for a larger plate thickness range; **C** shows the residual projectile mass for those remainders recovered after impact; **D** shows the plug mass of those plugs recovered after impact.

of the residual projectile and the plug, we use linear regression as a linear function represents the data well.

For Figure 8.6C, an extrapolation of the linear regression to $x = 0$ and $y = 0$ can be used to interpret the results. The extrapolation towards $x = 0$ shows the approximation quality of the linear representation for thinner plates. The extrapolation crosses the y-axis at 0.93, which means that 7% of the mass is eroded if there is no plate at all (the analytical value would be 0%). This result is close to the analytical value. However, it is also possible that no erosion of the projectile is already observed for a small thickness. The second extrapolation proposes that the projectile is eroded for a plate thickness of 17.8 mm at the ballistic limit.

For Figure 8.6D, we see that the mass of the plug increases linearly with the plate thickness. This increase suggests that the diameter of the plug stays constant, and the erosion of the plate is negligible. This corresponds to the failure mechanism “plugging” of pointed penetrators rather than “petalling” (compare Figure 2.6). Similar to Figure 8.6B, we can extrapolate the regression curve. No plug is extruded for a plate thickness of 5.5 mm, and the plug is precisely the mass of the projectile for a plate thickness of 14.5 mm. If the first hypothesis is correct, this means that the fracture mechanism for this combination of material and impactor shape changes for $D < 5.5$ mm to dishing without a plug (thin targets in Figure 2.6). In cases of

protection, the bulging of the plate was little. For the perforation case, no erosion was observed at the plate, and the failure mechanism is (adiabatic) shear failure.

In summary, we obtain reproducible and consistent results with the given plate thicknesses and extrapolated the ballistic limit curve. Furthermore, we use an extrapolation of the residual projectile mass to determine the maximum plate thickness that can be perforated by the impactor. The approximation of the maximum plate thickness is 58% of the surrogate length (17.7 mm), and the corresponding velocity to provoke the complete erosion of the surrogate is about 1.1 km/s. Regarding oblique experiments, we aim for an impact velocity of 800 m/s and want to avoid penetration. Hence, we have to use the thickest plate (10.5 mm). For this plate thickness, the ballistic limit is 770 m/s, and for oblique experiments, we expect that the plate withstands higher impact speeds since the normal velocity component is smaller than for perpendicular impact.
The results can be used in future studies to validate the fracture mechanisms of the plate. For us, the experiments mainly serve to determine suitable plate dimensions for the experimental validation of our simulations.

8.1.5 Terminal ballistics II: oblique impact

Oblique impact adds complexity to the experiment compared to the perpendicular impact presented above. Figure 8.7 illustrates the definition of oblique angle and deflection angle. In general, the barrel is immobile. For an impact under an angle, the target plate has to be rotated and fixed in the rotated position (compare experimental setup depicted in Figure 8.2). Since the projectile ricochets off under a flat oblique angles, the experimental setup needs to be designed such that it captures the ricochet before it damages the equipment. One aim of the experiments is to understand the fracture behaviour of the surrogate. Therefore, different methods to recover and examine the fragments were investigated. In a first test series, card boxes covered all possible directions to capture as many fragments as possible and to obtain a mass-distribution similar to Application I (compare Figure 6.8). However, this metric was not useful as only a small amount of the little fragments was recovered. In a second test series, a half-sphere of styrofoam was used to measure the exit angle and, therefore, the deflection angle of all fragments. The results were no meaningful description of the experiment either, as all fragments were going in a similar direction. Finally, we concluded that the only reasonable approach to investigate and compare many experiments for this application is to recover and analyze only the largest fragment.

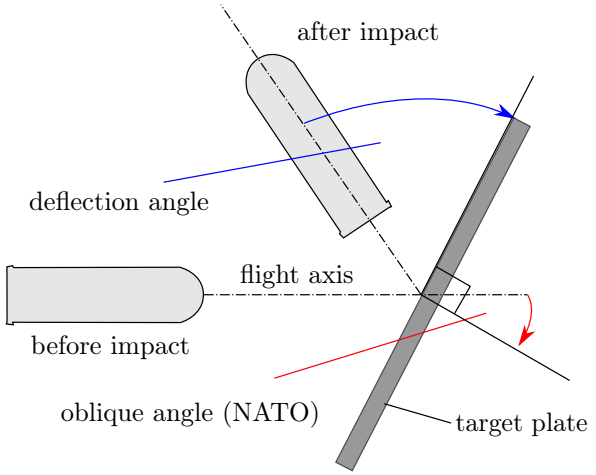

FIGURE 8.7 Application III: Setup for oblique impact. Illustration of the oblique angle (NATO) and deflection angle for a typical experiment under an angle.

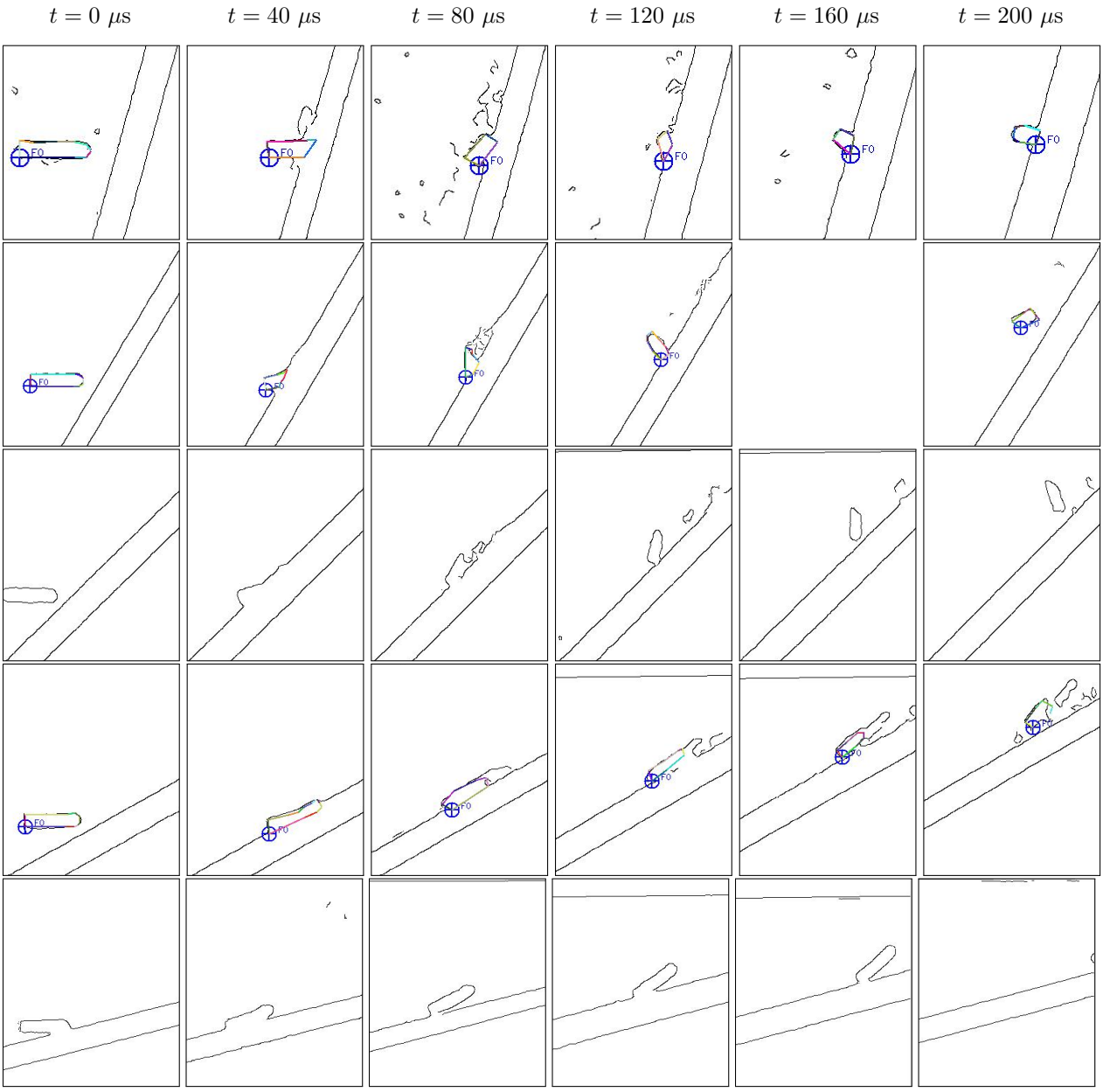

FIGURE 8.8 Largest fragment tracking for Application III: Aligned contour plot of the experimental results. The largest fragment is highlighted in colour.

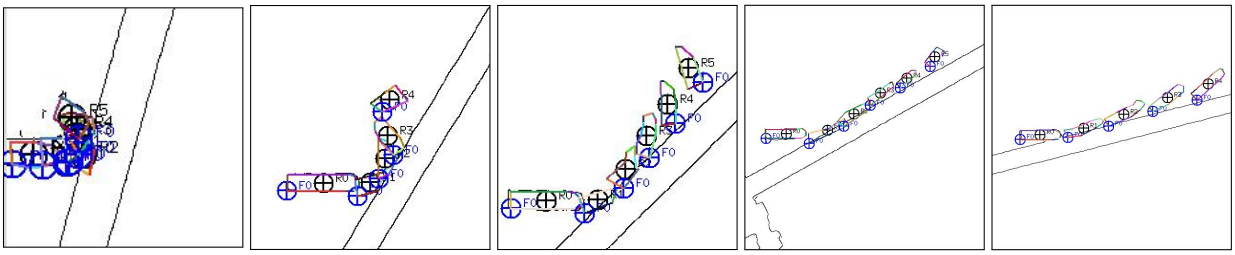

FIGURE 8.9 Largest fragment tracking for Application III: Overlay of time series of largest fragments for all different angles.

Extraction of the velocity from X-ray

Since dust occurs during an oblique impact, we can not use high-speed cameras. Therefore, we use X-ray cinematography (compare Section 5.2.2) to observe the impact. The X-ray images are processed and evaluated with FXRIP (compare Section 5.5). Figure 8.8 shows the aligned contour plots of these images captured at the time series (0 μs, 40 μs, 80 μs, 120 μs, 160 μs, and 200 μs). Results of single experiments per oblique angle (15°, 30°, 45°, 60°, and 75°) are shown in each row of the image grid. For consistency, we focus on images with little yaw, which have the same exposure times.

In the following, we argue why the description of the tip fragmentation is secondary and why we focus on the largest remainder in our comparison. A practical reason is that only the largest fragment is visible in the processed images. Smaller fragments that emerge due to fragmentation of the tip are, for most oblique angles, below the threshold sensitivity of the edge detection. Also, they are hardly distinguishable in the raw image. Moreover, the largest remainder is the only real threat to protective structures and therefore relevant for protective design.

While the detected residual fragment is highlighted in each image for 15°, 30°, and 60° obliquity, only the contour is shown for 45° and 75°. The comparison of the two visualisation techniques indicates the difficulty of defining the fragment in some images. Moreover, the automatic fragment detection is limited to images where there is a continuous edge surrounding the fragment that is not connected to the edge of the plate. This criterion is often not satisfied, which is the reason why most of the times the user has to define the outline of the fragment manually by selecting points on the outline.

The detected fragments can then be combined in one image (compare Figure 8.9). Each subfigure describes one oblique angle. From the combined image, we extract the qualitative behaviour of the impact—the steeper the impact angle, the smaller the distance between the residual fragment at different times. E.g., for 15°, the fragment nearly remains in one position, whereas all exposures of the largest fragment are distinguishable for 75°. Moreover, the rotation decreases for larger impact angle, and also the deflection of the fragment appears to be the largest for smallest obliquity.

We use the software developed as part of this work, FXRIP, to quantify these findings. Up to now, no commercial alternative is available for this evaluation. Only image processing software can be used for manual extraction as an alternative.

Figure 8.10A shows the normalised residual translational velocities after the impact of the fragment. We decompose the velocity in x and y direction: x points in the direction of the flight axis, and y is perpendicular to x in the plane of observation. Theoretically, there is no velocity component in z-direction (normal to the

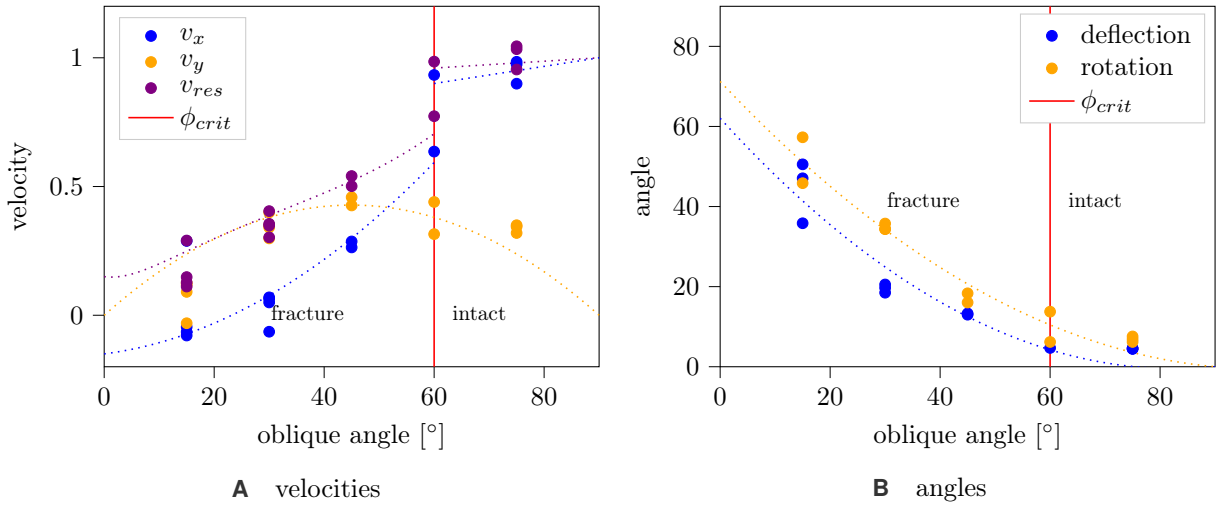

FIGURE 8.10 Application III, oblique impact: Extraction of parameters from our real-world experiment with the FXRIP software: **A** translational velocities; **B** ricochet angle and rotational velocity.

plane of observation). Due to the arrangement of the flashes, we can not verify this with the X-ray images; previous experiments with styrofoam showed this. The general spread of the experiments in terms of residual velocity is acceptable. Therefore, we can use the data to calculate regression curves which are indicated with dotted lines. We consider the transition between fractured and intact ricochet in the definition of the regression, allowing a discontinuity at the transition. According to our experimental findings, this transition occurs approximately at an oblique angle of 60°. We also include two physical assumptions in the regression: (i) the y-velocity is $v_y = 0$ for 0° and 90°, (ii) the x-velocity is $v_x = 1$ for 90°. The resulting regression for the x-velocity increases non-linearly up to the critical angle. Above this angle, a small linear increase is assumed that accounts for less friction for a larger angle. For the y-velocity, there is one degree of freedom less for the regression due to assumption (ii). However, the resulting curve represents the data well and predicts a maximum at 45°. The regression curve for the velocity magnitude is calculated with the Euclidean norm of v_x and v_y and matches the data well.

In conclusion, we successfully extracted fragment velocities from the X-ray images and computed linear and non-linear regression curves to the data. The data are self-consistent and also satisfy the physical assumptions (i) and (ii).

In a further step, we analyse the motion after impact in Figure 8.10B regarding two properties: First, we compute the deflection angle (compare Figure 8.7). Second, we extract the rotation velocity of the fragment according to Section 5.5.3. Since the rotation velocity can be expressed as a rotation angle with regards to a given time, we decided to put both results in one plot. A reasonable time for our experiments is the difference between two subsequent X-ray images (40 μs). Here, the regression curves are defined without any physical assumption. One reason for not implementing physical assumptions is that, in terms of the rotation, the 0° case describes a singularity: the rotation velocity increases for a smaller angle; at the same time, it is theoretically zero for perpendicular impact. Thus, hard constraints negatively affect the quality of the regression unless the singularity is included in the function basis. The rotation and the deflection show the same trend; the deflection increases for a smaller angle. Theoretically, it would be 90° for the perpendicular

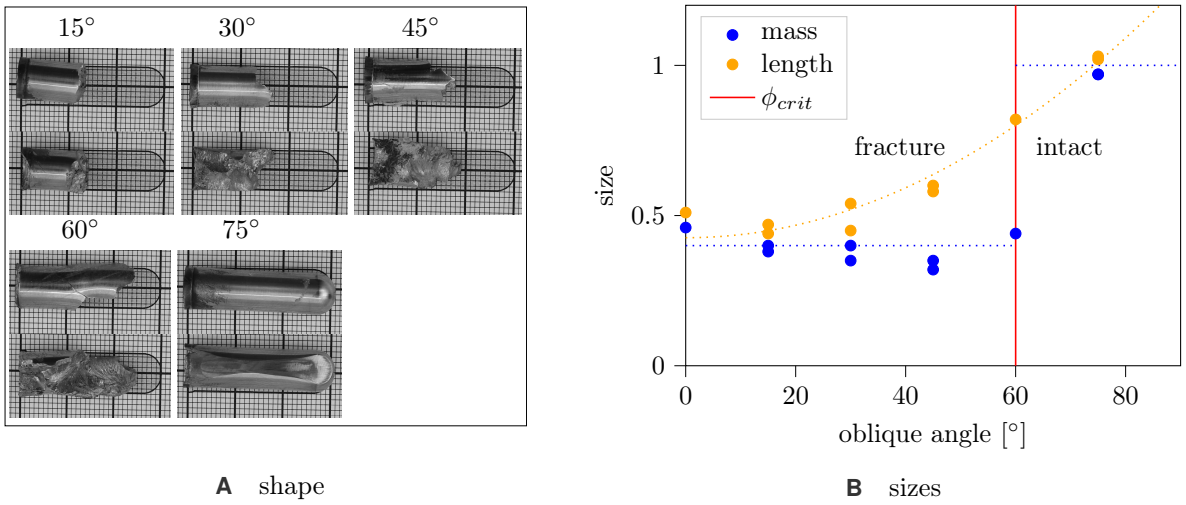

A shape **B** sizes

FIGURE 8.11 Remainders after impact. Only the largest fragment is evaluated, since the rest of the projectile fragmented in small pieces which could not be recovered. In **B** the size is normalised with the initial mass and length of the surrogate.

case and 0° for the 90° case. From a physical point of view, it makes sense that the deflection and rotation decrease for larger oblique angles since the kinetic energy, which transfers to deflection and rotation, decreases.

In conclusion, we presented the X-ray images of the experiments for different obliquity and extracted the motion after the impact of the surrogate remainder regarding translational velocity, deflection and rotation speed. These properties are quantitative metrics to evaluate and validate our numerical simulations.

Evaluation of the captured fragments

In the following analysis, we examine the fragments: first, qualitatively and then, quantitatively regarding mass and length. Figure 8.11A shows the remainders of each impact angle from both sides. The bottom image shows the side, which was in direct contact with the plate; the top image shows the upward-pointing side. For all angles up to 60°, part of the tip is eroded—the smaller the angle, the more considerable the amount of the eroded tip (more than half of the length for 15° obliquity). While only little material erosion at the bottom part is observed for the 15° angle, there is significant material erosion for 30° to 60°. For the angle of 75°, there is only plastic deformation but no erosion at all.

The normalised mass and length of the fragments from all experiments are quantified in Figure 8.11B. Similar to Figure 8.10, we fit the data with a polynomial function of polynomial degree two. The non-linear increase in length can be well described with this approach. Only the curve must be limited to one as the length of the projectile can not increase. For the mass of the fragment, we observe that up to 60° obliquity the mass stays constant. With an increasing angle, less material is eroded from the tip, but more material is eroded from the side; this results in a constant amount of erosion in this range of angles. If there is no fracture (75°), we assume that the erosion is zero. Both the qualitative and quantitative evaluation of the remainder are valuable validation data for our numerical model.

8.1.6 Concluding remarks

This section presented the results of the real-world experiments for a new kind of impactor that represents a surrogate for small calibre projectiles. We presented various aspects of the impact properties. First, we showed the spread in the muzzle velocity for the powder mass (internal ballistics). Then, we analysed the flight stability, both theoretically and with the analysis software *PRODAS* (external ballistics). There, we concluded that the barrel has to be close to the target to obtain good results. Finally, we conducted two types of terminal ballistic experiments: First, we investigated the ballistic limit to identify the ideal dimensions of the plate and determined the ballistic limit curve. Then, we investigated the oblique impact and extracted a database for numerical validation. This database contains the translational velocity components, the deflection angle, the rotation velocity, the mass, and the length of the largest remainder.

The next section addresses the numerical modelling of the oblique TB tests with three different numerical approaches. Besides the database mentioned above, the processed X-ray images are used for qualitative validation of our numerical models.

TABLE 8.1 Projectile and target material for Application III: Material parameters MARS®300: (i) in general, (ii) for the Johnson-Cook plasticity, (iii) for the Johnson-Cook fracture model, and (iv) for the Grüneisen EOS [67, 68].

parameter	value	comment
ρ [kg/m^3]	7850	(i) density
G [GPa]	79.6	(i) shear modulus $G = E/(2(1+\nu))$
ν [−]	0.34	(i) Poisson's ratio
c_p [J/(kg K)]	470	(i) heat capacity
A [MPa]	1400	(ii) yield strength
B [MPa]	1550	(ii) strain hardening
n [−]	0.15	(ii) strain hardening
C [−]	0.0018	(ii) strain rate hardening
m [−]	1.39	(ii) temperature softening
T_m [K]	1800	(ii) melting temperature
$\dot{\varepsilon_0}$ [−]	0.001	(ii) testing strain rate
D_1 [−]	0.2	(iii) brittle damage
D_2 [−]	0.248	(iii) triaxiality damage dependence
D_3 [−]	-3.275	(iii) triaxiality damage dependence
D_4 [−]	0.0385	(iii) strain rate damage dependence
D_5 [−]	0	(iii) thermal damage dependence
C [m/s]	4570	(iv) speed of sound in the material
S_1 [−]	1.4	(iv) linear shock parameter
γ_0 [−]	1.97	(iv) Grüneisen parameter

8.2 Validation of the numerical model

This section presents the validation of our numerical models in *LS-DYNA®* with the experimental data obtained in the previous section. In principle, we developed and improved two models: one FE model and one SPH model. The SPH model uses the hybrid approach for the target, and the FE model uses only FE. In the following, we first demonstrate the most critical improvement for either model exemplary for 30° obliquity and then compare the final models against each other. The calibration of the model included the investigation of more settings than the ones presented explicitly (e.g., resolution of the discretisation, element formulation, scaling factors, material properties, and material laws). Regarding the material, we already demonstrated in Application I that little influence is expected; for the impact case, we validated this with tests at ETH Zurich, who propose a more detailed plasticity model (Swift-Voce strain hardening) and fracture model (Hosford-Coulomb) for the same material [67, 68]. The material data for this study, which uses the Johnson-Cook plasticity and fracture model, are also extracted from these two papers (compare Table 8.1). Regarding the discretisation, grid convergence studies have been conducted. However, since our non-regularised fracture model is optimised to one given resolution, the converged solution might be less accurate than the one computed with the resolution the model was optimised for. We use a resolution that gives results that are sufficiently close to the results obtained with the resolution proposed by the fracture model, as the latter is too fine for running all simulations.
In general, impact modelling is a challenging task for numerical models due to high pressures and considerable deformation. Modelling options that are not robust enough lead to either normal termination with wrong results, normal termination with all elements deleted, or error termination. Possible causes are limitations of the model (negative pressures are not allowed), amplification of disturbances (e.g., contact forces, shock waves), or poor interpolation on highly distorted elements. Therefore, unlike static or moderate dynamic problems, a physical approximation of the problem already requires to choose many properties satisfactory when using a solver that is optimised for much lower velocities such as *LS-DYNA®*.

This section is structured as follows: First, we give an overview of state-of-the-art methods in numerical modelling of HVI. We use three different approaches: (i) a model using finite elements (FEM), (ii) an SPH model (SPH), and (iii) a hybrid approach which combines both methodologies (SPH-H).

- For (i), we investigate the benefit of the improved contact description which was determined in Section 8.2.1 in Application I.
- For (ii), we simplify the target to a rigid wall and compare different particle distributions, that were introduced in Section 4.4.1, in the SPH model (Section 8.2.2).
- For (iii), we compare the run time between different combinations of FEM and SPH discretisations, in particular, regarding our black-box model introduced in Section 4.4.2 (Section 8.2.3).

Finally, we compare the two models, qualitatively and quantitatively to the data obtained in the real-world experiment for all oblique angles that were also tested in the real-world experiments (Section 8.2.4).

8.2.1 FEM: improved contact algorithm

The FE model is, in particular, determined by the material parameters, element technology, and contact description. We use the material data provided by Fras et al. [67]. In a parameter study, we verified that

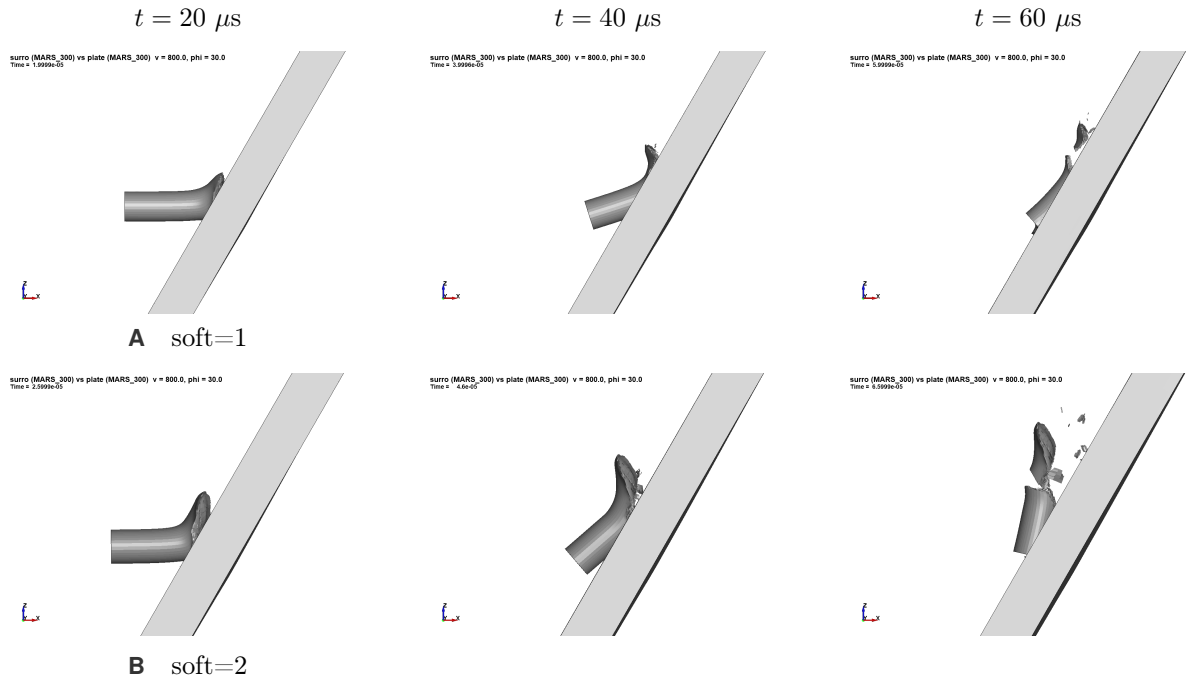

FIGURE 8.12 FEM simulation results for Application III: HVI of the surrogate at 30° and 800 m/s. Comparison of two different contact types ($SOFT$=1 and $SOFT$=2). A correct contact force description is required to predict the ricochet and fracture.

a small change of material parameters does not significantly change the behaviour in terms of fracture and motion after impact. Regarding element technology, we limit ourselves to hexahedral elements. For this kind of elements, several options that differ in integration points and integration rule exist in *LS-DYNA*®. Although there are particular implementations for large deformations, no considerable difference was observed compared to the standard one-point integration (compare Figure 3.4). As pointed out in Chapter 7, the contact description is essential for the modelling of impact. If the contact algorithm does not transfer the forces correctly, the impactor behaves differently. For our example, this was the critical property that enabled the FEM to predict the fracture behaviour.

The qualitative difference between the two methods is shown in Figure 8.12. For $SOFT$=1[2], the projectile is not correctly deflected (the same applies to $SOFT$=0 which is not shown here). Instead, it penetrates the plate and gets stuck. Only $SOFT = 2$ predicts the rebound and fracture similar to the result observed in real-world experiment (compare Figure 8.8 with Figure 8.12B).

8.2.2 SPH: improved particle distribution (PD)

In Section 4.4.1, we proposed different PDs to populate particles in computational domains (e.g., the surrogate geometry). In the following, we show that the choice of an appropriate PD is essential for the stability of the simulation. Figure 8.14 shows the result for different PDs. We use an X-ray-like side view of the 3D simulation to see the crack propagation. From left to right, the complexity of the PD increases, and the representation of the geometry improves.

[2]the contact options are described in Section 4.2.2

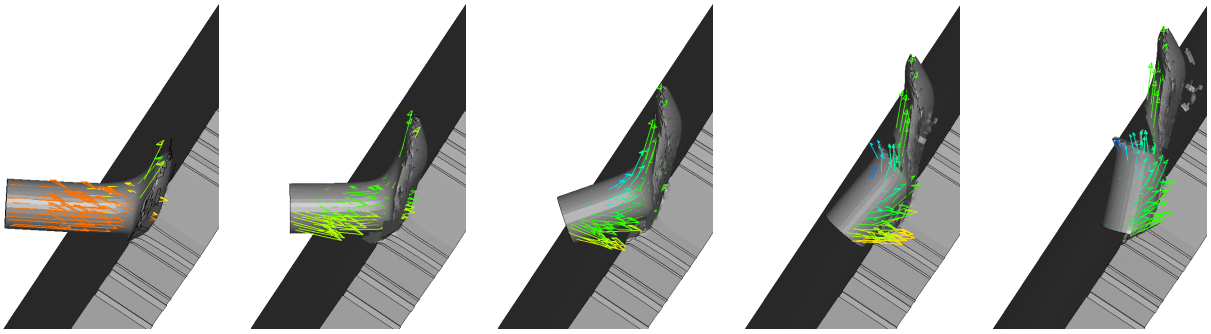

A 20 μs **B** 40 μs **C** 50 μs **D** 60 μs **E** 80 μs

FIGURE 8.13 FEM simulation results for Application III: HVI of the surrogate at 30° obliquity: Velocity vectors illustrate why the front and back part of the projectile break during oblique impact. The front part goes in a different direction than the back part and tensile stresses exceed the strength of the material.

Since the impactor is still in one piece during the first time steps, we only show the time step 60 μs after impact. The reason that no difference occurs in the early stage of the impact is that the material is mostly under compression, which is, in terms of stability, no problem with SPH. In the evolution of the simulation, the front part is deflected earlier; the velocity of the front part points already in a different direction than the back part, which still moves in the initial direction. This difference leads to stresses in the material that ultimately lead to the fracture (illustrated with the velocity field in Figure 8.13).

The most significant difference is observed between the PD based on a FE mesh 8.14A and the other discretisations. For the PD based on the FE mesh, the surrogate fractures artificially at many axial positions. The simulation based on a regular grid in 8.14B shows the start of a crack that is not fully developed at the same axial position as the other PDs. For 8.14C to 8.14E, the axial position of the crack is consistent. Only the fragmentation of the tip changes.

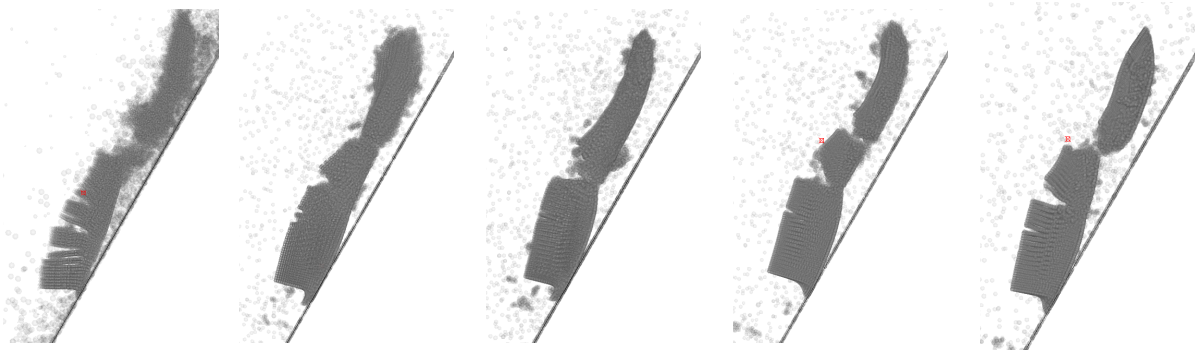

A based on FE **B** regular grid **C** dense grid **D** cylindrical **E** spherical nose

FIGURE 8.14 SPH simulation results for Application III: HVI of the surrogate against a rigid plate at 30°. Qualitative fracture behaviour for different PDs. **A** particle distribution based on a FE mesh; **B** particle distribution cut from a regular grid; **C** particle distribution cut from a densely meshed regular grid; **D** particle distribution based on cylindrically aligned particles; **E** shows **D** with the PD of the nose spherically aligned.

While, for the regular dense grid 8.14C, the tip remains intact, it fractures at a second axial position for 8.14D and 8.14E. Using a spherical approach to populate the particles in the tip (compare Figure 8.14E) does improve the description of the geometry but not of the fragmentation. Since a different meshing of the tip requires special treatment in the preprocessor and does not result in a significant improvement in terms of the approximation, we do not support the spherical option in the final version of the software. However, we showed that the cylindrical PD is not only better in terms of the description of the geometry, but is also more robust for the description of an impact compared to the available options in the *LS-DYNA®* preprocessor (Version 4.3). Therefore, the cylindrical distribution is used in our software as the default option to generate the SPH particle distribution of the impactor.

8.2.3 Hybrid method: improved run time

The main drawback of pure SPH for generating a discretisation of the target plate is that adaptive meshing with SPH requires a particular treatment in the solver, which is not available in *LS-DYNA®*. As a workaround, we implemented the hybrid FEM-SPH approach (compare Section 4.4.2). This workaround allows us to capture the boundary conditions of the real-world experiment correctly since we do not need to reduce the plate size in our model due to run time or memory limitations. Instead, we use high-resolution SPH in the impact area of the plate and FEM in the plate remainder. In this section, we compare the run time between four different numerical descriptions of the impact: (i) surrogate (FEM) against target plate (FEM), (ii) surrogate (SPH) against the target (FEM), (iii) surrogate (SPH) against the target (HYBRID), (vi) surrogate (SPH) against a rigid wall (illustrated in Figure 8.15). We use the same settings as in the previous case. The surrogate impacts the plate with 800 m/s at an angle of 30° for a duration of 100 μs. Table 8.2 sums up the setup and results of this study. The number of elements and particles to discretise the projectile is approximately 50,000. The hybrid target consists of approximately 240,000 particles and 60,000 elements, and the pure FEM target consists of approximately 170,000 elements. This difference in the total amount of discretisation points arises from the construction of the mesh. For all methods, the same FEM elements are used outside the impact zone. For the pure FE mesh, a standard cylindrical mesh is generated for the impact

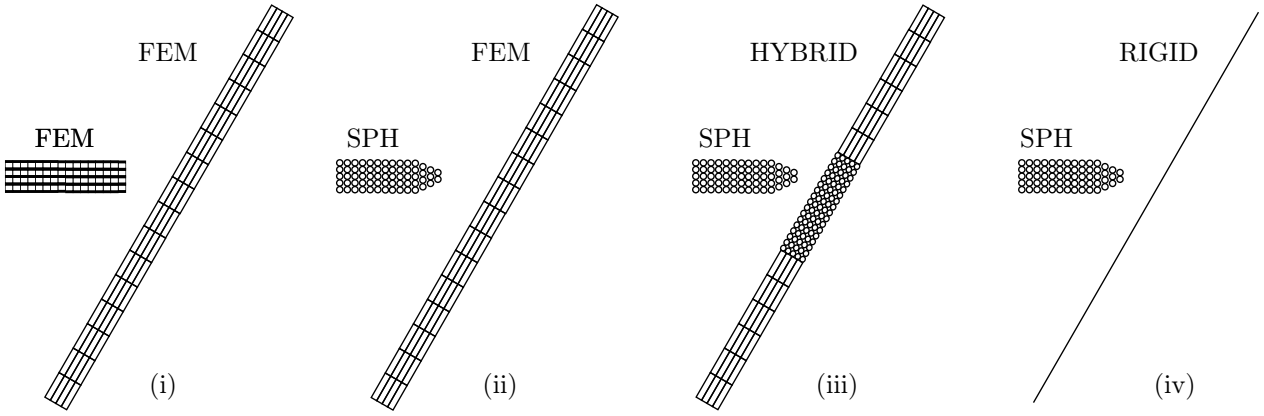

FIGURE 8.15 Simulation initialization for Application III: HVI of the surrogate against an armour steel plate. Discretisation methods: (i) FEM vs FEM, (ii) SPH vs FEM, (iii) SPH vs HYBRID, (iv) SPH vs RIGID.

case	(i) FEM - FEM	(ii) SPH - FEM	(iii) SPH - HYBRID	(iv) SPH - RIGID
run time [min]	442	92	30	6
steps [-]	78,430	18,345	3052	2194
run time / step [ms]	413	300	600	160
particles	0	50,000	290,000	50,000
elements	220,000	50,000	0	0

TABLE 8.2 Application III: Runtime evaluation of different numerical models and the corresponding number of particles and elements in the simulation domain. Calculated on eight cores of the Intel Xeon Gold 6130 CPU (16 cores/ 32 threads at 2.1 GHz).

zone based on the discretisation of the outer part. For the hybrid mesh, the same domain is equally filled with particles. The size of the particles is chosen similar to the size of particles of the impactor. The amount of particles and elements results from this consistent construction.

All calculations are distributed with shared memory processing on eight cores of the Intel Xeon Gold 6130 CPU (16 cores/ 32 threads at 2.1 GHz). This represents the typical setup at our institute. Case (i) is the baseline case as this is the approach which is by default used for TB simulations and requires about nine hours. If we replace the impactor by an SPH discretisation, the run time reduces by a factor of six. This reduction is not only due to a more economical time step in SPH than in FEM (which is around 30% cheaper with regard to the run time), but also due to a significantly reduced number of time steps that have to be calculated with approach (ii). The time step is determined by the size of the smallest edge length in the FEM (compare (3.2.16)), and the smallest distance between two particles in the SPH model. Since particles can only move slightly towards each other due to limited compression of the material, it is less restrictive than the FEM, where elements can deform in distorted, thin shapes at constant density. The deformation at the surrogate is more critical than at the plate for (i) and (ii). Thus, more time steps have to be computed with (i), and the overall run time is higher than with (ii). Using the SPH impactor against a hybrid meshed target (iii) decreases the number of time steps even more: by a factor of six compared to (ii). The cost for a single time step increases by a factor of two between (i) and (ii), which might also be due to a higher amount of particles required in the impact region than FEM elements. Therefore, the overall run time is still three times shorter than (ii). If the influence of the target is neglected by using a rigid wall (iv), the run time reduces to six minutes. However, this does not describe the impact behaviour correctly and is not an option for our application.

In conclusion, the hybrid meshing improves the run time by a factor of twelve compared to the classical approach with FE only. The main reason is that SPH does not affect the time step as much as FEM and no elements are distorted in the hybrid approach.

8.2.4 Final comparison

In this section, we compare the newly developed hybrid FEM-SPH method, which we call “SPH-H” in the following, and the optimised FE model (FEM) with the real-world experiments for different oblique angles (0°, 15°, 30°, 45°, 60°, and 75°). First, we discuss the qualitative results using a visualisation similar to the X-ray shadow images. Next, we show a quantitative comparison of the extracted translational and rotational velocities. Finally, we compare the largest remainder regarding its shape and size.

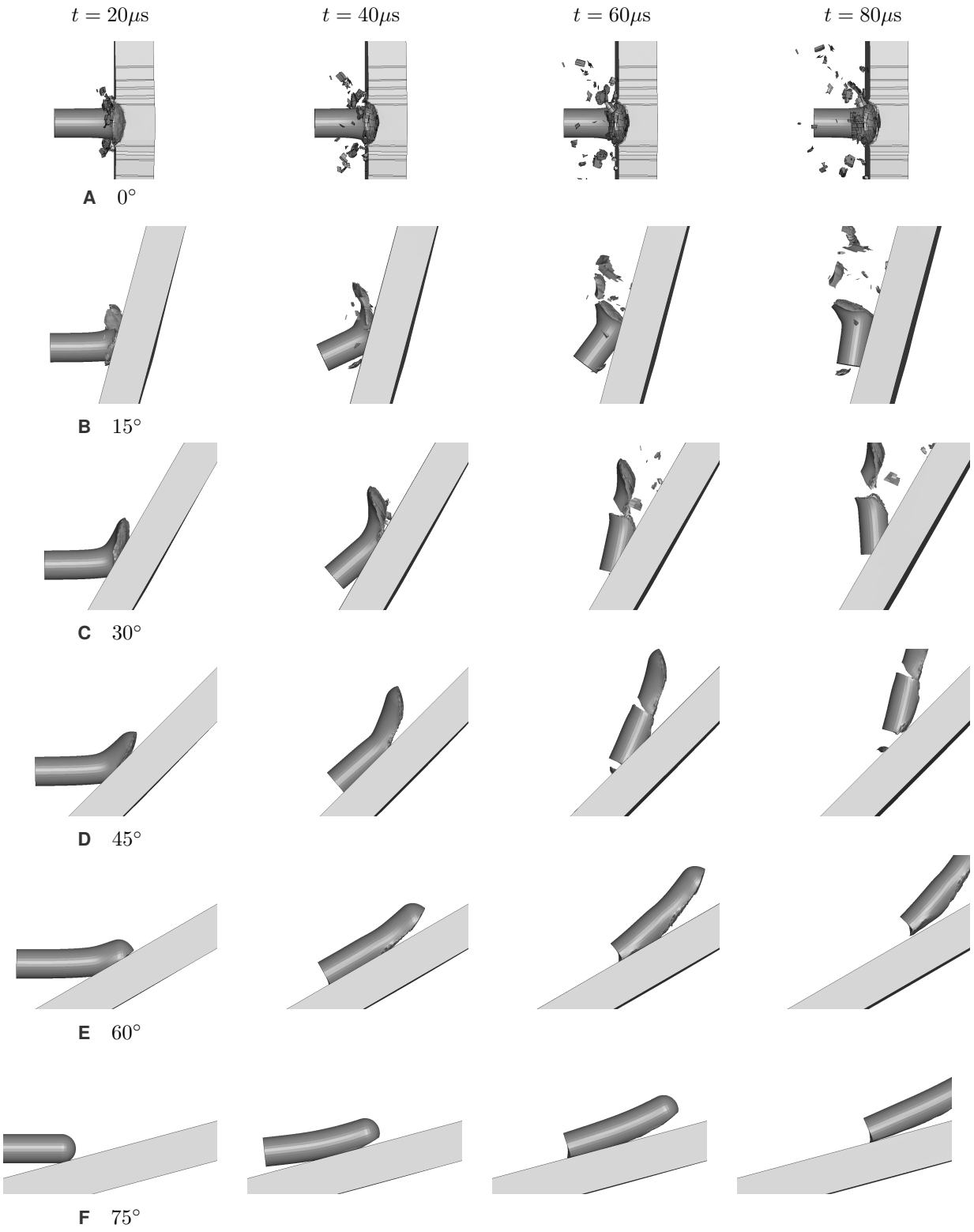

FIGURE 8.16 Application III: HVI of the surrogate: FEM results with the final model for different impact angles (rows) at different times after impact (columns).

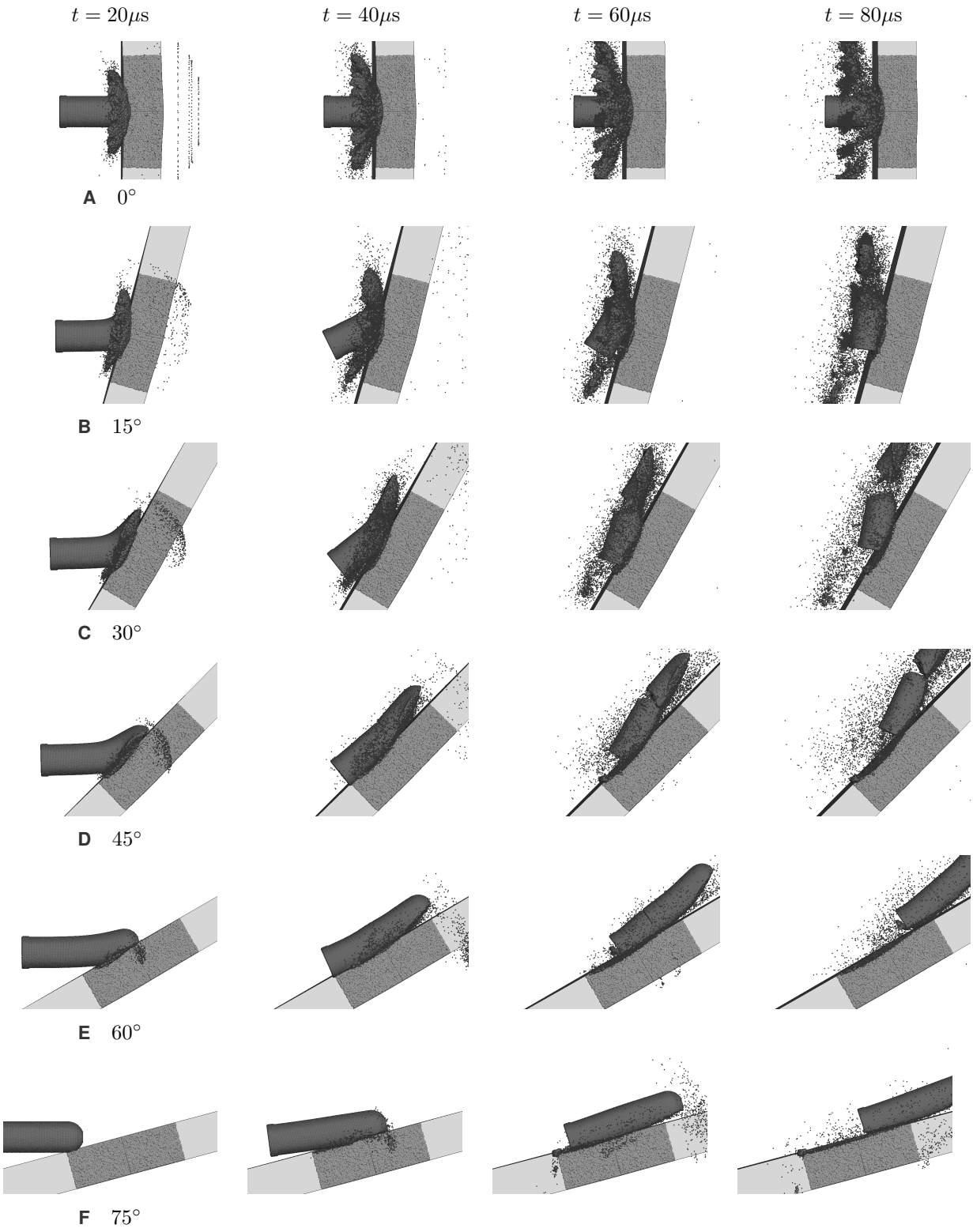

FIGURE 8.17 Application III: HVI of the surrogate: SPH-H results with the final model for different impact angles (rows) at different times after impact (columns).

Figure 8.16 shows the impact behaviour predicted with the FE model at four time steps (20 μs, 40 μs, 60 μs, and 80 μs after impact). For the perpendicular impact case, we hide one symmetry plane of the plate to uncover the mushrooming of the impactor. Similar to the observations in the experiment, the tip is fragmented into small pieces. The final length of the impactor is about half of its initial length. For 15° obliquity, the fragmentation of the core results into larger fragments than for the perpendicular case. Due to the asymmetric deceleration at the plate (compare Figure 8.13), the surrogate obtains a rotational momentum, and the remainder shows plastic deformation. For 30° obliquity, the tip does not fragment any more but breaks into two pieces in the middle. The remainder starts to rotate as well, but at a lower angular velocity. For 45° obliquity, the critical angle of fracture is reached. The projectile cracks particularly late into two pieces. Nearly no fragmentation occurs apart from the crack. For 60° and 75° obliquity, the surrogate ricochets off and stays intact. The amount of plastic deformation, and the angle of deflection, is larger for the 60° case than for the 75° case.

Figure 8.17 shows the analogous image to Figure 8.16 for SPH-H results. In comparison to the FEM results, a significant amount of particles are detaching during the impact. In all other aspects, similar behaviour is observed. The amount of tip fragmentation and rotation decreases for larger oblique angles. However, the rotation of the remainder is smaller than for the FEM results. The critical angle between fracture and no fracture is about 45°, too.

Since the most meaningful image is the one at $t = 80$ μs, we compare those of FEM, SPH-H, and the real-world experiment at this time step in Figure 8.18. Due to non-consistent exposure times in the real-world experiment, the figures show the exposure, which is closest to 80 μs after impact. In the direct comparison, we can see that in terms of the fragmentation, the real-world experiment predicts a more brittle behaviour of the core and the fragment rotates faster. Also, the critical angle is flatter (60° instead of 45°). Besides these minor differences, the FEM and SPH-H agree well in their description with the experiments. Since we use two fundamentally different numerical approaches, the difference is likely due to something other than the numerical description, such as the description of the material. Therefore, a further improvement of the accordance between numerical and real-world experiments requires an improvement of the material description, which is out of scope here. In the following, we see that the proposed model already predicts the rebound angle and the size of the remainder precisely.

Figure 8.19 shows the translational velocity components, the rotation velocity, and the deflection angle of the remainder. The regression curve of the experiment and the corresponding values have been discussed in Figure 8.10 and are shown with reduced opacity to identify the data points obtained with FEM and SPH-H better. Each colour represents a different property. Figure 8.19A shows the velocity of the remainder after impact in flight direction v_x and perpendicular to flight direction v_y and the magnitude of the velocity v_{res}. Both numerical approaches predict the velocity component v_x accurately for the fracture case. For the case of an intact ricochet, SPH-H predicts a smaller value than observed in real-world. The velocity reduction might be due to an artificial, highly adhesive force during the interaction of the two contact partners. Since the magnitude of v_x is small for 15° and 30°, the values for v_{res} and v_y are almost identical. For these two angles, the value of v_y predicted with both numerical approaches is smaller than in the experiment. The difference to the real-world experiments is larger for the approximation with SPH-H than with the FEM approximation. For larger oblique angles, v_y coincides well with the experiments.

Figure 8.19B shows the rotational velocity in terms of the rotation of the remainder within 40 μs and the

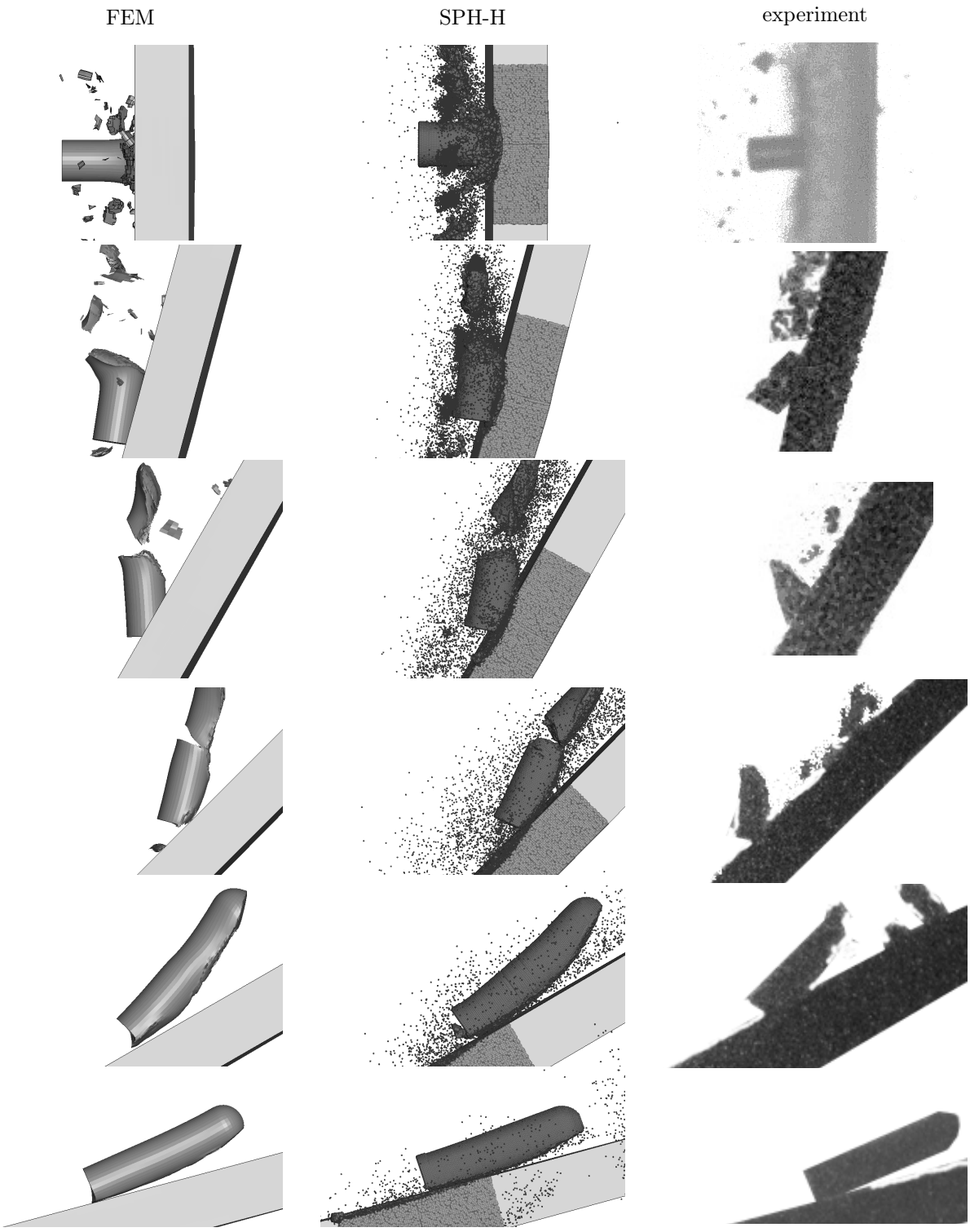

FIGURE 8.18 Application III: Comparison between FEM, SPH-H and experiment at $t = 80\mu$s after impact. Each row represents an impact angle $(0°, 15°, 30°, 45°, 60°, 75°)$.

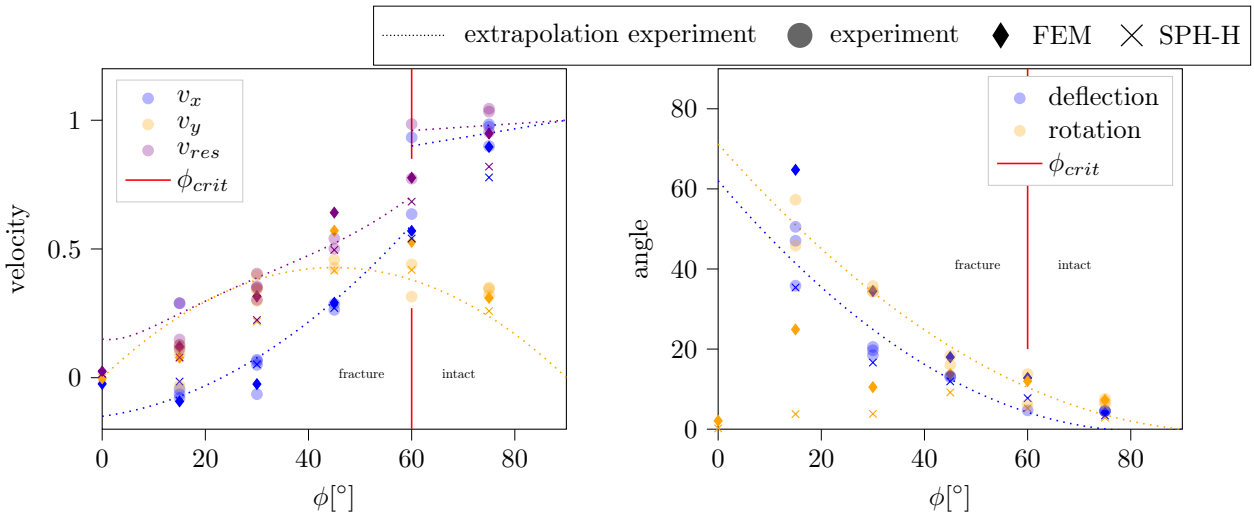

A residual velocity components **B** rotational velocity/ deflection angle

FIGURE 8.19 Application III: Quantitative comparison of the remainder for numerical simulation results with the real-world experiments. The experimental results are discussed in Figure 8.10A. Data points of the experiments are plotted with reduced opacity.

deflection angle towards the plate (compare Figure 8.7). The deflection predicted with SPH-H is closer to the experimental results than the FEM approximation. The rotation of the residual part is much smaller in both numerical experiments than in real-world. In particular, for 15° and 30°, SPH-H is barely predicting any rotation. It is not clear which mechanisms trigger the rotation and how to improve its prediction. According to Application II, it is strongly linked with the contact description but might also be triggered by inner material tension that is released after the impact, which is described with the constitutive equation.

Finally, we investigate the remainders of the surrogate in Figure 8.20. In the qualitative comparison of two selected angles 8.20A, we observe that SPH-H describes the material erosion on the bottom side, which is in contact with the plate during the impact, better than the FEM. In terms of the length, both numerical models correspond well with the real-world experiments. 8.20B elaborates on the quantitative metrics. Both numerical approaches predict an almost constant length of the surrogate in the "fracture" region, in contrast to a non-linear increase which is observed in real-world. The average value observed with SPH-H for the length corresponds to the largest value observed in real-world in the fracture region, and the average FEM value is close to the smallest value observed in real-world. In the "intact" region, the length predicted with SPH-H is slightly larger than the length predicted with the FEM. Regarding the mass of the ricochet, the SPH-H approximation is closer to the real-world observations than the FEM. The better accordance can be explained by the fact that SPH-H erodes more material on the contact side of the surrogate.

In conclusion, we showed that both numerical models predict the impact behaviour well concerning fractured and intact ricochet except for the following three limitations: (i) SPH-H does not predict the rotation of the remainder for small oblique angles, (ii) the FEM does not predict the erosion of elements on the contact surface of the surrogate, and (iii) both methods predict the critical angle between fractured and intact ricochet 15° smaller than observed in real-world and less fragmentation of the tip.

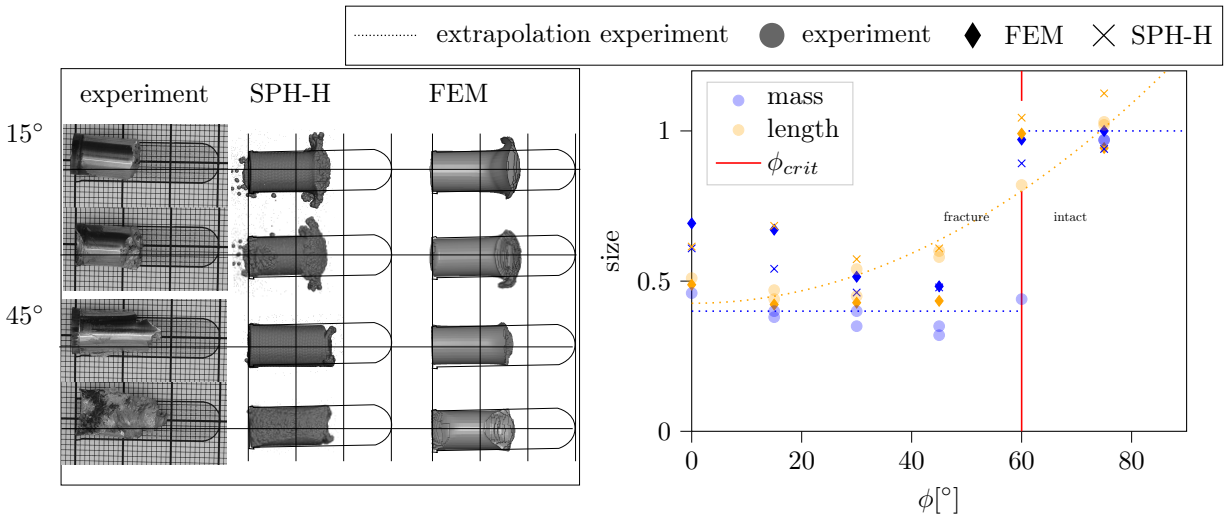

A qualitative comparison for 15° and 45° **B** quantitative comparison of the remainder size

FIGURE 8.20 Application III: Investigation of the remainder after impact. Only the largest fragment is evaluated, since the rest of the projectile fragmented in small pieces which could not be recovered.

8.2.5 Concluding remarks

We used the real-world data of the experiments with obliquity to validate our numerical model (FEM and SPH-H). Exemplary, we demonstrated the improvements implemented in the FEM (contact algorithm) and SPH-H (initial particle distribution and hybrid target). Also, we showed that, besides better accuracy in some aspects, the hybrid meshing improves the run time significantly. In a final comparison, we extended the investigation to the whole range of impact angles observed in the experiment. We identified the limitations of both models: while SPH-H is not describing the rotation correctly, the FEM does not predict the material erosion at the contact surface. Therefore, the FEM is better suited to predict the ricochet in terms of force transmission, and SPH-H is better suited to predict fracture and material erosion. Based on the differences observed between the numerical model and real-world experiments, also a better-suited material model might be required to describe the tip fragmentation correctly. In comparison to other studies, where the impactor consists of a different material than the target plate, and the material parameters can be adjusted arbitrarily for one of the two materials to match experimental and numerical results, we are using the same material for impactor and target. Thus, we cannot change the parameters of one of the bodies in contact individually to obtain the desired contact behaviour. Instead, the validation is only successful if the numerics and the material model are set correctly. Since we were able to reproduce the real-world results, we are confident that our model is—except for the limitations explained above—well-suited for this application.

8.3 Summary and discussion

This chapter is structured in two parts: In the first part, we showed a comprehensive analysis of the surrogate in real-world experiments concerning internal ballistics, external ballistics and terminal ballistics. For the latter, we conducted perpendicular and oblique TB experiments. The perpendicular impact tests are, in

particular, characterising the target response and failure mechanism at the target. Investigating this part of the problem was not the primary purpose of this work. Instead, we focus on the ricochet and the fragmentation of the surrogate and use the results of the perpendicular impact to set up the oblique experiments. In further investigations, these results can be valuable to improve the description of the material in terms of the failure mechanisms of the target.

In the second part, we use the oblique impact experiments to validate our numerical models for the surrogate (one FE model (FEM), and one hybrid FEM-SPH model (SPH-H)). We show for FEM that the findings for the contact description in Application II are transferable to our application and compulsory to describe the impact correctly. In terms of SPH, we compare different discretisation techniques for the distribution of SPH particles of the surrogate. For an accurate description, a uniform distance between particles improves the stability of SPH. For this application, a definition of the particles based on cylindrical coordinates is best suited as it represents the impacting bodies best and prevents cracks due to regular discretisation patterns. In the next chapter, we see other examples at a higher velocity where only SPH-H is describing the impact correctly. However, for this application, both strategies, FEM and SPH-H, have advantages in the description of some details. In terms of run time, SPH-H is faster by a factor of twelve compared to the FEM approach. The reason for the shorter run time is that the time step changes only little over the simulated time with SPH during impact, as the particles do not deform like the elements in FEM, which then demand for a restrictive time step. The model setup for an SPH-H model is straight forward with the implemented software.

To determine the range of applications of SPH-H, we present some selected applications that are set up with our preprocessing software and calculated with *LS-DYNA*® in the next chapter.

9

Real-world applications

The main contribution of the numerical part is the black-box preprocessor of HVI cases (compare Section 4.4). In the last chapters, we determined suitable settings for the numerical simulations. In particular, we investigated the contact and a proper discretisation of the impactor. These findings are implemented in the preprocessor and applied for all applications shown in this chapter. Typical applications in TB differ in terms of the material and shape of the interacting bodies. Therefore, the material parameters and the outline of the impactor have to be user-defined. Our preprocessor generates the rest of the setup for many more applications than the ones presented so far. We implemented particular features for the target and the impactor to be able to treat a wide range of applications. The target can either be clamped in a device, which corresponds to the typical setup of small calibre projectile TB experiments, or a concrete wall restricts the motion, which is the usual approach for depth-of-penetration tests of long rod penetrators. Furthermore, perforated plates or sandwich layers of different material are of particular interest and have also been included. In terms of the impactor, the common problem is that it consists of different layers. Therefore, we support multi-layered projectiles in our software. In the following, we present three applications to showcase the capabilities of our preprocessor and give an outlook on how the software can be used in future applications.

9.1 Energetic material fragments

One of the successor projects of this thesis investigates energetic materials. Here, the TB-template could be directly applied by only adding the respective material and changing the geometry. In the case depicted in Figure 9.1, a fragment is launched against an armour steel plate. The fragment is made of Auer material [166] and has a diameter of 5 mm. The impact velocity is 1225 m/s, and the steel plate has a thickness of 5 mm. The fracture patterns correspond well with those published by Woodward [228] depicted in Figure 2.6. The main advantage of our software is that it creates both geometries with the same discretisation, thus, the user can define it for the whole geometry by changing a single parameter. Therefore, we can easily realise different fragment and plate sizes with a consistent discretisation.

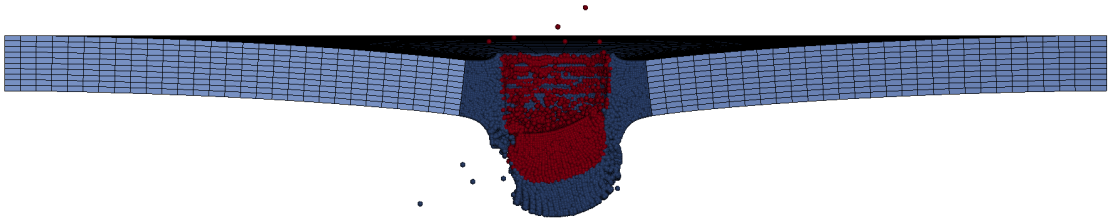

FIGURE 9.1 Impact of an energetic fragment (Auer steel, $d = 5$ mm, $v_0 = 1225$ m/s) against an armour steel plate ($t = 5$ mm). The fracture patterns correspond to those published in Woodward [228].

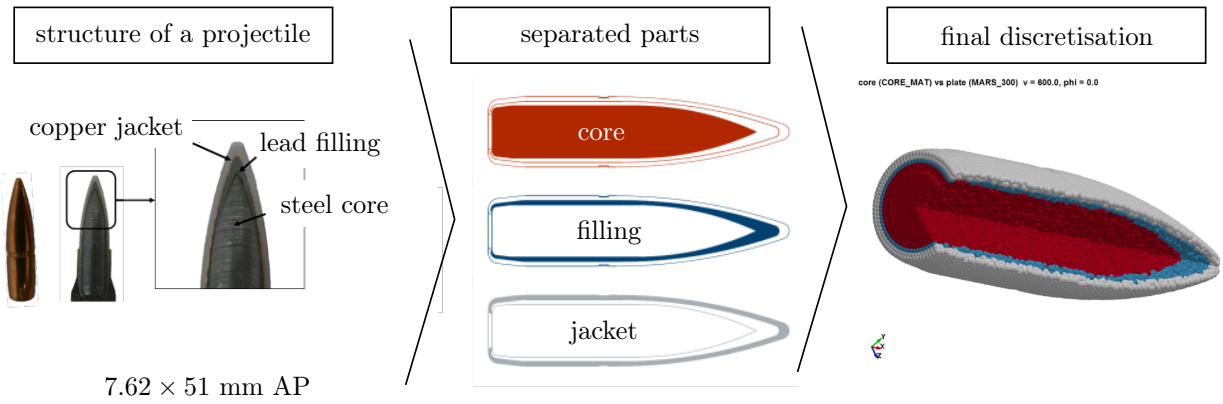

FIGURE 9.2 Discretisation of the 7.62 × 51 mm M352 NATO projectile that consists of different material layers. First, the outline of the layers is extracted and, then, the respective distribution is generated.

9.2 Small calibre projectile

The difference between a small calibre projectile and our surrogate, in terms of composition, is that the small calibre projectile is composed of different materials. We compared two approaches to realise the SPH particle distribution for this application. First, we populated the SPH particles for each part separately. Second, we populated them for the entire geometry and assigned each particle to the correct material. While the first approach triggered initial tension in the projectile due to a non-uniform distribution of particles that were overlapping, the second approach creates a stable discretisation for bullets composed of different parts. Figure 9.2 depicts the exemplary discretisation of the M352 NATO projectile using the second approach. We applied the numerical model to perpendicular and oblique impact. The results are shown in Figure 9.3. For the perpendicular impact 9.3A, the brass jacket peels off, which we also observed in real-world experiments. For the oblique impact 9.3B, we predict a fracture of the ricochet as found in the real-world experiment 9.3C. Thus, without going too much into detail, our model is well able to reproduce the TB behaviour of the M352 NATO projectile qualitatively.

Creating the setup with our software has the following advantages for these kind of applications: First, creating the SPH-particle distribution of the projectile manually is challenging. Second, in comparison to the manual setup, the software arranges the plate correctly for each oblique angle. Without the use of our software, the user needs to rotate the plate and move the projectile such that it stays in the SPH region of

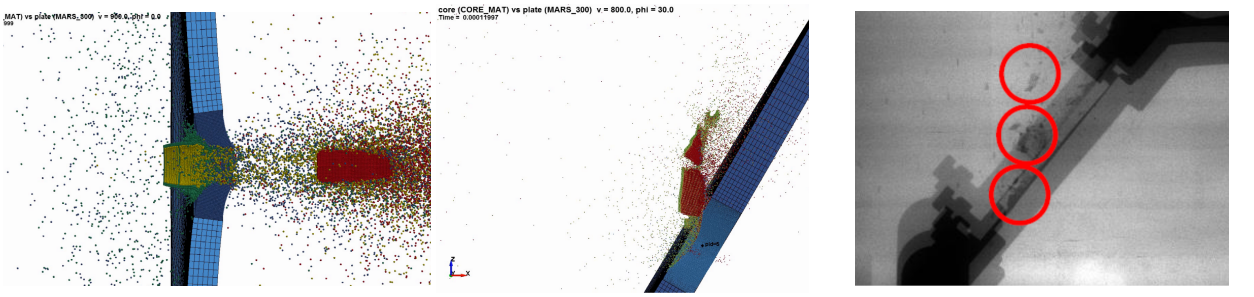

A perpendicular impact (SPH) **B** oblique impact (SPH) **C** oblique impact (experiment)

FIGURE 9.3 Application of the numerical model for the M352 NATO projectile. The particle distribution is stable during impact and reproduces cracks during oblique impact.

the hybrid mesh of the target domain during the impact.

A second application which ISL investigates is the performance of perforated plates. We implemented a modification, such that our software can generate the particle distribution for a perforated plate automatically. The user defines the dimensions and distances between the holes in the plate. Figure 9.4 shows that the results obtained with our numerical model are in good agreement with the real-world experiments. The model describes, in particular, the damage at the plate and the extruded plug very accurately. For the impactor, the model can still be improved. The material behaves much more brittle in real-world than in the numerical description. In comparison to the FEM results, the run time and the time needed to set up the model are one of the main advantages of our approach besides accuracy. The user can define similar applications with the perforated plate template.

9.3 Hyper-velocity impact

The hypervelocity impact of kinetic energy penetrators is the last example which we show in this outlook. In comparison to previous examples the velocity is significantly higher and almost hydrodynamic behaviour occurs. Hydrodynamic behaviour means that the strength of the material is secondary. Instead, the density of the impactor and the target, and the impact velocity determine the impact behaviour. As a simplification, these impacts can be described by the Bernoulli equation for fluids. Therefore, Eulerian codes are often used to simulate hydrodynamics (e.g., CTH of Sandia Labs [143]). SPH was initially developed for hydrodynamic applications as well.

We have used our framework to simulate the impact of kinetic energy penetrators with various shapes and materials. Most of these simulations are confidential, as we computed them for industrial partners. Figure 9.5 shows the qualitative behaviour of an exemplary rod. The principal value of investigation of these studies is the depth of penetration (d_P). Qualitatively, we are interested in the crater shape. SPH reproduces both properties well: the deviation regarding the predicted d_P is less than 5% with our hybrid SPH model compared to 30% with the original FE model. In particular, the setup and the run time were considerably faster and, therefore, allowed to compare different discretisation and boundary conditions within a single day. On the other hand, a single FEM simulation with a suitable discretisation requires an entire day, and a comprehensive investigation takes several weeks. We explained the reason for the improved run time of our model in Section 8.2.3.

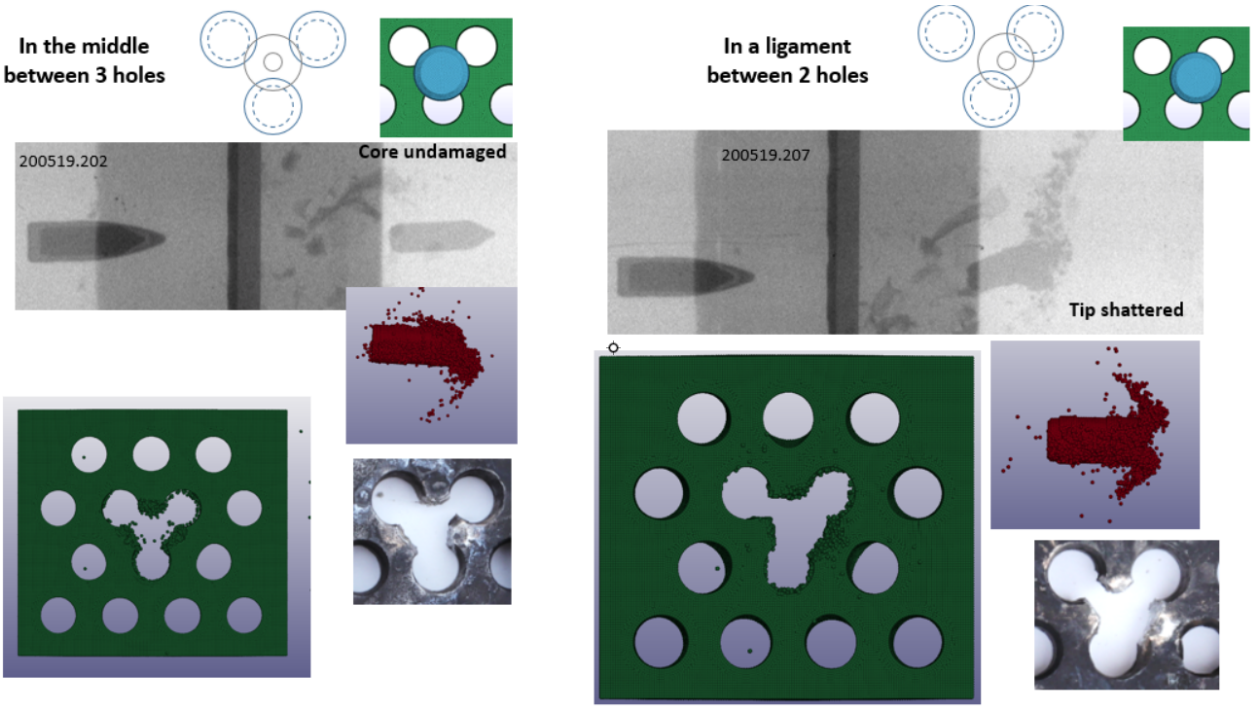

FIGURE 9.4 Two exemplary cases of the impact against a perforated plate. We compare the damage of the target and the projectile. In particular, the target deformation is in good agreement with the experiment.

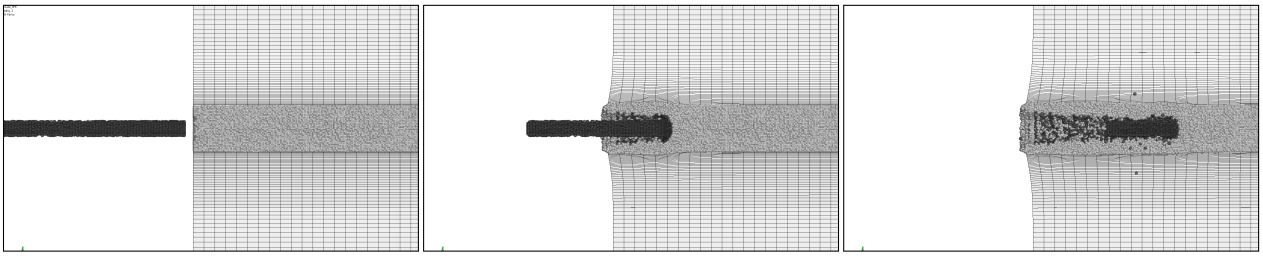

before impact erosion of rod final depth of penetration

FIGURE 9.5 Penetration of an aluminum block by an armour-steel long rod (MARS®190) with 1500 m/s. We observe hydrodynamic erosion of the rod. In the final state, part of the rod remains. For higher impact-velocity, the entire rod is eroded.

9.4 Conclusion

Our numerical template is applicable to a wide range of applications. For three typical example cases, we prove that our template is more efficient and more accurate. In particular, for hyper-velocity impact, the SPH approach is superior to standard FEM. Another main advantage is that the model can be set up quickly and consistently.

10

Conclusion

State of the art numerical methods are not predictive in terminal ballistics (TB) and need extensive validation.

In this work, we first discussed the general continuum mechanics framework with particular regard to all components required during TB modelling and fracture description. The result of this derivation is the underlying boundary value problem of continuum mechanics. Numerical solvers approximate this set of equations. The numerical solvers FEM and SPH are compared in this work, the first being the state of the art method in simulating TB, and the second being a promising alternative which was initially designed to predict hydrodynamic behaviour. We outlined the limitations of both methods and tailor-made solutions. E.g., for FEM, the locking has to be addressed by a suitable element formulation, and for SPH, the tensile instability can be solved with stabilisation techniques such as shifted integration.

Next, specific modelling techniques that are used in both numerical solvers are outlined, such as material models, contact description and coupling options. The first main contribution from the modelling point of view is a black-box HVI framework that combines all the findings of suitable parameters and options for TB. This framework allows the user to define the geometry and the material parameters and generates the entire input-deck for the simulation. The second main contribution is a framework to detect fragments from a point cloud which is required to process the SPH simulations.

Next, we described the methods to process real-world experiments. The first contribution is a mathematical framework to calculate the yaw angle from perforated paper sheets. The main contribution for the evaluation of real-world experiments is a software (FXRIP) to detect and track fragments in X-ray images which contain considerable noise and parallax. We suggest a methodology to reduce the noise, eliminate the parallax and extract the velocity (translational and rotational) from the images.

To define the back-end of the numerical black-box HVI framework, we use three dedicated applications:

Application I investigated the natural fragmentation of explosively driven cylinder rings to quantify the influence of different settings on the resulting fragmentation patterns. We identified an additional criterion

in the fracture model that prevents damage during compression as the essential modification for fracture description in highly dynamic events. The material parameters and the plasticity algorithm are secondary.

Application II is an entirely numerical experiment of a sphere impacting a plate. We compared different contact settings for SPH and FEM and determined a suitable parameter set that can be applied to TB applications. The parameters are implemented in the black-box model and applied in Application III.

Application III deals with the high-velocity impact of a projectile surrogate. The surrogate and the experimental setup of this application have been developed in the scope of this work. We performed a comprehensive analysis with real-world experiments to understand the internal, external, and terminal ballistics of the surrogate. Our software FXRIP is applied to extract the velocities which are used to validate our two numerical models. The first model is an improved FEM setup (FE model), and the second model is created with the black-box HVI framework. This framework generates a hybrid FEM-SPH discretisation of the plate and an SPH discretisation of the impactor (hybrid model). We validated the FEM and the hybrid model and observe, in particular, a run time improvement of the hybrid approach. Both the FEM and the hybrid approach describe the impact accurately due to the improved contact settings determined in Application II.

The real strength of our black-box model can be seen in real-world applications. With minimal effort, we set up four different applications that can hardly be described with FEM. Our model is superior in accuracy, run time and setup time. Therefore, it is a reliable framework to predict the impact behaviour in TB.

This work gives deep insight into the numerical description of TB. For future applications, we developed software to analyse real-world experiments. The software allows to analyse experiments faster and with better accuracy. Furthermore, we implemented a black-box model that can generate the input for *LS-DYNA®* simulations for a wide range of impact scenarios. The black-box model simplifies the work significantly and allows using numerical simulations for the computer-aided design of protective structures and not only to reproduce real-world experiments.

Our framework opens up many possibilities to predict TB behaviour and accelerate the development of advanced protective structures. We look into a promising future of computer-aided design in TB.

Bibliography

[1] M. A. Abbas. Comparison of convergence rate of higher order tetrahedral and hexahedral elements for linear static structural FEA. International Journal of Pure and Applied Mathematics, 119(10):1927–1933, 2018.

[2] B. Adams. Simulation of ballistic impacts on armored civil vehicles. Master's thesis, Eindhoven University of Technology, 2003.

[3] J. Ahrens, B. Geveci, and C. Law. Paraview: An end-user tool for large data visualization. The visualization handbook, 717, 2005.

[4] E. Anderheggen, D. Ekchian, K. Heiduschke, and P. Bartelt. A contact algorithm for explicit dynamic FEM analysis. WIT Transactions on Engineering Sciences, 1, 1970.

[5] C. Anderson and S. Bodner. Ballistic impact: The status of analytical and numerical modelling. International Journal of Impact Engineering, 1988.

[6] J. Argyris, H. Balmer, J. Doltsinis, P. Dunne, M. Haase, M. Kleiber, G. Malejannakis, H.-P. Mlejnek, M. Müller, and D. Scharpf. Finite element method - the natural approach. Computer Methods in Applied Mechanics and Engineering, 17-18:1 – 106, 1979.

[7] J. Argyris and D. Scharpf. Finite elements in time and space. The Aeronautical Journal, 73(708):1041–1044, 1969.

[8] M. Backman and W. Goldsmith. The mechanics of penetration of projectiles into targets. International Journal of Engineering Science, 1978.

[9] D. S. Balsara. Von Neumann stability analysis of smoothed particle hydrodynamics - suggestions for optimal algorithms. Journal of Computational Physics, 121(2):357–372, 1995.

[10] A. Banerjee, S. Dhar, S. Acharyya, D. Datta, and N. Nayak. Numerical simulation of ballistic impact of armour steel plate by typical armour piercing projectile. Procedia Engineering, 173:347 – 354, 2017. Plasticity and Impact Mechanics.

[11] V. Barger and M. Osson. Classical Mechanics, A Modern Perspective. McGraw-Hill, 1973.

[12] R. S. Barsoum and R. H. Gallagher. Finite element analysis of torsional and torsional–flexural stability problems. International Journal for Numerical Methods in Engineering, 2(3):335–352, 1970.

[13] P. Barton, R. Deiterding, D. Meiron, and D. Pullin. Eulerian adaptive finite-difference method for high-velocity impact and penetration problems. Journal of Computational Physics, 240:76 – 99, 2013.

[14] M. Becker. Fragment detection algorithm for postprocessing high velocity impact and natural fragmentation. In Proceedings of 8th GACM Colloquium on Computational Mechanics, 2019.

[15] M. Becker, T. De Vuyst, M. Seidl, and M. Mehl. Investigation into improvements to constitutive modelling for natural fragmentation applications. Journal of Computational Mechanics, 2021 (tbp).

[16] M. Becker, M. Seidl, T. de Vuyst, M. Mehl, and M. Souli. Numerical and experimental evaluation of natural fragmentation of explosively driven cylinders rings. In Proceedings of the Light-Weight Armor Group Symposium 2019, 2019.

[17] M. Becker, M. Seidl, and M. Mehl. Numerical ricochet model of a 7.62 mm projectile penetrating an armor steel plate. In 15th International LS-DYNA Users Conference, 2018.

[18] R. Becker. Ring fragmentation predictions using the Gurson model with material stability conditions as failure criteria. International Journal of Solids and Structures, 39(13):3555 – 3580, 2002.

[19] N. Beckmann, H.-P. Kriegel, R. Schneider, and B. Seeger. The r*-tree: An efficient and robust access method for points and rectangles. SIGMOD Rec., 19(2):322–331, May 1990.

[20] R. Beckmann, R. Mella, and M. Wenman. Mesh and timestep sensitivity of fracture from thermal strains using peridynamics implemented in Abaqus. Computer Methods in Applied Mechanics and Engineering, 263:71–80, 2013.

[21] S. Beissel and T. Belytschko. Nodal integration of the element-free Galerkin method. Computer methods in applied mechanics and engineering, 139(1-4):49–74, 1996.

[22] T. Belytschko, K. W. Liu, and B. Moran. Nonlinear finite elements for continua and structures. Wiley, 2013.

[23] T. Belytschko and M. O. Neal. Contact-impact by the pinball algorithm with penalty and Lagrangian methods. International Journal for Numerical Methods in Engineering, 31(3):547–572, 1991.

[24] W. Benz. Smooth particle hydrodynamics: a review. In The numerical modelling of nonlinear stellar pulsations, pages 269–288. Springer, 1990.

[25] J.-M. Bergheau. How many Gauss points are needed for a full integration of an 8-node solid brick element? does it depend on the degree of the shape functions?, 03 2015.

[26] R. Biswas and R. C. Strawn. Tetrahedral and hexahedral mesh adaptation for CFD problems. Applied Numerical Mathematics, 26(1-2):135–151, 1998.

[27] T. Borvik, M. Langseth, O. Hopperstad, and K. Malo. Ballistic penetration of steel plates. International Journal of Impact Engineering, 22(9):855 – 886, 1999.

[28] T. Borvik, L. Olovsson, S. Dey, and M. Langseth. Normal and oblique impact of small arms bullets on AA6082-T4 aluminium protective plates. International Journal of Impact Engineering, 38(7):577–589, 2011.

[29] X. Bourdin, X. Trosseille, P. Petit, and P. Beillas. Comparison of tetrahedral and hexahedral meshes for organ finite element modeling: an application to kidney impact. In 20th International technical conference on the enhanced safety of vehicle, Lyon, 2007.

[30] A. F. Bower. Applied mechanics of solids. CRC press, 2009.

[31] G. Bradski. The OpenCV library. Dr. Dobb's Journal of Software Tools, 2000.

[32] L. Bresciani, A. Manes, T. Romano, P. Iavarone, and M. Giglio. Numerical modelling to reproduce fragmentation of a tungsten heavy alloy projectile impacting a ceramic tile: Adaptive solid mesh to the SPH technique and the cohesive law. International Journal of Impact Engineering, 87:3 – 13, 2016. SI: Experimental Testing and Computational Modeling of Dynamic Fracture.

[33] M. Brünig and L. Driemeier. Numerical simulation of Taylor impact tests. International Journal of Plasticity, 23(12):1979 – 2003, 2007.

[34] A. Buades, B. Coll, and J.-M. Morel. Non-local means denoising. Image Processing On Line, 1:208–212, 2011.

[35] M. C. A formulation of finite elastoplasticity based on dual co- and contravariant eigenvector triads normalized with respect to a plastic metric. Computer Methods in Applied Mechanics and Engineering, 1998.

[36] J. Canny. A computational approach to edge detection. IEEE Transactions on pattern analysis and machine intelligence, (6):679–698, 1986.

[37] T. Cesko. Implementierung einer Erweiterung zur Behandlung von Hochgeschwindigkeitsaufprall mit dem SiPER SPH-Code. Master's thesis, University of Stuttgart, 2019.

[38] J.-S. Chen, C. Pan, C.-T. Wu, and W. K. Liu. Reproducing kernel particle methods for large deformation analysis of non-linear structures. Computer Methods in Applied Mechanics and Engineering, 139(1):195 – 227, 1996.

[39] P. G. Ciarlet, M. Schultz, and R. Varga. Numerical methods of high-order accuracy for nonlinear boundary value problems. Numerische Mathematik, 9(5):394–430, 1967.

[40] A. Cifuentes and A. Kalbag. A performance study of tetrahedral and hexahedral elements in 3-D finite element structural analysis. Finite Elements in Analysis and Design, 12(3):313 – 318, 1992.

[41] S. J. Cimpoeru. The mechanical metallurgy of armour steels. Technical report, Defence Science and Technology Group Fishermans Bend VIC Australia, 2016.

[42] R. W. Clough. The finite element method in plane stress analysis. In Proceedings of 2nd ASCE Conference on Electronic Computation, Pittsburgh Pa., Sept. 8 and 9, 1960, 1960.

[43] M. Cockcroft and D. Latham. Ductility and the workability of metals. Journal of the Institute of Metals, 1968.

[44] A. Collé, J. Limido, and J.-P. Vila. An accurate SPH scheme for dynamic fragmentation modelling. In EPJ Web of Conferences, volume 183, page 01030. EDP Sciences, 2018.

[45] S. Collins. Challenges of urban cities in 2035 - NATO needs to act today to prepare the alliance for the future. Allied Commander Transformation, 2015.

[46] G. Corbett, S. Reid, and W.Johnson. Impact loading of plates and shells by free-flying projectiles: A review. International Journal of Impact Engineering, 1996.

[47] R. Courant. Variational methods for the solution of problems of equilibrium and vibrations. Bull. Amer. Math. Soc., 49:1–23, 1943.

[48] G. Cowper and P. Symonds. Strain hardening and strain rate effects in the impact loading of cantilever beams,. Technical report, Brown Univ., Div. of Appl. Mech, 1952.

[49] T. De Vuyst and R. Vignjevic. Total Lagrangian SPH modelling of necking and fracture in electromagnetically driven rings. International Journal of Fracture, 180(1):53–70, 2013.

[50] T. De Vuyst, R. Vignjevic, and J. Campbell. Coupling between meshless and finite element methods. International Journal of Impact Engineering, 31:1054–1064, 2005.

[51] T. De Vuyst, R. Vignjevic, J. Campbell, A. Klavzar, and M. Seidl. A study of the effect of aspect ratio on fragmentation of explosively driven cylinders. Procedia Engineering, 204:194–201, 2017.

[52] W. Deal. Measurement of Chapman-Jouguet pressure for explosives. The Journal of Chemical Physics, 27(3):796–800, 1957.

[53] P. Degond and M. Tang. All speed scheme for the low mach number limit of the isentropic Euler equations. Communications in Computational Physics, 10(1):1–31, 2011.

[54] W. Dehnen and H. Aly. Improving convergence in smoothed particle hydrodynamics simulations without pairing instability. Monthly Notices of the Royal Astronomical Society, 425(2):1068–1082, 2012.

[55] B. M. Dobratz. LLNL explosives handbook: properties of chemical explosives and explosives and explosive simulants. Technical report, Lawrence Livermore National Lab., CA (USA), 1981.

[56] M. Dolinski and D. Rittel. Experiments and modeling of ballistic penetration using an energy failure criterion. Journal of the Mechanics and Physics of Solids, 83:1–18, 2015.

[57] M. Dolinski, D. Rittel, and A. Dorogoy. Modeling adiabatic shear failure from energy considerations. Journal of the Mechanics and Physics of Solids, 58(11):1759–1775, 2010.

[58] Q. Du and D. Wang. Recent progress in robust and quality Delaunay mesh generation. Journal of Computational and Applied Mathematics, 195(1):8 – 23, 2006. Special Issue: The International Symposium on Computing and Information (ISCI2004).

[59] C. Dyka and R. Ingel. An approach for tension instability in smoothed particle hydrodynamics SPH. Computers & Structures, 57(4):573 – 580, 1995.

[60] P. e. a. Elek. Determination of detonation products equation of state from cylinder test: analytical model and numerical analysis. Thermal science, 19(1):35–48, 2015.

[61] T. Erhart. Strategien zur numerischen Modellierung transienter Impaktvorgaenge bei nichtlinearem Materialverhalten. PhD thesis, University of Stuttgart, 2004.

[62] T. N. Erke Wang and R. Rauch. Back to elements - tetrahedra vs. hexahedra. In Proceedings of the 2004 international ANSYS conference, 2004.

[63] M. Ester, H.-P. Kriegl, J. Sander, and X. Xu. A density-based algorithm for discovering clusters in large spatial databases with noise. Prodeedings of the Second International Conference on Knowledge Discovery and Data Mining (KDD-96), 1996.

[64] N. Faderl and M. Becker. High-speed 300keV flash X-ray cinematography for investigations of the ballistic impact behavior of target materials and structures. Technical report, Institute of Saint-Louis, 2018.

[65] M. Fischer. PRODAS user manual - version 3.1. General Electric Armament Systems Dept, 1989.

[66] J. Forsberg. Segment based contact - soft=2. dynamore.se, 2020.

[67] T. Fras, C. C. Roth, and D. Mohr. Fracture of high-strength armor steel under impact loading. International Journal of Impact Engineering, 111:147–164, 2018.

[68] T. Fras, C. C. Roth, and D. Mohr. Dynamic perforation of ultra-hard high-strength armor steel: Impact experiments and modeling. International Journal of Impact Engineering, 131:256–271, 2019.

[69] T.-P. Fries, H. Matthies, et al. Classification and overview of meshfree methods. 2004.

[70] R. A. Gingold and J. J. Monaghan. Smoothed particle hydrodynamics: theory and application to non-spherical stars. Monthly notices of the royal astronomical society, 181(3):375–389, 1977.

[71] E. Giroux. HEMP user's manual. Technical report, California Univ., 1973.

[72] W. Goldsmith. Non-ideal projectile impact on targets. International Journal of Impact Engineering, 1999.

[73] I. J. S. Gómez. Implementación de las ecuaciones constitutivas de tipo elasto-plástico y elasto-termo-viscoplástico en el código de elementos finitos MORFEO e identificación de sus parámetros mediante análisis inverso por algoritmos genéticos. Aplicación a la ecuación constitutiva de Rusinek-Klepaczko. PhD thesis, Universidad Carlos III de Madrid, España, 2005.

[74] D. Grady. Fragmentation of rings and shells: the legacy of NF Mott. Springer Science & Business Media, 2007.

[75] D. Grady, M. Kipp, and D. Benson. Energy and statistical effects in the dynamic fragmentation of metal rings. Technical report, Sandia National Labs., Albuquerque, NM (USA), 1984.

[76] H. Grisaro and A. N. Dancygier. Numerical study of velocity distribution of fragments caused by explosion of a cylindrical cased charge. International Journal of Impact Engineering, 86:1 – 12, 2015.

[77] A. Gronheim. Standardization agreement (STANAG): Test procedure for measuring behind-armour effects of anti-armour ammunition. Technical report, Military agency for standardization, 1998.

[78] D. Gross and T. Seelig. Fracture mechanics: with an introduction to micromechanics. Springer, 2017.

[79] S. Grottel, M. Krone, C. Muller, G. Reina, and T. Ertl. MegaMol - a prototyping framework for particle-based vizualization. IEEE Transactions on Visualization, 2015.

[80] C. Guenther, D. L. Hicks, and J. W. Swegle. Conservative smoothing versus artificial viscosity. Technical report, Sandia National Labs., Albuquerque, NM (United States), 1994.

[81] R. W. Gurney. The initial velocities of fragments from bombs, shell and grenades. Technical report, Army Ballistic Research Lab Aberdeen Proving Ground Md, 1943.

[82] A. I. Gurson. Plastic flow and fracture behavior of ductile materials incorporating void nuleation, growth and interaction. PhD thesis, Brown University, 1975.

[83] J. Hallquist. LS-PREPOST manual, version 1.0. Livermore Software Technology Corporation, 2002.

[84] J. Hallquist, G. Goudreau, and D. Benson. Sliding interfaces with contact-impact in large-scale Lagrangian computations. Computer methods in applied mechanics and engineering, 51(1-3):107–137, 1985.

[85] J. O. Hallquist et al. LS-DYNA theory manual. Livermore software Technology corporation, 2019.

[86] J. O. Hallquist and R. G. Whirley. DYNA3D user's manual: (nonlinear dynamic analysis of structures in three dimensions): Revision 5. 1989.

[87] P. Harris. Some physics of the Gruneisen parameter. Technical report, no 4423, 1972.

[88] M. W. Heinstein, F. J. Mello, S. W. Attaway, and T. A. Laursen. Contact impact modeling in explicit transient dynamics. Computer methods in applied mechanics and engineering, 187(3-4):621–640, 2000.

[89] J. Hertel and S. Eugene. Comparison of analytic whipple bumper shield ballistic limits with CTH simulations. Technical report, Sandia National Labs., Albuquerque, NM (United States), 1993.

[90] R. Hill. Constitutive inequalities for isotropic elastic solids under finite strain. Department of Applied Mathematics and Theoretical Physics, 1970.

[91] G. Holzapfel. Nonlinear Solid Mechanics: A Continuum Approach for Engineering. Wiley, 2000.

[92] J. Hopkinson. Original papers by J. Hopkinson, Vol 2, B. Hopkinson, Ed, 1901.

[93] M. Hopp-Hirschler, M. S. Shadloo, and U. Nieken. A smoothed particle hydrodynamics approach for thermo-capillary flows. Computers & Fluids, 176:1 – 19, 2018.

[94] A. Hrennikoff. Solution of problems of elasticity by the framework method. J. appl. Mech., 1941.

[95] H. Huang, C. T. Dyka, and S. Saigal. Hybrid particle methods in frictionless impact-contact problems. International Journal for Numerical Methods in Engineering, 61(13):2250–2272, 2004.

[96] M. Ihmsen, J. Bader, G. Akinci, and M. Teschner. Animation of air bubbles with SPH. pages 225–234, 01 2011.

[97] Y. Itin and F. W. Hehl. The constitutive tensor of linear elasticity: Its decompositions, Cauchy relations, null Lagrangians, and wave propagation. Journal of Mathematical Physics, 54(4):042903, Apr 2013.

[98] S. J.C. Algorithms for static and dynamic multiplicative plasticity that preserve the classical return matpping schemes of the infinitesimal theory. Computer Methods in Applied Mechanics and Engineering, 1992.

[99] S. J.C. and M. C. Associative coupled thermoplasticity at finite strains: formulation, numerical analysis and implementation. Computer Methods in Applied Mechanics and Engineering, 1992.

[100] T. Jiang, J. Huang, Y. Wang, Y. Tong, and H. Bao. Frame field singularity correctionfor automatic hexahedralization. IEEE Transactions on Visualization and Computer Graphics, 20(8):1189–1199, 2013.

[101] Y. Jiang, T. Tay, L. Chen, and Y.-W. Zhang. Extended finite element method coupled with face-based strain smoothing technique for three-dimensional fracture problems. INTERNATIONAL JOURNAL FOR NUMERICAL METHODS IN ENGINEERING, 07 2015.

[102] J. W. Jingxiao Xu. Interaction methods for the SPH parts (multiphase flows, solid bodies) in LS-DYNA. In 13th International LS-DYNA Conference, 2014.

[103] G. R. Johnson. Artificial viscosity effects for SPH impact computations. International Journal of Impact Engineering, 18(5):477 – 488, 1996.

[104] G. R. Johnson and S. R. Beissel. Normalized smoothing functions for SPH impact computations. International Journal for Numerical Methods in Engineering, 39(16):2725–2741, 1996.

[105] G. R. Johnson and W. H. Cook. A constitutive model and data for metals subjected to large strains, high strain rates and high temperature. In Proceedings of the 7th International Symposium on Ballistics. Hague, Netherlands: IBC, pages 541–547, 1983.

[106] G. R. Johnson and W. H. Cook. Fracture characteristics of three metals subjected to various strains, strain rates, temperatures and pressures. Engineering Fracture Mechanics, 1985.

[107] D. Jones, D. Eakins, A. Savinykh, and S. Razorenov. The effects of axial length on the fracture and fragmentation of expanding rings. In EPJ Web of Conferences, volume 26, page 01032. EDP Sciences, 2012.

[108] W. Kabsch. A solution for the best rotation to relate two sets of vectors. Acta Crystallographica Section A, 32(5):922–923, Sep 1976.

[109] L. Kazaz. Untersuchung von Schmierstoff-Wirkungsgradverlusten in Zahnradgetrieben durch FSI mittels Ko-Simulation zwischen GTM und Pasimodo. Master's thesis, University of Stuttgart, 2016.

[110] B. Kilic and E. Madenci. Coupling of peridynamic theory and the finite element method. Journal of mechanics of materials and structures, 5(5):707–733, 2010.

[111] N. Kılıç, S. Bedir, A. Erdik, B. Ekici, A. Taşdemirci, and M. Güden. Ballistic behavior of high hardness perforated armor plates against 7.62 mm armor piercing projectile. Materials & Design, 63:427–438, 2014.

[112] M. Kipp and D. Grady. Experimental and numerical studies of high-velocity impact fragmentation. In High-pressure shock compression of solids II, pages 282–339. Springer, 1996.

[113] J. Klepaczko. Thermally activated flow and strain rate history effects for some polycrystalline FCC metals. Materials Science and Engineering, 18(1):121–135, 1975.

[114] S. Klinkel and W. Wagner. A geometrical non-linear brick element based on the EAS-method. International Journal for Numerical Methods in Engineering, 40(24):4529–4545, 1997.

[115] H. Kolsky. An investigation of the mechanical properties of materials at very high rates of loading. Proceedings of the physical society. Section B, 62(11):676, 1949.

[116] F. Koschnick. Geometrische Locking-Effekte bei Finiten Elementen und ein allgemeines Konzept zu ihrer Vermeidung. PhD thesis, Technical University of Munich, 2004.

[117] S. Kumar, I. Singh, and B. Mishra. A coupled finite element and element-free galerkin approach for the simulation of stable crack growth in ductile materials. Theoretical and Applied Fracture Mechanics, 70:49–58, 2014.

[118] J. Kury, H. Hornig, E. Lee, J. McDonnel, D. Ornellas, M. Finger, F. Strange, and M. Wilkins. Metal acceleration by chemical explosives. In fourth symposium (International) on Detonation, pages 3–13. US Government Printing Office Washington, DC, 1965.

[119] E. Lee, H. Hornig, and J. Kury. Adiabatic expansion of high explosive detonation products. Technical report, Univ. of California Radiation Lab. at Livermore, Livermore, CA (United States), 1968.

[120] E. H. Lee. Elastic-plastic deformation at finite strains. Journal of applied mechanics, 36(1):1–6, 1969.

[121] M. Lee and Y. J. Cho. Characterization of the ballistic limit curve for hypervelocity impact of sphere onto single plate. Journal of mechanical science and technology, 25(9):2457, 2011.

[122] U. Lee. Spectral element method in structural dynamics. 2009.

[123] W.-S. Lee and G.-W. Yeh. The plastic deformation behaviour of AISI 4340 alloy steel subjected to high temperature and high strain rate loading conditions. Journal of Materials Processing Technology, 71(2):224 – 234, 1997.

[124] T. Legaud. Improvement of satellites shielding under high velocity impact using advanced SPH method. In 12th European LS-DYNA Conference 2019, 2019.

[125] J. Lemaitre. A continuous damage mechanics model for ductile fracture. Transactions of the ASME. Journal of Engineering Materials and Technology, 107(1):83–89, 1985.

[126] Y. Li, Y. hua Li, and Y. quan Wen. Radial distribution of fragment velocity of asymmetrically initiated warhead. International Journal of Impact Engineering, 99:39 – 47, 2017.

[127] L. D. Libersky and A. G. Petschek. Smooth particle hydrodynamics with strength of materials. In H. E. Trease, M. F. Fritts, and W. P. Crowley, editors, Advances in the Free-Lagrange Method Including Contributions on Adaptive Gridding and the Smooth Particle Hydrodynamics Method, pages 248–257, Berlin, Heidelberg, 1991. Springer Berlin Heidelberg.

[128] L. D. Libersky, A. G. Petschek, T. C. Carney, J. R. Hipp, and F. A. Allahdadi. High strain Lagrangian hydrodynamics: a three-dimensional SPH code for dynamic material response. Journal of computational physics, 109(1):67–75, 1993.

[129] E. Lidén and A. Helte. The break-up tendency of long rod projectiles. Defence Technology, 12(2):177–187, 2016.

[130] J. Limido, M. Trabia, S. Roy, B. O'Toole, R. Jennings, W. L. Mindle, M. Pena, E. Daykin, R. Hixson, and M. Matthes. Modeling of hypervelocity impact experiments using gamma-SPH technique. In ASME 2017 Pressure Vessels and Piping Conference. American Society of Mechanical Engineers Digital Collection, 2017.

[131] T. Limin, C. Wanji, and L. Yingxi. Formulation of quasi-conforming element and Hu-Washizu principle. Computers & Structures, 19(1-2):247–250, 1984.

[132] L. Linsen, P. Rosenthal, P. Dobrev, S. Rosswog, T. Van Long, and V. Molchanov. Smoothviz: Visualization of smoothed particles hydrodynamics data. INTECH Open Access Publisher, 2011.

[133] M. B. Liu and G. R. Liu. Smoothed particle hydrodynamics (SPH): an overview and recent developments. Archives of computational methods in engineering, 17(1):25–76, 2010.

[134] W. K. Liu, S. Jun, S. Li, J. Adee, and T. Belytschko. Reproducing kernel particle methods for structural dynamics. International Journal for Numerical Methods in Engineering, 38(10):1655–1679, 1995.

[135] S. Lo. Volume discretization into tetrahedra II. 3D triangulation by advancing front approach. Computers & Structures, 39(5):501 – 511, 1991.

[136] J. Lubliner. Plasticity theory. Courier Corporation, 2008.

[137] L. B. Lucy. A numerical approach to the testing of the fission hypothesis. The astronomical journal, 82:1013–1024, 1977.

[138] D. Macdougall. Determination of the plastic work converted to heat using radiometry. Experimental mechanics, 40(3):298–306, 2000.

[139] R. W. Macek and S. A. Silling. Peridynamics via finite element analysis. Finite Elements in Analysis and Design, 43(15):1169–1178, 2007.

[140] D. S. Malkus and T. J. Hughes. Mixed finite element methods - reduced and selective integration techniques: a unification of concepts. Computer Methods in Applied Mechanics and Engineering, 15(1):63–81, 1978.

[141] S. J. Marcadet, C. C. Roth, B. Erice, and D. Mohr. A rate-dependent Hosford-Coulomb model for predicting ductile fracture at high strain rates. In EPJ Web of Conferences, volume 94, page 01080. EDP Sciences, 2015.

[142] F. McClintock. A criterion for ductile fracture by the growth of holes. Journal of applied mechanics, 1968.

[143] J. McGlaun, S. Thompson, and M. Elrick. CTH: A three-dimensional shock wave physics code. International Journal of Impact Engineering, 10(1):351 – 360, 1990.

[144] M. Meyers. Dynamic behavior of materials. J. Wiley and Sons, 1994.

[145] N. Moës, J. Dolbow, and T. Belytschko. A finite element method for crack growth without remeshing. International journal for numerical methods in engineering, 46(1):131–150, 1999.

[146] J. J. Monaghan. SPH compressible turbulence. Monthly Notices of the Royal Astronomical Society, 335(3):843–852, 2002.

[147] J. J. Monaghan and R. A. Gingold. Shock simulation by the particle method SPH. Journal of computational physics, 52(2):374–389, 1983.

[148] J. P. Morris. A study of the stability properties of smooth particle hydrodynamics. Publications of the Astronomical Society of Australia, 13:97–102, 1996.

[149] N. F. Mott. Fragmentation of shell cases. Proceedings of the Royal Society of London. Series A. Mathematical and physical sciences, 189(1018):300–308, 1947.

[150] N. Myagkov and V. Stepanov. On projectile fragmentation at high-velocity perforation of a thin bumper. Physica A: Statistical Mechanics and its Applications, 410:120 – 130, 2014.

[151] M. A. Neto, A. Amaro, L. Roseiro, J. Cirne, and R. Leal. Engineering computation of structures: the finite element method. Springer, 2015.

[152] A. Öchsner. Continuum damage and fracture mechanics. Springer, 2016.

[153] A. Öchsner. Computational statics and dynamics. Springer, 2020.

[154] L. Olovsson, J. Limido, J.-L. Lacome, A. G. Hanssen, and J. Petit. Modeling fragmentation with new high order finite element technology and node splitting. In EPJ Web of Conferences, volume 94, page 04050. EDP Sciences, 2015.

[155] S. Osovski, D. Rittel, P. Landau, and A. Venkert. Microstructural effects on adiabatic shear band formation. Scripta Materialia, 66(1):9–12, 2012.

[156] B. O'Toole, M. Trabia, R. Hixson, S. K. Roy, M. Pena, S. Becker, E. Daykin, E. Machorro, R. Jennings, and M. Matthes. Modeling plastic deformation of steel plates in hypervelocity impact experiments. Procedia Engineering, 103:458–465, 2015.

[157] M. Peleg, M. D. Normand, and M. G. Corradini. The Arrhenius equation revisited. Critical Reviews in Food Science and Nutrition, 52(9):830–851, 2012. PMID: 22698273.

[158] N. Perez. Introduction to fracture mechanics. In Fracture Mechanics, pages 53–77. Springer, 2017.

[159] T. H. Pian. Derivation of element stiffness matrices by assumed stress distributions. AIAA journal, 2(7):1333–1336, 1964.

[160] P. Piper. A concept for future military operations on urbanized terrain. Department of the Navy Marine Corps Combat Development Command, Quantico, 1997.

[161] A. Popp. Mortar Methods for Computational Contact Mechanics and General Interface Problems. PhD thesis, Technische Universitaet Muenchen, 2012.

[162] T. Rabczuk and J. Eibl. Simulation of high velocity concrete fragmentation using SPH/MLSPH. International Journal for Numerical Methods in Engineering, 56(10):1421–1444, 2003.

[163] S. A. Rackley. 23 - carbon dioxide transportation. In S. A. Rackley, editor, Carbon Capture and Storage (Second Edition), pages 595 – 611. Butterworth-Heinemann, Boston, second edition edition, 2017.

[164] P. W. Randles and L. D. Libersky. Smoothed particle hydrodynamics: Some recent improvements and applications. Computer methods in applied mechanics and engineering, 139(1-4):375–408, 1996.

[165] P. W. Randles and L. D. Libersky. Normalized SPH with stress points. International Journal for Numerical Methods in Engineering, 48(10):1445–1462, 2000.

[166] K. Reinhardt and H. Winkler. Cerium mischmetal, cerium alloys, and cerium compounds. Ullmann's encyclopedia of industrial chemistry, 2000.

[167] B. Ren, C. Wu, and E. Askari. LS-Dyna peridynamics for brittle fracture analysis. In 14th International LS-DYNA Users Conference. Detroit, MI, USA, 2016.

[168] J. Rice and D. Tracey. On the ductile enlargement of voids in triaxial stress fields. Journal of Mechanics and Physics of Solids, 1969.

[169] D. Rittel, A. Kidane, M. Alkhader, A. Venkert, P. Landau, and G. Ravichandran. On the dynamically stored energy of cold work in pure single crystal and polycrystalline copper. Acta Materialia, 60(9):3719–3728, 2012.

[170] Z. Rosenberg and E. Dekel. Terminal ballistics. Springer, 2012.

[171] A. Rusinek, J. Rodríguez-Martírnez, J. Klepaczko, and R. Pęcherski. Analysis of thermo-visco-plastic behaviour of six high strength steels. Materials & Design, 30(5):1748 – 1761, 2009.

[172] A. Rusinek and R. Zaera. Finite element simulation of steel ring fragmentation under radial expansion. International Journal of Impact Engineering, 34(4):799 – 822, 2007.

[173] A. Rusinek, R. Zaera, and J. Klepaczko. Constitutive relation in 3-D for a wide range of strain rates and temperatures - application to mild steels. International Journal of Solids and Structures, 2007.

[174] W. Rust. Non-linear finite element analysis in structural mechanics. Springer, 2015.

[175] J. Sarrate Ramos, E. Ruiz-Gironés, and F. J. Roca Navarro. Unstructured and semi-structured hexahedral mesh generation methods. Computational Technology Reviews, 10:35–64, 2014.

[176] M. Scapin. Shock-wave and high strain-rate phenomena in matter: modeling and applications. PhD thesis, Politecnico di Torino, 2013.

[177] H. Scharr. Optimal filters for extended optical flow. In B. Jähne, R. Mester, E. Barth, and H. Scharr, editors, Complex Motion, pages 14–29, Berlin, Heidelberg, 2007. Springer Berlin Heidelberg.

[178] C. Schmied and T. Erhart. Updated review of solid element formulations in LS-DYNA. 2020.

[179] W. J. Schroeder and M. S. Shephard. A combined octree/delaunay method for fully automatic 3-D mesh generation. International Journal for Numerical Methods in Engineering, 29(1):37–55, 1990.

[180] M. Seidl, T. Wolf, and R. Nuesing. Numerical investigations on ricochet of a spin-stabilised projectile on differently shaped target surfaces. In 30th ISB, Long Beach, 2017.

[181] F. Shang, Y. Gan, and Y. Guo. Hexahedral mesh generation via constrained quadrilateralization. PloS one, 12(5), 2017.

[182] S. Silling. Reformulation of elasticity theory for discontinuities and long-range forces. Journal of the Mechanics and Physics of Solids, 48(1):175 – 209, 2000.

[183] S. Silling. Peridynamic modeling of the Kalthoff–Winkler experiment. Submission for the, 2001.

[184] J. Simo and T. Hughes. Computational Inelasticity. Interdisciplinary applied mathematics. Springer, 1998.

[185] J. Simo and T. Hughes. Computational inelasticity, volume 7. Springer Science & Business Media, 2006.

[186] E. Stein and F.-J. Barthold. Der Ingenieurbau, Grundwissen: Werkstoffe, Elastizitaetstheorie, chapter Elastizitätstheorie, pages 165–428. Ernst und Sohn, 1996.

[187] R. Sundaria, A. Lehikoinen, A. Hannukainen, and A. Arkkio. Higher-order finite element modeling of material degradation due to cutting. In 2017 IEEE International Electric Machines and Drives Conference (IEMDC), pages 1–6. IEEE, 2017.

[188] J. Swegle, D. Hicks, and S. Attaway. Smoothed particle hydrodynamics stability analysis. Journal of Computational Physics, 116:123–134, 01 1995.

[189] J. W. Swegle, S. W. Attaway, M. W. Heinstein, F. J. Mello, and D. L. Hicks. An analysis of smoothed particle hydrodynamics. Technical report, Sandia National Labs., Albuquerque, NM (United States), 1994.

[190] S. Tanimura and J. Duffy. Strain rate effects and temperature history effects for three different tempers of 4340 VAR steel. International journal of plasticity, 2(1):21–35, 1986.

[191] G. I. Taylor. The use of flat-ended projectiles for determining dynamic yield stress I. theoretical considerations. Proceedings of the Royal Society of London. Series A. Mathematical and Physical Sciences, 194(1038):289–299, 1948.

[192] G. I. Taylor and H. Quinney. The plastic distortion of metals. Philosophical Transactions of the Royal Society of London. Series A, Containing Papers of a Mathematical or Physical Character, 230(681-693):323–362, 1931.

[193] X. Teng. High Velocity Impact Fracture. PhD thesis, MIT, 2005.

[194] F. Tornabene, N. Fantuzzi, and M. Bacciocchi. The strong formulation finite element method: Stability and accuracy. Frattura ed Integritá Strutturale, 29:251–265, 07 2014.

[195] M. J. Turner, R. W. Clough, H. C. Martin, and L. Topp. Stiffness and deflection analysis of complex structures. journal of the Aeronautical Sciences, 23(9):805–823, 1956.

[196] R. Vignjevic and J. Campbell. A penalty approach for contact in smoothed particle hydrodynamics. International Journal of Impact Engineering, 23(1, Part 2):945 – 956, 1999.

[197] R. Vignjevic and J. Campbell. Review of development of the smooth particle hydrodynamics (SPH) method. In Predictive modeling of dynamic processes, pages 367–396. Springer, 2009.

[198] R. Vignjevic, J. R. Reveles, and J. Campbell. SPH in a total Lagrangian formalism. CMC -Tech Science Press-, 4(3):181, 2006.

[199] J. Vila. On particle weighted methods and smooth particle hydrodynamics. Mathematical models and methods in applied sciences, 9(02):161–209, 1999.

[200] W. Wang, L. Sluys, and R. De Borst. Viscoplasticity for instabilities due to strain softening and strain-rate softening. International Journal for Numerical Methods in Engineering, 40(20):3839–3864, 1997.

[201] Web. Abaqus - SIMULIA Dassault Systems. `https://www.3ds.com/de/produkte-und-services/simulia/produkte/abaqus/abaqusstandard/`, 2020. accessed 03.06.2020.

[202] Web. ANSYS - official webpage. `https://www.ansys.com`, 2020. accessed 03.06.2020.

[203] Web. Computational and multi-scale mechanics group. `https://www.lstc-cmmg.org`, 2020. accessed 14.09.2020.

[204] Web. Gitlab repository PySPH. `https://github.com/pypr/pysph`, 2020. accessed 07.05.2020.

[205] Web. Impetus - official webpage. `https://www.impetus-afea.com`, 2020. accessed 07.05.2020.

[206] Web. Inpartik - official webpage. `http://www.inpartik.de/`, 2020. accessed 07.05.2020.

[207] Web. ISL - official webpage. `https://www.isl.eu/en/`, 2020. accessed 13.08.2020.

[208] Web. LS-DYNA - official webpage. `http://www.lstc.com/products/ls-dyna`, 2020. accessed 07.05.2020.

[209] Web. Pasimodo - official webpage. urlhttps://www.itm.uni-stuttgart.de/software/pasimodo/, 2020. accessed 07.05.2020.

[210] Web. PERMAS - official webpage. https://www.intes.de/kategorie_permas/einfuehrung, 2020. accessed 03.06.2020.

[211] Web. SIMSCALE- official webpage. https://www.simscale.com/, 2020. accessed 03.06.2020.

[212] Web. Spheric community - official webpage. https://spheric-sph.org/, 2020. accessed 07.05.2020.

[213] Y. Wen, D. L. Hicks, and J. W. Swegle. Stabilizing SPH with conservative smoothing. Technical report, Sandia National Labs., Albuquerque, NM (United States), 1994.

[214] M. L. Wilkins. Calculation of elastic-plastic flow. Technical report, California Univ Livermore Radiation Lab, 1963.

[215] P. Wriggers. Nonlinear finite element methods. Springer Science & Business Media, 2008.

[216] Y. Wu, C. Wu, and W. Hu. Parametric and convergence studies of the smoothed particle galerkin (SPG) method in semi-brittle and ductile material failure analyses. In 15th International LS-DYNA Users Conference, 2018.

[217] J. Xu, W. Hu, B. Ren, Y. Wu, X. Pan, and C. Wu. Adaptive smoothed particle hydrodynamics and higher order kernel function in LS-DYNA. In 2019 LS-DYNA China, 2019.

[218] J. Xu, Jingxiao; Wang. Node to node contact for SPH applied to multiple fluids with large density ratio. In 9th European LS-DYNA Conference, 2013.

[219] Y. H. Yoo and M. Lee. A three-dimensional FE analysis of large deformations for impact loadings using tetrahedral elements. Computational Mechanics, 30(2):96–105, Jan. 2003.

[220] E. Yreux. MLS-based SPH in LS-DYNA for increased accuracy and tensile stability. In 15th International LS-DYNA Users Conference, 2015.

[221] E. Yreux and J.-S. Chen. A quasi-linear reproducing kernel particle method. International Journal for Numerical Methods in Engineering, 109(7):1045–1064, 2017.

[222] R. Zaera, J. Rodríguez-Martínez, and D. Rittel. On the Taylor-Quinney coefficient in dynamically phase transforming materials. application to 304 stainless steel. International Journal of Plasticity, 40:185 – 201, 2013.

[223] H. Zhang and K. Ravi-Chandar. On the dynamics of necking and fragmentation - II. effect of material properties, geometrical constraints and absolute size. International journal of fracture, 150(1-2):3, 2008.

[224] H. Zhang and K. Ravi-Chandar. On the dynamics of localization and fragmentation - IV. expansion of Al 6061-O tubes. International Journal of Fracture, 163(1-2):41–65, 2010.

[225] J. Zhu, Y. Zheng, W. Li, Y. Yang, X. Wang, X. Qiao, and R. Li. Axial distribution of fragments from the dynamic explosion fragmentation of metal shells. International Journal of Impact Engineering, 123:140 – 146, 2019.

[226] O. C. Zienkiewicz and Y. K. Cheung. The finite element method for analysis of elastic isotropic and orthotropic slabs. Proceedings of the Institution of Civil Engineers, 28(4):471–488, 1964.

[227] O. C. Zienkiewicz and R. L. Taylor. The finite element method for solid and structural mechanics. Elsevier, 2005.

[228] J. A. Zukas. High Velocity Impact Dynamics, chapter Material failure at high strain rates, pages 65–125. John Wiley & Sons, Inc., 1990.

[229] J. A. Zukas. High Velocity Impact Dynamics. John Wiley & Sons, Inc., 1990.

[230] J. A. Zukas. Introduction to hydrocodes, volume 49. Elsevier, 2004.

[231] J. A. Zukas and D. R. Scheffler. Practical aspects of numerical simulations of dynamic events: effects of meshing. International journal of impact engineering, 24(9):925–945, 2000.